FACULTAD DE CIENCIAS
Departamento de Física Aplicada. Área de Óptica

# SPATIOTEMPORAL CHARACTERIZATION OF ULTRASHORT LASER PULSES

VNiVERSiDAD D SALAMANCA

CAMPUS DE EXCELENCIA INTERNACIONAL

**TESIS DOCTORAL**

**BENJAMÍN ALONSO FERNÁNDEZ**

**DIRECTORES**

**DR. ÍÑIGO JUAN SOLA LARRAÑAGA**

**DR. JULIO SAN ROMÁN ÁLVAREZ DE LARA**

Salamanca, Octubre 2012

VNiVERSiDAD
D SALAMANCA
Facvltad D Ciencias
Departamento Đ Física Aplicada

Don **ÍÑIGO JUAN SOLA LARRAÑAGA**, Profesor Contratado Doctor del Departamento de Física Aplicada de la Universidad de Salamanca

Don **JULIO SAN ROMÁN ÁLVAREZ DE LARA**, Profesor Contratado Doctor del Departamento de Física Aplicada de la Universidad de Salamanca

CERTIFICAN

Que la presente memoria titulada "**SPATIOTEMPORAL CHARACTERIZATION OF ULTRASHORT LASER PULSES**" ha sido realizada bajo su dirección por Don **BENJAMÍN ALONSO FERNÁNDEZ**.

Que dicha memoria presenta un trabajo de investigación original y constituye la Tesis Doctoral presentada por el doctorando para optar al grado de Doctor en Física con Mención Internacional.

Y para que conste, AUTORIZAN su presentación firmando la presente en Salamanca a 10 de octubre de 2012.

Fdo.: ÍÑIGO JUAN SOLA LARRAÑAGA. Fdo.: JULIO SAN ROMÁN ÁLVAREZ DE LARA.

# AGRADECIMIENTOS

Ahora que se acerca el final de la tesis, me dispongo a afrontar uno de los últimos pasos. Ha sido tanta la gente que ha estado ahí, que espero no dejar a nadie en el tintero.

En primer lugar, quiero mostrar mi gratitud hacia Íñigo y Julio, ellos han inspirado mis andaduras científicas desde casi el primer momento en el Fotón Charro. Aún recuerdo el día que conocí a Íñigo, siempre cercano y con curiosidad por lo nuevo, y una fuente interminable de ideas y motivación. Ha tenido más paciencia de la que yo jamás habría podido imaginar. Julio, gracias por aportar tu templanza y por no dejarte absorber por "el lado oscuro de la teoría". Últimamente, te veo en tu salsa en el laboratorio. Ha sido un placer trabajar y aprender con ellos sin barreras, tanto desde el punto de vista científico como del humano.

Tampoco querría crear intriga posponiendo la mención especial que merecen los *trigger boys*. Fue una época muy buena y divertida en el laboratorio, por la que pido disculpas a los que pudieran ser damnificados por el *show* de los *trigger boys*. Óscar para mí ha sido más que un buen compañero, y a él le agradezco su apoyo en mis inicios y etapa posterior en el laboratorio. Juntos sobrevivimos a las medidas sistemáticas… ¡y al aeropuerto de São Paulo enfurecido! Carolina y Rocío, ¡gracias por ser las más fieles seguidoras del *show*! Como todo evoluciona en esta vida, Íñigo incorporó un nuevo fichaje, Warein, siempre dispuesto para una *francesinha* y la *super bock* de las 11:30, y siempre al límite de la raya piano-karma.

Agradezco a todos los "habitantes del sótano" por todo lo que hemos vivido juntos durante estos años (Carlos, seguirás siendo de los nuestros aunque nos hayas abandonado…), por ayudarme a no sentirme solo ni loco al hacer experimentos de óptica con la luz apagada, viendo un láser invisible, o al salir a la calle y sufrir con la luz natural, o peor aún, no verla en todo el día. Al equipo técnico que siempre estaba ahí, con gran disposición y paciencia. Con ellos ha sido posible llevar a término esta tesis: Camilo P, Juan, Javi S, Isa G y, especialmente, Cruz.

Siempre recordaré los momentos *Toby*, "*unbelievable, this is unbelievable*", *entschuldigung*, Ferrol, Mahón, etc.

Quiero mostrar mi gratitud hacia todos los profesores del área, que lograsteis transmitirme vuestra pasión por la óptica, tanto en la carrera como en el máster: Isabel Arias, Luis Roso, Luis Plaja, Ana, Javi R, Enrique, Pablo…; y en general a todo el Fotón Charro: Mari Carmen, Camilo R, Ricardo…, que habéis demostrado ser una gran piña y un grupo muy acogedor. Gracias por vuestra "hiperactividad", también conocida como "proyectitis múltiple", ha sido muy positiva. Las gracias van también para Amelle, por su aportación para que ahora me encuentre "filamentoso".

Desde la hura o, siendo políticamente correcto, desde el garito, algo brotaba que a nadie ha dejado indiferente: era la OSAL. Gracias a todos los que habéis formado parte de ella y tirado del carro: José Antonio, Alexis, y a las nuevas generaciones: Fran, Camilo G, José Luis, Alex…

A Cristina y a Javier, también por su paciencia. Y a todos los que habéis ido llegando a la USAL y al CLPU: David, Mauri, Yaiza, Álvaro, Marina…

No me es posible dejar atrás a aquellos que me introdujeron en la investigación allá por el año 2007. Doy las gracias por ello al grupo de visión del Instituto de Óptica del CSIC y, especialmente, a Carlos Dorronsoro y a Susana Marcos. Gracias por brindarme esa oportunidad.

A nuestro "amigo" SAUUL he de agradecerle muchas cosas, de entre las que destacan las magníficas personas que he podido conocer repartidas por toda España: Juanma, Vincent… Y especialmente, el grupo de la UJI con el que ha habido una estrecha relación. Para mí no ha sido una colaboración, sino que han sido unos excelentes compañeros, a los que solo puedo "recriminar" que se nos acumulen las cañas por las celebraciones, tanto profesionales como personales. Gladys, Omel, Raúl, Jorge, Jesús, todos: ¡muchas gracias! Gracias también a la colaboración con Zaragoza.

Siempre tiré por mi tierra, Zamora, y río abajo pude encontrar Oporto. Allí comprobé que no somos tan distintos (de hecho, apenas pude hablar portugués…). Helder, ¡muchas gracias por tu acogida, por todo lo que me has enseñado, por la confianza que depositaste en mí y por iluminarme el camino hacia la gastronomía portuguesa! Agradezco a Miguel y a Francisco la enorme ayuda recibida en el laboratorio, y a todos los miembros del grupo por ayudarme a sentirme como si estuviera en mi tierra: Cledson, Ana, Isabel… Rosa, te incluyo aquí.

A los amigos que han tenido la virtud de la paciencia durante estos años de tesis, y que me han ayudado a "conectar con la realidad". No procede que haga aquí mención expresa a ningún ejemplo, ¿verdad, Jorge? Gracias a los que os habéis ido incorporando y a los que me acompañasteis desde el principio. Gracias por los momentos compartidos en Salamanca, y en especial a David, por aceptar desinteresadamente revisar el "spanglish" de esta tesis. Y, cómo no, al grupillo de Física por los años compartidos.

A mi familia quiero mostrarle un reconocimiento especial. Ellos son el apoyo incondicional e infinito para mí. Gracias a mi padre y a mis hermanas. Y en especial a mi madre, pues gracias a ti ahora estoy aquí, deseo que puedas disfrutar de este momento. Gracias también a mi "otra" familia por tratarme como uno más y por apoyarme durante todos estos años.

Y gracias a Sara, gracias por muchas cosas. Gracias por cada día, por tu paciencia, por tu apoyo y comprensión, por ser así de especial y por dar juntos el paso para formar nuestra familia. Gracias por crecer conmigo.

# CONTENTS

**PART I**: ***The technique STARFISH for spatiotemporal characterization***

# LIST OF ACRONYMS

| | |
|---|---|
| BBO | Beta-Barium Borate ($\beta$-$BaB_2O_4$) |
| BK7 | Boro-silicate |
| CCD | Charge-Coupled Device |
| CEP | Carrier-Envelope Phase |
| CM | Chirped Mirror |
| CPA | Chirped Pulse Amplification |
| DCM | Double-Chirped Mirror |
| DL | Diffractive Lens |
| DOE | Diffractive Optical Element |
| d-scan | Dispersion-scan |
| FFT | Fast Fourier-Transform |
| FP | Focal Plane |
| FraGZP | Fractal Generalized Zone Plate |
| FROG | Frequency Resolved Optical Gating |
| FT | Fourier-Transform |
| FTL | Fourier-Transform Limit |
| FTSI | Fourier-Transform Spectral Interferometry |
| FWHM | Full-Width at Half Maximum |
| FZP | Fractal Zone Plate |
| GDD | Group Delay Dispersion |
| GRENOUILLE | Grating-Eliminated No-nonsense Observation of Ultrafast Incident Laser Light E-fields |
| GVD | Group Velocity Dispersion |
| HCF | Hollow-Core Fiber |
| HHG | High Harmonic Generation |
| IFFT | Inverse Fast Fourier-Transform |

| | |
|---|---|
| IFT | Inverse Fourier-Transform |
| KDL | Kinoform Diffractive Lens |
| KDP | Potassium Dihydrogen Phosphate |
| LIBS | Laser-Induced Breakdown Spectroscopy |
| MIIPS | Multiphoton Intrapulse Interference Phase Scan |
| NA | Numerical Aperture |
| NSOM | Near-field Scanning Optical Microscopy |
| OAP | Off-Axis Parabola |
| OSA | Optical Spectrum Analyzer |
| POLLIWOG | POLarization Light Interference versus Wavelength of Only a Glint |
| QDST | Quasi-Direct Space-to-Time |
| SEA TADPOLE | Spatially Encoded Arrangement TADPOLE |
| SHG | Second Harmonic Generation |
| SI | Spectral Interferometry |
| SMA | Sub Miniature A |
| SPIDER | Spectral Phase Interferometry for Direct Electric-field ReconstructionSpectral Phase Interferometry for Direct Electric-field Reconstruction |
| SPM | Self Phase Modulation |
| SRSI | Self-Referenced Spectral Interferometry |
| STARFISH | SpatioTemporal Amplitude-and-phase Reconstruction by Fourier-transform of Interference Spectra of Highly-complex-beams |
| STRIPED FISH | Spatially and Temporally Resolved Intensity and Phase Evaluation Device: Full Information from a Single Hologram |
| TADPOLE | Temporal Analysis by Dispersing a Pair of Light Electric-fields |
| THG | Third Harmonic Generation |
| TOD | Third-Order Dispersion |
| TURTLE | Tomographic Ultrafast Retrieval of Transverse Light E-fields |
| UV | UltraViolet |
| XPW | Cross-Polarized Wave |
| XUV | eXtreme UltraViolet |

# LIST OF PUBLICATIONS

PUBLICATIONS PRESENTED IN THIS THESIS:

- B. Alonso, I. J. Sola, O. Varela, C. Mendez, I. Arias, J. San Román, A. Zaïr, and L. Roso, "Spatio-temporal characterization of laser pulses by spatially resolved spectral interferometry," Opt. Pura Apl. 43, 1-7 (2010).
- B. Alonso, I. J. Sola, O. Varela, J. Hernández-Toro, C. Méndez, J. San Román, A. Zaïr, and L. Roso, "Spatiotemporal amplitude-and-phase reconstruction by Fourier-transform of interference spectra of high-complex-beams," J. Opt. Soc. Am. B. 27, 933-940 (2010).
- O. Mendoza-Yero, B. Alonso, O. Varela, G. Mínguez-Vega, I. J. Sola, J. Lancis, V. Climent, and L. Roso, "Spatiotemporal characterization of ultrashort pulses diffracted by circularly symmetric hard-edge apertures: theory and experiment," Opt. Express 18, 20900–20911 (2010).
- B. Alonso, I. J. Sola, J. San Román, O. Varela, and L. Roso, "Spatiotemporal evolution of light during propagation in filamentation regime", J. Opt. Soc. Am. B 28, 1807-1816 (2011).
- O. Mendoza-Yero, B. Alonso, G. Mínguez-Vega, Í. J. Sola, J. Lancis, and J. A. Monsoriu, "Synthesis of fractal light pulses by quasi-direct space-to-time pulse shaping," Opt. Lett. 37, 1145-1147 (2012).
- R. Martínez-Cuenca, O. Mendoza-Yero, B. Alonso, Í. J. Sola, G. Mínguez-Vega, and J. Lancis, "Multibeam second-harmonic generation by spatiotemporal shaping of femtosecond pulses," Opt. Lett. 37, 957-959 (2012).
- B. Alonso, R. Borrego-Varillas, O. Mendoza-Yero, I. J. Sola, J. San Román, G. Mínguez-Vega, and L. Roso, "Frequency resolved wavefront retrieval and dynamics of diffractive focused ultrashort pulses," J. Opt. Soc. Am. B 29, 1993-2000 (2012).
- B. Alonso, M. Miranda, I. J. Sola, and H. Crespo, "Spatiotemporal characterization of few-cycle laser pulses," Opt. Express 20, 17880-17893 (2012).
- B. Alonso, M. Miranda, F. Silva, V. Pervak, J. Rauschenberger, J. San Román, I. J. Sola, and H. Crespo, "Generation and spatiotemporal characterization of 4.5-fs pulses from a hollow-core fiber compressor," submitted (2012).

OTHER PUBLICATIONS NOT PRESENTED IN THIS THESIS:

- B. Alonso, J. R. Vázquez de Aldana, and L. Roso, "Simulating beam-shape effects in non-collinear second harmonic generation," Opt. Pura Apl. 42, 71-81 (2009).
- O. Varela, A. Zaïr, J. San Román, B. Alonso, I. J. Sola, C. Prieto, and L. Roso, "Above-millijoule super-continuum generation using polarisation dependent filamentation in atoms and molecules," Opt. Express 17, 3630-3639 (2009).
- B. Alonso, O. Varela, I. J. Sola, J. San Román, A. Zaïr, C. Méndez and L. Roso, "Energy scaling-up of stable single filament," Appl. Phys. B 101, 15-22 (2010).
- B. Alonso, A. Zaïr, O. Varela, J. San Román, and L. Roso, "Femtosecond multi-filamentation control by mixture of gases: towards synthesised nonlinearity," Opt. Express 18, 15467-15474 (2010).
- O. Varela, B. Alonso, I. J. Sola, J. San Román, A. Zaïr, C. Méndez, and L. Roso, "Self-Compression controlled by the chirp of the input pulse," Opt. Lett. 35, 3649–3652 (2010).
- B. Alonso, R. Borrego Varillas, C. Hernández-García, J.A. Pérez-Hernández, and C. Romero (editors), "El láser, la luz de nuestro tiempo" book ISBN 978-84-92997-10-7 (2010).
- B. Alonso, R. Borrego-Varillas, Í. J. Sola, Ó. Varela, A. Villamarín, M. V. Collados, J. San Román, J. M. Bueno, and L. Roso, "Enhancement of filamentation postcompression by astigmatic focusing," Opt. Lett. 36, 3867-3869 (2011).
- A. Villamarín, I. J. Sola, M. V. Collados, J. Atencia, O. Varela, B. Alonso, C. Méndez, J. San Román, I. Arias, L. Roso, and M. Quintanilla, "Compensation of second-order dispersion in femtosecond pulses after filamentation using volume holographic transmission gratings recorded in dichromated gelatin," Appl. Phys. B 136, 135-141 (2012).
- M. Miranda, T. Fordell, C. Arnold, F. Silva, B. Alonso, R. Weigand, A. L'Huillier, and H. Crespo, "Characterization of broadband few-cycle laser pulses with the d-scan technique," Opt. Express 20, 18732-18743 (2012).

# BRIEF SUMMARY

This thesis is devoted to the development of a technique for the measurement of the spatiotemporal amplitude and phase of ultrashort laser pulses and its applications. The core of the thesis is divided into three parts, which correspond to the presentation of the technique (Part I), its applications to diffractive optics (Part II) and to nonlinear optics and few-cycle pulses (Part III). Each part is divided into three chapters. The core of the thesis is preceded by an introductory chapter, which contains the scope and motivation of the thesis, the basic concepts about ultrashort laser pulses, and the state of the art of the already existing techniques for pulse characterization. Part I begins with a review of the temporal pulse characterization carried out by means of spectral interferometry (Chapter 2). Then, in Chapter 3, its extension to the spatial domain is introduced and, finally, in Chapter 4 we present the technique that we developed for spatiotemporal pulse characterization (STARFISH), which is based on a fiber optic coupler as part of the interferometer. In Part II, we will present its applications where diffractive optical elements in linear propagation regime are involved. This part covers the fundamentals of spatiotemporal coupling during propagation of pulses diffracted by a zone plate (Chapter 5), the application to a focusing kinoform diffractive lens, including the frequency-resolved wavefront measurement (Chapter 6), the production of fractal-shaped pulses and a dispersion compensated module for a diffraction grating (Chapter 7). The application to nonlinear processes and few-cycle pulses is discussed in Part III. In Chapter 8, we track the propagation dynamics of intense pulses under the regime of filamentation. Then, we present the application of STARFISH to few-cycle pulses delivered by an ultrafast oscillator (Chapter 9) and after post-compression of amplified pulses in a hollow-core fiber (Chapter 10). Finally, the main conclusions of this thesis are highlighted. The characteristics of the laser systems employed in the experiments are detailed in Appendix A.

# CHAPTER 1

# INTRODUCTION

**Contents**

## 1.1. Scope and motivation

Since the discovery of the laser, this source of light with such particular properties has been continuously evolving in parallel to its applications in many fields of science and technology. Coherence is possibly the property that makes laser radiation significantly different from other types of radiation. Although monochromaticity is often said to be a property of lasers, this is not the case with ultrashort laser pulses, which are dealt with in this thesis. Monochromatic radiation is composed of a single frequency (or wavelength, or color) and, in the time domain, corresponds to a continuous and infinite emission. This work deals with pulsed laser, which are very brief (finite) emissions of laser radiation distributed ─in our case, regularly─ in time (the temporal separation between pulses is given by the inverse of the repetition rate of the laser). One way to produce pulsed radiation consists in introducing temporal losses in the laser cavity, a mechanism known as Q-switching [1], which reaches the regime of nanoseconds. However, the range of ultrashort laser pulses (for us, it generally means below 100 fs) is achieved by means of mode-locking, which relies on the coupled emission of the multiple longitudinal modes (with different frequencies) of the laser cavity. In pulsed radiation, time dependent short emissions of radiation, known as laser pulses, are produced. In the frequency (spectral) domain, the pulse is defined by the amplitude of the modes and the relation between the emissions of the different modes, which is known as the spectral phase. Analogously, the pulse in the time domain is defined by a temporal amplitude and phase. The relation between the pulse in the frequency and the temporal domain is the Fourier-transform. In order to have shorter pulses, it is necessary to have larger spectral bandwidths of emission. In our case, we will work with titanium:sapphire lasers, which have a broad gain curve approximately covering the wavelength range from 660 nm to 1180 nm. The broadband emission spectrum of these solid state lasers allows to directly produce pulses with a duration below 10 fs.

In many applications, detailed knowledge of the electric pulse field is of high interest, whether these are the outcome or the basis of the experiment. The aim of this thesis is the measurement of the amplitude and phase of the pulses. As will be discussed in more detail in Section 1.3, those pulse durations are too short to be directly measured by electronic methods. For this reason, pulses are characterized using optical methods, in which it is typically the short pulse itself that acts as the probe [2,3]. The electric field is a magnitude that depends on time and the three spatial coordinates, that is to say, $E(x,y,z,t)$. The z-axis is defined as the propagation direction of the pulse (please note that, despite not always being strictly true, laser radiation is considered directional). At a certain propagation distance, i.e. the plane $z = z_0$, the electric field $E(x,y,t)$ depends on the time $t$ and the two transverse spatial coordinates $x, y$. The spatial $(x,y)$ dependence of the pulse can be characterized disregarding the temporal evolution (e.g. [4]), whose dependence is integrated. In many cases, however, the electric field is not a separable function in the form $E(x,y,t) = E_{xy}(x,y)E_t(t)$. In these cases, therefore, a separated characterization of the temporal profile $E_t(t)$ and the spatial profile $E_{xy}(x,y)$

is not a valid approach to determine the pulse electric field. We will propose a new technique to characterize the spatiotemporal coupling of the pulses, which is called STARFISH [5] (see Part I). Our interest in characterizing ultrashort pulses comes from their applications. On the one hand, ultrashort pulses are used to probe materials with an excellent temporal resolution. On the other hand, the concentration of the pulse energy in such short events increases the peak intensity of the light up to extreme values, opening a new regime of light-matter interaction [6]. In any of those applications, complete knowledge of the electric field is essential.

Spatiotemporal coupling in ultrashort laser pulses is very diverse, as it is originated both in linear and nonlinear regimes of light propagation. In [7], the authors review different kinds of spatiotemporal distortions (e.g., see Fig. 1.1). In linear regime, they typically arise from geometrical issues often caused by the wavelength-dependent propagation of light, combined with a broadband spectrum. For example, a homogeneous (undistorted) input pulse becomes spatially chirped after refraction in a plane-parallel tilted window (Fig. 1.1a). By spatial chirp (or spatial dispersion) we mean a space-dependent distribution of the pulse frequencies. In the case of a prism or a diffraction grating, the pulse will present angular dispersion and pulse-front tilt (Fig. 1.1b). Owing to angular dispersion, the frequencies of the pulse propagate in different directions. The pulse-front is tilted when the frequencies arrive at different times at a certain propagation distance or observation plane.

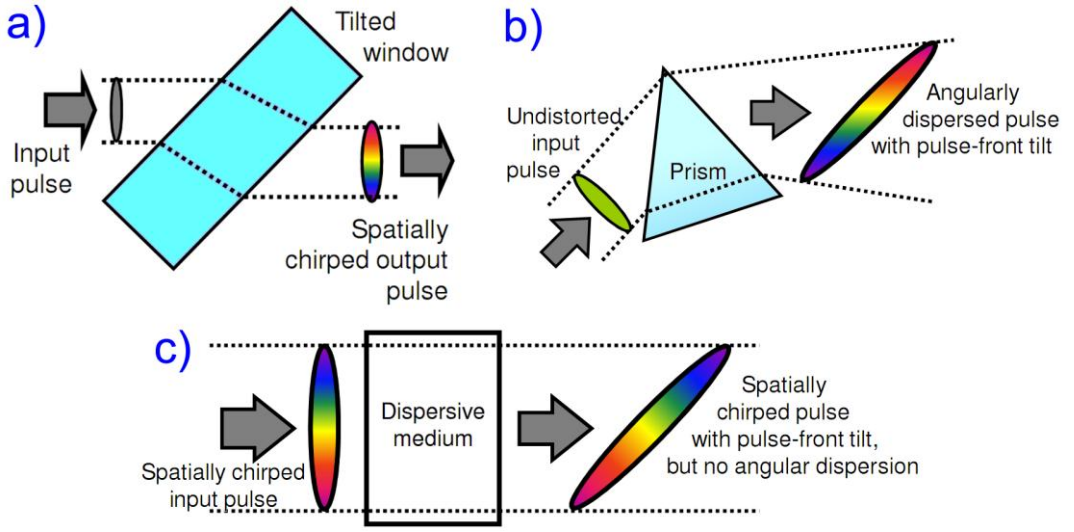


Fig. 1.1. Examples of spatiotemporal distortions. (a) Spatial chirp originated from a tilted window. (b) Angularly dispersed pulse with spatial chirp and pulse-front tilt after a prism (the same applies to a diffraction grating). (c) The combination of input spatial chirp with a dispersive medium introduces pulse-front tilt. Figure extracted from [3].

Thanks to these simple pictures, it is easy to understand that, while we consider here only the most “simple” cases of spatiotemporal distortions, these are closely related and often difficult to discriminate. For example, an input pulse only with spatial chirp, acquires pulse-front tilt after a dispersive medium (where the frequencies propagate at different velocities), as illustrated in Fig. 1.1c. Apart from these examples, optical elements such as lenses also introduce spatiotemporal distortions owing to aberrations, such as chromatic aberration, spherical aberration, and astigmatism [8,9]. In fact,

focusing ultrashort pulses is often associated with aberrations due to the large spectral content of the pulse.

The light propagating after diffractive optical elements (DOEs) is an excellent example of spatiotemporal coupling. Part II is devoted to the characterization and applications of diffractive optics in the field of ultrashort pulses. Owing to the intrinsic wavelength (or chromatic) dependence of diffraction and, taking again into account the broadband spectrum of the pulses, DOEs will naturally introduce spatiotemporal coupling. For an idea of its complexity, we provide here an example of the distribution of the pulse in the spatiospectral and the spatiotemporal domains, (Fig. 1.2a and 1.2b, respectively) for the focus of a DOE [10]. In this case, the above mentioned types of spatiotemporal distortion cannot be distinguished, or even defined.

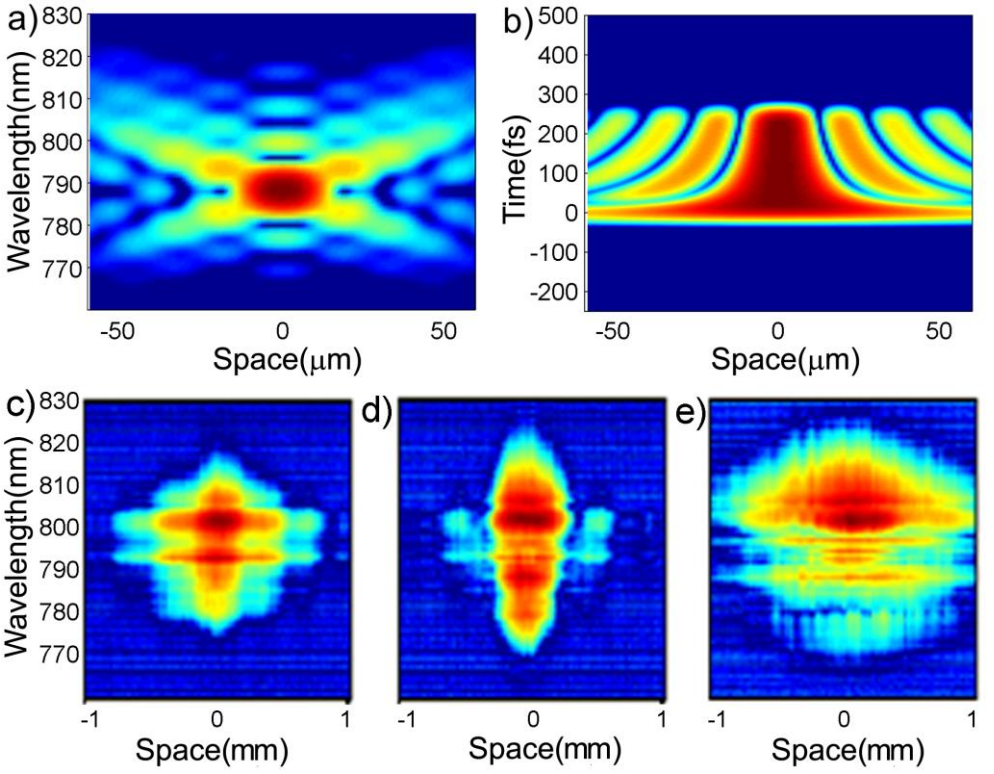


Fig. 1.2. (a) Spatiospectral and (b) spatiotemporal distribution of an ultrashort pulse focused by a diffractive optical element [10]. (c,d,e) Evolution of the spatiospectral distribution of the pulse during filament propagation [11].

In the way towards ultra-intense pulses there was a key-enabling technology, the chirped pulse amplification (CPA) [12], which relies on stretching the pulse in time before the amplification, and then compressing it. The compression in the amplifiers is often done with grating pairs or prism pairs in a configuration that introduces negative dispersion. As a consequence, the output pulse of an amplifier may present spatial chirp and/or pulse-front tilt if the amplifier is not perfectly compensated. Except for the ultrafast oscillator used in Chapter 9, CPA laser systems were used in the experiments carried out through the present work.

In Part III, we will present results regarding nonlinear processes and few-cycle ($<10\,fs$) optical pulses. In nonlinear processes such as filamentation [11,13] (Chapter

8), there is a strong spatiotemporal (and spatiospectral) coupling originated by the dependence of the propagation not only on the phase, but also on the intensity. During filament propagation, the spectrum of the pulse is modified. Owing to the spatially-dependent intensity of the pulse, this modification depends on the spatial coordinate. For example, in the evolution of the spatiospectral distribution of the pulse, different structures can be observed during propagation (Fig. 1.2c to 1.2e). In this case, the structure of the spatial chirp is more complex than in the cases presented in Fig. 1.1. In the spatiotemporal domain, there is also a strong coupling associated to a very rich dynamics, including pulse-splitting (in the temporal domain) or conical emission (angular and spectral dependent radiation) [13].

In general, the spatiotemporal couplings described above have already been studied from the theoretical point of view. For example, a theory has been developed to describe spatiotemporal distortions [14] and chromatic aberrations of lenses have also been studied analytical [15] and numerically [16]. DOEs have also been studied numerically, including the space-time and space-frequency dependence [17], as well as there are theoretical studies about the filamentation dynamics [13,18].

However, until the first spatiotemporal characterization techniques were recently introduced [5,9,19-23], the difficulty to measure spatiotemporal couplings entailed an incomplete knowledge of the pulses from the experimental point of view. The experimental information about the spatiotemporal structure of the pulses is very enriching and allows to optimize the design of optical systems and the propagation of pulses, both in linear and nonlinear regimes. In fact, the spatiotemporal characterization of ultrashort laser pulses is a hot topic. In Section 1.3, we will present the techniques for their spatial, temporal and spatiotemporal characterization. There is a large range of applications for the spatiotemporal characterization, which are expected to grow in the future.

## 1.2. Description of ultrashort laser pulses: basic concepts and definitions

In this section, we will introduce the concepts of optics required for the description and characterization of ultrashort laser pulses, including the physical and mathematical definitions of the pulses (such as electric field, amplitude and phase), as well as the mathematical tools to deal with the pulses. Here, we will not go into the basics of laser radiation generation, the types of lasers, or their applications [24], but we will simply describe laser pulses. The light is an electromagnetic wave consisting of a vibrating electromagnetic field [25]. The electric field $E$ and the magnetic field $B$ are related by Maxwell's equations. Therefore, it is enough to consider the electric field for the description of the laser radiation, so we will disregard the magnetic field from now on. Moreover, in many situations the electric field is a vector that oscillates in the plane perpendicular to the propagation direction. The trajectory described by the electric field vector in that plane is known as polarization. In our case, the lasers employed in the experiments were linearly polarized (oscillating in one direction), so we can consider the pulses as a scalar electric field.

### 1.2.1. Basic definitions regarding the electric field

As has been said in the previous section, the electric field is a magnitude with amplitude and phase that depends on the three spatial coordinates ($x, y, z$) and the time $t$ [25]. Despite being a real function (since it stands for a physical magnitude), it is usually expressed as a complex function $E = A\exp\{i\Omega\}$. The magnitude $A = |E|$ is the amplitude and $\Omega$ is the phase, both of them being functions of $x, y, z, t$ in the case of ultrashort laser pulses [26]. The actual electric field is simply the real part of the complex representation, that is to say, $E = |E|\cos(\Omega)$. The complete expression for the electric field is given by

$$E(x,y,z,t) = A(x,y,z,t)\times\exp\left\{i\left[\omega_0 t - \vec{k}\cdot\vec{r} + \varphi(x,y,z,t)\right]\right\}, \qquad (1.1)$$

where $\omega_0$ is the central angular frequency and $\vec{k}$ is the wave vector, whose orientation $\vec{k}/|\vec{k}|$ gives the propagation direction of the pulse. By agreement, the propagation direction of the pulse is chosen to be the $z$-axis and, when $\vec{k}$ can be considered a scalar, then $\vec{k}\cdot\vec{r}$ is simply $kz$. The module $k$ is known as the wave number and is the spatial equivalent to the angular frequency $\omega_0$ in time. Therefore, the electric field (real part) oscillates in time $t$ and space $z$ (propagation direction). In Eq. (1.1), the quantity $\varphi$ is the spatiotemporal phase after subtraction of the oscillatory terms $\omega_0 t$ and $-kz$.

The angular frequency $\omega_0$ and the linear frequency $\nu$ are related by $\omega_0 = 2\pi\nu$. The frequency $\nu = 1/T$ is the number of oscillations per second (measured in $Hz$), where $T$ is the period of the oscillations. The spatial period is known as the wavelength $\lambda_0$ of the light in vacuum and is related to the wave number by $k = 2\pi/\lambda_0$. The space and time magnitudes of the electromagnetic wave are connected by the speed of light in vacuum $c$ through the relations $\lambda_0 = cT$ and $\omega_0 = ck$.

If the pulse propagates inside a medium, the velocity of propagation is given by $v = c/n(\omega)$, where $n(\omega)$ is the refractive index of the medium. Since $n(\omega) \geq 1$, the velocity is always $v \leq c$. Also, the wavelength in the medium is $\lambda_n = \lambda_0/n(\omega_0)$ and the wave number is modified accordingly, $k = 2\pi n(\omega_0)/\lambda_0 = \omega_0 n(\omega_0)/c$.

Since the pulse propagates in the $z$-axis, in general we will observe the electric field at a certain plane corresponding to the propagation distance $z = z_0$. Thus, we will obviate the dependence on $z$, expressing the electric field as

$$E(x,y,t) \equiv E(x,y,z,t)|_{z=z_0} = A(x,y,t)\times\exp\left\{i\left[\omega_0 t + \varphi(x,y,t)\right]\right\}. \qquad (1.2)$$

Note that the term $-kz_0$ is a simple constant that can be included in the definition of $\varphi$. In the cases where we include the propagation of the pulses in their study, we will consider the spatiotemporal electric field $E(x,y,t)$ for different propagation distances. The objective of the spatiotemporal characterization is the measurement of the amplitude and phase of the pulses that appear in Eq. (1.2).

### 1.2.2. Ultrashort laser pulses in the temporal domain

In order to describe the temporal dependence of ultrashort laser pulse in more detail, we will momentarily leave aside the spatial dependence ($x, y$). Later, we will deal with

the complete spatiotemporal dependence to discuss the coupling and its characterization. In this approach, the time dependent electric field $E(t)$ of an ultrashort pulse is expressed as

$$E(t) = A(t)\exp\left\{i\left[\omega_0 t + \varphi(t)\right]\right\}, \tag{1.3}$$

where $\omega_0$ is the carrier frequency (or central frequency), and $\varphi(t)$ is the temporal phase. The function $A(t)$ is known as the envelope of the pulse, because the oscillations of the electric field are contained between the curves $+A(t)$ and $-A(t)$, as illustrated in Fig. 1.3a. In this example, a Gaussian pulse has been considered, with its envelope given by $A(t) = A_0 \exp\{-2\ln 2\left(t/\Delta t\right)^2\}$. The electric field is the product of the envelope and the carrier oscillations (with a period $T$). In this example, we have plotted two different electric fields, corresponding to two different phase offsets. The carrier-envelope offset phase (CEP) at the maximum of the envelope is given by $\varphi_{CEP} = \varphi(t=0)$ for the present definition. In the case of few-cycle pulses (as illustrated in the example), the two values of the $\varphi_{CEP}$ determine the two maximum values of the electric field, which is very relevant for electric-field-sensitive nonlinear processes, for example high-harmonic generation (HHG). In the case of pulses with many optical cycles (oscillations), the envelope is smoother and the effect of the $\varphi_{CEP}$ is negligible. In this thesis we will not work with the CEP and we will not use techniques to stabilize it or to measure it.

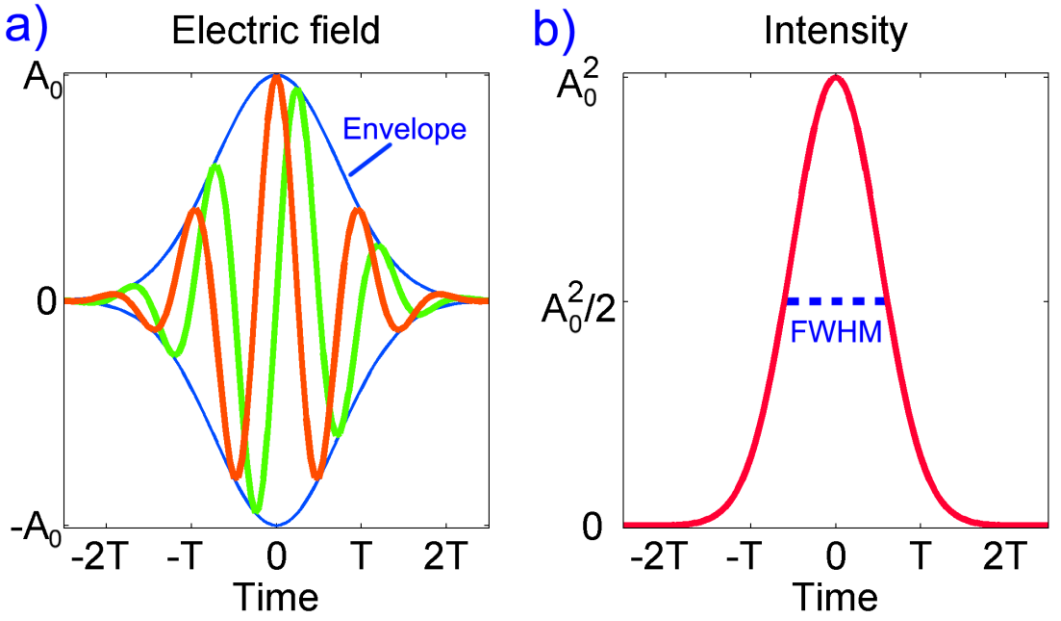


Fig. 1.3. (a) Envelope and electric field of an ultrashort laser pulse of two optical cycles for two values of the carrier-envelope phase, $\varphi_{CEP} = 0$ and $\varphi_{CEP} = \pi/2$. (b) Temporal intensity profile of the pulse represented in (a).

In the temporal domain, the intensity of the pulse, $I(t)$, is defined as the square of the module of the electric field $I(t) = |E(t)|^2 = [A(t)]^2$ and it is measured in units of power (whenever the definition of the electric field includes the appropriate constants). Although the correct term used in radiometry to refer to $I(t)$ is the radiant flux or radiant power, in our field it is usually known as intensity. Therefore, we will use the

term temporal intensity to refer to $I(t)$. In Fig. 1.3b, we represent the intensity of the pulse considered above. In order to quantify the pulse duration, the most widespread definition is the full-width at half maximum (FWHM). For the previous definition, $I(t) = A_0^2 \exp\{-4\ln 2\left(t/\Delta t\right)^2\}$ and the FWHM of the pulse is $\Delta t$.

### *1.2.3. Electric field in the spectral domain and Fourier-transform*

As said above, ultrashort laser pulses are not monochromatic. In fact, the pulse is composed of multiple waves with different frequency, amplitude and phase. The laser spectrum represents its frequency content. In fact, the electric field can be expressed, equivalently, in temporal and frequency domains. In the spectral domain, the complex representation of the field $E_f(\omega) = A_f(\omega)\exp\{i\phi(\omega)\}$ is determined by the spectral amplitude $A_f(\omega)$ and the spectral phase $\phi(\omega)$. The spectral density power is defined as $S(\omega) = |E_f(\omega)|^2 = [A_f(\omega)]^2$. We will simply refer to it as the spectrum, which gives the information of the pulse spectral amplitude. Note that the field can be expressed as

$$E_f(\omega) = \left|E_f(\omega)\right| \exp\left\{i\phi(\omega)\right\} = \sqrt{S(\omega)}\exp\left\{i\phi(\omega)\right\}. \tag{1.4}$$

In fact, the representation of the field in temporal or spectral domain is equivalent, whenever the amplitude and phase of the field are known. The transformation between these domains is given by $\mathcal{F}$, the Fourier-transform (FT). Since we work with the complex representation of the field, we will use the complex FT. Different definitions of the FT exist depending on the area. In our case, the FT of a function $g\left(t\right)$ in the temporal domain gives the equivalent in the spectral domain $G(\omega)$ according to

$$\begin{aligned} \mathcal{F}\left\{g\left(t\right)\right\} &= G(\omega) = \int_{-\infty}^{\infty} g(t)\exp\left\{-i\omega t\right\} dt \\ \mathcal{F}^{-1}\left\{G(\omega)\right\} &= g\left(t\right) = (2\pi)^{-1}\int_{-\infty}^{\infty} G(\omega)\exp\left\{i\omega t\right\} d\omega \end{aligned} \tag{1.5}$$

The inverse Fourier-transform (IFT) operation, denoted by $\mathcal{F}^{-1}$, makes the inverse transformation. Therefore, the electric field in the temporal and the frequency domain are related by the expressions $\mathcal{F}\{E(t)\} = E_f(\omega)$ and $\mathcal{F}^{-1}\{E_f(\omega)\} = E(t)$.

Among others, the FT (and IFT) has the properties of linearity and translation. The translation property implies the relation $\mathcal{F}\{g(t-\tau)\} = \exp\{-i\omega\tau\}G(\omega)$, which we will use later. Also, it verifies the relation $\mathcal{F}^{-1}[\mathcal{F}\{g(t)\}] = g(t)$ for every function $g(t)$, that is, $\mathcal{F}^{-1}\circ\mathcal{F} = \mathcal{F}\circ\mathcal{F}^{-1} = \mathrm{Id}$, where $\mathrm{Id}$ is the identity function.

In the particular case of ultrashort laser pulses, their spectrum is a broad distribution of frequencies, so it is said that they have a broadband spectrum or a wide spectral bandwidth. As said above, the temporal duration $\Delta t$ and spectral bandwidth $\Delta\omega$ of the pulses are typically given as the FWHM of the intensity and the spectrum, respectively. In the case of Gaussian pulses, the spectrum is given by

$$S\left(\omega\right) = A_{f,0}^2 \exp\left\{-4\ln 2\left[\left(\omega-\omega_0\right)/\Delta\omega\right]^2\right\}, \tag{1.6}$$

where the FWHM are related by $\Delta t\,\Delta\omega = 4\ln(2)$. This explains that in order to reduce the pulse duration, we need to increase the spectral bandwidth.

It has to be brought to attention that the power spectral density $S(\omega)$ is the density of power spectral with respect to the variable $\omega$ (the angular frequency). In the case of expressing it with another variable, for example the wavelength $\lambda$, the transformation to the new density is not just a change of axis. However, owing to the conservation of the integral of the density, it has to verify the following property [27]

$$\int_0^\infty S_\omega(\omega)d\omega = \int_0^\infty S_\lambda(\lambda)d\lambda \tag{1.7}$$

The subscripts distinguish the variable in which $S(\omega)$ is expressed. Since $\omega = 2\pi c/\lambda$, the differentials are related by $d\omega = -(2\pi c/\lambda^2)d\lambda$, and, from this, it is derived that $S_\omega(\omega) = [(\lambda^2/2\pi c)\cdot S_\lambda(\lambda)]_{\lambda\to 2\pi c/\omega}$. As a result, besides the change of variable (of axis), there is a scaling factor. In particular, the factor $\lambda^2$ means a reshaping of the spectrum that is very important to take into account for few-cycle pulses (with an ultra-broadband spectrum), as those used in Chapters 9 and 10. This factor shifts the central wavelength towards the redder part of the spectrum for $S_\omega$ in comparison with $S_\lambda$. As a practical issue, it is necessary to know that most spectrometers give the spectral density $S_\lambda$ referred to $\lambda$, whereas the transformation to $S_\omega$ is required if the pulse is going to be expressed in the temporal domain by applying an IFT.

### *1.2.4. Importance of the phase: the chirp*

At this point, it is important to discuss the influence of the phase. From the experimental side, it makes more sense to think of a certain spectrum $S(\omega)$ that can have different phases $\phi(\omega)$. This is so because materials dispersion is defined in the frequency domain and, often, linear processes do not modify the spectral amplitude (e.g., excluding absorption). The pulse in the temporal domain (the IFT of $E_f(\omega)$) will be different depending on the phase $\phi(\omega)$. If the spectral phase is $\phi(\omega) = const$, it is said that the pulse is Fourier-transform limited (FTL) and therefore it has the shortest temporal duration ($\Delta t$) compatible with that spectrum (Fig. 1.4a). Let us consider a Gaussian spectrum $S(\omega)$ centered at the frequency $\omega = \omega_0$, given by Eq. (1.6). If this spectrum is FTL, then the electric field will oscillate at the carrier frequency $\omega_0$. From the translation property of the FT, a linear spectral phase $\omega t_0$ just introduces a shift of the pulse in the temporal domain $t = t - t_0$, which can be understood as a change in the time axis origin. Conversely, if the pulse has an arbitrary spectral phase, the amplitude and the phase of the pulse in the temporal will be modified. Regarding the temporal phase, $\Omega(t) = \omega_0 t + \varphi(t)$, we wish to note that $\varphi(t)$ depends on time. The consequence is that the frequency of the temporal oscillation varies within the pulse, which can be calculated as

$$\omega(t) = \omega_0 + d_t\varphi(t) = d_t\Omega(t), \tag{1.8}$$

where $d_t$ denotes the derivative with respect to the time. The function $\omega(t)$ is called the instantaneous frequency of the pulse. Whenever the $\omega(t)$ is not a constant, it is said that the pulse has a temporal chirp or it is temporally chirped.

A common case is a quadratic phase in frequency, $\phi(\omega) = -GDD \cdot (\omega - \omega_0)^2 / 2$, where $GDD$ refers to the group delay dispersion. The $GDD$ is caused by the accumulated group velocity dispersion ($GVD$) during propagation through a dispersive medium with thickness $L$, that is, $GDD = GVD \cdot L$. The $GVD$ of the medium is calculated as $GVD = [d_\omega^2 k(\omega)]_{\omega=\omega_0}$, where $d_\omega^2$ is the second derivative with respect to the frequency, evaluated at $\omega = \omega_0$. This phase is often originated by a dispersive material, which has a frequency-dependent refractive index, so $k(\omega) = n(\omega) \cdot \omega / c$. In a first approach, one can consider that the medium only introduces this quadratic spectral phase. In the temporal domain, the pulse intensity is stretched (Fig. 1.4a) and the phase is quadratic, which implies a linear instantaneous frequency $\omega(t)$. Then, it is said that the pulse is linearly chirped or has a linear chirp. If $GDD > 0$, the $\omega(t)$ increases linearly with time, which is known as positive chirp (as illustrated in Fig. 1.4b). This means that the redder frequencies arrive before the bluer frequencies (the contrary applies for negative chirp). This phenomenon is known as spectral/temporal dispersion. The separation in time of the frequencies is responsible for the increase of the pulse duration, which is also translated in a decrease of peak intensity.

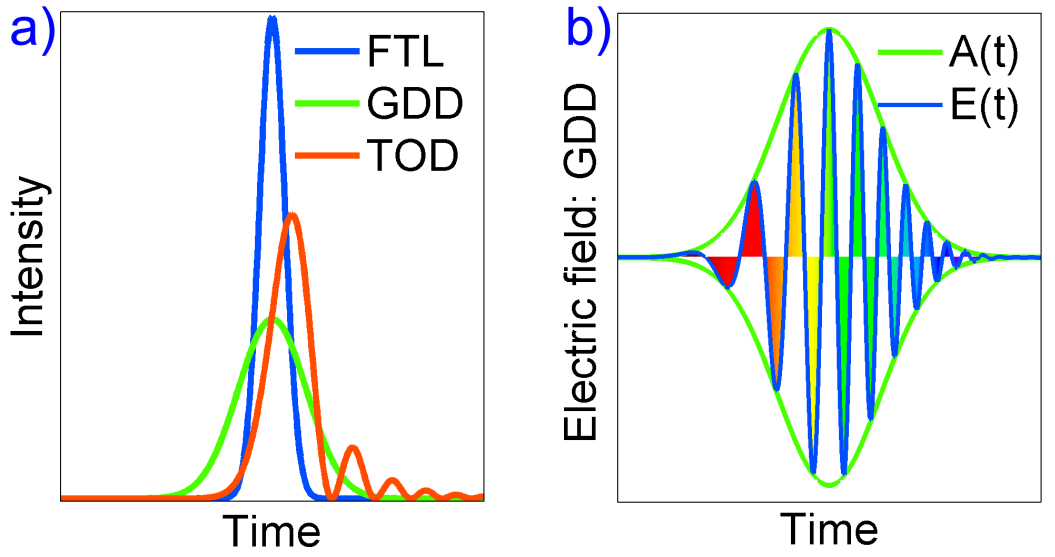


Fig. 1.4. Temporal intensity of a Gaussian spectrum (a) Fourier-transform limited (FTL), with group delay dispersion (GDD) and third-order dispersion (TOD). (b) Electric field, E(t), and envelope, A(t), of a pulse positive linear chirp (GDD>0).

In the case of a more complex spectral phase, the temporal intensity and phase of the pulse will have a different structure. For example, a cubic spectral phase due to the presence of third order dispersion (TOD) will cause a pulse with lateral satellites after or before the mean peak depending on the sign of the TOD (Fig. 1.4a). The pulse energy spreading in time is again associated to a peak intensity reduction compared to the FTL. Moreover, it would be possible, for example, to have a spectrum with modulations instead of a Gaussian-shape. In these cases, defining a carrier frequency is more difficult. Sometimes, depending on the case, the gravity center of the spectrum is considered. The gravity center of the spectrum is $\omega_0 = \int \omega \cdot S(\omega) d\omega \Big/ \int S(\omega) d\omega$. Other times, the carrier frequency is taken as the instantaneous frequency evaluated at the maximum of the main pulse.

Therefore, a simple measurement of the spectrum is not enough to determine the temporal intensity and duration of the pulse, but the spectral phase is also required. We have seen that the same spectrum, with different spectral phases, may correspond to very different intensity profile, duration, chirp and amplitude.

### *1.2.5. Spatiotemporal and spatiospectral dependence of the pulses*

Here, we review the spatial dependence together with the temporal dependence. The electric field in a certain observation plane, defined by $z = z_0$, can be expressed in the spatiotemporal domain, as given by Eq. (1.2). We have seen that the temporal dimension is analogous to the frequency dimension, which are connected by the FT. Then, the field can be equivalently expressed in the spatiospectral domain through

$$E_f(x, y, \omega) = \mathcal{F}\{E(x, y, t)\}, \tag{1.9}$$

where $\mathcal{F}$ denotes the FT from time to frequency.

Some important definitions have to be explained regarding the amplitude and phase of the pulses in the spatiotemporal and spatiospectral domains, respectively. The pulse-front is the surface defined by the temporal location of the intensity maxima across the spatial profile $(x, y)$. That is to say, it corresponds to the surface $\rho(x, y, t_{pulse})$ that, for every spatial position $(x_0, y_0)$, verifies the condition $I(x_0, y_0, t_{pulse}) = \max_t[I(x_0, y_0, t)]$ (where $\max_t$ denotes the maximum function in the time dimension). For example, the pulse-front curvature of a convergent beam is quadratic, whereas a collimated beam has a flat pulse-front. In Fig. 1.1c, an example of pulse-front tilt is depicted. In the case of complex spatiotemporal distributions (e.g. Fig. 1.2b), it may be difficult to define the pulse-front.

Regarding the phase, in the spatiospectral domain, the wavefront of a pulse is defined (for each frequency $\omega = \omega_j$) as a surface of constant phase. Again, following the latter example, a convergent beam has a spherical wavefront and a collimated beam has a flat wave-front. Note that the pulse wavefront can be frequency dependent, for example when different frequencies of the pulse are diverging or converging, as will be seen in Chapter 6. Disregarding the temporal dependence (or, e.g., considering monochromatic radiation), the propagation of the pulse is imposed by the wavefront. The propagation direction is, in fact, the perpendicular direction to the surface of the wavefront. Therefore, in a general situation (e.g. converging or diverging beam), the wave vector $\vec{k}$ can have different components across the spatial profile of the pulse.

In radiometric terms, the irradiance of the pulse is given by $I(x, y, t) = |E(x, y, t)|^2$, and corresponds to the power of electromagnetic radiation per unit of surface. Analogously to the temporal domain, $I(x, y, t)$ is traditionally referred to as intensity. In the space domain, we can define the spatial intensity (note that, in fact, it is the fluence and is measured in $J/cm^2$), which is given by

$$I(x, y) = \int_{-\infty}^{\infty} |E(x, y, t)|^2 \, dt \, . \tag{1.10}$$

In the case that the electric field were a separable function, then it could be expressed as $E(x,y,t) = E_{xy}(x,y)E_t(t)$, and the spatial intensity would be

$$I(x,y) = \left|E_{xy}(x,y)\right|^2 \left[\int_{-\infty}^{\infty} |\, E_t(t)\,|^2 \, dt\right] \propto \left|E_{xy}(x,y)\right|^2 . \qquad (1.11)$$

However, many times this assumption is invalid, such as in those cases described in Section 1.1. During their propagation, the pulses experience diffraction, dispersion, nonlinear effects, etc. The combination of these processes can lead to spatiotemporal couplings, since the pulse evolves with a coupling between the four coordinates: three spatial coordinates $(x,y,z)$ and the time/frequency.

In those cases, a full characterization of the electric field $E(x,y,t)$, for a certain $z = z_0$, is mandatory. However, this measurement is difficult to be accomplished. Many times, a separate characterization of the temporal and the spatial profile of the pulses is carried out, with a subsequent loss of information. In Section 1.3, we will present the well-established techniques for the separate (uncoupled) characterization of the temporal and the spatial profile. Then, their adaptations, improvements or combinations will be presented, which have been developed in the last years to measure the spatiotemporal coupling of the pulses.

### *1.2.6. Spatial and spectral interferences*

We have already said that the electric field is coherent since it has a well defined phase. Interference of light is a physical phenomenon arising from the superposition principle of light. When two or more waves are superposed (summed), the electric field of the resulting wave is the sum of the fields of each wave (principle of superposition). Since the electric field is a magnitude with amplitude and phase, the superposition is the coherent sum instead of a simple arithmetic sum. The consequence is that, in general, the intensity of the sum is not the sum of the components' intensity, but will have maxima and minima depending on the relative phase between the waves. Two consecutive maxima (or minima) are associated to a relative phase change of $2\pi$. This phenomenon is known as interferences.

Waves can interfere in different forms, depending on the configuration. Let us consider first the interference of two waves in the spatial domain. For example, if a plane and a spherical wave propagating collinearly are superposed, the total intensity in a transverse plane will show dark and bright rings corresponding to the relative variation. In the case of two plane waves crossing at an angle, a set of equally spaced and parallel fringes will be produced. We will see that the latter case can be used for pulse characterization [9].

Analogously, the pulses can interfere in the spectral domain. Let us consider two pulses $E_1(t)$ and $E_2(t)$ (disregarding spatial dependence), which can be expressed $E_{f,1}(\omega) = |\, E_{f,1}(\omega)\,| \exp\{i\phi_1(\omega)\}$ and $E_{f,2}(\omega) = |\, E_{f,2}(\omega)\,| \exp\{i\phi_2(\omega)\}$ in the frequency domain, respectively. If the two pulses are collinear and have a relative temporal delay $\tau$, applying FT properties their superposition will be given by

$$S_{total}(\omega) = |\mathcal{F}\{E_1(t) + E_2(t-\tau)\}|^2 = |E_{f,1}(\omega) + \exp\{-i\omega\tau\}E_{f,2}(\omega)|^2$$
$$= S_1(\omega) + S_2(\omega) + \sqrt{S_1(\omega)S_2(\omega)}\left[\exp\left\{i\left(\phi_2(\omega) - \phi_1(\omega) - \omega\tau\right)\right\} + c.c.\right] \quad (1.12)$$
$$= S_1(\omega) + S_2(\omega) + 2\sqrt{S_1(\omega)S_2(\omega)}\cos\left[\phi_2(\omega) - \phi_1(\omega) - \omega\tau\right]$$

The total spectrum $S_{total}(\omega)$ now is not only the sum of the individual spectra, but also has an oscillating cross term, responsible spectral fringes with a period given by $1/\tau$. The cross term (with the cosine) is known as the interference term. The signal of Eq. (1.12) will be used in spectral interferometry (SI) to measure the phase of the pulses (see more details in Chapter 2) and, in fact, is the basis of this thesis.

### *1.2.7. Second harmonic generation*

Although SI is a very powerful method, it will be discussed later that it is a referenced (not absolute) technique. This means that it relies on any other self-referenced technique to characterize a first pulse. Self-referenced methods are based on nonlinear processes, the most widespread of which is the second harmonic generation (SHG).

Briefly, SHG is a nonlinear optical process that can be understood both from the corpuscular and the wave point of view. For certain materials the refractive index is not a linear response function, but it has a dependence on the intensity of the pulse. If the intensity of the pulse is high, it can modify the refractive index. If a Taylor series is done for the index, and it is truncated at second order, then optical parametric processes of two-wave mixing are allowed. This opens the door to the process of SHG, which consists in the sum of two photons of the fundamental (input) frequency $\omega_0$ to give a single photon of double frequency $2\omega_0$. From the wave side, the new field of SHG is proportional to the squared input field, so it is consistent with the oscillation at $2\omega_0$ [6].

In the case of two different pulses –or two replicas with a certain configuration– mixed in the nonlinear process, the SHG signal can encode the information of the amplitude and phase of the pulse. This can be used to characterize ultrashort pulses, as detailed in the next section.

## 1.3. State of the art of ultrashort pulse characterization

The central wavelength of pulsed titanium:sapphire lasers is around $\lambda_0 = 800\,nm$, which means that the pulses oscillate with an optical frequency $\nu_0 = 0.375{\cdot}10^{15}\,rad/s$, the period of the optical cycle being $T = 2.67{\cdot}10^{-15}\,s$. This rapid variation is impossible to be detected by the response of electronic devices. As mentioned above, this limitation is overcome using optical methods instead. In this section, we will present these methods and will discuss their advantages and disadvantages. Mainly, a linear process alone provides only the spectrum, or the relative phase compared with a reference pulse (e.g., spectral interferometry). Therefore, self-referenced methods, which measure the amplitude and phase of the pulse, are usually based on SHG or other nonlinear process. We will first focus our attention on the separate temporal or spatial characterization, and then, on the spatiotemporal coupling characterization.

### 1.3.1. Temporal pulse characterization

The advances in laser technology are very fast and, consequently, the techniques to characterize them have to be adapted or invented for the emerging challenges. The field of ultrashort laser is not an exception. Over the last few decades, many techniques have been developed to measure the temporal profile of the pulses, which are reviewed in [2]. The most basic one is the optical autocorrelation of the pulse [28]. The two main types of autocorrelation are the intensity autocorrelation (nonlinear and non-interferometric) and the interferometric autocorrelation (nonlinear and interferometric). Both require an interferometer in their experimental setup and are based on the measurement of a signal with respect to the relative delay of two replicas of the original pulse. The intensity autocorrelation provides partial information of the pulse shape and duration. In fact, a reliable value for the pulse duration can be given if a certain pulse shape is known or assumed (e.g. Gaussian or hyperbolic secant). The interferometric autocorrelation is more demanding (interferometric precision in the delay scan), but provides more information. Although it does not retrieve the amplitude and phase of the pulse, numerical algorithms can be used to obtain an estimation of them from the interferometric autocorrelation signal [29].

One of the most consolidated techniques for the measurement of ultrashort pulses is known as FROG (Frequency-Resolved Optical Gating) [27]. A common scheme of FROG uses second order autocorrelation from the SHG of the pulse in a nonlinear crystal, but many other schemes are also employed. For example, other widespread types of FROG are based on self-diffraction [30], polarization gating [31] or third harmonic generation (THG) [32]. In general, a 2D-trace of experimental data is obtained in the form

$$S_{FROG}(\omega,\tau)=\left|\int_{-\infty}^{\infty}P(t)G(t-\tau)e^{-i\omega t}dt\right|^2, \qquad (1.13)$$

where $P(t)$ is the probe pulse and $G(t)$ is the gate pulse. These functions are directly related with the electric field of the pulse to be measured and their particular form depends on the type of FROG. Experimentally, a delay line scans the relative time $\tau$ between two replicas of the pulse that undergo a certain process (e.g. SHG), as illustrated in Fig. 1.5. The resulting signal is then spectrally resolved with a spectrometer. The experimental trace $S_{FROG}(\omega,\tau)$, known as the spectrogram, encodes full information of the pulse. This technique requires a numerical algorithm to recover the pulse. The algorithm optimizes the retrieved pulse by comparing a simulated trace with the experimental trace, $S_{FROG}(\omega,\tau)$, in an iterative way. This is a self-referenced method that retrieves both the temporal intensity and phase of the pulse. The redundancy of data in the trace (a 2D function is used to obtain the 1D field) gives robustness to the retrieval. Moreover, the marginals of the trace can be used to cross-check the retrieval given by the algorithm. The frequency and delay marginals are the integral of the spectrogram with respect to the delay and the frequency, respectively. They are useful functions that provide redundant information, for example, the frequency and delay marginals can be compared, respectively, to the pulse spectrum and

the pulse autocorrelation, which can be measured independently [27]. Therefore, they can be used to cross-check a FROG trace. In Sections 9.2 and 10.3.1, we will recall the use of marginals regarding the trace of the d-scan technique (see below) and the time-frequency Wigner representation of the pulse, respectively.

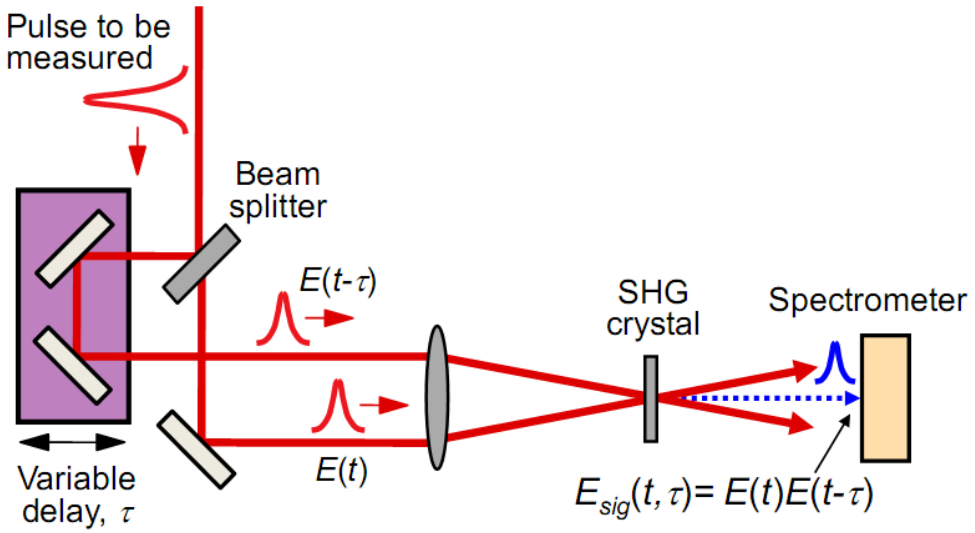


Fig. 1.5. Experimental layout for second-harmonic generation (SHG) frequency-resolved optical gating (FROG). The spectrum of the SHG (in a nonlinear crystal) of two pulse replicas is measured as a function of the relative delay $\tau$. Figure extracted from [3].

The requirement of a delay scan in the FROG implementation makes it a multi-shot technique. However, it is possible to implement it in a single-shot, compact configuration, known as GRENOUILLE (GRating-Eliminated No-nonsense Observation of Ultrafast Incident Laser Light E-fields) [33]. In this type of FROG, a Fresnel biprism replaces the beamsplitter and the delay line. The usual thin nonlinear optical crystal (to allow broadband efficiency) is replaced by a thick nonlinear crystal with a narrow and angular-dependent response in wavelengths. The up-converted wavelength dependence on the angle is used to spectrally resolve the signal, which substitutes the spectrometer. Cylindrical lenses are used to get the two-dimensional signal, encoding the $(\omega,\tau)$ dependence of the spectrogram in perpendicular directions in the detection plane. The GRENOUILLE requires a beam with homogeneous spatial profile.

Another consolidated method that also measures the amplitude and phase of the pulses is SPIDER (Spectral Phase Interferometry for Direct Electric-field Reconstruction). It is a direct and self-referenced technique to measure ultrashort pulses [34]. Two replicas of the unknown pulse are frequency summed with a pulse that has been stretched in time, which has a chirp in order to have a different instantaneous wavelength along the temporal profile (similarly to the example in Fig. 1.4). For this reason, and the delay $\tau$ between the replicas, each of them is summed with two quasi-monochromatic waves, whose frequencies are separated by a small quantity $\Omega$ (the spectral shear). Then, the two resulting up-converted pulses interfere in the spectral domain, analogously to Eq. (1.12), providing the SPIDER signal

$$S_{SPIDER}(\omega) = S(\omega) + S(\omega+\Omega) + 2\sqrt{S(\omega)S(\omega+\Omega)}\cos\left[\phi(\omega+\Omega) - \phi(\omega) + \omega\tau\right]. \quad (1.14)$$

From FT analysis of the interference fringes [35], it can be calculated the difference of spectral phase of the pulse evaluated at frequencies separated by the shear, that is to say, $\phi(\omega-\Omega)-\phi(\omega)$. This quantity is related to the derivative of the spectral phase, which is the frequency-dependent group delay. Therefore, the unknown pulse phase is computed from that quantity via concatenation of the phase for consecutive frequencies, that is to say, by integrating the phase difference. This requires a very precise calibration of the shear $\Omega$, which depends on the chirp of the stretched pulse and the delay $\tau$ between the two replicas. Experimentally, the spectral shear is done by tightly chirping a replica of the pulse, so the chirped pulse can be considered locally monochromatic, as illustrated in Fig. 1.6. In the past few years, different improvements of the technique have derived in new versions of the SPIDER, such as Homodyne Optical Technique (HOT-SPIDER) [36], Zero-Added-Phase SPIDER (ZAP-SPIDER) [37] or Spatially Encoded Arrangement for SPIDER (SEA-SPIDER) [38,39]. In the case of two-dimensional spectral shearing interferometry (2DSI) [40], it is remarkable that a second dimension encodes the phase, reducing the demands of the shear calibration.

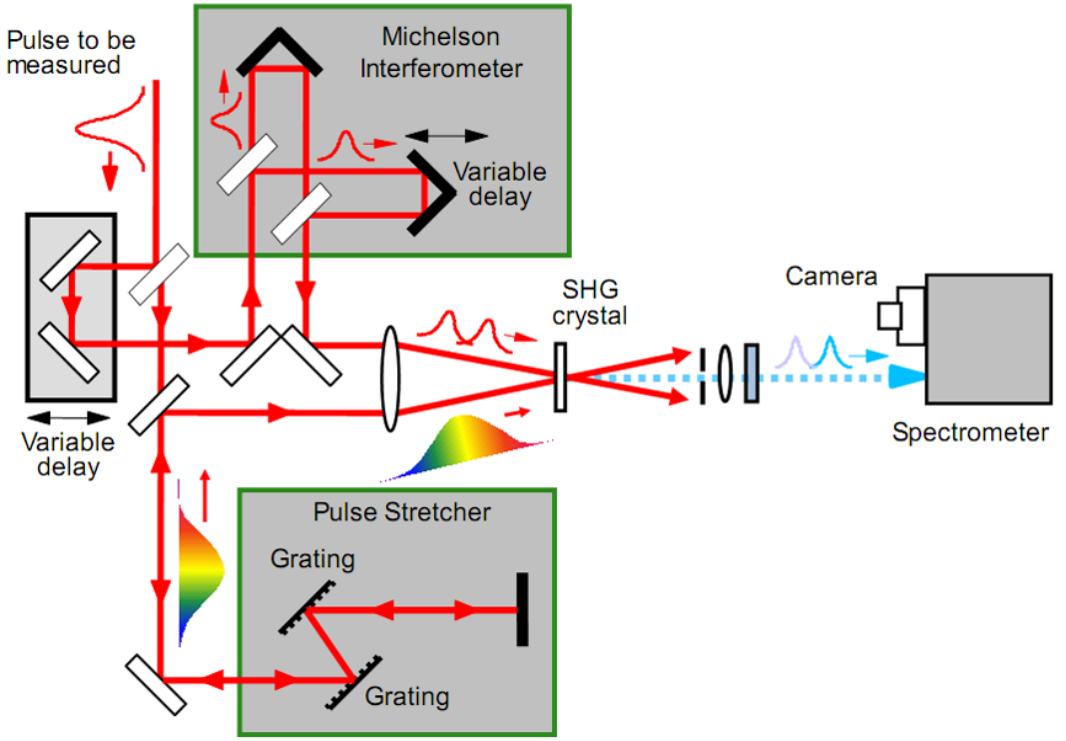


Fig. 1.6. Experimental setup for the SPIDER technique. The input pulse (unknown) is divided into two replicas in a beam splitter. Then, one replica is chirped (e.g. in a diffraction grating stretcher) and the other replica is divided into two replicas with a controlled temporal delay. The two delayed replicas are frequency summed in a nonlinear crystal, and the spectral interference of the two up-converted pulses is recorded in a spectrometer. Figure extracted from [3].

In our opinion, together with FROG and SPIDER, the other widespread technique is spectral interferometry (SI) [41,42]. As explained in Section 1.2.6, the interference term of the total spectrum of two delayed collinear pulses encodes the difference of their spectral phases. This phase difference can be extracted from Fourier-transform analysis

[35]. Then, if the phase of one of the pulses is known (reference pulse), the phase of the unknown pulse (test pulse) can be obtained. For this reason, it is said that SI is a referenced method. Therefore, it relies on the previous characterization of the pulse by any other self-referenced method (e.g., SPIDER or FROG). In Chapter 2, we will thoroughly explain SI, since it is the basis of the STARFISH technique (Chapter 4). The combination of SI with a known reference pulse is often referred to as TADPOLE (Temporal Analysis by Dispersing a Pair Of Light E-fields) [43]. Despite requiring a previously characterized reference pulse, SI is a very powerful technique, since it is very simple and fast, just requiring an interferometer and the linear detection of the spectrometer, so it can also be applied to very weak pulses.

In the past few years, several emerging techniques have been introduced. One of them is known as MIIPS (Multiphoton Intrapulse Interference Phase Scan) [44,45]. In MIIPS, different quadratic spectral phases are introduced to the pulse and the corresponding SHG is measured. The local group delay dispersion (GDD) that compensates the phase of the pulse for each wavelength is obtained by tracking the maximum signal in the SHG trace. Therefore, the second-derivative of the spectral phase of the pulse is obtained.

Another relevant technique is SRSI (Self-Referenced Spectral Interferometry) [46,47]. In this case, the cross-polarized wave (XPW) nonlinear process [6] is used to generate a FTL pulse from a replica of the input pulse. The chirp of the incoming pulse is limited so that the FTL is achievable. Then, the FTL pulse is used as the reference and the unknown pulse is later measured via SI with the known reference. As SI, this technique is then very powerful. As of late SRSI has been implemented using self-diffraction [48].

Very recently, a new technique known as d-scan (from dispersion-scan) has been demonstrated with few-cycle pulses [49,50]. This technique uses the compressor (in this case, a combination of glass wedges and chirped mirrors) to compress and characterize the pulse. The variable insertion of the wedges controls the glass thickness and a continuous dispersion scan is carried out around the optimum compression of the pulse, while tracking the SHG spectrum. Therefore, a two-dimensional trace (d-scan trace) is recorded, corresponding to the SHG as a function of the glass thickness $d$ and the frequency $\omega$. In order to retrieve the phase of the pulse, it is expressed in a certain basis (e.g. Fourier or Taylor series) and the coefficients in that basis are numerically calculated by comparing a simulated trace with respect to the experimental d-scan trace using an iterative optimization algorithm [51]. In Section 9.2 we will explain this technique in greater detail. We have used it to measure the reference pulse for STARFISH in the case of few-cycle pulses delivered by an ultrafast oscillator and amplified pulses post-compressed in a hollow-core-fiber, which are presented in Chapters 9 and 10, respectively.

Here, we have presented the most relevant techniques related to our work. Apart from the d-scan, we have used SPIDER and GRENOUILLE to measure the reference pulse in different experiments presented in this thesis. A further review of temporal characterization of ultrashort pulses is made in [2].

Although we will not use arbitrarily polarized pulses, we would like to briefly comment the techniques that have been developed to characterize them. As mentioned above, the electric field of the pulses can be in general a vector and it is reduced to a scalar in the case of linear polarization, which is the case in many situations. The electric field can be expressed in two components in the oscillation plane (perpendicular to the propagation). Depending on the trajectories that the electric field describes in that plane during its oscillations, the polarization of the pulses is called linear, circular or elliptical.

All the techniques presented above can be applied only to linearly polarized pulses. However, the polarization of the ultrashort laser pulses plays an important role in many physical processes, for example in HHG [52]. The polarization of ultrashort laser pulses is a time dependent function, so it can be different along the pulse evolution. Measuring the time-dependent polarization of the pulses means the knowledge of the time-evolution of the amplitude and phase of the two orthogonal components of the field (the $x$ and $y$ projections in the transverse plane). The polarization state (linear, circular or elliptical) depends not only on the amplitudes, but also on the relative phase between these components. Therefore, a separate temporal characterization of both components is not enough. In fact, the relative phase is essential and one critical point for this characterization.

To our knowledge, two well-established techniques are available for this purpose. The first one is known as POLLIWOG (POLarization Light Interference versus Wavelength of Only a Glint) [53]. This technique consists in using a known reference pulse (therefore relying on any other temporal characterization technique) to perform SI of the two components of the field. The use of the same reference pulse for both components allows us to retrieve the phase of the individual components and also the relative phase.

The other technique to measure the polarization of the pulses is the TURTLE (Tomographic Ultrafast Retrieval of Transverse Light E-fields) [54]. In TURTLE, two orthogonal components of the electric field are measured by means of any temporal characterization technique. Then, another temporal measurement is done in a third projection (contained in the oscillation plane). The relative phase between the two first is obtained from the cross projection by means of an optimization algorithm.

### *1.3.2. Spatial pulse characterization*

In this part, we will discard the temporal dependence of the pulses, in order to describe the characterization of their spatial profile. This characterization implies the knowledge of the amplitude and phase of the electric field as a function of the transverse spatial coordinates $(x, y)$. In order to measure the amplitude, a simple charge coupled device (CCD) can be used to record the spatial intensity $I(x, y)$.

Regarding the measurement of the spatial phase of the pulse (i.e., the wavefront), the most widespread technique is the Hartmann-Shack technique [4]. The sensor consists of a matrix of microlenses that focus small spatial samples of the pulse, which are detected

on a CCD, as illustrated in Fig. 1.7. The position of each focus will not be deviated with respect to the optical axis for flat phases. The deviation of the matrix of focal spots from the respective centers gives the local magnitude of the tilt of the wavefront (Fig. 1.7). The combination of this information over the spatial profile provides the whole information of the wavefront. Moreover, from the intensity of the matrix of foci, the spatial profile intensity can be obtained.

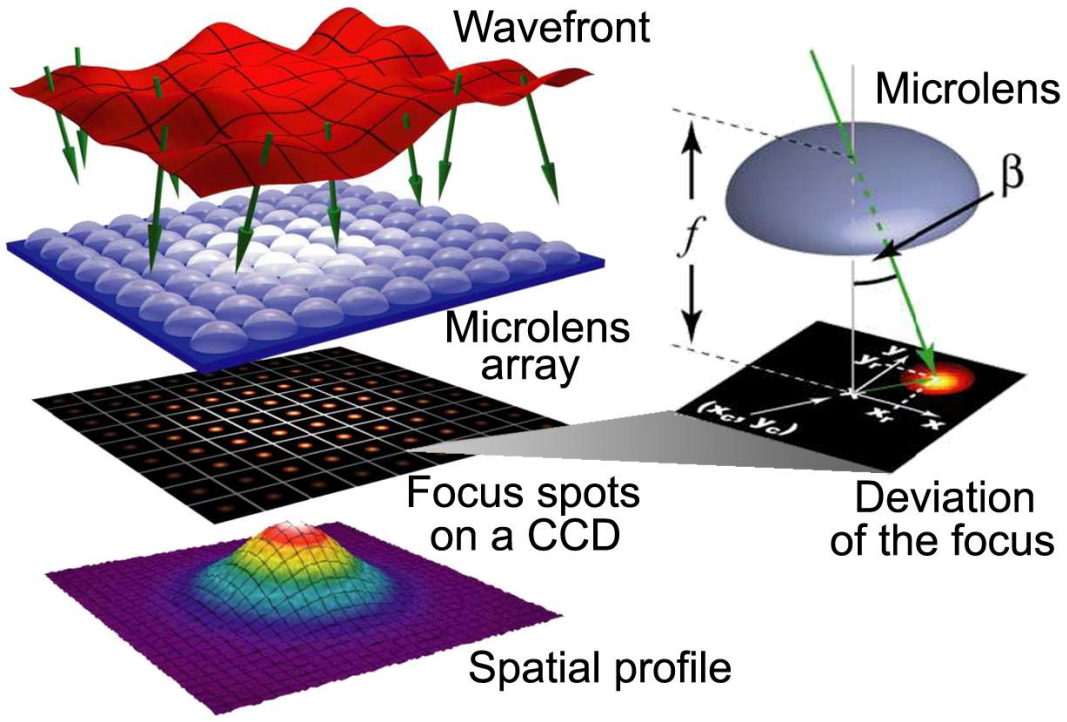


Fig. 1.7. Scheme of a Hartmann-Shack wavefront sensor (red: wavefront, blue: microlens array, black: CCD, profile: integrated intensity distribution). The deviation of each focus provides the local tilt of the wavefront. Figure extracted from [55].

Another wavefront sensor is based on multi-wave shearing interferometry [56]. In this approach, the spatial interference of several crossing replica of the pulse is used to infer the spatial phase of the pulse. In Section 3.2, we will use a commercial device based on this sensor to measure the wavefront of the reference pulse.

Recently, a technique based on SHG has been introduced. It takes advantage of the conversion efficiency dependence on the wave vector orientation in nonlinear processes due to the phase-matching condition [57].

Wavefront sensing is necessary for applications due to its influence, for example, in nonlinear processes (SHG, THG, HHG, filamentation…) and in the focusing of the pulses. Adaptive optics has been applied to correct wavefront distortions of intense ultrashort pulses [58].

### *1.3.3. Spatiotemporal characterization*

Most of the techniques for spatiotemporal characterization of ultrashort pulses have been introduced in the last decade. Initial schemes for this purpose were aimed at measuring phase differences introduced by optical elements [8] and more recently by

nonlinear propagation [59]. These approaches were based on spatially-resolved SI and did not characterize the reference beam, so they were unable to perform complete spatiotemporal reconstructions.

Spatially resolved SI consists in measuring the spectral interferences of a test and a reference beam across the spatial profile $(x, y)$. If the spatiospectral phase of the reference beam is known (i.e., it has been previously characterized), the spatiotemporal coupled amplitude and phase of the test pulse can be retrieved just by extending SI to the spatial domain. In the work of [60], a Mach-Zehnder interferometer was used. The reference beam was spatially filtered and measured in a single position, assuming a constant spectral phase. In Chapter 3, we will implement this scheme and will argue that the spatial cleaning of the reference beam is complicated and does not ensure a perfectly homogeneous reference, especially when filtering complex pulses [61].

A second approach consisted in measuring the wavefront for different frequencies using a tunable filter, and then connecting these wavefronts by means of a temporal (and equivalently, spectral) measurement of the pulse at a spatial position that contains all the wavelengths [19]. This approach gives the full spatiospectral phase that can be combined with the measurement of the spatiospectral amplitude to reconstruct the spatiotemporal amplitude and phase of the pulse. The same scheme was applied more recently by combining a Hartmann-Shack sensor and a FROG measurement [23,62]. This combination is known as Shackled-FROG. In [23] the spectral selection of the multiple wavefront was done with an imaging spectrometer and in [63] by using an acousto-optic programmable dispersive filter.

In [20], the authors used two-dimensional spatial and spectral shearing interferometry, extending the concept of SPIDER to measure simultaneously the spatial dependence. Therefore, the spatiospectral phase can be retrieved from the gradients in the two dimensions (space and frequency), similarly to the retrieval in the SPIDER. The technique conserves the self-referenced property.

In order to study nonlinear propagation, the authors developed a technique that measures the spatially resolved temporal cross-correlation [21], by measuring the sum frequency of the test pulse (unknown) with a shorter, collinear and spatially homogeneous probe. The relative delay between the probe and the test pulse is scanned to sample short time-slices of the spatial profile of the pulse. This technique provides an image of the spatiotemporal intensity (but not the phase) of the pulse, which is a valuable piece of information that has been used, for example, for the measurement of X-waves [21]. The same idea has been applied in a non-collinear geometry to measure the pulses after a quasi-direct space-to-time diffractive shaper [64].

More recently, a holographic method known as STRIPED FISH (Spatially and Temporally Resolved Intensity and Phase Evaluation Device: Full Information from a Single Hologram), demonstrated the ability to measure three-dimensional $(x, y, t)$ electric fields in single-shot [22]. The technique encodes the spatial amplitude and phase for each frequency in a large hologram.

A very successful technique is based on Spatially Encoded Arrangement Temporal Analysis by Dispersing a Pair of Light Electric-fields (SEA TADPOLE) [65] scanning the test beam as proposed in [9]. The SEA TADPOLE technique measures the spatial interferences (spectrally resolved) of two non-delayed crossed beams (see Fig. 1.8). This idea had already been implemented in [66] in a primitive scheme which involved crossing the beams directly, and has been adapted in [65] by guiding a spatial selection of the test (unknown) and the reference (known) pulses with equal-length, single-mode optical fibers. SEA TADPOLE gives the difference of spectral phase between the test and the reference pulse from the analysis of the spatial fringes in an equivalent way than SI, so it can be understood as the spatial version of SI. By scanning the transverse profile of the test pulse with the corresponding fiber, the spatiotemporal amplitude and phase of the pulse can be obtained [9].

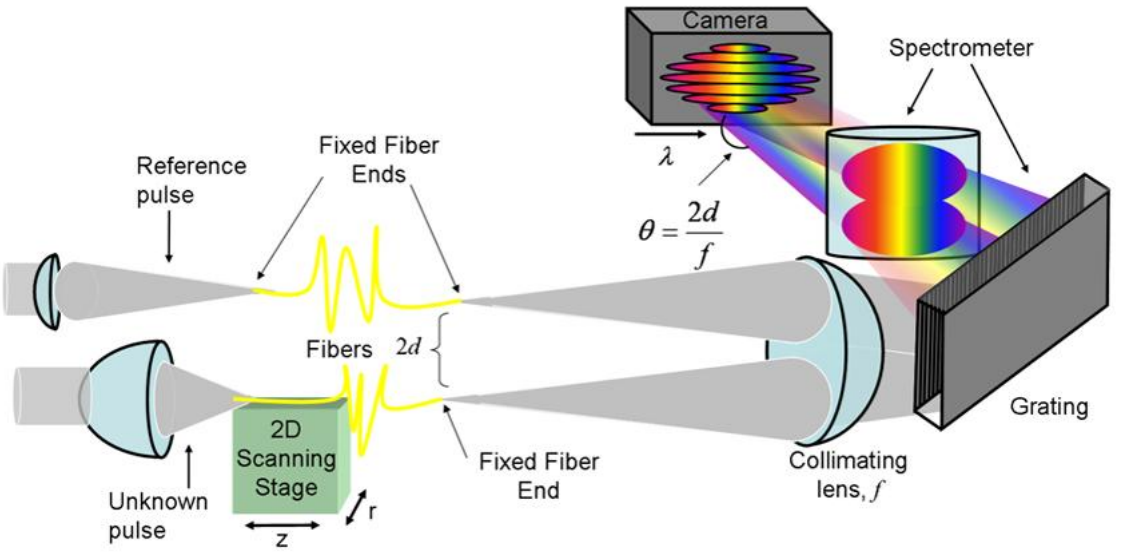


Fig. 1.8. Experimental setup used for the SEA TADPOLE technique. Two optical fibers collect a reference and a test pulse (being the latter spatially scanned). At the output of fibers, the spatial interferes of the pulses is spectrally resolved, which encodes their phase difference. Figure extracted from [9].

Very recently, the measurement of SEA SPIDER [34] completed with a separate spatial measurement has been shown to provide spatiotemporal features of the pulse from multiple spectral-shearing interferometry [67].

In this thesis, we report a novel scheme to perform spatially resolved SI based on a fiber-optic coupler. We refer to it as STARFISH (SpatioTemporal Amplitude-and-phase Reconstruction by Fourier-transform of Interference Spectra of Highly-complex-beams) [5]. In this technique, the fiber coupler is the key part and makes the system simple, robust and versatile. The technique will be presented in detail in Chapter 4.

## References


[1] Anthony E. Siegman, Chapter 17: "Physical properties of Gaussian beams" in *Lasers*, University Science Books (1986).

[2] I. A. Walmsley and C. Dorrer, "Characterization of ultrashort electromagnetic pulses," Adv. Opt. Photon. 1, 308-437 (2009).

[3] Tutorials and references regarding ultrashort laser pulses and their characterization can be found in the web of Prof. Trebino's group http://frog.gatech.edu/

[4] R. V. Shack and B. C. Platt, "Production and use of a lenticular Hartmann screen," J. Opt. Soc. Am. 61, 656-660 (1971).

[5] B. Alonso, I. J. Sola, O. Varela, J. Hernández-Toro, C. Méndez,, J. San Román, A. Zaïr, and L. Roso "Spatiotemporal amplitude-and-phase reconstruction by Fourier-transform of interference spectra of high-complex-beams," J. Opt. Soc. Am. B. 27, 933-940 (2010).

[6] Robert W. Boyd, *Nonlinear Optics*, 2nd Ed., Academic Press (2003).

[7] S. Akturk, X. Gu, P. Bowlan, and R. Trebino, "Spatio-temporal couplings in ultrashort laser pulses," J. Opt. 12, 093001 (2010).

[8] J. Jasapara and W. Rudolph, "Characterization of sub-10-fs pulse focusing with high-numerical-aperture microscope objectives," Opt. Lett. 24, 777-779 (1999).

[9] P. Bowlan, P. Gabolde, and R. Trebino, "Directly measuring the spatio-temporal electric field of focusing ultrashort pulses," Opt. Express 15, 10219-10230 (2007).

[10] O. Mendoza-Yero, B. Alonso, O. Varela, G. Mínguez-Vega, I. J. Sola, J. Lancis, V. Climent, and L. Roso, "Spatio-temporal characterization of ultrashort pulses diffracted by circularly symmetric hard-edge apertures: theory and experiment", Opt. Express 18, 20900-20911 (2010).

[11] B. Alonso, I. J. Sola, J. San Román, O. Varela, and L. Roso, "Spatiotemporal evolution of light during propagation in filamentation regime", J. Opt. Soc. Am. B 28, 1807-1816 (2011).

[12] D. Strickland, and G. Mourou, "Compression of amplified chirped optical pulses," Opt. Commun. 56, 219-221 (1985).

[13] A. Couairon and A. Mysyrowicz, "Femtosecond filamentation in transparent media," Phys. Rep. 441, 47-189 (2007).

[14] S. Akturk, X. Gu, P. Gabolde, and R. Trebino, "The general theory of first-order spatio-temporal distortions of Gaussian pulses and beams," Opt. Express 13, 8642-8661 (2005).

[15] Z. Bor, "Distortion of femtosecond laser pulses in lenses," Opt. Lett. 14, 119-121 (1989).

[16] U. Fuchs, U. D. Zeitner, and A. Tünnermann, "Ultra-short pulse propagation in complex optical systems," Opt. Express 13, 9903–9908 (2005).

[17] S. P. Veetil, C. Vijayan, D. K. Sharma, H. Schimmel, and F. Wyrowski, "Diffraction induced space-time splitting effects in ultra-short pulse propagation," J. Mod. Opt. 53, 1819–1828 (2006).

[18] A. Couairon, M. Franco, G. Méchain, T. Olivier, B. Prade, and A. Mysyrowicz, "Femtosecond filamentation in air at low pressures: Part I: theory and numerical simulations," Opt. Commun. 259, 265-273 (2006).

[19] S. Rivet, "Caractérisation complète d'un faisceau laser impulsionnel femtoseconde: mise en évidence et analyse du couplage spatio-temporel dans la propagation linéaire et non-linéaire," Ph.D. Thesis, Université de Bordeaux I (2001).

[20] C. Dorrer, E. M. Kosik, and I. A. Walmsley, "Direct space-time characterization of the electric fields of ultrashort optical pulses," Opt. Lett. 27, 548-50 (2002).

[21] J. Trull, O. Jedrkiewicz, P. Di Trapani, A. Matijosius, A. Varanavicius, G. Valiulis, R. Danielius, E. Kucinskas, A. Piskarskas, and S. Trillo, "Spatiotemporal three-dimensional mapping of nonlinear X waves," Phys. Rev. E 69, 026607 (2004).

[22] P. Gabolde and R. Trebino, "Single-shot measurement of the full spatio-temporal field of ultrashort pulses with multi-spectral digital holography," Opt. Express 14, 11460-7 (2006).

[23] E. Rubino, D. Faccio, L. Tartara, P. K. Bates, O. Chalus, M. Clerici, F. Bonaretti, J. Biegert, and P. Di Trapani, "Spatiotemporal amplitude and phase retrieval of space-time coupled ultrashort pulses using the Shackled-FROG technique," Opt. Lett. 34, 3854-3856 (2009).

[24] B. Alonso, R. Borrego-Varillas, C. Hernández-García, J. A. Pérez-Hernández, and C. Romero (editors), *El láser, la luz de nuestro tiempo*, Globalia Ediciones Anthema (2010).

[25] Eugene Hecht, *Optics*, 4th Ed., Addison Wesley (2002).

[26] Claude Rullière (editor), *Femtosecond Laser Pulses: Principles and Experiments*, 2nd ed., Springer (2004).

[27] Rick Trebino (editor), *Frequency-Resolved Optical Gating: The Measurement of Ultrashort Laser Pulses*, Kluwer Academic, (2002).

[28] H. P. Weber, "Method for pulsewidth measurement of ultrashort light pulses generated by phase locked lasers using nonlinear optics," J. Appl. Phys. 38, 2231–2234 (1967).

[29] J. C. M. Diels, J. J. Fontaine, I. C. McMichael, and F. Simoni, "Control and measurement of ultrashort pulse shapes (in amplitude and phase) with femtosecond accuracy," Appl. Opt. 24, 1270–1282 (1985).

[30] D. J. Kane and R. Trebino, "Characterization of arbitrary femtosecond pulses using frequency-resolved optical gating," IEEE J. Quantum Electron. 29, 571–579 (1993).

[31] R. Trebino and D. J. Kane, "Using phase retrieval to measure the intensity and phase of ultrashort pulses: frequency-resolved optical gating," J. Opt. Soc. Am. A 10, 1101–1111 (1993).

[32] T. Tsang, M. A. Krumbügel, K. W. Delong, D. N. Fittinghoff, and R. Trebino, "Frequency-resolved optical-gating measurements of ultrashort pulses using surface third-harmonic generation," Opt. Lett. 21, 1381–1383 (1996).

[33] P. O'Shea, M. Kimmel, X. Gu, and R. Trebino, "Highly simplified device for ultrashort-pulse measurement," Opt. Lett. 26, 932-934 (2001).

[34] C. Iaconis and I. A. Walmsley, "Spectral phase interferometry for direct electric-field reconstruction of ultrashort optical pulses," Opt. Lett. 23, 792–794 (1998).

[35] L. Lepetit, G. Cheriaux, and M. Joffre, "Linear techniques of phase measurement by femtosecond spectral interferometry for applications in spectroscopy," J. Opt. Soc. Am. B 12, 2467-74 (1995).

[36] C. Dorrer, P. Londero, and I. A. Walmsley, "Homodyne detection in spectral phase interferometry for direct electric-field reconstruction," Opt. Lett. 26, 1510-1512 (2001).

[37] P. Baum, S. Lochbrunner, and E. Riedle, "Zero-additional-phase SPIDER: full characterization of visible and sub-20-fs ultraviolet pulses," Opt. Lett. 29, 210-212 (2004).

[38] E. M. Kosik, A. S. Radunsky, I. A. Walmsley, and C. Dorrer, "Interferometric technique for measuring broadband ultrashort pulses at the sampling limit," Opt. Lett. 30, 326-328 (2005).

[39] A. S. Wyatt, I. A. Walmsley, G. Stibenz, and G. Steinmeyer, "Sub-10 fs pulse characterization using spatially encoded arrangement for spectral phase interferometry for direct electric-field reconstruction," Opt. Lett. 31, 1914–1916 (2006).

[40] J. R. Birge, R. Ell, and F. X. Kärtner, "Two-dimensional spectral shearing interferometry for few-cycle pulse characterization," Opt. Lett. 31, 2063-2065 (2006).

[41] C. Froehly, A. Lacourt, et J.Ch. Vienot, "Notion de réponse impulsionnelle et de fonction de transfert temporelles des pupilles optiques, justifications expérimentales et applications," Nouv. Rev. Opt. 4, 183-196 (1973).

[42] J. Piasecki, B. Colombeau, M. Vampouille, C. Froehly, and J. A. Arnaud, "Nouvelle méthode de mesure de la réponse impulsionnelle des fibres optiques," Appl. Opt. 19, 3749-3755 (1980).

[43] D. N. Fittinghoff, J. L. Bowie, J. N. Sweetser, R. T. Jennings, M. A. Krumbügel, K. W. DeLong, R. Trebino, and I. A. Walmsley, "Measurement of the intensity and phase of ultraweak, ultrashort laser pulses," Opt. Lett. 21, 884 (1996).

[44] V. V. Lozovoy, I. Pastirk, and M. Dantus, "Multiphoton intrapulse interference. IV. Ultrashort laser pulse spectral phase characterization and compensation," Opt. Lett. 29, 775-777 (2004).

[45] V. V. Lozovoy, B. Xu, Y. Coello, and M. Dantus, "Direct measurement of spectral phase for ultrashort laser pulses," Opt. Express 16, 592-597 (2008).

[46] T. Oksenhendler, S. Coudreau, N. Forget, V. Crozatier, S. Grabielle, R. Herzog, D. Kaplan and O. Gobert, "Self-referenced spectral interferometry," Appl. Phys. B 99, 7-12 (2010).

[47] A. Moulet, S. Grabielle, C. Cornaggia, N. Forget, and T. Oksenhendler, "Single-shot, high-dynamic-range measurement of sub-15 fs pulses by self-referenced spectral interferometry," Opt. Lett. 35, 3856-3858 (2010).

[48] J. Liu, Y. Jiang, T. Kobayashi, R. Li, and Z. Xu, "Self-referenced spectral interferometry based on self-diffraction effect," J. Opt. Soc. Am. B 29, 29-34 (2012).

[49] M. Miranda, T. Fordell, C. Arnold, A. L'Huillier, and H. Crespo, "Simultaneous compression and characterization of ultrashort laser pulses using chirped mirrors and glass wedges," Opt. Express 20, 688-697 (2012).

[50] M. Miranda, T. Fordell, C. Arnold, F. Silva, B. Alonso, R. Weigand, A. L'Huillier, and H. Crespo, "Characterization of broadband few-cycle laser pulses with the d-scan technique," Opt. Express 20, 18732- 18743 (2012).

[51] J. A. Nelder and R. Mead, "A simplex method for function minimization," Comput. J. 7, 308–313 (1965).

[52] I. J. Sola, E. Mével, L. Elouga, E. Constant, V. Strelkov, L. Poletto, P. Villoresi, E. Benedetti, J.-P. Caumes, S. Stagira, C. Vozzi, G. Sansone, and M. Nisoli, "Controlling attosecond electron dynamics by phase-stabilized polarization gating," Nat. Phys. 2, 319-322 (2006).

[53] W. J. Walecki, D. N. Fittinghoff, A. L. Smirl, and R. Trebino, "Characterization of the polarization state of weak ultrashort coherent signals by dual-channel spectral interferometry," Opt. Lett. 22, 81-83 (1997).

[54] P. Schlup, O. Masihzadeh, L. Xu, R. Trebino, and R. A. Bartels, "Tomographic retrieval of the polarization state of an ultrafast laser pulse," Opt. Lett. 33, 267-269 (2008).

[55] Figure extracted from the web of the group of Dr. Klaus Mann, Laser-Laboratorium Göttingen e.V. http://www.llg-ev.de/en/departments/optics-short-wavelengths/beam-propagation.html

[56] S. Velghe, J. Primot, N. Guérineau, M. Cohen, and B. Wattellier, "Wave-front reconstruction from multi-directional phase derivatives generated by multilateral shearing interferometers," Opt. Lett. 30, 245-247 (2005).

[57] R. Borrego-Varillas, C. Romero, J. R. Vázquez de Aldana, J. M. Bueno and L. Roso, "Wavefront retrieval of amplified femtosecond beams by second-harmonic generation," Opt. Express 19, 22851-22862 (2011).

[58] F. Druon, G. Chériaux, J. Faure, J. Nees, M. Nantel, A. Maksimchuk, G. Mourou, J. C. Chanteloup, and G. Vdovin, "Wave-front correction of femtosecond terawatt lasers by deformable mirrors," Opt. Lett. 23, 1043-1045 (1998).

[59] D. E. Adams, T. A. Planchon, A. Hrin, J. A. Squier, and C. G. Durfee, "Characterization of coupled nonlinear spatiospectral phase following an ultrafast self-focusing interaction," Opt. Lett. 34, 1294-6 (2009).

[60] S. A. Diddams, H. K. Eaton, A. A. Zozulya, and T. S. Clement, "Full-field characterization of femtosecond pulses after nonlinear propagation," in Conference on Lasers and Electro-Optics (CLEO/US) OSA Technical Digest Series, 6, paper CFF3 (1998).

[61] B. Alonso, I. J. Sola, O. Varela, C. Mendez, I. Arias, J. San Román, A. Zaïr, and L. Roso, "Spatio-temporal characterization of laser pulses by spatially resolved spectral interferometry," Opt. Pura Apl. 43, 1-7 (2010).

[62] F. Bonaretti, D. Faccio, M. Clerici, J. Biegert, and P. Di Trapani, "Spatiotemporal Amplitude and Phase Retrieval of Bessel-X pulses using a Hartmann-Shack Sensor," Opt. Express 17, 9804-9809 (2009).

[63] S. L. Cousin, J. M. Bueno, N. Forget, D. R. Austin, and J. Biegert, "Three-dimensional spatiotemporal pulse characterization with an acousto-optic pulse shaper and a Hartmann–Shack wavefront sensor," Opt. Lett. 37, 3291-3293 (2012).

[64] V. Loriot, O. Mendoza-Yero, G. Mínguez-Vega, L. Bañares, and R. de Nalda, "Experimental Demonstration of the Quasi-Direct Space-to-Time Pulse Shaping Principle", IEEE Photonics Technology Letters 24, 273-275 (2012).

[65] P. Bowlan, P. Gabolde, A. Shreenath, K. McGresham, R. Trebino, and S. Akturk, "Crossed-beam spectral interferometry: a simple, high-spectral-resolution method for completely characterizing complex ultrashort pulses in real time," Opt. Express 14, 11892-11900 (2006).

[66] D. Meshulach, D. Yelin, and Y. Silberberg, "Real-time spatial-spectral interference measurements of ultrashort optical pulses," J. Opt. Soc. Am. B, 14, 2095-8 (1997).

[67] A. S. Wyatt, A. Grün, P. K. Bates, O. Chalus, J. Biegert, and I. A. Walmsley, "Accuracy measurements and improvement for complete characterization of optical pulses from nonlinear processes via multiple spectral-shearing interferometry," Opt. Express 19, 25355-25366 (2011).

# CHAPTER 2

# SPECTRAL INTERFEROMETRY

**Contents**

## 2.1. Principles of spectral interferometry

### *2.1.1. History and applications*

Spectral interferometry (SI) was first introduced in a context of temporal holography with the interference of two (or more) polychromatic beams [1], where the authors studied the transfer function (the time and frequency response) of different optical pupils.

The natural dependence of the SI on the relative phase of the two interfering beams was initially used to measure the full temporal response of optical fibers in linear regime in the range of picosecond pulses [2], comparing the multi-mode fiber dispersion with respect to a single-mode fiber [3]. Later, SI was applied to measure the nonlinear time response of optical fibers [4-6]. Over the next few years, SI was applied to many other fields, including ultrashort [7,8] and XUV [9] pulses characterization, microscopy [10], data storage [11], and biomedical imaging [12]. Its high sensitivity (linear detection) and simplicity (the phase is extracted by Fourier-analysis) have made possible all these applications.

### *2.1.2. Measurement of ultrashort laser pulses*

We are interested in the application of SI to the characterization of ultrashort laser pulses. The philosophy of SI lies on encoding the difference of phase between two pulses in their interference spectrum. This relative phase can be extracted from the fringes analysis [13] (the algorithm is explained in Section 2.2). If one of the pulses is known, then the unknown pulse phase can be obtained. This technique is known as TADPOLE [7]. The reference pulse can be calibrated with any temporal measurement technique, such as FROG [14] or SPIDER [8]. SI is also involved in other techniques. For example, SPIDER is a self-referenced SI thanks to a nonlinear process and a spectral shearing [8], POLLIWOG relies on dual-channel SI to retrieve the time dependent polarization of the pulses [15], and spatially-resolved SI has been applied to measure the spatiospectral (and spatiotemporal) amplitude and phase of ultrashort pulses [16,17] (see also Chapter 3). The spatial encoding of the interferences in SEA TADPOLE has been demonstrated for the same purpose [18]. Finally, SI is the basis of STARFISH [19], our proposal for spatiotemporal characterization of pulses, which will be detailed in Chapter 4.

In SI, two collinear pulses, namely the test and the reference, are delayed in time by a magnitude $\tau$ as shown in Fig. 2.1a. The reference is the known pulse, whose spectral phase must be previously characterized. The test is the unknown pulse that we wish to characterize. The electric field of each pulse in the spectral domain $E_f(\omega)$ is expressed as $E_f(\omega) = |E_f(\omega)| \exp\{i\phi(\omega)\}$, where $\omega$ is the angular frequency, $\phi(\omega)$ is the spectral phase and we define $S(\omega) = |E_f(\omega)|^2$ as the power spectral density or, simply, the pulse spectrum. From the definitions of the Fourier-transform (FT or $\mathcal{F}$) and its inverse (IFT or $\mathcal{F}^{-1}$), shown in Eq. (1.5), and their properties, we can calculate the interference spectrum, that is to say, the spectrum of the sum of the test and reference pulses, whose

derivation is shown in Eq. (1.12). At this point, it is worth recalling that we defined the pulse in the temporal domain as $E(t)=\sqrt{I(t)}\exp\{i[\omega_0 t+\varphi(t)]\}$, where $I(t)$ is the temporal intensity, $\omega_0$ is the carrier (or central) frequency and $\varphi(t)$ is the temporal phase. The electric field in temporal and spectral domain are related by $\mathcal{F}\{E(t)\}=E_f(\omega)$ and $\mathcal{F}^{-1}\{E_f(\omega)\}=E(t)$. The total spectrum $S(\omega)$ is then expressed as

$$S(\omega)=S_{test}(\omega)+S_{ref}(\omega)+2\sqrt{S_{test}(\omega)S_{ref}(\omega)}\cos[\phi_{test}(\omega)-\phi_{ref}(\omega)-\omega\tau], \qquad (2.1)$$

which is the sum of the test and reference spectra ─the non-interfering contributions─ and the interference cross term. An example is provided in Fig. 2.1b. The interference term is an oscillating contribution, whose amplitude is proportional to the cross product of the test and reference spectra, whereas the fringes come from the cosine and are periodic in frequency with a period proportional to the inverse of the delay $1/\tau$. In our case, the sign of the delay $\tau$ in Eq. 2.1 is positive because we choose the criterion that the reference pulse arrives before the test pulse. Unless otherwise stated, we will keep this criterion, paying special attention to it in the experiments.

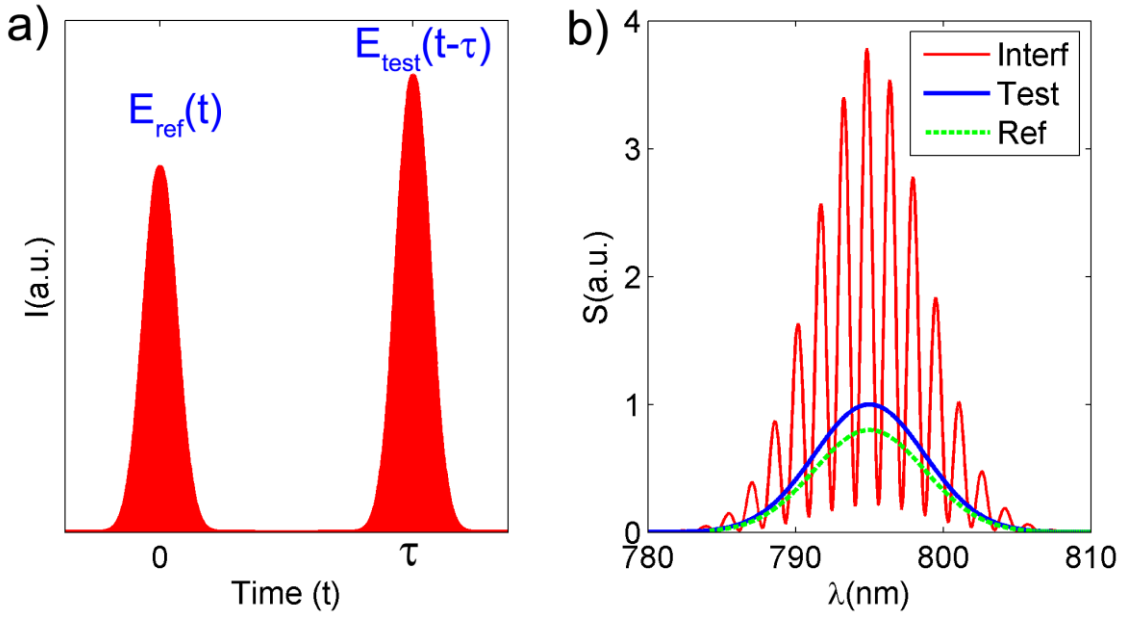


Fig. 2.1. (a) Picture of two pulses, the test and the reference, delayed in the time domain. As a criterion, the reference arrives before the test pulse. (b) Spectral power density of the individual pulses (test and reference) and their spectral interferences.

### *2.1.3. Relevant requirements and parameters*

The first requirement for SI is that the two pulses are collinear. Therefore, careful alignment of the pulses is generally mandatory to obtain the interferences in the spectral domain. The second requirement is that they should be linearly polarized in the same direction. In the case of non-parallel orientation or elliptical/circular polarization, the contrast will be reduced and the spectral phase encoded in the SI will have a different dependence.

The delay between the two pulses is related to the fringes period. The valid range for the delay has inferior and superior limits. On the one hand, the delay has to be longer

that the pulse duration to discern the interference term from the non-interfering contribution during the FT analysis. On the other hand, large delays produce rapidly oscillating spectral fringes that should be resolved by the sampling in the spectrometer. Both limits will be studied in detail in Section 2.3.

Additionally, the reference spectrum must comprise at least the test pulse spectrum to obtain the phase difference for the whole spectrum of the test pulse. This phase is extracted from the cross-term of the SI, which is present in the region of the spectrum where the two pulses overlap. When measuring processes that maintain the spectral amplitude of the pulses, this is fulfilled whenever the reference and test are replicas of the same laser source. In nonlinear processes, the test pulse often experiences spectral broadening. In those cases, the reference can be taken as a sample of the test pulse (as we did in the post-compression inside a hollow-fiber in Chapter 10) or can be spectrally broadened in a parallel nonlinear experiment (we took this option for the measurement of the filamentation in Chapter 8).

Apart from these mandatory constraints, there are other experimental parameters that play a role in SI. A relatively good contrast of the fringes is necessary to obtain a correct reconstruction. This means that the relative amplitude of the test and reference pulses in spectral domain has to be comparable. If one of the pulse signals is much weaker, then the interference term vanishes because it is proportional to the amplitude of both pulses, thus preventing the phase extraction from the fringes. Nevertheless, the fact that the interferences are proportional to the amplitude of both pulses can be an advantage to enhance the fringes (the signal of the interference term) in the spectral regions where the test pulse signal is too low, whenever the reference pulse amplitude is higher (e.g. in the case of a modulated spectrum of a diffracted test pulse interfering with a Gaussian-like reference spectrum). Also, the noise in the detection (the spectral measurement) can introduce noise in the retrieval. For this reason, it is recommended to use the full dynamic range of the spectrometer (while avoiding saturation), in order to have a good signal to noise ratio.

### *2.1.4. Experimental setup*

The experimental implementation of SI requires the use of an interferometer. An often used option is a Mach-Zehnder interferometer (see Fig. 2.2). Firstly, a replica of the input laser pulse is created with a beam splitter. A delay line is necessary to control the relative delay between the pulses. The test pulse undergoes a certain process or experiment that we wish to characterize. The reference pulse is measured with an additional temporal characterization device. At the end of the interferometer, both pulses are recombined collinearly with another beam splitter. The SI is measured with a standard interferometer, in our case a spectrometer with SMA (Sub Miniature A) connectorized fiber input (AvaSpec 2048-USB1, Avantes Inc.). The free spectral range of the spectrometer is 700-900 nm and the resolution is 0.1 nm. As stated above, the two pulses have to be carefully aligned at the output of the interferometer.

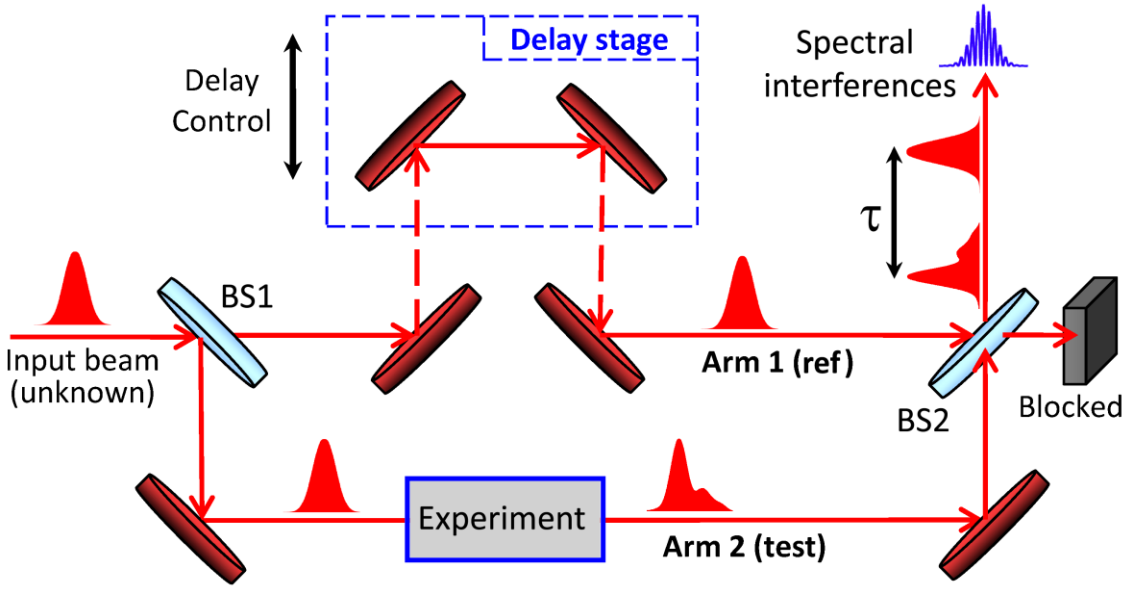


Fig. 2.2. Experimental setup for the spectral interferometry: Mach-Zehnder interferometer. The laser input is divided into two arms by a beam splitter (BS1). The reference pulse optical path is controlled by a delay stage to adjust the relative delay with the test pulse. In the test arm, a certain process or experiment modifies the test pulse that is going to be characterized. The test and reference pulses are recombined in a second beam splitter (BS2) and aligned. Their spectral interferences are measured with a standard spectrometer.

Once the reference is calibrated, SI allows us to easily measure the pulse test under many different conditions just by changing any parameter over the test pulse experiment, as long as the alignment, bandwidth and other requirements are preserved. Since SI is very low-demanding in terms of acquisition (just the spectral measurement) and retrieval (a three-step FT algorithm), this opens the possibility to fast parametric measurements on the experiment (for example, varying the chirp, propagation distance, or any other parameter). This is the reason why we choose SI to characterize the pulses, and is the basis of the extension of the temporal measurements to the spatial domain as well.

## 2.2. Phase extraction algorithm: Fourier-transform spectral interferometry

The relative phase between the test and reference pulses is encoded in the SI given by Eq. (2.1) and shown in Fig. 2.1b. In particular, it is encoded in the cosine term, so data processing is required to obtain it. Different implementations are possible to extract this information [1,3,4,13,20,21]. In [1], the spectrogram was examined by Fourier-analysis and the diffraction of a beam was used to reconstruct the 'hologram'. Initially, Piasecki and co-workers [3] recorded the SI in a photographic plate, which was reconstructed by illuminating with a helium-neon laser, whose far field was recorded. The central portion of the reconstruction corresponded to the non-interfering signal, whereas two side antisymmetric signals gave the pulse response. In [4], the authors used the fact that each maximum in the SI corresponds to an increase of $2\pi$ in the phase difference, and, analogously, in [6] the authors extracted the phase by measuring the shift of the interference fringes.

The direct extraction of the numerical phase from the argument of the cosine poses ambiguities because the inverse of the cosine is a multi-valued function (the quadrant of the argument is not univocally determined). Furthermore, a previously used fringe-contour analysis for interferometry could not retrieve the phase with sub-$2\pi$ precision. To our knowledge, the first numerical extraction of the phase with such precision is reported in [21], where the authors measure the wavefront of a beam using spatial interferometry. Assuming a single spatial dimension, the interferences are proportional to $2\cos\beta$, where the argument $\beta$ is the sum of the phase $\phi(x)$ and a term coming from a relative tilt $2\pi k_0 x$. The method is based on the FT-analysis of the fringes and the relation $2\cos\beta = \exp\{+i\beta\} + \exp\{-i\beta\}$. Taking into account the term $2\pi k_0 x$, when an FT is applied to the signal, in the frequency domain there are two signals corresponding to $\exp\{\pm i\beta\}$ centered at the spatial frequencies $k = \pm k_0$. Then, one of those signals is gated, shifted to $k = 0$, and an IFT is applied. The resulting signal in the spatial domain allows us to obtain the phase $\phi(x)$, in this case encoded in the imaginary exponential $\exp\{+i\beta\}$. Now, the argument $\beta$ can be easily calculated, although it is obtained wrapped in a range of $[-\pi, \pi]$, owing to the multi-valuation of the argument function (the quadrant is determined, but there is a $2n\pi$ shift ambiguity, $n$ being an integer).

The algorithm that we will follow is in essence the proposal of [21], although in this case it is applied to spectral interferometry ($\omega, t$ spectrum-time domains) instead of spatial interferences ($x, k$, spatial-frequency domains). This algorithm is known as Fourier-transform spectral interferometry (FTSI) [13] and is the most widely used because the phase is retrieved precisely and univocally with an FT analysis. Also, the use of fast algorithms for the numerical computation of the FT allows a fast retrieval of the phase.

At this point, a detailed explanation of FTSI [13] is provided. The scheme of Fig. 2.4 represents all the steps carried out in the algorithm. First, an IFT is applied to the interference spectrum, seen in Eq. (2.1), thus yielding in the time domain the three peaks represented in Fig. 2.3. One peak is centered at $t = 0$ corresponding to the background or non-interfering contribution of the individual pulse spectra. The other two peaks, coming from the interference term, are centered at $t = \pm\tau$. If desired, the test and reference spectra can be subtracted before this step to get rid of the central peak (we will discuss this in the next section). With the criterion that we have chosen for the delay sign (reference pulse before the test pulse), the cosine of the interferences can be expressed as the sum of two imaginary exponential functions, namely $\exp\left\{i\left(+\phi_{test}(\omega) - \phi_{ref}(\omega) - \omega\tau\right)\right\}$ and $\exp\left\{i\left(-\phi_{test}(\omega) + \phi_{ref}(\omega) + \omega\tau\right)\right\}$, corresponding respectively to the signals centered at $t = +\tau$ and $t = -\tau$. Then, we select the right-hand-side peak ($t = +\tau$) multiplying the IFT by a numerical gate. We use a supergaussian function as gate to avoid introducing sharp steps in the numerical calculation (dashed green line in Fig. 2.3). The signal filtered in the time domain is plotted in red (the lateral peak centered at $t = +\tau$). Note that the experimental data are acquired in wavelengths and the conversion to frequencies has to be done before applying the IFT.

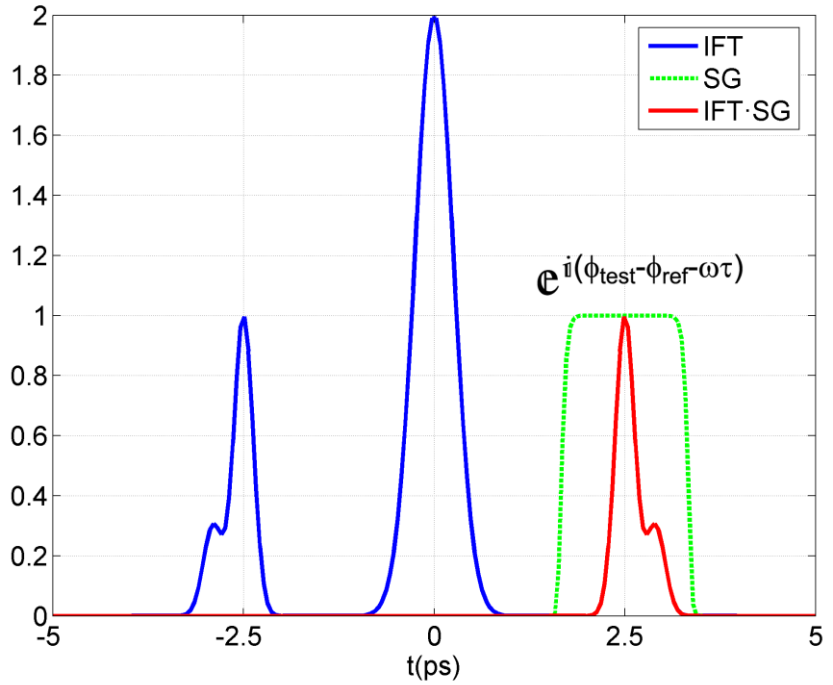


Fig. 2.3. Inverse Fourier-transform (IFT) of the spectral interferences (blue line) in the time domain. The gate applied is a supergaussian (SG) function centered at the position of the lateral peak (green dashed line). The filtered signal is the product of the both, selecting only one lateral peak (red line).

By this procedure, the two imaginary exponential functions are uncoupled. Then, a direct FT is applied to the remaining signal (the filtered peak). As a result, the new signal in the spectral domain corresponds to

$$S_{FTSI}(\omega) = \sqrt{S_{test}(\omega)S_{ref}(\omega)}\exp\left\{i\left(+\phi_{test}(\omega)-\phi_{ref}(\omega)-\omega\tau\right)\right\} \qquad (2.2)$$

Since the delay is given by the position of the lateral peak, we can multiply $S_{FTSI}(\omega)$ by $\exp\{i\omega\tau\}$ to obtain the phase difference between the two pulses $\phi_{test}-\phi_{ref}$ in the frequency domain, which can be numerically extracted from the argument of $S_{FTSI}(\omega)\mathrm{e}^{i\omega\tau}$. Despite not being mandatory for the calculation, the phase can be unwrapped to get a continuous function in order to visualize it or to fit the phase to a polynomial, for example. The numerical unwrap is, in fact, not mandatory. Next, the reference phase calibration is introduced to calculate the spectral phase of the test pulse $\phi_{test}(\omega)$. The spectrum of the test pulse can be measured separately $S_{test}(\omega)$, which completes the amplitude and phase characterization. Since the reference spectrum is also known, another possibility would be to extract the test pulse amplitude from the FTSI, in particular dividing the magnitude $\left|S_{FTSI}(\omega)\right| = \sqrt{S_{test}(\omega)S_{ref}(\omega)}$ by the reference's amplitude. We will use the alternative of directly measuring the test pulse spectrum since just blocking the reference pulse is very easy and the division may enhance the noise in the tails of the spectrum. This way, the electric field in the frequency domain is calculated as $E_f(\omega) = \sqrt{S_{test}(\omega)}\exp\left[i\phi_{test}(\omega)\right]$. Finally, the pulse in the temporal domain is calculated by applying an IFT to the spectrum, that is, $E(t) = \mathcal{F}^{-1}\{E_f(\omega)\}$. To plot the temporal phase, the fast carrier frequency contribution

$\omega_0 t$ is subtracted (see the last subplot in Fig. 2.4). For the numerical implementation of the algorithm we will mainly use fast Fourier-transform (FFT) codes to reduce the computation time. The extension of SI to the spatial domain will require many FT calculations (3 times per spatial point), so for us it is worth to save time.

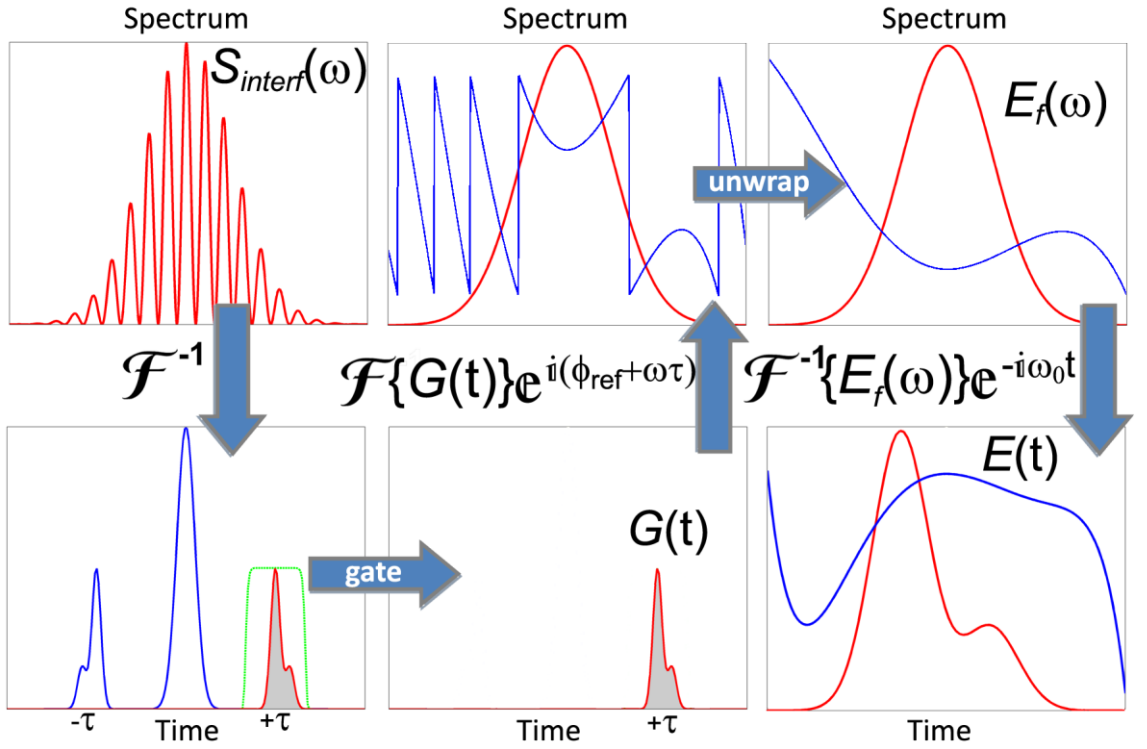


Fig. 2.4. Scheme of the algorithm implemented for Fourier-transform Spectral Interferometry. First, an inverse Fourier-transform is applied to the spectral interferences. In the time domain, one lateral peak is gated and direct Fourier-transformed. In frequency domain, the term $\omega\tau$ and the reference phase are corrected, and the phase is unwrapped. This gives the spectral amplitude and phase of the test pulse, which can be translated to the temporal domain by applying again an inverse Fourier-transform. In our case, we measure the spectral amplitude of the pulse directly with the spectrometer.

## 2.3. Estimation of the temporal limits and eligible delay

The aim of this section is to analyze the range of temporal duration of the pulses that can be measured by SI depending on the spectrometer resolution. First, we will present a standard case and then particular situations, e.g. chirped pulses or multiple pulses, which we will find in different applications of STARFISH. Further analysis of SI can be found in previous works dealing with the consequences of the calibration of the detection and the delay [22], and the effect of the spectrometer resolution and sampling, FT algorithm and experimental noise [23].

### *2.3.1. Consideration of pulse duration and delay due to the spectral resolution*

The range of application of SI depends on the pulse and the spectrometer parameters. In fact, the spectrometer's resolution $\delta\omega$ is related to the longer pulses that can be measured with a certain setup. The Nyquist-Shannon sampling theorem establishes that for a frequency sampling $\delta\omega$, the maximum temporal range in which the corresponding signal can be perfectly reconstructed is given by the relation $t_{max} = \pi / \delta\omega$. Note that our

signal remains within the range $[-t_{\max}, t_{\max}]$, so the full width of the temporal range is $2{\cdot}t_{\max}$. The resolution in the spectral domain for an experimental measurement can be estimated from the resolution in wavelengths $\delta\lambda$ of the spectrometer as $\delta\omega \approx (2\pi c/\lambda_0^2){\cdot}\delta\lambda$, for a central wavelength $\lambda_0$. For example, the spectrometer that we used to measure pulses longer than 25 fs centered at $\lambda_0 = 800\,nm$ had a resolution of $\delta\lambda = 0.1nm$ that corresponds to $t_{\max} \approx 10.7\ ps$.

In order to analyze the spectral phase encoded in the SI (using the FTSI algorithm), it is necessary that the three peaks centered at $t = \{0, \pm\tau\}$ in the time domain after IFT are well separated (see Fig. 2.3). This constraint imposes limits on the maximum pulse duration and the range of delays $\tau$ that can be used. As said before, the central peak could be reduced subtracting the test and reference spectra from the total spectrum (Eq. (2.1)) and this could reduce the minimum delay between the reference and the test pulses (and thus increment the range of work). However, the noise and fluctuations in the experiment could prevent a perfect depletion of the central peak, so we prefer to be more restrictive and assume that this peak is not removed.

Depending on the particular cases of the reference and test pulses involved in the SI, the maximum temporal duration of the pulses to be measured will be different. Let us call $\Delta t_{test}$ and $\Delta t_{ref}$ the full widths ─defined as the temporal range that includes the whole pulse─ of the test pulse and reference pulse, respectively. The equivalents for their Fourier-transform limit (FTL) will be denoted respectively as $\Delta t_{test}^{FTL}$ and $\Delta t_{ref}^{FTL}$. In a first approach, we will consider that the reference and the test pulse durations are similar and not much longer than their Fourier-transform limits (FTL). This means that the durations $\Delta t_{test}$, $\Delta t_{test}^{FTL}$, $\Delta t_{ref}$ and $\Delta t_{ref}^{FTL}$ are all of the same order which we call $\Delta t_0$. In order to be conservative, $\Delta t_0$ is the largest of the values.

At this point it is important to realize that the widths of the peaks shown in Fig. 2.3 (that is, the IFT of the Eq. (2.1)) will be different. The central peak is the sum of the FTL of the test and the reference pulses, so its full width can be approximated by $\Delta t_0$. The lateral peaks are the IFT of the quantity $\sqrt{S_{test}S_{ref}}\exp\{\pm i(\phi_{test} - \phi_{ref} - \omega\tau)\}$, so for this approach its width will be also $\sim \Delta t_0$.

Therefore, the temporal range $t_{\max}$ must comprise at least half the width of the central peak and the full width of the lateral one. Together with the Nyquist -Shannon theorem, this gives the upper limitation for the pulse duration

$$(3/2){\cdot}\Delta t_0 < t_{\max} \le \pi/\delta\omega. \qquad (2.3)$$

The same reasoning can be applied to infer the limits of the eligible delay. In this case, the delay has to be high enough to separate the signal of the central and lateral peaks and small enough to keep the lateral peak under the value $t_{\max}$, which impose the limits given by

$$\Delta t_0 \le \tau \le t_{\max} - \Delta t_0/2. \qquad (2.4)$$

The implication of Eq. (2.4) is shown in Fig. 2.5, considering the value of $t_{\max} \approx 10.7\ ps$ set by the spectrometer used in the present example. In Fig. 2.5, the right-hand side of the Eq. (2.4) is labelled "Large $\tau$" and shaded in blue, whereas the left-

hand side is labelled "Small $\tau$" and shaded in red. The region in which the delay verifies both inequalities is labelled "Valid $\tau$" (shaded in green). The eligible delay for a certain pulse length $\Delta t_0$ is inside the green region. The maximum pulse duration of a theoretically measurable pulse is $\Delta t_{0,\max} = (2/3)t_{\max} = 7.1\,ps$, as given by Eq. (2.3). This situation corresponds to the intersection point illustrated in the graphic, $\tau = \Delta t_{0,\max}$.

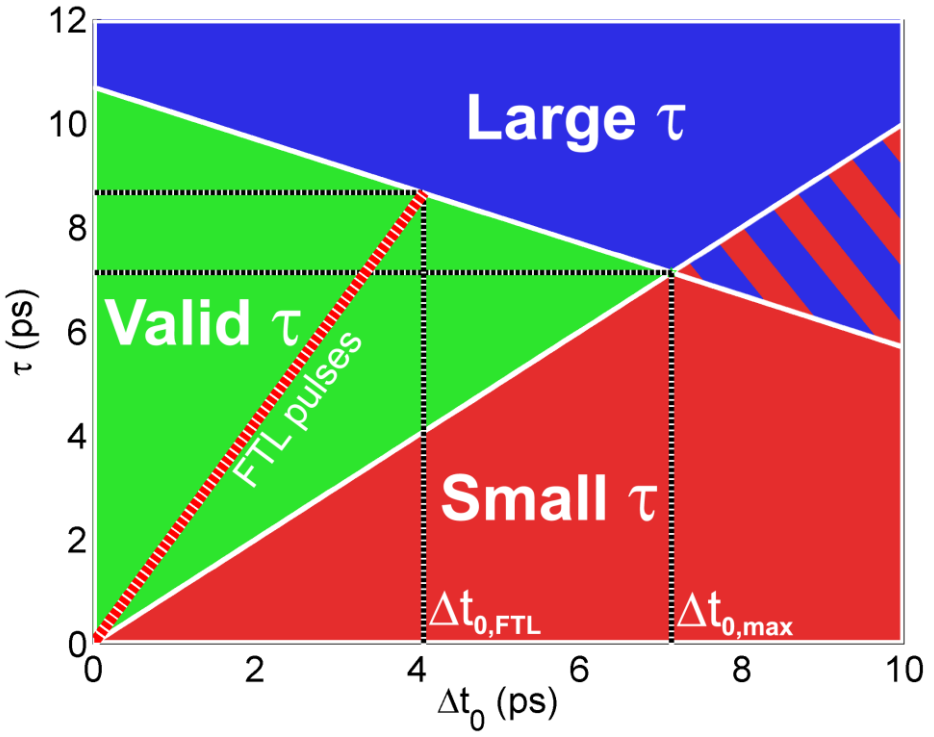


Fig. 2.5. Diagram of measurable pulse durations and eligible delays. The valid region of work is shaded in green.

However, there is another limitation for FTL pulses: the minimum number of fringes. If a Gaussian pulse is assumed where $\Delta t$ and $\Delta\omega$ denote the intensity FWHM in the time and the spectral domain, respectively, then it verifies: $\Delta t \cdot \Delta\omega = 4\ln 2$. Moreover, the period of the spectral fringes is $\omega_\tau = 2\pi/\tau$. The number of periods of the fringes inside the FWHM of the spectrum can be evaluated by the ratio $N_{50\%} = \Delta\omega/\omega_\tau$, which corresponds to the quantity $N_{50\%} = [2\ln 2/\pi]\cdot\tau/\Delta t$. For example, in the case of a Gaussian pulse of intensity FWHM of $\Delta t = 3\,ps$ and a delay of $\tau = 7\,ps$, this number is $N_{50\%} \approx 1$, which makes the number of fringes insufficient to retrieve the phase. Since the delay cannot be increased, as a result such pulse cannot be measured. In particular, using a delay $\tau = 7\,ps$ and a Gaussian pulse, we have found numerically a minimum number of fringes $N_{50\%} \approx 3$ (corresponding to $\Delta t = 1\,ps$) for which the spectral phase is correctly retrieved by SI (introducing the effect of the spectrometer's resolution).

To see the equivalent on the diagram of Fig. 2.5, we consider the full width of the pulse $\Delta t_0$ as the temporal range in which the pulse intensity falls to 0.1% from the maximum, which, for a Gaussian pulse, gives the equivalence $\Delta t_0 \approx 3.2\Delta t$. In general, the condition $N_{50\%} \geq N_{\min} = 3$ is translated to the pulse duration by the relation

$$\Delta t_0 \leq \frac{3.2\cdot 2\ln 2}{\pi}\frac{\tau_{\max}}{N_{\min}} \leq \frac{\beta}{1+\beta/2}t_{\max}, \qquad (2.5)$$

where we have defined the constant $\beta = (3.2 \cdot 2\ln 2)/(\pi N_{\min}) \approx 0.47$ and have used the right-hand side of Eq. (2.4) to estimate the maximum delay $\tau_{\max}$. From Eq. (2.5) we calculated a maximum pulse duration of full width $\Delta t_{0,\mathrm{FTL}} \approx 4.1 ps$ (FWHM $\Delta t \approx 1.3 ps$) that could be measured with a delay $\tau \approx 8.7\, ps$. Finally, the restriction ($N_{50\%} \geq 3$) on the delay for FTL pulses is $\tau \geq \Delta t_0 / \beta$, which can be derived from Eq. (2.5). We have included it as a dashed red line on Fig. 2.5.

To conclude, we would like to stress that for this estimation, we have considered a particular case of test and reference pulses with similar bandwidth and slight chirp. The next subsection discusses how these limitations may be modified for different situations. In general, the diagram of Fig. 2.5 can be used as a guideline to estimate the delay required and the maximum pulse duration. Specific cases may require, however, to be considered separately. For example, if the test pulse spectrum is considerably narrower than the reference spectrum (and they are slightly chirped), then the peak widths of the IFT of the SI will be less than or equal to the test pulse duration. The same applies to the minimum number of fringes in the SI. Precisely, the full width of the lateral peak will be within the range $[\Delta t_{ref}, \Delta t_{test}]$ because the spectrum $\sqrt{S_{test} S_{ref}}$ is narrower than $S_{ref}$ and broader than $S_{test}$ and, to be conservative, we can use $\Delta t_{test}$ for its upper limit. Therefore, the expressions above are still valid when using $\Delta t_0 = \Delta t_{test}$.

### *2.3.2. Chirped pulses and multiple pulses*

The most frequent situations that significantly modify the scenario described above are chirped pulses and multiple pulses, in which the test pulse is much longer than its FTL. We start with the study of the case of strongly chirped test pulses. For the sake of simplicity, we will consider a slightly chirped reference pulse, both pulses having similar bandwidths. In this case, the width of the central peak ($t = 0$) of the IFT (see Fig. 2.3) will also be the FTL of the pulses $\Delta t_{test}^{FTL} \sim \Delta t_{ref}^{FTL} \equiv \Delta t_{FTL}$. Regarding the lateral peak ($t = +\tau$), if we recall Eq. (2.2), we can see that the spectral bandwidth is similar to the test pulse bandwidth and that the relative phase is approximately that of the test pulse, so the width of this signal will be $\sim \Delta t_{test} \gg \Delta t_{ref}, \Delta t_{FTL}$. The main point here is that the central peak is not broadened independently on the pulse chirp. Therefore, the left-hand side of Eq. (2.3) and (2.4) are modified in the following way

$$\begin{aligned} \Delta t_{FTL}/2 + \Delta t_{test}/2 < t_{\max} &\leq \pi/\delta\omega \\ \Delta t_{FTL}/2 + \Delta t_{test}/2 \leq \tau &\leq t_{\max} - \Delta t_{test}/2. \end{aligned} \qquad (2.6)$$

Since $\Delta t_{FTL} \ll \Delta t_{test}$ the temporal window in Fig. 2.3 will allow the measurement of larger pulse durations $\Delta t_{test}$. To study this property, we simulated the SI of linearly chirped laser pulses with $120\, fs$ duration (FTL, intensity FWHM). In the results presented in Fig. 2.6 and 2.7, we have used experimental spectra (from our two main laser systems) for the pulses to be closer to the experimental conditions. We varied the group delay dispersion ($GDD$) of the test pulse from –80000 to +80000 $fs^2$. The results are presented in Fig. 2.6. For negative chirp ($GDD < 0$), the bluer wavelengths arrive first. Taking into account that the reference is before the test pulse, this means that the redder wavelengths are more delayed with respect to the FTL reference pulse

than the bluer wavelengths. In Fig. 2.6a, the period of the fringes varies with the wavelength and the *GDD* following the dependence $\sim 1/\tau$ (for the central wavelength the delay is set to $4\,ps$ in all cases). We imposed the experimental resolution and applied the FTSI algorithm to the fringes. In Fig. 2.6b, the IFT of the SI is represented in logarithmic scale as a function of the *GDD*, where we have depleted the background contribution of the individual spectra. The width variation of the lateral peak is clearly observed. Next, the spectral phase, the temporal intensity profile and the instantaneous wavelength of the pulses were calculated as a function of the *GDD*, and plotted respectively in Fig. 2.6c, 2.6d, and 2.6e. The quadratic spectral phase is correctly retrieved, explaining the broadening of the pulses and their linear chirp. Finally, the second order of the retrieved spectral phase is fitted and corroborated by the theoretical phase (Fig. 2.6f). The pulse duration of the largest chirps (both negative and positive) was $4\,ps$ (full width).

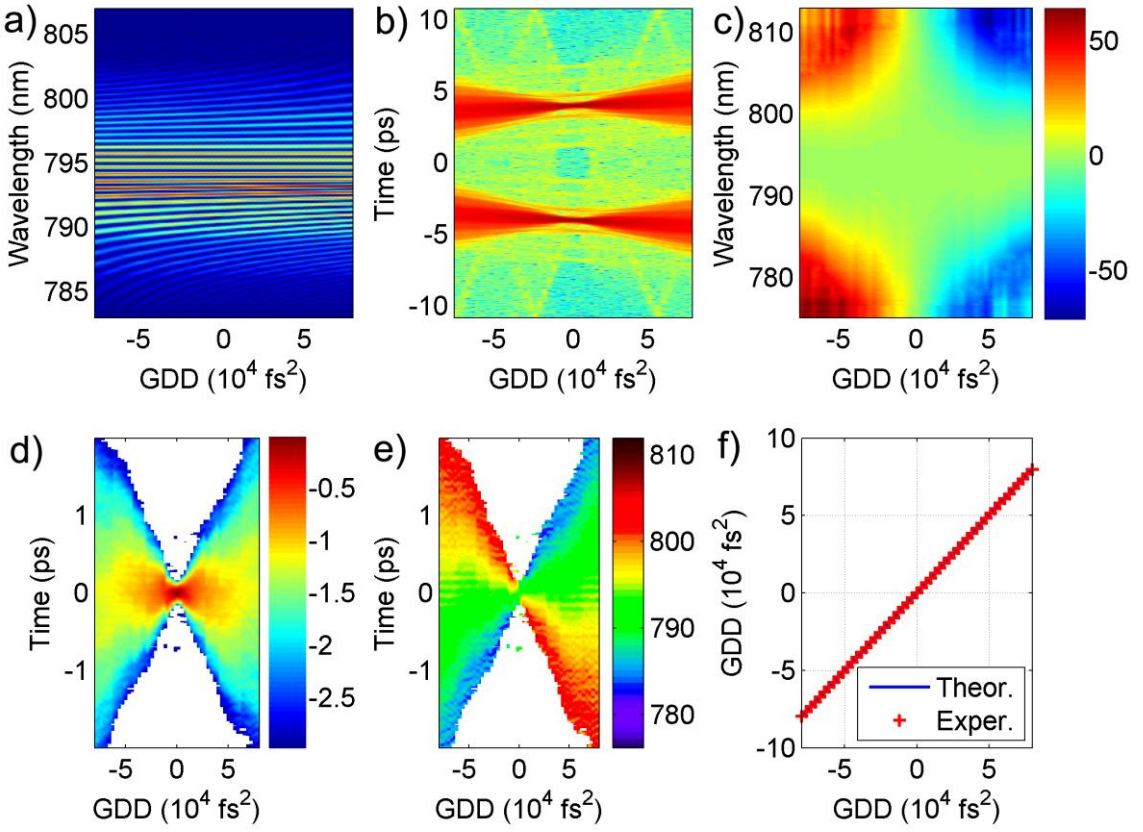


Fig. 2.6. Simulation of the spectral interferometry of strongly chirped 120 fs (FTL) pulses. As a function of the group delay dispersion (GDD): (a) Spectral interferences, (b) Inverse Fourier-transform, (c) Spectral phase retrieved, (d) reconstructed pulses (logarithmic scale), (e) Instantaneous wavelength of the pulses, and (f) GDD retrieved from the fit of the phase.

To complete the result, we simulated in a similar way linearly chirped $35\,fs$ pulses (FWHM). In this case, owing to the larger bandwidth, we could also vary the *GDD* from $-40000$ to $+40000\,fs^2$, since the temporal pulse broadening is higher (see Fig. 2.7). In Fig. 2.7a, the IFT of the SI is represented in logarithmic scale for a delay of $6\,ps$ for the central wavelength. In that plot, it is clear how we can take advantage of the fact that the central peak (not shown in the figure since the background spectra were subtracted) has always the same width (in this case, $35\,fs$ FWHM). In Fig. 2.7b, the

quadratic spectral phase used in the simulation is shown. The temporal profile (the pulse intensity) is represented as a function of the GDD in Fig. 2.7c, where the maximum temporal duration reached the value of $7\,ps$ (full width). The instantaneous wavelength of the pulses is also shown (Fig. 2.7d), exhibiting the expected linear chirp dependence on the $GDD$.

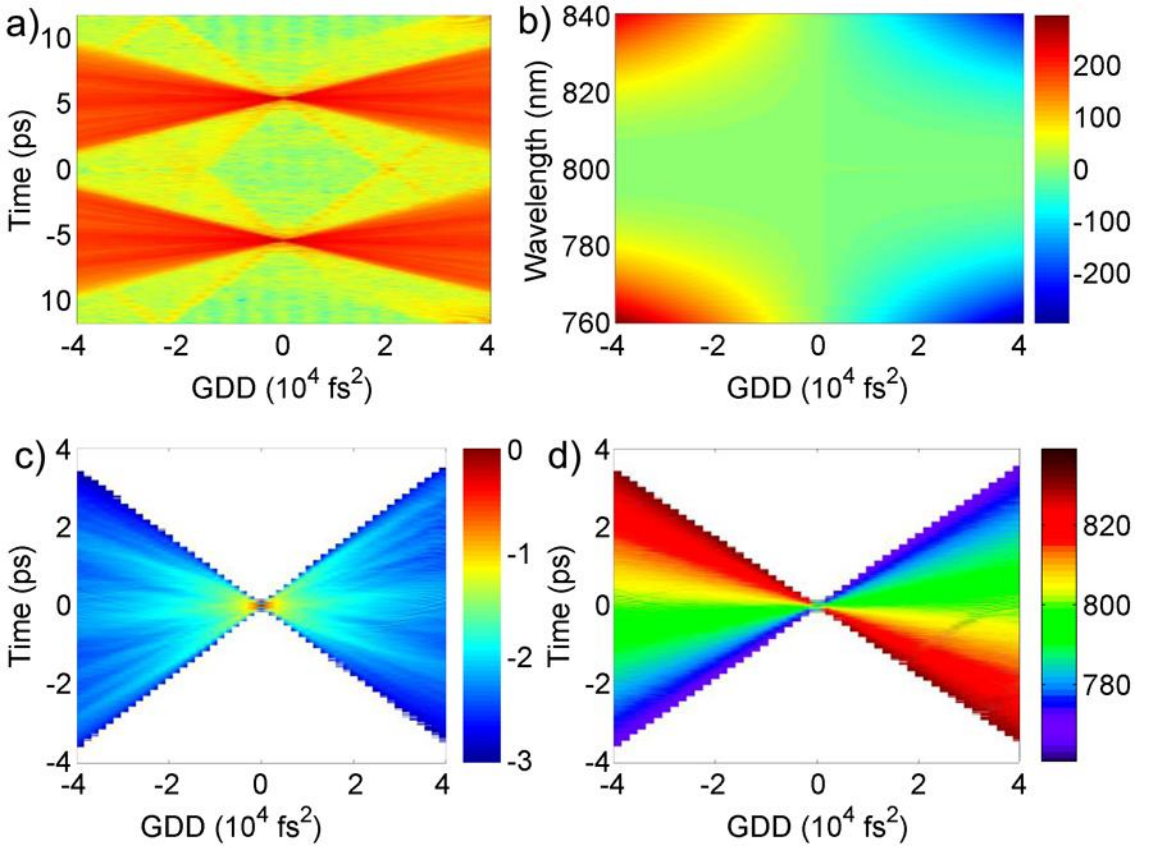


Fig. 2.7. Simulation of the spectral interferometry of strongly chirped 35 fs (FTL) pulses. As a function of the group delay dispersion (GDD): (a) Inverse Fourier-transform of the interferences, (b) Spectral phase retrieved, (c) reconstructed pulses, and (d) Instantaneous wavelength of the pulses.

This type of tests has been carried out experimentally in the range available in the laboratory using a pair of gratings stretcher to negatively chirp the pulses. The results will be detailed in Section 4.3.2. The stretcher introduced a $GDD$ from $-1000$ to $-7000\,fs^2$ on the input pulses ($35\,fs$, FTL). The pulse duration for the highest negative chirp was $1.3\,ps$ ($1/e^2$ full width).

To summarize, theoretical estimations have been given here, and should not be considered as universal laws. In the experiments, the signal to noise ratio (dynamic range) of the detection or other parameters can reduce the range of work of the SI. For example, in the case of strongly chirped pulses, the lateral peak has a huge broadening and therefore its amplitude is reduced. This may conflict with the tails of the central peak. Although the central peak may be reduced before applying the FTSI algorithm, the noise or the fluctuations prevent a perfect depletion.

The other example that we will see here is the case of multiple pulses: double pulses or trains of pulses, such as those coming from diffractive optical elements (DOEs),

which will be presented in detail in Part II. This case was dealt with only experimentally. To conduct a systematic experimental study, the SI of a double pulse will be measured varying the distance between the two pulses (Fig. 2.8). This experiment was carried out using the fiber optic coupler of STARFISH (see Chapter 4). The double test pulse was created with a Mach-Zehnder interferometer, while the reference pulse was a replica of the laser pulses picked up before the interferometer. One of the test pulses was fixed during the scan, with a delay of $\tau_0 = 6\,ps$ after the reference. The second pulse was translated in the temporal domain with a motorized delay line. The relative delay $\tau_{rel}$ with respect to the first pulse was varied from $-4$ to $+4\,ps$ while measuring the SI (consequently, its delay with respect to the reference varied from $2$ to $10\,ps$). The IFT of the SI as a function of the double pulse internal delay is represented in Fig. 2.8. We have calculated it with and without subtraction of the non-interfering spectrum (the test and reference individual spectra) in the SI before the IFT (Fig. 2.8b and 2.8a, respectively). This result helps us to interpret how the pulse duration may be limited and the delay has to be appropriately chosen in SI.

For the interpretation of Fig. 2.8a, it is convenient to identify the origin of each peak. This will help us to distinguish between the peaks corresponding to the central peak and those corresponding to the lateral (sideband) peaks, which will be useful to determine whether both peaks (central and lateral) overlap or not. First, we see an invariant central peak ($t = 0$) corresponding to the IFT reference spectrum. The IFT of the test spectrum possesses a triple peak structure, the first peak being centered at $t = 0$, the second varying from $-4$ to $+4\,ps$, and the third varying $+4$ to $-4\,ps$ (the second and the third come from the double pulse: $|\tau_{rel}|$). These signals are the trace of the FTL of the test spectra, which in this case is a double pulse (actually, the double pulses interfere in the spectral domain). The SI of the test with the reference pulse gives two double peaks: centered at $\pm 6\,ps$ (from the fixed pulse at $\tau_0$) and varying from $\pm 2$ to $\pm 10\,ps$ (from the scanning pulse, at $\tau_0 + \tau_{rel}$). The constant lower signal centered at $t \sim 3\,ps$ comes from the ripples of the laser spectrum; therefore it disappears after the subtraction of the background (Fig. 2.8b). In this case, owing to the modulation of the test pulse spectrum caused by the double pulse self-interference, it is impossible to completely deplete the background. However, the effect of the subtraction is noticeable (the plots are in logarithmic scale). In this case, the width of the FTL of the test spectrum is varying from $8\,ps$ in the extremes to $\sim 35\,fs$ in the center of the scan, whereas the test pulse duration varies from $4\,ps$ in the extremes to $\sim 35\,fs$ in the center, and the central delay ($\tau_0 + \tau_{rel}/2$) of the double pulse (with respect to the reference) varies from $4$ to $8\,ps$. Following the criterion of separated (non overlapping) central and lateral peaks of the IFT, in this case the valid configurations of SI will be for $\tau_{rel} > -3\,ps$, since the test spectrum and the interferences with the reference do not overlap. Note that the two double pulses of the extreme have a distance of $|\tau_{rel}| = 4\,ps$, but the delay of $8\,ps$ is valid for the case $\tau_{rel} = +4\,ps$, while the delay $4\,ps$ is not sufficient for the case $\tau_{rel} = -4\,ps$. In this example, the previous knowledge of the pulse structure allows us to deduce a valid delay. In a general case, the pulse duration may be unknown, what introduces additional difficulties.

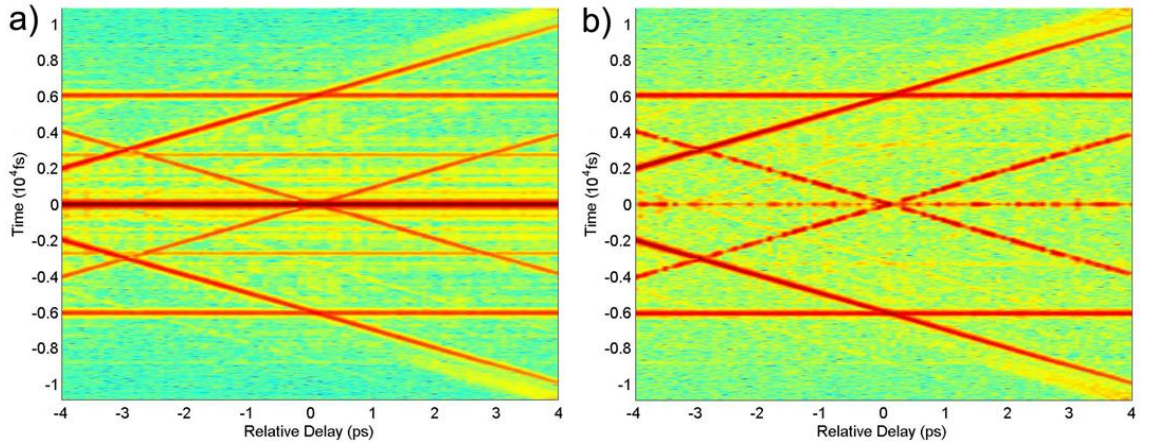


Fig. 2.8. Inverse Fourier-transform of the spectral interferences of a double pulse as a function of the pulse's distance (in logarithmic scale), (a) without and (b) with subtraction of the non-interfering contribution of the spectrum.

It should be brought to attention that the use of spatial interferences of two crossed beams instead of SI to encode the spectral phase (in two dimensions: space and frequency) has been shown to improve the temporal range of the measurement, since the full spectrometer resolution is available contrary to the FTSI retrieval in the SI scheme [24]. In our case, we are interested on ultrashort pulses, so this will not be a limitation. In the case of longer pulses, the spectrometer could just be replaced by another with better resolution.

Finally, regarding the shortest measurable pulses, spectrometer resolution does not play a role. In this case, the pulse spectrum is very large, so the only requirement is a broadband spectral response of the interferometer and a broadband free spectral range (or operating bandwidth) of the spectrometer. This point will be discussed in greater depth in Chapter 4 (Section 4.2.4) and in connection with the application of STARFISH to few-cycle laser pulses in Chapters 9 and 10.

## 2.4. Conclusions

One of the main advantages of SI is that a measurement of the test pulse is possible just by acquiring a single spectrum. Also, the process of phase extraction from the experimental data is very fast and univocal, since it essentially relays on the FT. In addition, it does not involve nonlinear processes in the detection. Therefore, it is a very sensitive technique for the measurement of very weak pulses. Of course, the calibration of the reference requires a nonlinear process. Also, if only a relative phase is desired, the calibration of the reference pulse is not required.

Although for the full phase retrieval (of the test pulse) the previous knowledge of a reference pulse is mandatory ─usually characterized by standard techniques as for example FROG or SPIDER─, this does not prevent SI from being a versatile technique: once the reference has been measured, it is possible to modify the test pulse in any given manner (except for processes that involve spectral broadening), and then easily characterize it with SI. This also allows measuring more complex pulses preserving a simple configuration (both the experimental setup and the acquisition/retrieval) and lays

the foundations for the extension of SI to the spatiotemporal characterization of the pulses or to systematic studies (e.g. *GDD* -scan, relative delay...).

The range of measurement of SI depends on the spectrometer resolution and the spectral bandwidth of response. Longer pulses require better spectral resolution. Therefore, appropriate elements should be chosen for a particular application.

## References


[1] C. Froehly, A. Lacourt, and J. Ch. Vienot, "Notion de réponse impulsionnelle et de fonction de transfert temporelles des pupilles optiques, justifications expérimentales et applications," Nouv. Rev. Opt. 4, 183-196 (1973).

[2] J. Piasecki, "Subpicosecond measurement of response of optical fibres," Electron. Lett. 16, 498 (1980).

[3] J. Piasecki, B. Colombeau, M. Vampouille, C. Froehly, and J. A. Arnaud, "Nouvelle méthode de mesure de la réponse impulsionnelle des fibres optiques," Appl. Opt. 19, 3749-3755 (1980).

[4] F. Reynaud, F. Salin, and A. Barthelemy, "Measurement of phase shifts introduced by nonlinear optical phenomena on subpicosecond pulses," Opt. Lett. 14, 275-277 (1989).

[5] E. Tokunaga, A. Terasakiy, and T. Kobayashi, "Femtosecond continuum interferometer for transient phase and transmission spectroscopy," J. Opt. Soc. Am. B 13, 496-513 (1996).

[6] C. X. Yu, M. Margalit, E. P. Ippen, and H. A. Haus, "Direct measurement of self-phase shift due to fiber nonlinearity," Opt. Lett. 23, 679-681 (1998).

[7] D. N. Fittinghoff, J. L. Bowie, J. N. Sweetser, R. T. Jennings, M. A. Krumbügel, K. W. DeLong, R. Trebino, and I. A. Walmsley, "Measurement of the intensity and phase of ultraweak, ultrashort laser pulses," Opt. Lett. 21, 884-886 (1996).

[8] C. Iaconis and I. A. Walmsley, "Spectral phase interferometry for direct electric-field reconstruction of ultrashort optical pulses," Opt. Lett. 23, 792-794 (1998).

[9] E. Cormier, I. A. Walmsley, E. M. Kosik, A. S. Wyatt, L. Corner, and L. F. DiMauro, "Self-referencing, spectrally, or spatially encoded spectral interferometry for the complete characterization of attosecond electromagnetic pulses," Phy. Rev. Lett. 94, 033905 (2005).

[10] E. Papastathopoulos, K. Körner, and W. Osten, "Chromatic confocal spectral interferometry," Appl. Opt. 45, 8244-8252 (2006).

[11] S. Keren, E. Brand, Y. Levi, B. Levit, and M. Horowitz, "Data storage in optical fibers and reconstruction by use of low-coherence spectral interferometry," Opt. Lett. 27, 125-127 (2002).

[12] A. B. Vakhtin, K. A. Peterson, W. R. Wood, and D. J. Kane, "Differential spectral interferometry: an imaging technique for biomedical applications," Opt. Lett. 28, 1332-1334 (2003).

[13] L. Lepetit, G. Cheriaux, and M. Joffre, "Linear techniques of phase measurement by femtosecond spectral interferometry for applications in spectroscopy," J. Opt. Soc. Am. B 12, 2467-74 (1995).

[14] R. Trebino and D. J. Kane, "Using phase retrieval to measure the intensity and phase of ultrashort pulses: frequency-resolved optical gating," J. Opt. Soc. Am. A 10, 1101-1111 (1993).

[15] W. J. Walecki, D. N. Fittinghoff, A. L. Smirl, and R. Trebino, "Characterization of the polarization state of weak ultrashort coherent signals by dual-channel spectral interferometry," Opt. Lett. 22, 81-83 (1997).

[16] J. Jasapara and W. Rudolph, "Characterization of sub-10-fs pulse focusing with high-numerical-aperture microscope objectives," Opt. Lett. 24, 777-779 (1999).

[17] B. Alonso, I. J. Sola, O. Varela, C. Mendez, I. Arias, J. San Román, A. Zaïr, and L. Roso, "Spatio-temporal characterization of laser pulses by spatially resolved spectral interferometry," Opt. Pura Apl. 43, 1-7 (2010).

[18] P. Bowlan, P. Gabolde, and R. Trebino, "Directly measuring the spatiotemporal electric field of focusing ultrashort pulses," Opt. Express 15, 10219-10230 (2007).

[19] B. Alonso, I. J. Sola, O. Varela, J. Hernández-Toro, C. Méndez, J. San Román, A. Zaïr, and L. Roso, "Spatiotemporal amplitude-and-phase reconstruction by Fourier-transform of interference spectra of high-complex-beams," J. Opt. Soc. Am. B. 27, 933-940 (2010).

[20] M. Kujawinska, in "*Interferogram Analysis*," D.W. Robinson and G. T. Reid, eds. (Institute of Physics, Bristol, UK), pp. 141-193 (1993).

[21] M. Takeda, H. Ina, and S. Kobayashi, "Fourier-transform method of fringe-pattern analysis for computer-based topography and interferometry," J. Opt. Soc. Am. 72, 156-160 (1982).

[22] C. Dorrer, N. Belabas, J.-P. Likforman, and M. Joffre, "Spectral resolution and sampling issues in Fourier transform spectral interferometry," J. Opt. Soc. Am. B. 17, 1795-1802 (2000).

[23] C. Dorrer, "Influence of the calibration of the detector on spectral interferometry," J. Opt. Soc. Am. B. 16, 1160-1168 (1999).

[24] P. Bowlan, P. Gabolde, A. Shreenath, K. McGresham, R. Trebino, and S. Akturk, "Crossed-beam spectral interferometry: a simple, high-spectral-resolution method for completely characterizing complex ultrashort pulses in real time," Opt. Express 14, 11892-11900 (2006).

# CHAPTER 3

# SPATIALLY RESOLVED SPECTRAL INTERFEROMETRY

**Contents**



*Some of the results in this chapter were originally presented in B. Alonso et al., Opt. Pura Apl. 43, 1-7 (2010).*

## 3.1. Extension of spectral interferometry to the spatial domain

The one-dimensional spectral interferometry (SI) [1,2] described in Chapter 2 allows us to measure the relative spectral phase of a test pulse (unknown) and a delayed reference pulse (known) from their spectral interferences in a collinear configuration. This measurement is taken in a certain position of the transverse profile of the pulse, that is, in a certain spatial position. This measurement provides the temporal amplitude and phase of the pulse after combination with the reference known phase [3], but lacks the spatial dependence. As discussed in Chapter 1, the retrieval of the pulses' full spatiotemporal profile is of high interest [4]. For this reason, we studied the extension of SI to the spatial domain [5].

The idea of spatially-resolved SI is illustrated in Fig. 3.1. It consists in measuring the SI of the two pulses (test and reference) at different spatial positions across the transverse profile of the pulses, i.e., at a particular propagation distance or $z$-plane. The spatial scan provides the SI as a function of the spatial coordinates. This information is used to obtain the temporal characterization ─extracting the phase from the SI─ as a function of the spatial position. This alone does not give the spatiotemporal coupling, since the connection of the pulse in the temporal domain for different spatial positions is required to retrieve the pulse-front curvature, for example. Here, the (temporal) connection between different spatial points (to extract the relative phase/delay) is possible thanks to the use of a homogeneous reference pulse that is a common reference for the whole pulse. The pulse-front curvature, for example, would not otherwise be retrieved.

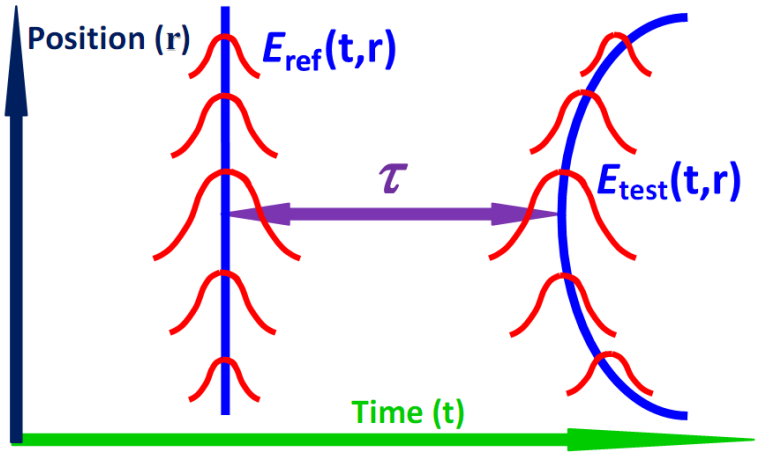


Fig. 3.1. Scheme of spatially resolved spectral interferometry. A homogeneous beam is used as a reference for each transverse position.

The requirements of the SI extended to the spatial domain are the same than for one-dimensional SI (Section 2.1). Therefore, the test pulse is delayed by a quantity $\tau$ with respect to the reference pulse. In Eq. 3.1, the expression for the SI is given as a function of the spatial coordinate $\mathbf{r}=(x,y)$ in the transverse plane

$$S(\omega,\mathbf{r}) = S_{test}(\omega,\mathbf{r}) + S_{ref}(\omega,\mathbf{r}) + 2\sqrt{S_{test}(\omega,\mathbf{r})S_{ref}(\omega,\mathbf{r})}\cos[\phi_{test}(\omega,\mathbf{r}) - \phi_{ref}(\omega,\mathbf{r}) - \omega\tau] \quad (3.1)$$

The spatially-resolved interferences will be referred to as the spectral trace or the interference trace, that is, the three-dimensional magnitude $S(\omega,\mathbf{r})$. In the experiments, we will often take advantage of the cylindrical symmetry of the pulse to measure it only in one spatial dimension (e.g., the $x$-axis). In the plane of the measurement, the spectrum depends both on the frequency $\omega$ and $\mathbf{r}$. The aim is to obtain the amplitude and phase of the test pulse in the spatiospectral domain. The phase will be extracted from the interferences analysis, whereas the amplitude $S_{test}(\omega,\mathbf{r})$ can be directly measured by an additional scan in this case only with the test pulse (blocking the reference beam).

The analysis of the interference trace is carried out by applying for each spatial position the FTSI algorithm detailed in Section 2.2 [6]. Examples will be provided of the implementation for spatially-resolved SI in Section 3.3.1. From Eq. 3.1, the retrieval of $\phi_{test}(\omega,\mathbf{r})$ implies the previous knowledge of $\phi_{ref}(\omega,\mathbf{r})$. However, this is precisely the problem we are dealing with. Therefore, we need to know the reference pulse not only in the temporal domain (or equivalently, its spectral phase), but also in the spatial domain. A solution to this issue is to use a reference pulse that is spatially homogeneous, in other words, flat pulse-front and wavefront, and no spatial chirp. This means that $\phi_{ref}(\omega,\mathbf{r})=\phi_{ref}(\omega)$, where the phase does not depend on $\mathbf{r}$. More discussion on its experimental achievement will be done in Section 3.2. From the FTSI algorithm, the phase difference $\phi_{test}(\omega,\mathbf{r})-\phi_{ref}(\omega,\mathbf{r})$ is obtained. The spatiospectral phase of the test pulse $\phi_{test}(\omega,\mathbf{r})$ is then calculated, since the reference spectral phase $\phi_{ref}(\omega,\mathbf{r})=\phi_{ref}(\omega)$ can be measured (by a standard temporal characterization). The knowledge of the pulse in the spatiospectral domain is equivalent to knowing the spatiotemporal intensity and phase of the pulse just by applying IFT from frequency to the temporal domain for each spatial position. It is important to note that the delay correction, multiplying by $\exp\{i\omega\tau\}$ during the FTSI, has to be done with the same value of $\tau$ for all the positions $\mathbf{r}$. Otherwise, one would lose the "common reference" pulse (the relative phase) that allows to reconstruct properly the spatial dependence.

At this point, we will do a brief demonstration of how the interference trace encodes the spatiotemporal information using a simple example of convergent/divergent beams. The variation of the period and the shift of the fringes will record the information of the pulse-front and wavefront of the test pulse. Now, we will see how the interference pattern is directly related to the test pulse structure. Firstly, we assume that the input pulse has different wavefront and pulse-front dependence on the spatial coordinate. We study the SI of the test pulse and a delayed reference pulse (with flat pulse-front and wavefront). If the SI is calculated for two Gaussian pulses with carrier frequency $\omega_0$, the interference oscillations of the cross term are given by $\cos\{(\omega\text{-}\omega_0)\tau_p+\omega_0\tau_w\}$, where $\tau_p$ and $\tau_w$ are, respectively, the delay of the pulse-front and the wavefront with respect to the reference pulse. As a result, the delay of the pulse-front $\tau_p$ always gives the period of the oscillations, while the delay of the wavefront $\tau_w$ introduces a constant phase that just shifts the fringes. Next, we do an analysis follows of the fringes pattern. At a given position we have a certain $\tau_p$ and $\tau_w$, and we consider that this corresponds to the frequency $\omega_C$ in which interference maximum (constructive interference) exists,

then the relation $(\omega_C - \omega_0)\tau_p^C + \omega_0 \tau_w^C = 2n\pi$ is verified. Now, we look at a nearby position and wish to find the shift in frequency of the constructive interference with respect to the variation of the pulse-front and the wavefront. The delays in the new position are $\tau_p = \tau_p^C + \delta\tau_p$ and $\tau_w = \tau_w^C + \delta\tau_w$, while the shift in frequency is $\delta\omega = \omega - \omega_C$. Assuming that we remain on the same fringe (and neglecting second order variations), the frequency shift will be given by $\delta\omega = [-(\omega_C - \omega_0)\delta\tau_p + \omega_0 \delta\tau_w]/\tau_w^C$. The conclusion is clear: if $\delta\tau_w = 0$, then $\delta\omega$ is proportional to $\delta\tau_p$; if $\delta\tau_p = 0$, then $\delta\omega$ is proportional to $\delta\tau_w$; and if $\delta\tau_p = \delta\tau_w$, it is trivial that $\delta\omega$ is proportional to both of them. In the case of $\delta\tau_p \neq \delta\tau_w$ and $\{\delta\tau_p, \delta\tau_w\} \neq 0$, the shift $\delta\omega$ is a linear combination of the two contributions $\delta\tau_p$ and $\delta\tau_w$. Note that this variation is directly related to the spatiotemporal pulse structure. For example, a quadratic pulse structure will produce an interference trace with a quadratic shift of the fringes. In Fig. 3.2a and 3.2b, the experimental traces are represented of a convergent beam and a divergent beam, respectively. Finally, it should be pointed out that the variation of the wavefront dominates the shift of the fringes whenever the condition $\omega_C - \omega_0 << \omega_0$ is verified.

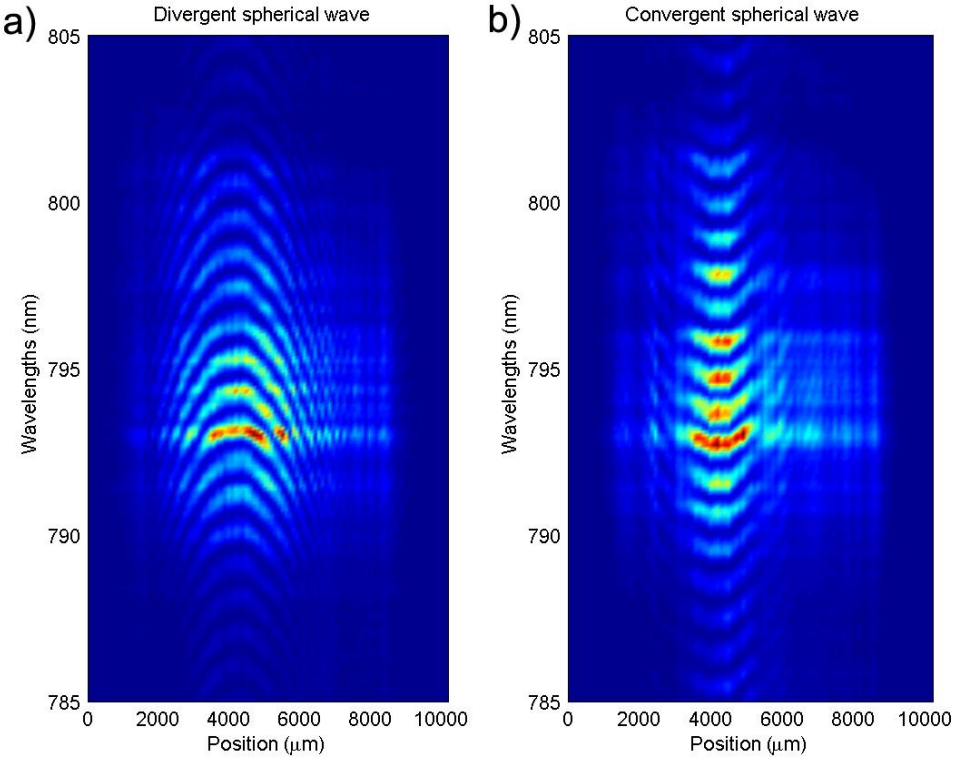


Fig. 3.2. Interference spectral trace of (a) a divergent and (b) a convergent wave using a collimated reference pulse.

## 3.2. First experimental setup: Mach-Zehnder interferometer and spatial filter

A standard Mach-Zehnder interferometer was utilized for the spatially-resolved SI [7]. The scheme of the experimental setup is presented in Fig. 3.3 and a picture is given in Fig. 3.4. First, the unknown pulse to be characterized was split into two arms. A delay stage in the test arm controlled the relative delay between the test and reference pulses. The reference beam was spatially filtered in order to have a homogeneous

reference pulse. Then, both pulses were aligned and sent collinearly to the detection devices, namely a GRENOUILLE device (Swamp Optics) [8] for the temporal characterization of the reference pulse, a standard spectrometer (Avantes Inc.) of resolution 0.1 nm and free spectral range from 700 to 900 nm, and multi-wave interferometry [9] commercial wavefront sensor (SID4-HR, Phasics S.A.) to check the filtered reference wavefront flatness.

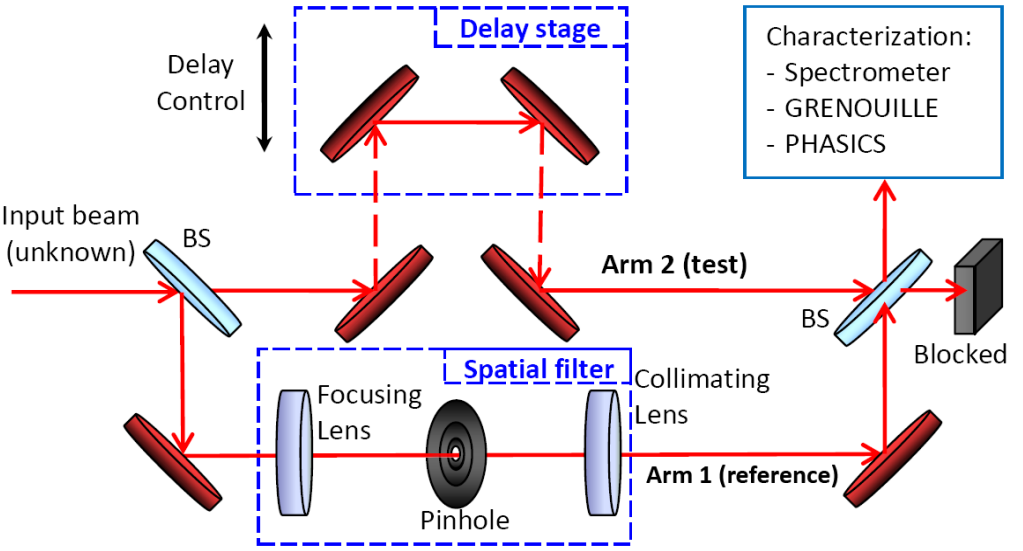


Fig. 3.3. Experimental setup for spatially resolved spectral interferometry. The unknown pulse is divided and recombined in a Mach-Zehnder type interferometer. The reference pulse is spatially filtered and the relative delay is controlled in a delay stage. BS = Beam splitter.

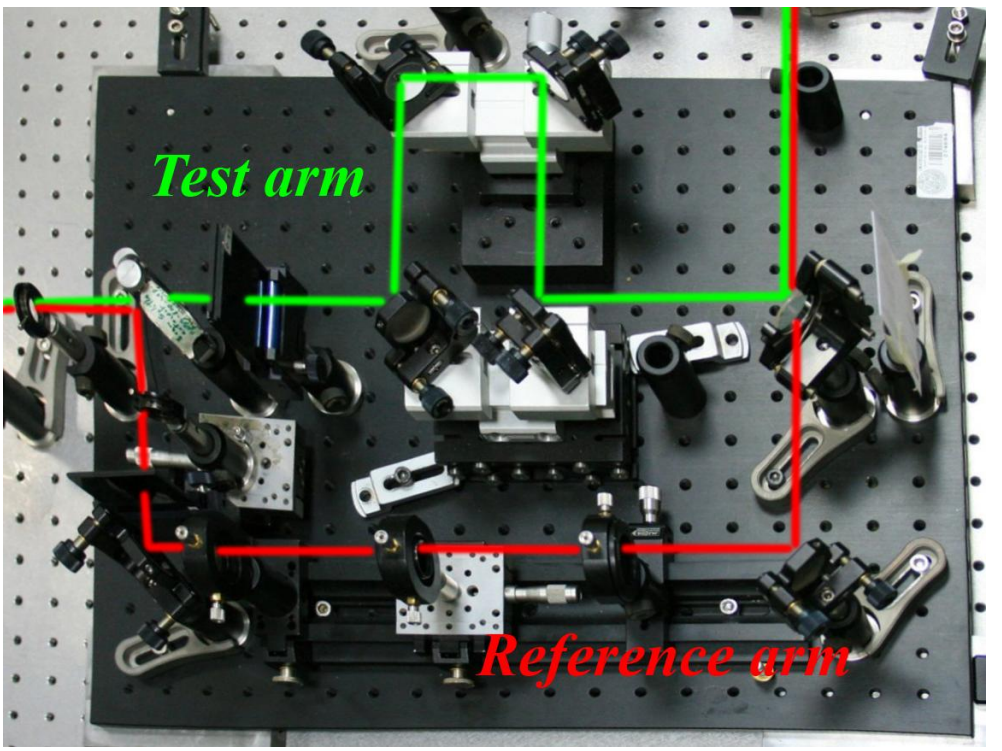


Fig. 3.4. Picture of the setup used for the experiments: a Mach-Zehnder interferometer is used to create the reference and test pulse, and then recombine them, by means of two beam splitters. There is a delay line in the test arm and a spatial filter (two lenses and a pinhole in the middle) in the reference arm.

The spatially resolved spectrum was measured using a motorized stage that transversely scanned the spatial profile of the pulse in small steps (depending on the spatial dimension of the pulse to be scanned) at the same time that the spectrum was acquired. In order to collect the pulse at each spatial position, an optical fiber (in a mount in the motorized stage) was used that was directly connected to the spectrometer. The test, reference and interference spectra were measured as a function of the spatial position, resulting in three experimental spectral traces: test, reference and interferences.

The spatial filter consisted in a system of two 2-f separated lenses ─where f=10cm is the focal length of the lenses─ and a pinhole in the intermediate focus that filtered the reference profile (Fig. 3.5). Ideally, inhomogeneous input beams can be filtered out to have a flat wavefront and homogeneous reference pulse by doing a selection of their wave vectors.

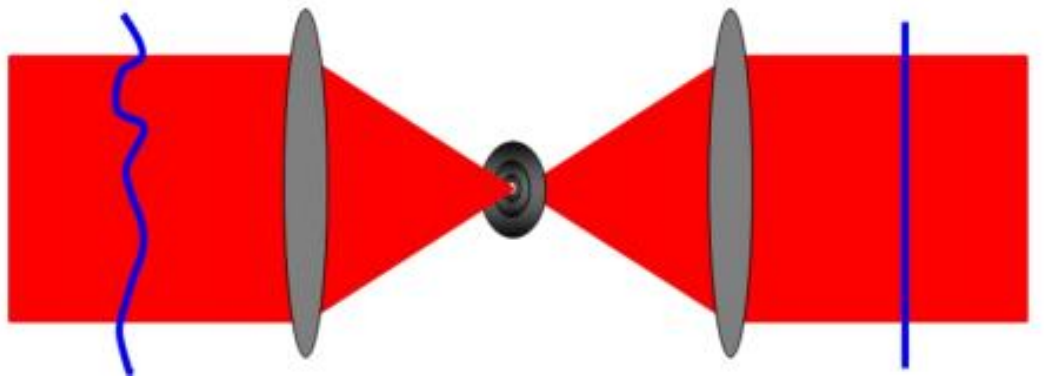

Fig. 3.5. Schematic diagram showing the performance of the reference beam spatial filter.

For the experiments, use was made of a Ti:sapphire CPA laser system (Spectra Physics) delivering 120-fs pulses (intensity FWHM) centered at 795 nm with a repetition rate of 10 Hz. In Fig. 3.6b and 3.6a, the spatial profile of the reference pulse is represented with and without the filter respectively, showing the pulse cleaning done by the pinhole. The reference wavefront with and without the filter was also characterized, and it was found that it is flat enough for our requirements when the spatial filter is used (Fig. 3.6d and 3.6c, respectively). Note the improvement in the wavefront flatness (the color scales are different in Fig. 3.6c and 3.6d). However, the use of a spatial filter is not an easy issue at all. For example, if the pulse is very intense (a minimum intensity is required for the SHG in the GRENOUILLE), it can produce nonlinear effects at the focus in the air (in vacuum this can be avoided). Also, the position of the second lens sometimes had to be displaced to collimate the beam, correcting the residual convergence or divergence with the help of an in situ wavefront measurement. The diameter of the pinhole had to be adapted for each pulse. Additionally, an iris was placed in the reference arm before the spatial filter to adjust the focal spot size with respect to the pinhole. Depending on the input beam diameter and the size of the iris before the spatial filter, pinholes were used with diameters of 10 and $20\mu m$. Finally, it was also observed that certain pulses coming from nonlinear processes have a very complex structure with different contributions that cannot be perfectly filtered out simultaneously with this design.

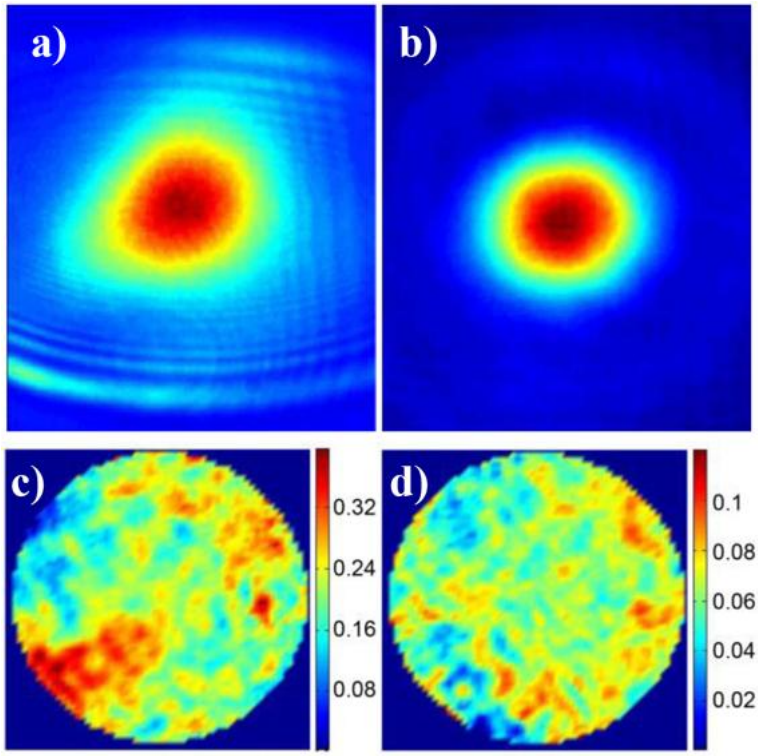


Fig. 3.6. Spatial profile of the reference pulse (a) without and (b) with filter. Wavefront of the reference pulse (c) without and (d) with filter: color scale is phase (rad).

## 3.3. Setting-up the spatiotemporal reconstruction system

In order to validate our spatiotemporal reconstruction implementation, we did the following. Firstly, different pulses were considered and their spectral interferences trace, their test and reference spectra were numerically simulated and expressed in the same form than the data acquired in the experiment, imposing the resolution of our spectrometer (0.1 nm). Then, the same program was applied with the reconstruction algorithm that was used with the experimental measurements. Both the simulations and reconstructions were implemented in Matlab®. Finally, experimental measurements were taken and their reconstructions of different cases were made for the final test of the system.

### *3.3.1 Numerical simulations of complex cases*

Firstly, a beam with a linear tilt with respect to the reference pulse was simulated. By linear tilt, it is in fact meant just a linear relative delay, which should not be confused with the pulse-front tilt and spatial chirp produced, for example, by a prism. Therefore, no spatial chirp is present. The experiment corresponding to this simulation is carried out by slightly crossing the test and reference pulses after being collinear (the experimental results will be shown in Fig. 3.13). Since this angle was very small, it still did not prevent the pulses from spectrally interfering. Then, a pulse was simulated with linear tilt varying from $-100$ to $100\,fs$ along the transverse position (see Fig. 3.7). The spatial profile was a Gaussian function with an intensity FWHM of $5000\mu m$. The

pulses had a duration of $100\,fs$ (FWHM) and were centered at $800nm$. The test pulse tilt on the interference spectrum results in fringes tilted with respect to the spatial axis (Fig. 3.7a) caused by the linearly dependent relative delay (that also changes the fringes period $\propto 1/\tau$) and pulse-front of the test pulse. To extract the phase difference from the SI, an IFT is applied in the frequency axis (converted from the wavelength axis) for each position. As shown in Fig. 3.7b, two side-bands centered at $\pm\tau_0$ ($\tau_0 = 2ps$ is the delay between the pulses) exhibit the expected linear variation with the position. The FTSI algorithm selects the side-band $+\tau_0$ and returns to the frequency domain (by applying FT), where the phase difference between the test and the reference pulses is obtained in the spatiospectral domain. The test spectrum $S(\lambda, x)$ is shown in Fig. 3.7c. The test pulse retrieved by this procedure corresponds to the simulated situation, thus giving us reliability on the implemented algorithm. The width and the position of the gate (a supergaussian function) used in the temporal domain to filter the peak centered at the delay are adjusted to the particular case. Here, the gate is shifted as the delay varies with the position.

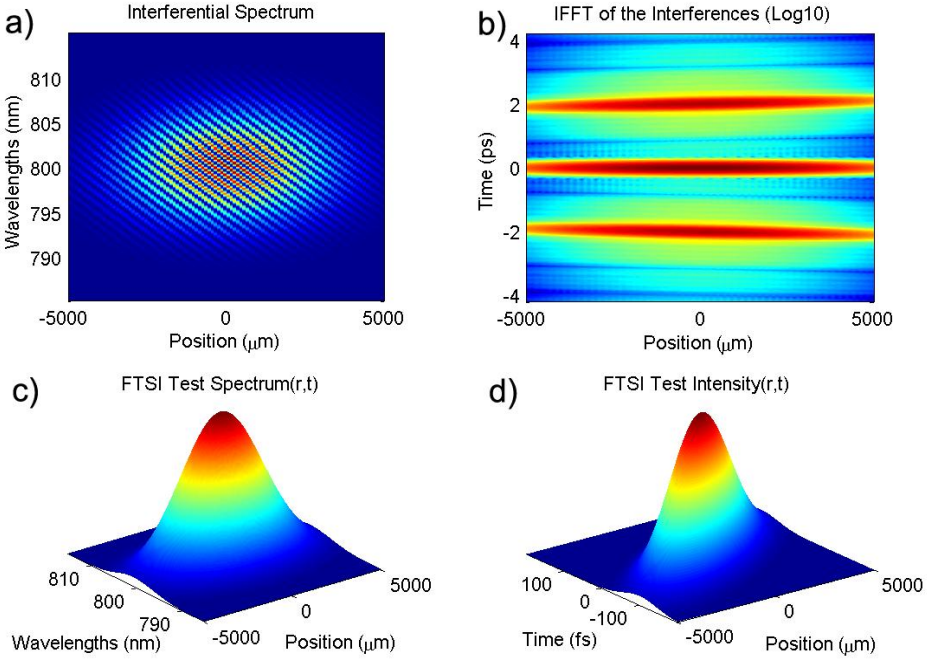


Fig 3.7. Reconstruction of a linearly tilted pulse: (a) simulated interference spectrum, (b) inverse Fourier-transform of the spectral trace (logarithmic scale), (c) test spectrum and (d) test temporal intensity retrieved by Fourier-transform spectral interferometry (FTSI).

In order to test spatiotemporal non trivial pulses, a test pulse was simulated composed of the spatiotemporal interference of a plane and a spherical wave of 100-fs duration (FWHM) without relative delay (overlapping in time). All the beams involved have a spatial FWHM of $5000\mu m$. In Fig. 3.8a, the interference spectrum between the reference pulse (2-ps delayed) and the test pulse is represented as a function of one spatial dimension varying from the center of the pulse to the periphery. The fast oscillations in the wavelength dimension are due to the spectral interferences with the reference pulse. These interferences have two types of evolution with respect to the position, quadratic due to the spherical wave and constant due to the plane wave. The fringes in the spatial dimension are caused by the spatial interference of the plane and

spherical wave, that is, they are in the test pulse structure and do not come from the SI. Fig. 3.8b shows the test pulse intensity FTSI reconstruction (it has been checked that it matches the pulse used to generate the simulation), which is the coherent sum of the plane and the spherical waves. The spatial interferences verify the property that the maxima and minima get closer in the periphery as expected owing to quadratic variation of the spherical wave, i.e. slower change in the center of the pulse (a Moiré effect is present for the higher positions owing to the spatial sampling).

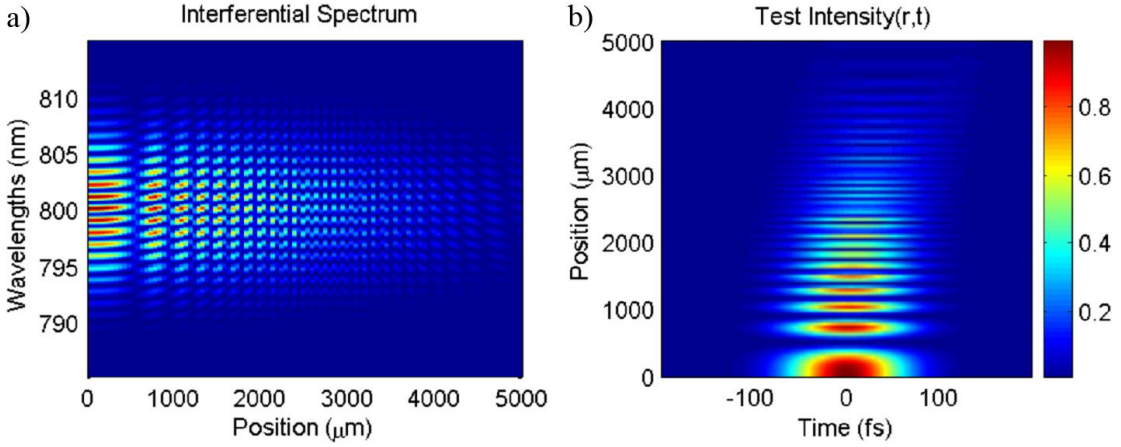


Fig. 3.8. Simulation of the spatiotemporal interference between a plane and a spherical wave: (a) interference spectra and (b) intensity retrieved by FTSI.

If a delay of 120 *fs* is introduced between the spherical and the plane waves of the previous example, their spatial interferences are dramatically reduced, thereby resulting in a double pulse structure. The test pulse spectrum is modulated according to the interference of the spherical and plane waves (Fig. 3.9b).

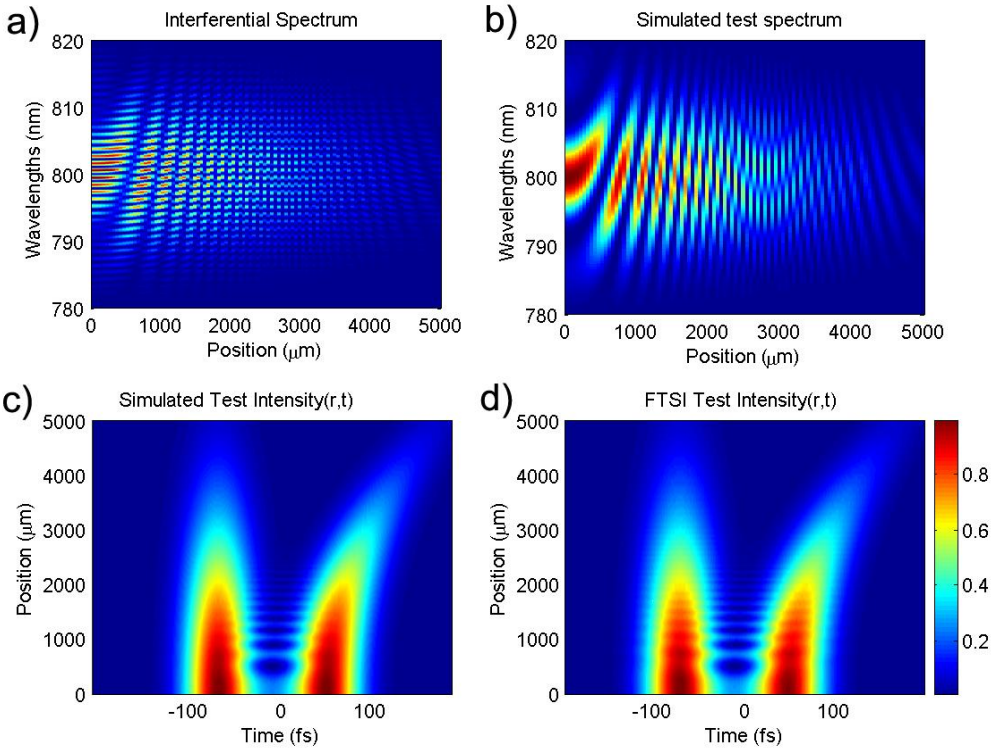


Fig. 3.9. Reconstruction of the plane and spherical waves separated by a delay: (a) simulated interference trace, (b) test spectra, (c) simulated and (d) retrieved test intensity.

The interference trace is similar to the test pulse spectrum with fast oscillations in the wavelength axis due to the spectral interference with the $2\,ps$ delayed reference pulse (Fig. 3.9a). Again, a Moiré effect appears off-axis. In the spatiotemporal intensity, the FTSI retrieval (Fig. 3.9d) reproduces the simulated data (Fig. 3.9c): the double pulse is observed, with the different curvature of the two pulses. Still, some remaining spatial interferences are present in the form of ripples in the position axis.

Following with the same case and taking into account the cylindrical symmetry of the test pulse, we computed the three-dimensional spatiotemporal structure of the double pulse through the representation as the iso-intensity surface given by the restriction $I_{test}(x,y,t) = 0.25 \cdot I_{\max}$ (Fig. 3.10). Both the plane and spherical waves are reconstructed with good resolution, showing the weak interference rings caused by the small spatial interferences.

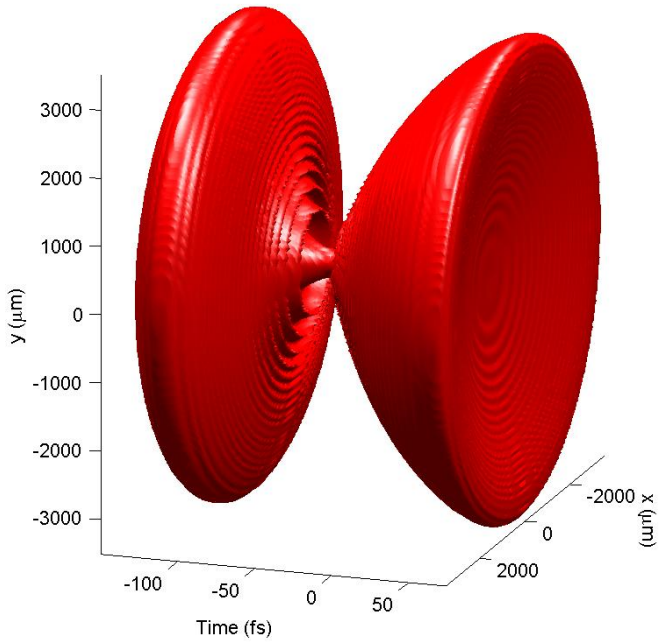


Fig. 3.10. Iso-intensity surface of a double pulse (spherical and plane waves) corresponding to 25% of the maximum intensity of the pulse.

### *3.3.2. Experimental measurements*

Experimental measurements of known simple cases have been taken to test the spatiotemporal reconstruction system. First, a scan has been carried out varying the delay between the reference pulse and the test pulse from -5.7 to +9.0 ps, the pulses being the same in this case. In Fig. 3.11a the interference spectrum is shown as a function of this delay, seeing how the period of the fringes varies (it is proportional to the inverse of the delay). The interferences beating is faster for the highest delays and at around zero delay the fringes vanish. In Fig. 3.11b, the magnitude of the delay retrieved by FTSI (red marks) can be seen it depends on the introduced delay and compare to the expected value (blue line). We find excellent agreement except for the zero delay because in this case the side peaks and the central peaks overlap in time domain after the IFT. The pulse reconstruction was also proven at different delays, obtaining good results.

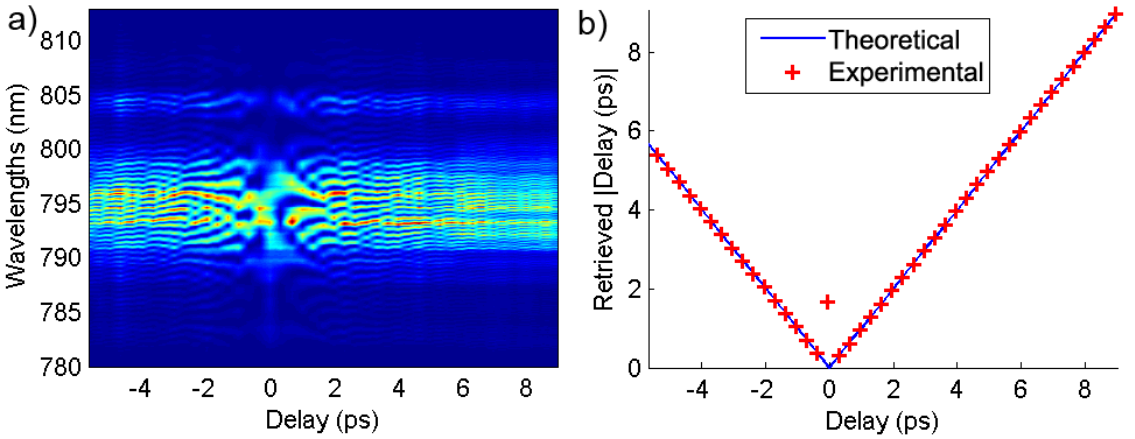


Fig. 3.11. Delay scan experiment: (a) interference spectrum and (b) retrieved delay as function of the introduced delay.

In a second measurement, the test pulse is made to pass through a half-beam plate, which represents that half the beam is delayed with respect to the part that does not go through the plate as illustrated in Fig. 3.12a. The difference of delay $\Delta\tau = 1671\,fs$ introduced by the plate is calculated from $(n-1)\cdot L = c\cdot\Delta\tau$ where $L = 1.1mm$ is the thickness of the plate and $n = 1.454$ is the refractive index of the fused silica at wavelength $\lambda = 795nm$. In Fig. 3.12b the interferences are shown as a function of the scanned transverse position seeing the variation of the fringes period in the two regions. In Fig. 3.12c, the FTSI retrieved delay is represented giving clear proof of the delay jump. The mean of the delays obtained by FTSI in each region is respectively $\tau_1 = 1757\,fs$ and $\tau_2 = 3453\,fs$. Thus, the experimental difference of delays between the two regions is $\Delta\tau = 1696\,fs$, which is in good agreement with our estimation with the plate characteristics.

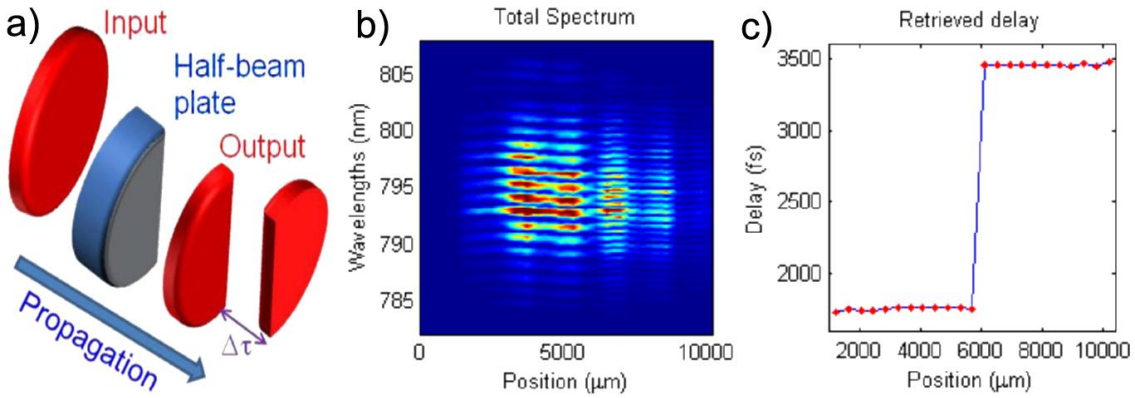


Fig. 3.12. (a) Half-beam plate experiment: a plate that delays a half of the test beam. (b) Interference spectrum and (c) retrieved delay as a function of the position.

A test pulse linearly tilted (just crossing at an angle) has also been measured with respect to the reference pulse. The interference spectrum traces for two opposite tilt cases are shown in Fig. 3.13a and b, presenting the expected fringes variation with the position. In Fig. 3.13c, the spatially-resolved spectrum (test pulse trace) is represented. Fig. 3.13d shows the spatiotemporal intensity reconstruction of the tilt case corresponding to Fig. 3.13a. We have checked that the retrieved tilt is in agreement with the introduced tilt (calibrated from the spatial interferences with the reference in zero

delay) and the fringes tilt in the spectral trace. The spatial intensity modulations observed in the spatiotemporal intensity (Fig. 3.13d) come from the fact that an amplified pulse is being measured and it does not present a smooth profile, as seen directly in the modulations of the spectrum of the test pulse (Fig. 3.13c).

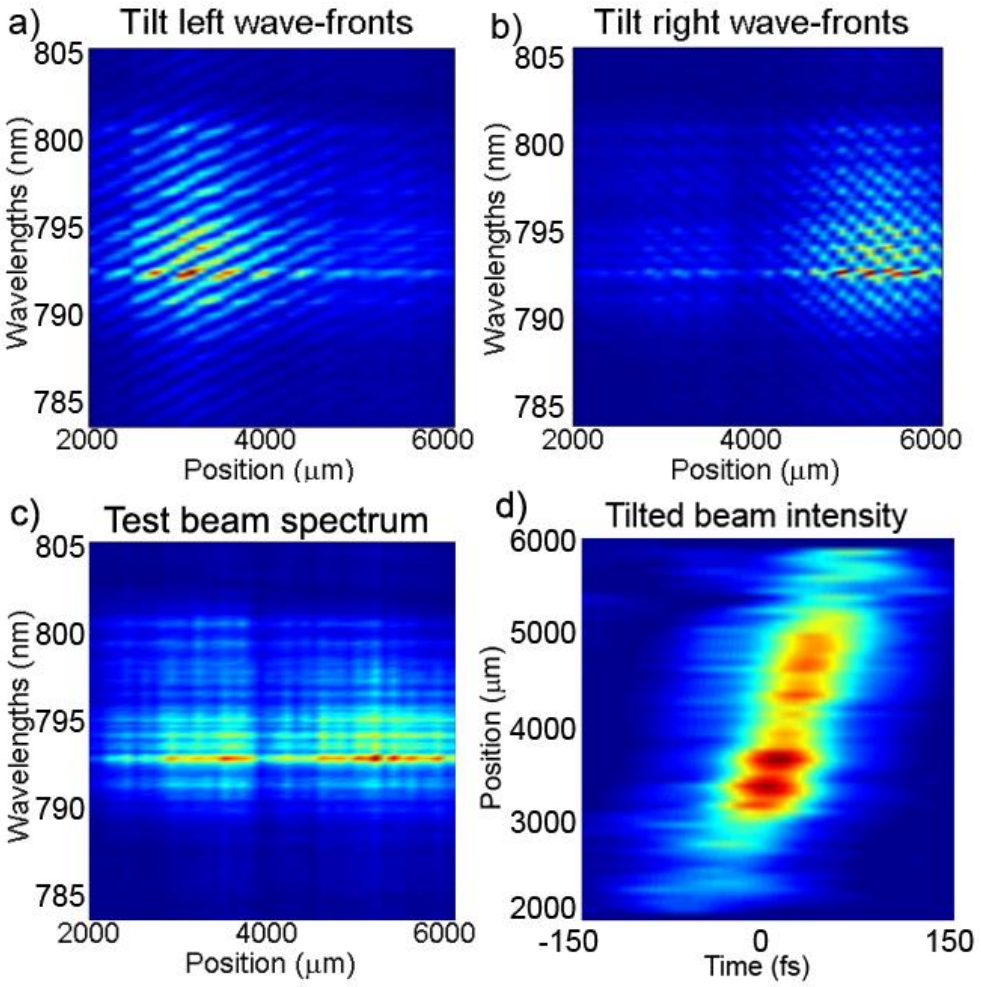


Fig. 3.13. Experimental spectral interferences for opposite orientation, (a) and (b), linearly tilted test pulses. (c) Spatially-resolved spectrum. (d) Spatiotemporal intensity reconstruction of a tilted test pulse.

The typical temporal duration of a spatial scan depends mainly on the number of points in the spatial sampling and the integration time. For a measurement with 100-200 points, the spatial scan takes approximately one minute. The algorithm of reconstruction can be done in situ and also takes around one minute.

## 3.4. Conclusions

By spatially scanning the transverse profile of two delayed pulses (the test and the reference), spectral interferometry can be extended to the spatial domain. The use of an appropriate spatial reference pulse allows for retrieving the spatiotemporal amplitude and phase of complex pulses without losing the coupling in space and time. The SI encodes the phase that can be extracted with the FTSI algorithm. Different cases have

been simulated and our reconstruction program has been run in order to test it and check the reliability of the method.

For the experiments, a setup based on a Mach-Zehnder interferometer has been implemented. An important issue here is to have a perfectly flat (pulse-front and wavefront) reference pulse, to avoid an unknown contribution to the SI. Therefore, a spatial filter was applied to the reference beam. As it is well known, we have found that the spatial profile and wavefront are improved in this way. Then, the setup has been applied to reconstruct a test pulse with the pulse-front tilted with respect to the reference pulse.

We have also seen, however, that cases exist (depending on the input pulse and the filter parameters) in which the quality (homogeneity) of the reference pulse is not the desired one and can introduce noise or distortion in the measurement. Moreover, since a replica of the test pulse is filtered to be used as the reference, depending on the test pulse, one can find more complex cases in which a correct spatial filtering is not possible, e.g. in the case of intense pulses after undergoing filamentation propagation. Also, the reference has to overlap the test pulse in the whole spatial profile and in the whole spectral bandwidth.

In addition, when the test pulse (the "experiment") is done before the interferometer, then the pulses at the output of the interferometer may have to be realigned, which is a critical point. Also, the reference pulse may have to be calibrated every time that the test pulse is changed, which is particularly inconvenient in the case of measuring the evolution of the test pulse with respect to any free parameter.

These reasons led us to propose another scheme, much more reliable and simple. It is based on the replacement of the last part of the Mach-Zehnder by a fiber optic coupler, which acts as the interferometer to recombine the test pulse and the reference pulse. This new technique, named STARFISH [10], is at the heart of this thesis. In Chapter 4 we present the technique, and in the following chapters we will present its different applications to diffractive optics, nonlinear optics and few-cycle pulses.

## References

[1] C. Froehly, A. Lacourt, and J. Ch. Vienot, "Notion de réponse impulsionnelle et de fonction de transfert temporelles des pupilles optiques, justifications expérimentales et applications," Nouv. Rev. Opt. 4, 183–196 (1973).

[2] J. Piasecki, B. Colombeau, M. Vampouille, C. Froehly, and J. A. Arnaud, "Nouvelle méthode de mesure de la réponse impulsionnelle des fibres optiques," Appl. Opt. 19, 3749-3755 (1980).

[3] D. N. Fittinghoff, J. L. Bowie, J. N. Sweetser, R. T. Jennings, M. A. Krumbügel, K. W. DeLong, R. Trebino, and I. A. Walmsley, "Measurement of the intensity and phase of ultraweak, ultrashort laser pulses," Opt. Lett. 21, 884 (1996).

[4] P. Bowlan, P. Gabolde, and R. Trebino, "Directly measuring the spatiotemporal electric field of focusing ultrashort pulses," Opt. Express 15, 10219-10230 (2007).

[5] J. Jasapara, "Characterization of sub-10-fs pulse focusing with high-numerical-aperture microscope objectives," Opt. Lett. 24, 777-9 (1999).

[6] L. Lepetit, G. Cheriaux, and M. Joffre, "Linear techniques of phase measurement by femtosecond spectral interferometry for applications in spectroscopy," J. Opt. Soc. Am. B 12, 2467-74 (1995).

[7] B. Alonso, I. J. Sola, O. Varela, C. Mendez, I. Arias, J. San Román, A. Zaïr, and L. Roso, "Spatio-temporal characterization of laser pulses by spatially resolved spectral interferometry," Opt. Pura Apl. 43, 1-7 (2010).

[8] P. O'Shea, M. Kimmel, X. Gu, and R. Trebino, "Highly simplified device for ultrashort-pulse measurement," Opt. Lett. 26, 932-934 (2001).

[9] S. Velghe, J. Primot, N. Guérineau, M. Cohen, and B. Wattellier, "Wave-front reconstruction from multi-directional phase derivatives generated by multilateral shearing interferometers," Opt. Lett. 30, 245-247 (2005).

[10] B. Alonso, I. J. Sola, O. Varela, J. Hernández-Toro, C. Méndez, J. San Román, A. Zaïr, and L. Roso, "Spatiotemporal amplitude-and-phase reconstruction by Fourier-transform of interference spectra of high-complex-beams," J. Opt. Soc. Am. B. 27, 933-940 (2010).

# CHAPTER 4

# STARFISH

**Contents**



*Some of the results in this chapter were originally presented in B. Alonso et al., J. Opt. Soc. Am. B 27, 933-940 (2010); B. Alonso et al., J. Opt. Soc. Am. B 29, 1993-2000 (2012); and B. Alonso et al., Opt. Express 20, 17880-17893 (2012).*

## 4.1. Introduction

As it has been said in the previous chapters, a separate temporal and spatial characterization of the pulses is not enough in many situations. Also, the full reconstruction of the spatiotemporal coupling of such pulses is often not trivial. Although other characterization techniques had already been proposed to this end ─for example SEA TADPOLE [1] and Shackled-FROG [2]─ we wanted a simple technique that could be applied easily to many different experiments. The system that we first implemented using a Mach-Zehnder interferometer (see Chapter 3) was a possible approach for this purpose. However, the problems regarding the homogeneous reference, alignment or stability, drove us to implement a new configuration.

In this chapter, we will present our proposal to characterize the pulses and the applications that we have performed to validate it. The technique is known as STARFISH, which stands for SpatioTemporal Amplitude-and-phase Reconstruction by Fourier-transform of Interference Spectra of Highly-complex-beams [3]. The main feature of STARFISH is that it uses a fiber optic coupler to recombine the pulse in the interferometer to perform the spatially-resolved spectral interferometry (SI). This point confers many advantages to the system. The use of SI confers the technique a high flexibility for the extension of SI to the spatial domain and to perform systematic studies involving a change of the pulses. The setup uses commercial elements ─the most critical one being the broadband single-mode fiber coupler─ that are connected in a plug-and-play manner. As will be seen along this chapter, the system is very simple, robust and reliable. Together with its versatility, this is the reason of the success of STARFISH and the high amount of applications carried out after its development.

## 4.2. STARFISH: Experimental setup and main characteristics

### *4.2.1. The technique STARFISH*

In Chapter 2, we explained the basis of SI to retrieve the temporal amplitude and phase of an ultrashort pulse, from the analysis of the interference of the test (unknown) pulse with a reference (known) pulse. In Chapter 3, we presented a first proposal for the extension of SI to spatial domain using a Mach-Zehnder interferometer. Here, we propose an advantageous experimental implementation of spatially-resolved SI, in which a single-mode fiber optic coupler (with almost equal-length arms) is used to recombine the two pulses in order to perform the SI. This proposal is the characterization technique STARFISH. Its development and applications constitute the main core of this thesis.

The scheme of the experimental setup of STARFISH is shown in Fig. 4.1. First, the input laser beam is divided by a beam splitter. One replica is used as reference pulse, so it has to be calibrated by a standard temporal measurement, typically SPIDER or FROG. The other replica is the test pulse that we wish to characterize. The interferometer is completed by a fiber optic coupler that recombines the pulses and sends them together to a standard fiber spectrometer. The setup is configured in order

for the optical path of the test and reference arm to be compensated (almost equal), and the delay $\tau$ required for SI is tuned by the longitudinal position of the fiber arm that collects the reference pulse. During a measurement, the reference fiber collects a fixed spatial point where the temporal calibration was done (an iris can be used to assure it experimentally). The fiber arm that collects the test pulse is the one that performs the spatial scan of the test pulse: the fiber input is displaced transversely to the propagation direction of the pulse, that is, across a z-plane, where z denotes a certain propagation distance. Since the reference and test pulses are temporally delayed, their spectral interferences can be measured in the spectrometer. The spatial scan of the test fiber allows us to perform the spatially-resolved SI, from which the test pulse will be determined.

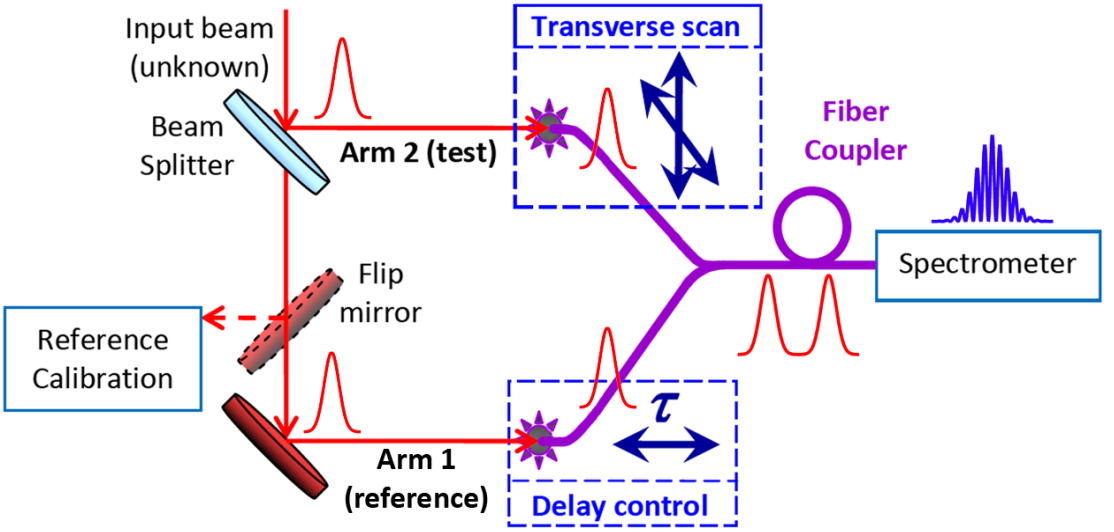


Fig. 4.1. Setup based on the fiber optic coupler interferometer for spatially-resolved spectral interferometry. The longitudinal position of one fiber arm controls the relative delay between reference and test pulses. The test pulse is scanned transversely (spatial) with its corresponding input fiber arm. The interferences of the two delayed pulses are measured in a standard fiber spectrometer.

To retrieve the amplitude and phase of the pulses by fringes analysis, we apply the Fourier-transform Spectral Interferometry (FTSI) algorithm [4], which was already explained in Section 2.2. We do the extension to spatial domain, similarly as done in Chapter 3, to obtain the pulse in the spatiospectral (and spatiotemporal) domain. Since it was already detailed in Chapters 2 and 3, here we will just briefly recall the algorithm FTSI. In SI, a reference (known) and a test (unknown) pulse delayed a time $\tau$ interfere in spectral domain. The resulting spectrum $S(\omega)$ can then be expressed as

$$S(\omega) = S_{test}(\omega) + S_{ref}(\omega) + 2\sqrt{S_{test}(\omega)S_{ref}(\omega)}\cos[\phi_{test}(\omega) - \phi_{ref}(\omega) - \omega\tau]. \qquad (4.1)$$

The last term contains the phase information. By applying FTSI, the phase difference between the test and the reference pulses can be extracted. To do so, the spectrum is inverse Fourier transformed to the temporal domain, where it consists of three peaks. The central one at t=0 corresponds to the non-interfering contribution (i.e., the sum of both spectra), while the others (centered at t=+τ and t=-τ) arise from the interference

term. By filtering one of the side peaks and applying direct Fourier transform, the phase difference between the test and the reference can be extracted in the frequency domain. Since the reference pulse is known, the test pulse phase is then recovered. The spectral amplitude of the test pulse can be recorded in a separate scan (blocking the reference pulse).

The SI is done at different positions of the spatial profile (see Fig. 4.1) of the test pulse (in a transverse plane), extending the phase difference retrieval to the spatial dimension. By this procedure, STARFISH directly yields the spatiospectral phase (i.e., the wavefront) of the pulses $\phi(x,\lambda)$ Because of the numerical calculation, this phase is obtained wrapped in the range $(-\pi,\pi)$. To obtain the wavefront as a continuous function of the wavelength $\lambda$, it is only necessary to unwrap this phase. The validity for wavefront retrieval is discussed in Section 4.4 and an application is presented in Chapter 6. Finally, the amplitude and phase in the spatiotemporal domain is obtained by inverse Fourier-transforming from frequency to time dimension.

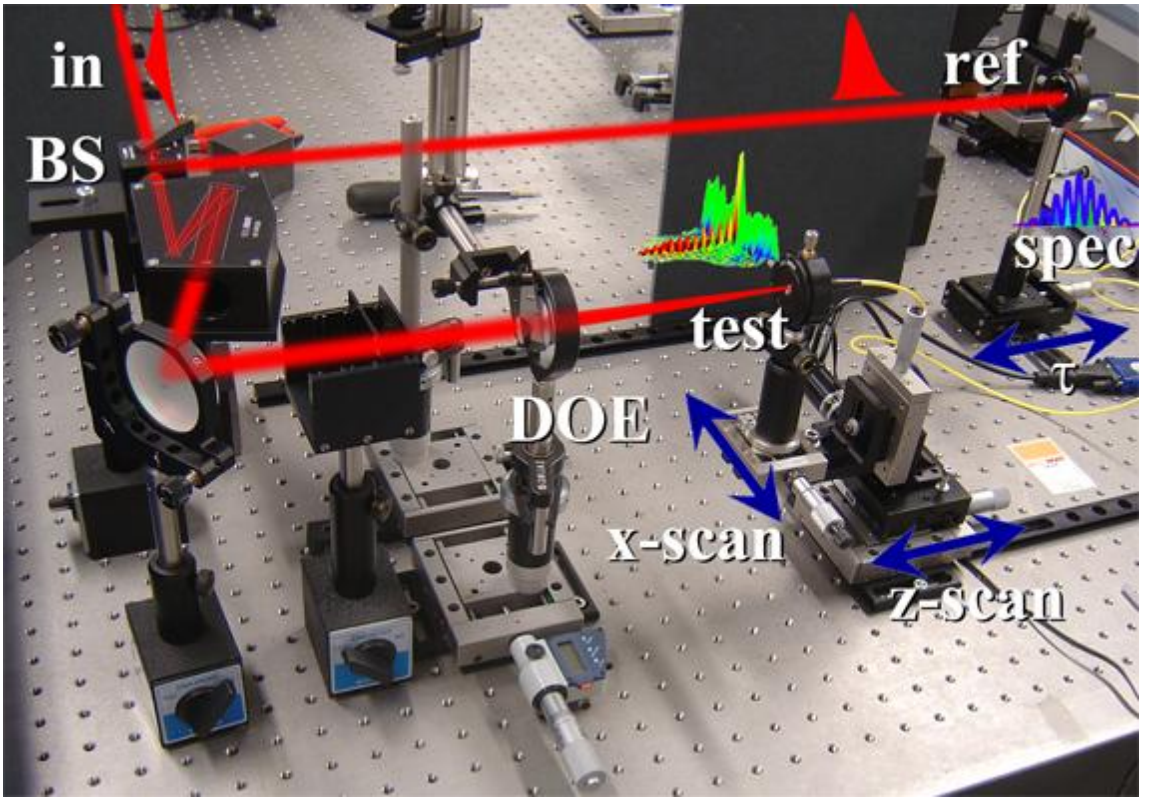


Fig. 4.2. Picture of the experimental setup of STARFISH applied to diffractive optical elements (DOEs). The input pulse (in) coming from the laser output is divided into two replicas by the beam splitter (BS). One replica is the reference pulse (ref) collected by one fiber arm. The other replica is spatially expanded to illuminate a DOE creating the test pulse that is collected by the other fiber arm with spatial resolution (transverse coordinate: x-scan) and longitudinally scanned (z-scan). The fiber coupler output is connected to the spectrometer (spec) where the spectral interferences of the two pulses due to their delay $\tau$ are measured.

The implementation in the laboratory is very straightforward. As an example, we show a picture of the experimental setup used in the work presented in Section 7.2 (see Fig. 4.2), which was carried out in the laboratory of the Universitat Jaume I (Castellón, Spain). The laser system output was divided into two beams to create a reference and a

test arm in the interferometer. The pulse in the test arm was spatially expanded before impinging a diffractive optical element (DOE). The focus of the DOE was directly sampled by the test arm of the fiber optic coupler. The test and reference pulse were combined with the appropriate delay (adjusted by the longitudinal position of the reference fiber) and their SI was measured in a standard spectrometer. The spatial scan ($x$-axis) is done with a motorized translation stage synchronized with the acquisition software of the spectrometer. Different planes were explored by changing the propagation distance $z$ in which the test fiber was placed.

The experimental setup for STARFISH is very simple, just needing a fiber optic coupler and a standard spectrometer for the detection. It is very versatile as well; one can just change the spectrometer in case that a different spectral range or resolution is required, in a plug-and-play configuration, without any variation of the optical setup (if the operating band of the other elements, e.g. the beam splitter and the mirrors, is adequate). The use of fibers to collect the pulses allows us to get rid of the alignment of the pulses in the recombination part of the interferometer. Note that the two pulses have to be collinear to carry out the SI. In a standard interferometer (e.g. Mach-Zehnder), this is very demanding, since every time a parameter is changed, the alignment has to be redone. In the case of the fiber coupler, one just needs to collect the two pulses in their respective fiber arm, and they will be always collinearly recombined in the common fiber portion. The advantage of alignment-free will permit to perform systematic studies more easily than with a conventional interferometer.

It is very important to realize that the reference fiber is fixed during a measurement. While the test fiber spatially scans the pulse, the reference fiber is fixed collecting the same spatial position of the reference pulse. This point corresponds to the position in which the reference pulse has been characterized, typically on-axis, although this is not mandatory. As a result, the reference does not need to be spatially homogeneous any more, in contrast with the system presented in Chapter 3. This advantage also implies that a spatial filter is not needed to create a homogeneous reference pulse. In fact, the effect of the reference fiber can be interpreted as a spatial filter since its small core collects a section of $4\mu m$ diameter from the reference pulse, which can be considered locally homogeneous. During the spatial scan of the test pulse, all the SI acquired are relative to that fixed reference, which allows the spatiotemporal reconstruction of the test pulse even in the case of an inhomogeneous reference pulse.

The use of a fiber coupler also gives more stability to the system, owing to the reduction of free-space propagation and optical components, which constitutes an advantage since we are conducting interferometry experiments. This point will be crucial for a direct and precise measurement of the wavefront and the pulse-front of the pulses.

As illustrated in Fig. 4.1, the spatiotemporal measurement is taken at a certain propagation distance *z*. This is enough in some experiments, whereas in others a propagation scan or *z*-scan is mandatory. To this end, two options are possible. One can change the longitudinal position of the test fiber to collect the pulse in a different *z*, as it was done, for example, in the *z*-scans of the experiment in Chapter 6. This requires the

readjustment of the longitudinal position of the reference fiber to set the optimum delay. In the case of a large distance of *z*-scan, "the experiment can be shifted in *z*", which means that the optics can be displaced in order to change the distance between them and the observation plane. For example, this is the case of the *z*-scan of filamentation presented in Chapter 8, in which the iris and the focusing lens were displaced with respect to the test fiber. In this approach the optical paths are nearly preserved and no major further adjustment is needed.

### *4.2.2. The fiber optic coupler characteristics*

The fiber optic coupler is the master key of STARFISH. For this reason we will briefly explain some of its basic concepts. For further knowledge the reader can consult [5,6]. In general, a fiber optic coupler is an optical element that couples the light coming from two input fibers in a single output fiber, as illustrated in Fig. 4.3. This definition suits our particular case, and is called a $2\times1$ fiber coupler. There are many variants of related elements, for example, most couplers are bidirectional, so they can be used in the inverse configuration, that is, as a $1\times2$ fiber splitter. Depending on the application, the coupling/splitting ratio will be different. We use a 50-50% coupler to have a good contrast of the test and reference pulse's amplitude, although couplers with 10-90% or other ratios can be designed. Furthermore, there are also $2\times2$ fiber couplers/splitters as those used in optical coherence tomography [7] or even what is known as star couplers with several inputs and outputs. Additionally, there are fiber couplers that operate at the same time with different wavelengths in a controlled way and can be used to multiplex and demultiplex signals. In our case, the two signals (test and reference pulses) have similar spectral content.

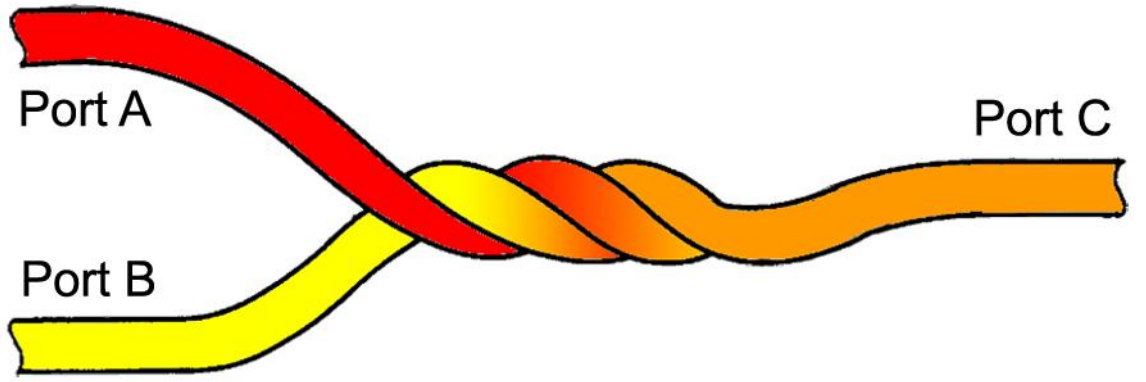


Fig. 4.3. Schematic representation of a fiber optic coupler. The light enters two different fiber through two ports (A and B) and is coupled to a common fiber, exiting through port C.

In order to manufacture fiber optic couplers different techniques can be used. One of them consists in mixing two fibers in a three-step process: a common portion of the fibers is twisted together, then it is heated until fused and then it is tapered, while applying a tension to the extremes of the fibers. Similarly, another approach is to cut longitudinally a transverse section of both fibers, which are put together. Both schemes rely on the transfer of optical power by the evanescent wave. Other compact schemes are based on gradient index microlenses, prisms or reflective glasses to guide the light

to the desired fiber [5]. Couplers can be designed to operate at the desired wavelength, coupling ratio, etcetera. The operating bandwidth available will depend on the physical mechanism and the manufacturing process. For us, this is very important, since we intend to apply the coupler to broadband (ultrashort) laser pulses.

In our case, the fiber coupler has to fulfill a set of requirements. In Table 4.1, we give the specifications of the fiber coupler provided by the manufacturer. First, the coupler should be single-mode in the whole spectrum of the pulse to avoid the introduction of modal dispersion in the fiber arms. A multi-mode fiber allows different modes propagating inside the fiber. Their different propagation would introduce a relative dispersion between the reference and test pulses, which would lead to a temporal distortion in the measurement. As a result, the pulse spectrum must fall above the cut-off wavelength (below this wavelength the coupler operates as multi-mode).

As said before, it requires a large spectral bandwidth of operation to be used with broadband ultrashort laser pulses. In our case, we apply it with Ti:sapphire laser systems with central wavelength around 800 nm. Since our aim is to use it to measure nonlinear processes characterized by involving spectral broadening, our coupler was designed to operate in a bandwidth as large as possible. In Section 4.2.4 we will present the characterization of the spectral transmission of the coupler, corresponding to a full-width at half maximum (FWHM) of around $200nm$. The shortest pulses measurable will be presented in Chapters 9 and 10.

| | |
|---|---|
| Operation | Single-mode |
| Central operation wavelength | 780 nm |
| Bandwidth (bandpass) | $\pm$ 100 nm |
| Coupling ratio | 50/50% |
| Arms length | 88 cm |
| Core diameter | 3.9 $\mu m$ |
| Mode field diameter | $5.4 \pm 1.0 \mu m$ |
| Cut-off wavelength | $580 \pm 40$ nm |
| Numerical Aperture | $0.11 \pm 0.02$ |
| Core index | 1.4618 |
| Cladding index | 1.4529 |
| Connectors | SMA905 |

Table 4.1. Fiber optic coupler specifications provided by the manufacturer.

Furthermore, the two arms of the coupler have to be of equal length in order to avoid introducing a relative dispersion between the pulses. Since SI measures the relative phase between the test and reference pulses, equal amounts of dispersion accumulated during propagation in the fiber arms will be compensated. The coupler was manufactured to satisfy this point, although in practice a perfect matching is not possible. The slight difference of dispersion between the two arms —due to a small fiber length difference $< 2mm$— can be characterized by SI and later taken into account as a calibration in the algorithm for the phase extraction. To characterize the dispersion

difference, we measured the SI of the same pulse, which gives the dispersion of the fiber length difference and the beam splitter (air dispersion will be compensated thanks to the similar optical paths of the two interferometer arms). Then, the dispersion of the beam splitter was separately measured by SI as well, comparing the phase with and without the beam splitter (with the same angle, namely 45º) in one arm of the interferometer. Depending on the experimental configuration, the calibration of the reference pulse can be done before or after the beam splitter. If done after it, it is not necessary to calibrate the beam splitter dispersion separately, since it has to be corrected together with the fiber length difference dispersion from the measurements. To measure directly the relative fiber arms dispersion, it is also possible to take two consecutive SI measurements by exchanging the fiber arms. In this case, the relative phase between the two SI acquisitions will give twice the fiber dispersion.

Note that a slight difference of length will be more and more dramatic for shorter pulses because of their ultra-broadband spectrum. In the case of few-cycle pulse, we will use a spectrometer with larger free spectral range and, consequently, with smaller spectral resolution. If the arms length were not well-balanced, the relative dispersion between the two arms of the interferometer would be arbitrarily large to the point that it would cause a large broadening of the side-peaks after calculating the Fourier-transform of the interference (see Section 2.2). In fact, the same thickness of dispersive material produces larger temporal stretching for broader spectra. These two peaks may overlap with the central peak and this fact may conflict with the measurable pulses owing to the limitations imposed by the experimental spectral resolution [8]. In our case, the signal broadening is well below this limit.

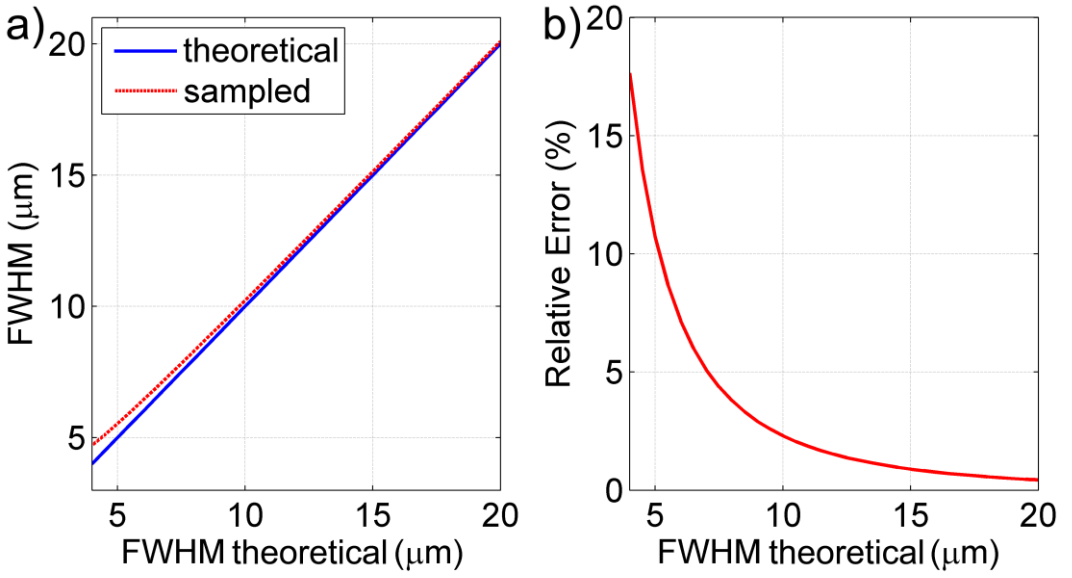


Fig. 4.4. (a) Spatial FWHM of different Gaussian beams (blue line) and retrieved FWHM from the pulse sampled by the collecting fiber (red dashed line). (b) Relative error of the spatial FWHM retrieved as a function of the simulated focal spot size.

### *4.2.3. Spatial resolution and focused pulses*

The technique has a high spatial resolution, which is given by the mode-field / fiber core diameter of the collecting fibers. This resolution is of around $4\mu m$, which means

that the fiber integrates a circular section of $4\mu m$ diameter. In the case of focused pulses, whose spatial profile is of the order of this size, we approach the limit. For this reason, we studied the effect of the resolution on the focal spot size theoretically. We simulated focal spots for Gaussian beams of different spatial sections and calculated the spatial profile sampled by the collection fiber taking into account the integration on the circular section (Fig. 4.4). The effect of sampling the pulse with a $4\mu m$ core diameter is shown in Fig. 4.4a, where it is shown higher spatial width than the actual value, especially for smaller beams. The deviation of the absolute value for focal spots of $\geq 10\mu m$ (FWHM) is small, the relative error being below 3% (Fig. 4.4b). As the focal size is reduced, the absolute and relative errors increase, and the precision of the spatial width retrieved is lost.

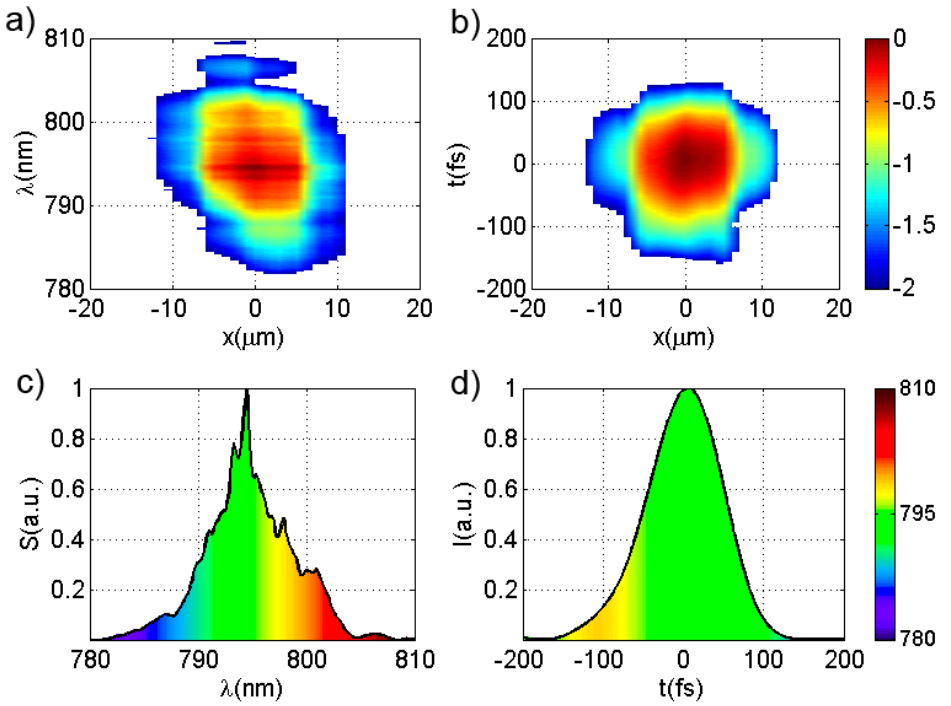


Fig. 4.5. Results of the characterization at the focus of the achromatic doublet lens: (a) Spatially resolved spectrum, (b) spatiotemporal intensity, (c) spectrum on axis, and (d) intensity on axis colored by the instantaneous wavelength. The plots (a) and (b) are in a logarithmic scale (see colorbar) that comprises two orders of magnitude.

To demonstrate the measurement of focused pulses, we characterized a pulse focused with an achromatic doublet (focal length $f = 100mm$) [9]. We used a Ti:sapphire laser system (Spectra Physics) that delivers pulses centered at $795nm$ with a $9nm$ spectral bandwidth (FWHM) at a repetition rate of 1kHz. The experimental results are shown in Fig. 4.5. The spatial scan was done with $1\mu m$ steps. Thanks to the achromatic focusing, the spatially-resolved spectrum (Fig. 4.5a) shows a spatial width of $\sim 10.8\mu m$ almost independent from the wavelength, whereas the spatiotemporal intensity (Fig. 4.5b) corresponds to a non-distorted focused pulse. The results on-axis ($x = 0$) show a non-distorted spectrum (Fig. 4.5c) with respect to the input spectrum, which in the temporal domain corresponds to a Gaussian pulse with duration $\sim 100\,fs$ similar to the input pulse duration (Fig. 4.5d). The intensity is colored by the instantaneous wavelength

obtained from the temporal dependence of the phase of the pulse, that is, the inverse of the instantaneous frequency calculated as the derivative of the temporal phase of the pulse. Further measurements of focused pulses for different applications and their comparison with simulations will be presented along the thesis.

### *4.2.4. Operating bandwidth and ultra-broadband pulses*

The design operating bandwidth provided by the manufacturer comprises a range of $\pm 100nm$ centered at $780nm$ (see Table 4.1). This means that the spectral amplitude of ultra-broadband spectrum pulses will be afflicted by the fiber coupler transmission. However, the transmission function can be calibrated and used to correct the spectral amplitude detected in the spectrometer. For this reason, we measured the spectral transmission of the coupler with a white-light calibration lamp (300-1050 nm, LS1-CAL, Ocean Optics Inc.). The transmission function, $\eta(\lambda)$, was obtained by comparing the power spectral density with and without the fiber coupler, measured with a calibrated broadband spectrometer (HR4000, Ocean Optics Inc.). The results are given in Fig. 4.6, where the experimental data are plotted in blue. We fitted an exponential function $\exp(a\lambda^4 + b\lambda^3 + c\lambda^2 + d\lambda + e)$ to the measured data, where we determined five free parameters (in order to avoid restrictions in the fit of the experimental curve) by least squares optimization. Only the gray shaded area was considered for the fit in order to avoid the noise in the tails. The red curve is the resulting transmission $\eta(\lambda)$ that will be taken into account to correct the amplitude response of the fiber coupler. From this curve, we see that wavelengths below 500 nm and above 1000 nm will not be coupled. Nevertheless, the broadband transmission of the coupler is still adequate for measuring few-cycle, near infrared pulses in that range, whenever there is contrasted signal in the detection. The results for few-cycle will be presented in Chapter 9 for an ultrafast oscillator [8] and Chapter 10 for the post-compression of amplified pulses [10].

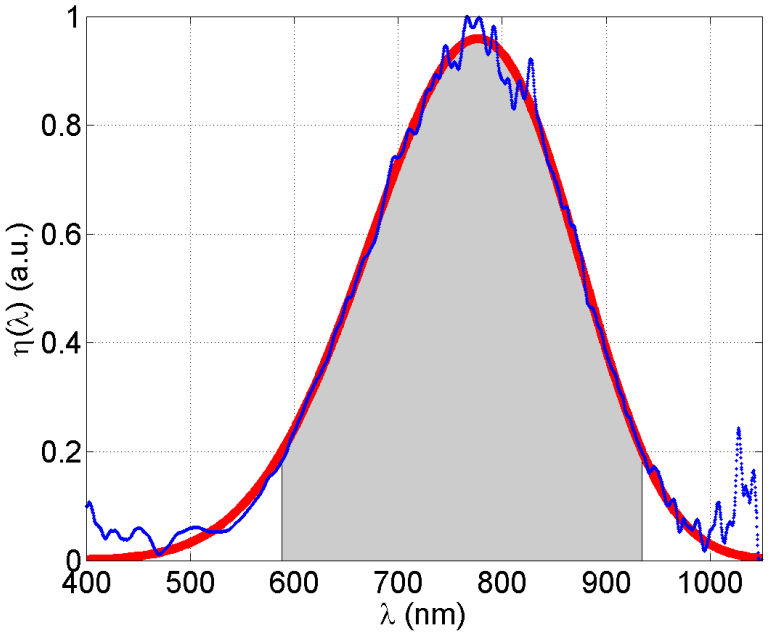


Fig. 4.6. Calibration of the spectral transmission of the fiber coupler measured with a white-light source.

To test the spectral range of the coupler acting as an interferometer, we measured the SI of the spectral broadening of amplified pulses in a hollow-fiber (Fig. 4.7a) from 550 to 1000 nm. To increase the range of operation, the signal fall due to the coupler transmission (Fig. 4.6) could be compensated by using a filter with the opposite response with respect to the coupler transmission. In order to see the softer tails of the spectrum, which are weakened by the coupler transmission, we increased the time integration of the spectrometer until saturation of the main part of the spectrum. In Fig. 4.7b and 4.7c, we depict respectively the bluer and the redder wavelengths measured with the fiber coupler. Note that for the bluer part (Fig. 4.7b) the fiber coupler operation is multi-mode and the redder part (Fig. 4.7c) the coupler transmission is too low, so we will not use the coupler to measure pulses in those wavelengths.

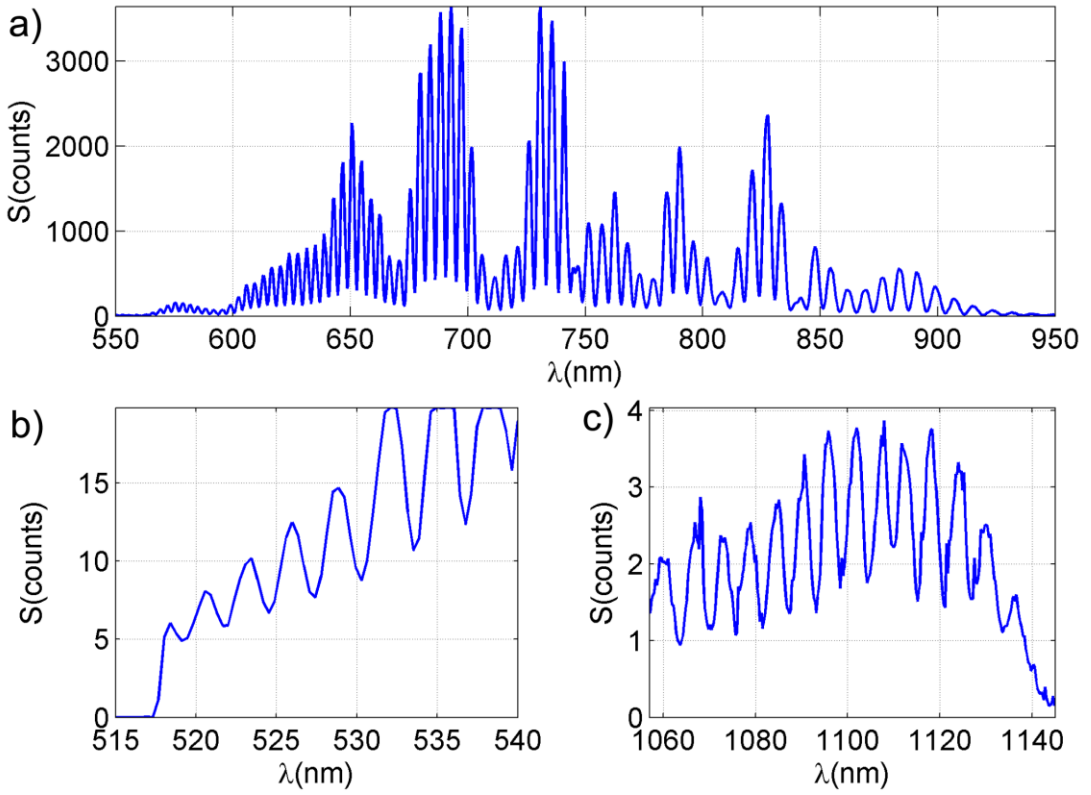


Fig. 4.7. (a) Spectral interferences of an ultra-broadband pulse. (b) Bluer and (c) redder part of the spectrum in which spectral interferences have been observed.

### *4.2.5. Numerical aperture*

The fact of using a fiber to collect the pulses marks the maximum numerical aperture measurable. The light parallel to the fiber is collected more efficiently than the one collected with an oblique angle, the fiber transmission being a bell-shaped function of the angle of incidence (wave vectors or k-vectors impinging the fiber with higher angle will be coupled with less efficiency). The maximum angle of incidence $\theta_C$ (cut-off) collected by the fiber is related to its numerical aperture $NA$ through the expression $NA = n \cdot \sin\theta_C$ ($n = 1$ in air), which determines a cone of coupled light. In our case, the manufacturer provided as the value $NA = 0.11 \pm 0.02$, which corresponds to an angle $\theta_C = 6.3^{\circ}$. By definition, the incident light with larger angle will not be collected by the fiber and thus it will be an information loss when measuring pulses with larger

numerical aperture. This issue will be relevant in the measurement of focused pulses, for example, in the near field of a Fresnel plate presented in Chapter 5 [11]). To deal with this, the observation distance can be increased, with the subsequent reduction of the angle of incidence on the fiber (Section 7.1, [12]). A solution to measure pulses with larger *NA* consists in using a NSOM (Near-field Scanning Optical Microscopy) fiber probe, characterized by having larger *NA* as well as better spatial resolution [13]. Note that, as a collateral consequence, one can use the fiber transmission function to balance the amplitude (similar to a variable attenuator) of the spectra of the reference pulse with respect to the test pulse, in order to have better contrasted fringes for the SI (see Section 2.1.3).

Since we were interested in the application to ultrashort (broadband) pulses and the *NA* of single-mode fibers depends on its physical properties, we could not discard a possible dependence on the wavelength (dispersion) of the *NA*. Also, we wished to simulate the effect of the *NA* for the applications of STARFISH, so we were interested in its characterization beyond the manufacturer's specifications. In the case of a dispersive *NA*, the transmission of the fiber would depend not only on the angle of incidence $\theta$, but also on the wavelength $\lambda$ [8]. Such situation would imply a spatiospectral distortion in the measurement of focused pulses.

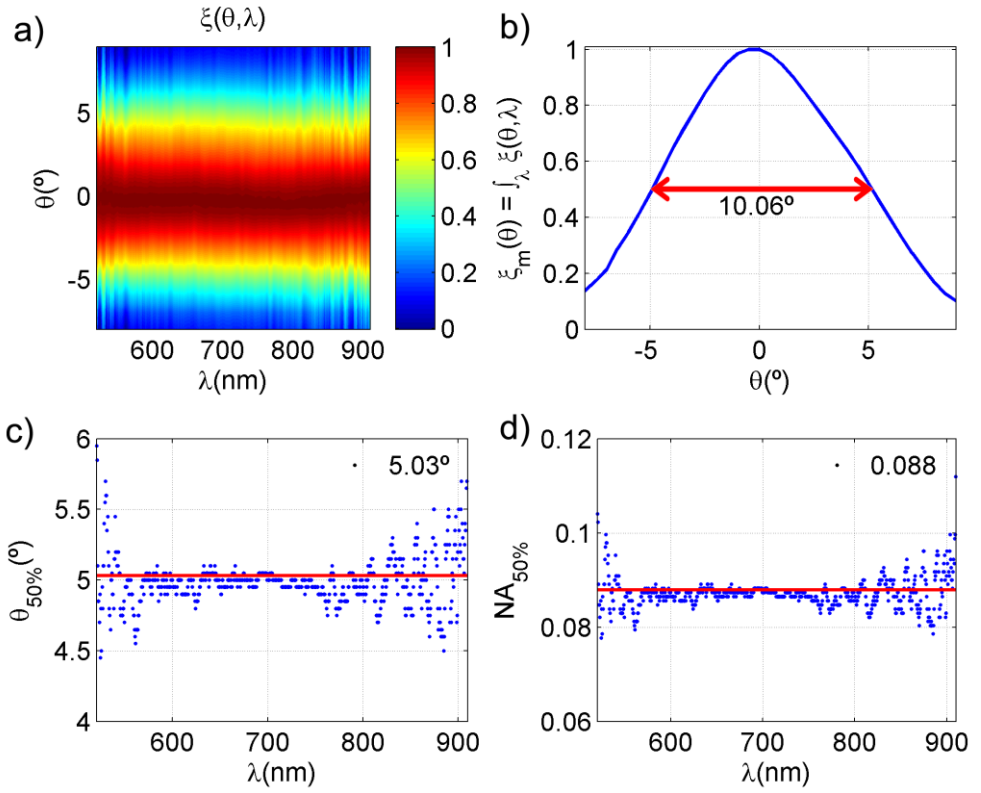


Fig. 4.8. (a) Transmission of the fiber as a function of the angle of incidence and the wavelength. (b) Transmission integrated in wavelength. (c) Angle of incidence for a decrease in efficiency of 50% with respect to the maximum. (d) Numerical aperture corresponding to the angle in (c).

For this reason, we calibrated the coupling efficiency of the fiber as a function of the angle of incidence and the wavelength. We used a white-light source (LS1-CAL, Ocean

Optics Inc.) and a rotation stage to vary the angle of the fiber with respect to the source while keeping the fiber input in the axis of rotation. The signal was detected with a fiber-coupled spectrometer (AvaSpec-2048, Avantes Inc.). The transmission function $\xi(\theta,\lambda)$, where the signal has been normalized for each wavelength, is represented in Fig. 4.8a. The angular dependence of $\xi(\theta,\lambda)$ is roughly constant with wavelength. In Fig. 4.8b we plot the integral of $\xi(\theta,\lambda)$ in the wavelength axis $\xi_m(\theta)=\int_\lambda \xi(\theta,\lambda)\,d\lambda$, obtaining a FWHM of the acceptance cone $\Delta\theta=10.06^{\circ}$. To study the dispersion of the acceptance angle (see Fig. 4.8c), we calculated the angle for which the signal falls to half the maximum from the center, $\theta_{50\%}$, as a function of wavelength (blue dots), and compared it to $\Delta\theta/2$ (red curve). If the noisy regions in the extremes of the spectrum are discarded, it can be concluded that the angular response is not dispersive in a broad spectral bandwidth. This means that the angular dependence of the light coupling in the fiber does not depend on the wavelength, so $\xi(\theta,\lambda)\approx\xi_m(\theta)$. In Fig. 4.8d we give the numerical aperture for the half-maximum of the cone, $NA_{50\%}=\sin\theta_{50\%}$, which is also independent from the wavelength. In the case of measuring pulses with higher numerical apertures, the signal coming from the peripheral part of the profile of the focused pulse will be detected with less efficiency and, therefore, the detection will modify the measured pulse by the function $\xi_m(\theta)$.

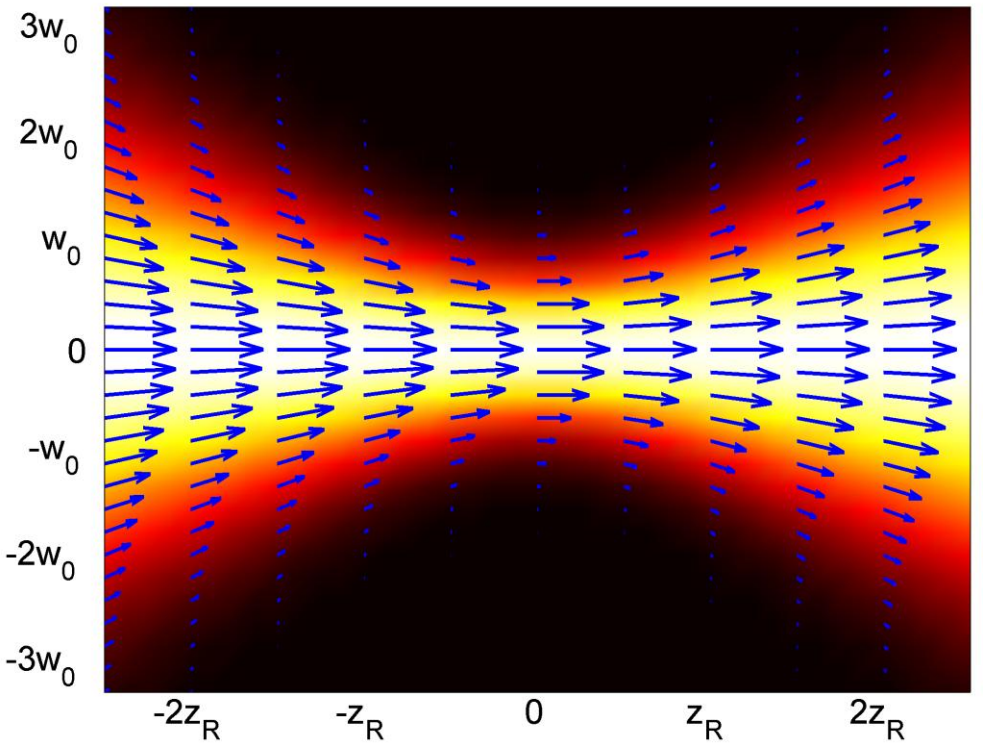


Fig. 4.9. Representation of the focusing region of a Gaussian beam and the orientation of the wave vectors as a function of the transverse coordinate and the propagation distance.

Now, we will present an analysis of the *NA* of the pulses and how the *NA* of the collection fiber can distort their measurement, considering the propagation of a monochromatic Gaussian beam [14]. We will first simply calculate the wave vector orientation and then we will present a deeper study using the Wigner function [15]. For this purpose, we simulated the propagation of a Gaussian beam in the focusing region,

considering a focal length $f = 50mm$, input beam radius $w_{in} = 12mm$ (at $1/e^2$ from the maximum) and wavelength $\lambda_0 = 800nm$. These parameters correspond to a Rayleigh length of $z_R = 4.42\mu m$ and a beam waist at focus of $w_0 = 1.06\mu m$. In Fig. 4.9, we represent the Gaussian beam intensity (normalized for each $z$-plane) as a function of the propagation distance $z$ around focus. Thanks to cylindrical symmetry, we just provide the results for one axis in the transverse $z$-plane. We also represent the wave vectors as a function of the transverse coordinate $x$ and the propagation distance $z$. Their orientations were calculated as the perpendicular to the simulated wavefront and their module is given by the local intensity. As a first approach, we conclude that their orientations out of focus are the same than those given directly by ray tracing, whereas inside the Rayleigh zone they tend to be parallel to the optical axis (in fact, in the focal plane all the wave vectors are parallel).

Nevertheless, the wave vector distribution inside the Gaussian beam is more complex than the picture given in Fig. 4.9. In general, at a certain position ($x$ and $z$ coordinates) the wave vector will be the sum of multiple contributions from different parts of the input plane, which are mixed due to the beam propagation. To have an insight into its structure, we will take advantage of the 1D-spatial Wigner function $W_X$ defined as [15]

$$W_X(x,k_x) = \int_{-\infty}^{\infty} E(x+\frac{x'}{2})E^*(x-\frac{x'}{2})e^{ik_x x'}dx', \qquad (4.2)$$

where $E(x)$ is the electric field at a certain propagation distance, $E^*$ denotes the conjugate of $E$, and $k_x$ is the wave vector corresponding to the coordinate $x$. The evaluation of this function for the simulated $E(x)$ directly yields the distribution of wave vectors $k_x$ for each spatial position $x$. In Fig. 4.10 we plot the spatial Wigner function $W_X$ for different propagation distances at and after the focus. Since the result has odd symmetry with respect to the focus, we do not plot the results before the focus (the trace will be flipped with respect to $x = 0$). In the left column of Fig. 4.10, we give the calculated Wigner function $W_X$, whereas the right column corresponds to the $W_X$ filtered by the $NA$ of the fiber. To simulate the effect of the $NA$ of the fiber, we multiplied the wave vector distribution by the experimental curve $\xi_m(\theta)$. The spatial profile, calculated as the integral over the wave vectors is plotted as a dashed curve.

As found in the literature [16], the distributions of the wave vectors inside the focused monochromatic Gaussian beam is like a delta function for each spatial point where the wave vectors with non-zero contributions correspond to the angle obtained by ray tracing. Since larger angles occur in the periphery of the beam, outside the focal region the angular filtering of the $NA$ of the fiber results in a reduction of the spatial width that depends on the $NA$ of the focused pulse (for example, see the variation of the spatial profiles from Fig. 4.10g to 4.10h). Conversely, at the focus position all the wave vectors contributions are overlapped (owing to the propagation) and the wave vector spreading is independent on the spatial coordinate, so the ray tracing approximation is obviously unacceptable there. For this reason, in the focus the effect of the $NA$ coupling will be ideally a reduction in the collected signal without spatial distortion (see the invariance of the spatial profile in Fig. 4.10a and 4.10b).

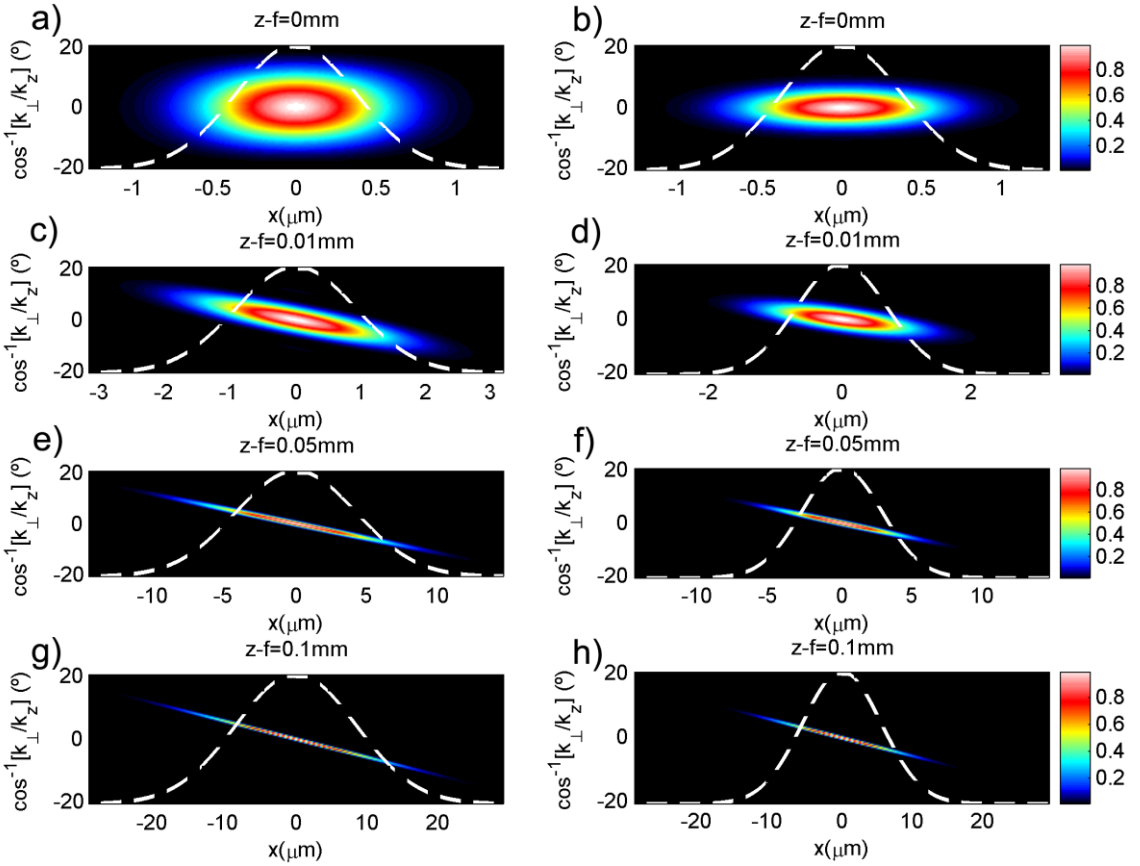


Fig. 4.10. Spatial Wigner function for different propagation distances. The results are given as a function of the spatial coordinate *x* and the angle of the wave vector with respect to the optical axis. The left column corresponds to the calculated function, whereas in the right column the correction of the fiber has been applied. The integral over the wave vector gives the spatial profile for each curve (white dashed curve). The traces correspond to the propagation distances (with respect to the focus) of 0mm (a,b), 0.01mm (c,d), 0.05mm (e,f), and 0.1mm (g,h).

The maximum $NA$ of a beam focused by a lens can be estimated by ray tracing from the plane of the focusing lens to the focal plane. For example, the maximum angle of incidence $\theta_M$ of a focused pulse (focal length $f$) will be the ray arriving from the most off-axis point in the input spatial profile (that is, in the lens). If the input pulse has a spatial radius $\rho$ and we observe at the focus that angle will be given by $\tan\theta_M = \rho/f$. If the condition $\theta_M \ll \theta_{50\%}$ is fulfilled, then the $NA$ will not distort the pulse retrieval. If $\theta_M \gg \theta_{50\%}$, the pulse $NA$ will be too high for the characterization with the collecting fiber. In intermediate cases, $\theta_M \sim \theta_{50\%}$, the $NA$ will have an effect on the measurement that may be estimated from the measurement of the input spatial profile. Following the example of a focusing beam, the spatial profile detected out of focus will be filtered by the transmission function $\xi(x)$ calculated from the fiber response $\xi_m(\theta)$ given in Fig. 4.8b. To do so, the spatial coordinate is connected to the angle by the relation $\tan\theta = x/f$. In many cases, the outer part of the spatial profile, which is the most affected by the filter of the fiber $NA$, is the weakest part and then the effect of the $NA$ is not dramatic (in the sense that the clipped part is the least intense). In the experiments, we will try to keep in the case $\theta_M \ll \theta_{50\%}$ and, if not possible, $\theta_M \sim \theta_{50\%}$. Here, the case that we have simulated in Fig. 4.10 corresponds to a beam with relatively

high $NA$, so the reduction of the spatial profile would not be negligible. In the case $\theta_M \sim \theta_{50\%}$, we can measure the actual experimental spatial profile $I(x)$ before the lens, and then estimate the corresponding spatial profile that would be detected as $I(x)\cdot\xi(x)$, which can be compared to $I(x)$ (an example of this estimation for a particular case will be presented in Chapter 10).

Of course, the present analysis would be more complex in the case of polychromatic non-Gaussian beams, which may also be inhomogeneous and present wavefront aberrations. This would cause a less predictable propagation (if the unfocused pulse is known, numerical simulations can still be performed). However, out-of-focus ray tracing can still give a first approximation of the wave vector distribution and an upper bound for the maximum angle $\theta_M$, as said before. Naturally, the effect of the $NA$ will not be felt by smaller beams or longer focal lengths (since $\theta_M \ll \theta_{50\%}$).

In Chapters 9 and 10, we will present the measurement of few-cycle pulses focused by an off-axis parabola and will take into account the calibrated response of the fiber, $\xi_m(\theta)$, to ensure that its effect on the detection is acceptable. Note that the calibrated $NA$ differs from the value given by the provider.

## 4.3. Experimental measurements of known cases: test of the STARFISH

In this section we present the experimental measurement of different pulses, which we carried out to validate and evaluate the possible limitations of our proposal (STARFISH) for the spatiotemporal characterization of ultrashort laser pulses [3]. First, we applied it to the measurement of negatively chirped pulses, in order to explore the temporal range of applicability of the SI. Then, we applied it to pulses with complex spatiotemporal dependence. We compared the measurements with the simulated pulses to verify the results in known cases.

### *4.3.1. Description of the laser system and detection devices*

The experiments presented in this section were carried out using two different terawatt-class Ti:sapphire chirped pulse amplification (CPA) laser systems (both at a 10 Hz repetition rate). The first system (Spectra Physics, Inc.) delivers laser pulses of 120 fs (Fourier limit) with its spectrum centered at 795 nm. The second system (Amplitude Technologies) provides 35 fs pulses centered at 805 nm. We worked with two different lasers to test STARFISH with pulses of different durations and bandwidths. For the temporal characterization of the reference beam we used the GRENOUILLE [17] (20-120 fs, single-shot FROG, Swamp Optics) and SPIDER [18] (10-40 fs, APE GmbH) devices, whereas for the spectra we used a commercial spectrometer (Avantes Inc.) with a resolution of 0.1 nm. Depending on the duration of the pulses, we characterized them with the SPIDER (35 fs pulses), where there is no ambiguity in the time direction, or with the GRENOUILLE (120 fs pulses). In the case of the GRENOUILLE device, we identified the temporal direction by performing a second measurement with additional known dispersion, as is usually done when using this apparatus. We observed that the GRENOUILLE spatial homogeneity requirements

were fulfilled (if not, a FROG, SPIDER or equivalent is mandatory) for the 120 fs laser by measuring the profile with a CCD. The spatial scan was performed with a motorized translation stage (with micrometric precision) at the same time as the spectrum was acquired.

### *4.3.2. Linear chirp experiments*

In order to explore the limitations of our setup for SI, we performed an experiment to measure the linear chirp. The test pulse was chirped through two passes in a diffraction-grating pair compressor using the 35-fs laser. We negatively chirped the pulse with Group Delay Dispersion (GDD) varying from $-7000\,fs^2$ to $-1000\,fs^2$ because these were the compressor limits for our setup. The linear chirp stretches the test pulse and this implies that the side-peaks in time of the Fourier-transform of the interferences broaden and decrease in amplitude. In our GDD scan, we varied the grating-distance, $L$, and hence the GDD calculated as in [19] is

$$GDD(L) \simeq -\frac{\lambda^3}{\pi c^2}\frac{L}{d^2\cos^2\theta_m}, \qquad (4.3)$$

where $\lambda$ is the central wavelength, $c$ is the speed of light, $1/d = 300\,gr/mm$ gives the groove density, and $\theta_m$ is the output angle calculated from the grating equation $\sin\theta_m - \sin\theta_0 = m\lambda/d$ (for the first order $m=1$ and the incidence angle in the grating $\theta_0 = 15^o$). The GDD is linearly dependent on the grating distance and from Eq. (4.3) we calculated the estimated slope $GDD(L)/L = -212.8\,fs^2/mm$. We measured the chirped pulses using the fiber coupler interferometer at 81 grating-distances and reconstructed them with FTSI. Thus, we obtained the spectral phase and calculated the experimental GDD from a quadratic fit, as shown in Fig. 4.11a, which corresponds to $GDD = -5200\,fs^2$. In Fig. 4.11b the GDD is represented as a function of the grating distance. The linear regression of these data afforded a slope of $-210.2\,fs^2/mm$, in very good agreement with the estimated value. Extrapolation of the fit to zero distance gives an acceptable deviation, $GDD(L=0) = -28.7\,fs^2$, and the correlation coefficient was $R = 0.99984$, revealing the good fit to the data. We also checked that the possible third-order dispersion (TOD) was completely negligible as compared to the GDD. Finally, we studied the instantaneous wavelength (as a function of the time) of the pulses, calculated from the electric field phase. In Fig. 4.11c, using a false color scale, we plot the instantaneous wavelength of the pulses as a function of the grating distance. We have cropped the plot for the decrease in pulse intensity larger than three orders of magnitude (shown in white). In this figure, we show the linear dependence on time of the instantaneous wavelength, explaining the pulse stretching. In Fig. 4.11d, we represent the temporal reconstruction and instantaneous wavelength of the pulse corresponding to $GDD = -5200\,fs^2$. We measured chirped pulses as long as 1.3 ps ($1/e^2$ width, decrease in intensity to 13.5%) for the highest GDD. We also explored the intensity profile caused by the GDD and found that for the lowest chirps pulse splitting occurred, due to the spectrum profile, but not to TOD (negligible).

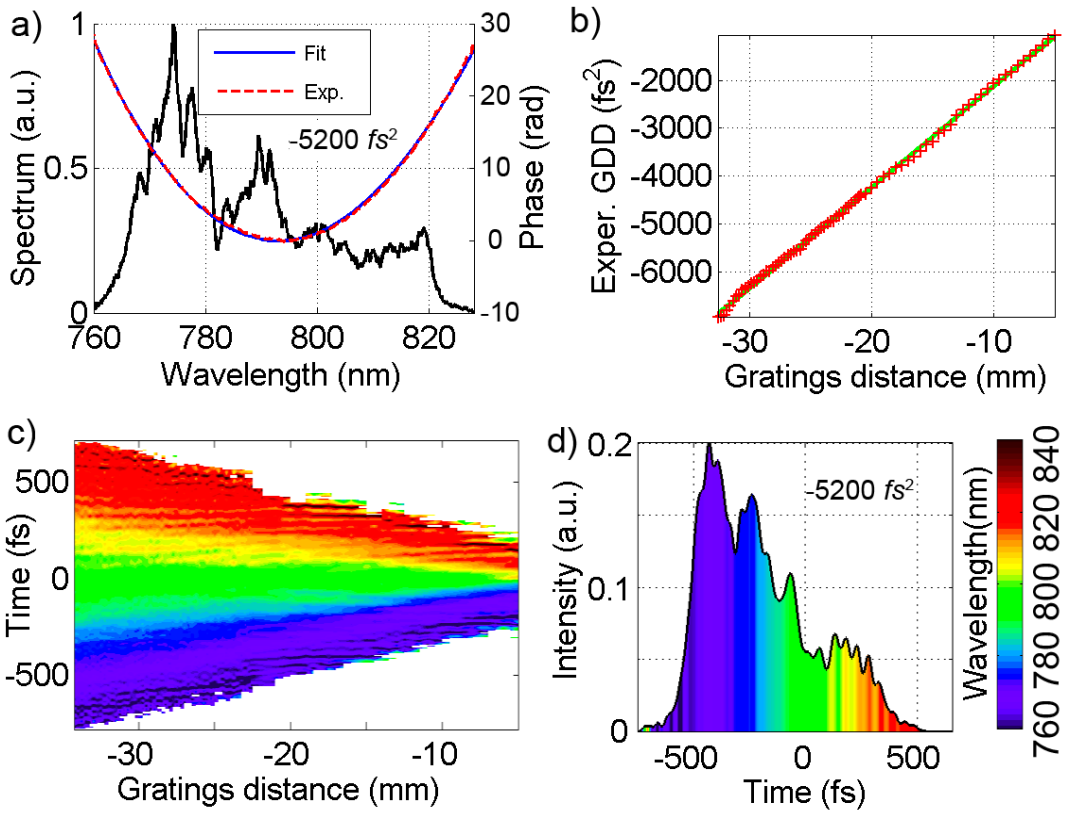


Fig. 4.11. (a) Experimental spectrum and phase of a negatively chirped pulse. Experimental scan on negative linear chirp: (b) GDD retrieved from FTSI and (c) instantaneous wavelength of the chirped pulses as a function of the grating-distance. (d) Temporal intensity and instantaneous wavelength of the chirped pulse.

As discussed in Section 2.3, the resolution of the spectrometer limits the longer pulses that can be measured. One of the main advantages of the technique is its simplicity, which allows the system to be adapted immediately to spectrometers or monochromators with much more resolution simply by plugging the fiber coupler to the input port of the device (common in most systems). It would be very easy to upgrade the STARFISH with commercial devices, with resolutions of around 0.02 nm for portable and small spectrometers in the visible and the infrared (capable of measuring Fourier-transform-limited narrowband pulses of 5 ps FWHM, and even longer in the case of broadband chirped pulses). Furthermore, resolutions of around 0.004 nm are available with optical spectrum analyzers and monochromators in the visible and the infrared (compatible with pulses of 25 ps FWHM), and even below 100 fm in the mid-infrared range with the BOSA High Resolution Optical Spectrum Analyzer (allowing in principle the reconstruction of Fourier-limited pulses of 1 ns FWHM).

### *4.3.3. Interference of two-crossed plane waves*

The spatiotemporal interference of two-crossed ultrashort waves constitutes an experimental complex situation that can also be simulated to validate the reconstruction. To create the test beam, we formed a double-beam structure using a Mach-Zehnder interferometer before the input arm of the fiber coupler (STARFISH setup) that collects the test pulse. Both beams were first aligned and temporally overlapped. Then, we

slightly crossed one beam with respect to the other, thus obtaining the spatial interferences of two crossing plane waves. In Fig. 4.12, we show the experimental results and simulations for this case using a different laser system of 120-fs pulses, also enabling us to reconstruct pulses with a narrower spectrum (FWHM~9 nm). In this case, we used the GRENOUILLE technique to characterize the reference that preserves the spatial homogeneity (required by GRENOUILLE), because we split the laser beam before the Mach-Zehnder device.

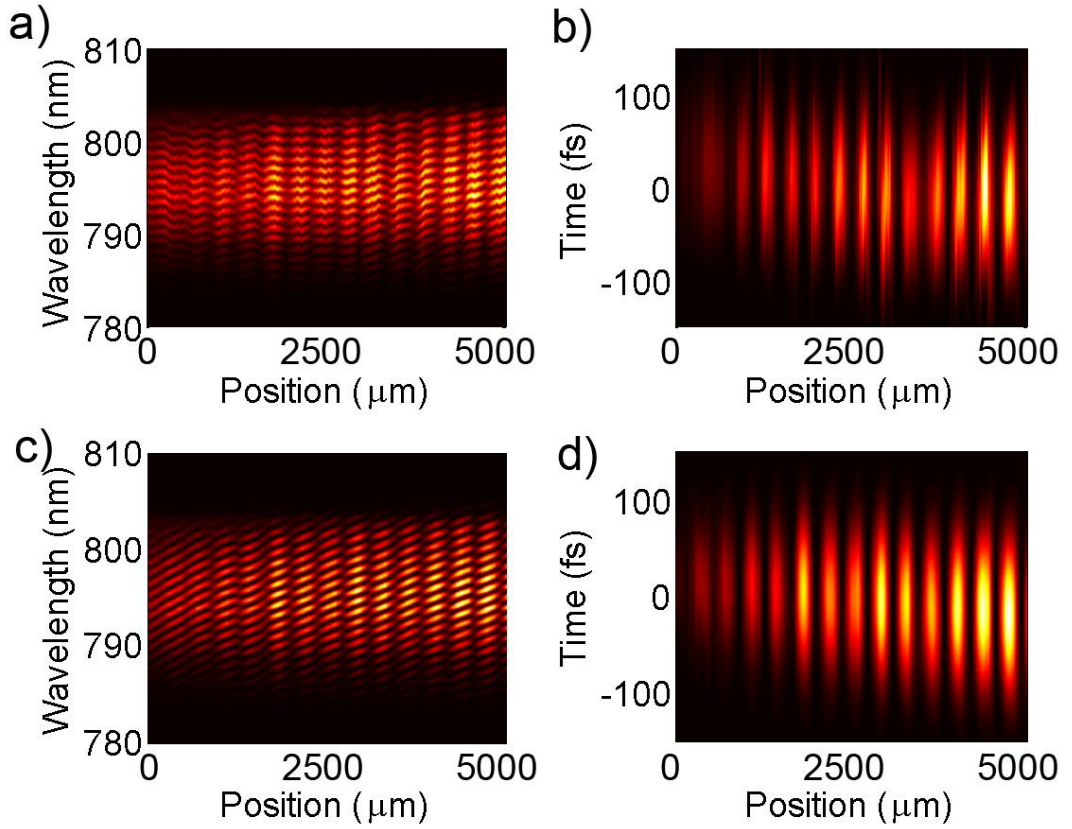


Fig. 4.12. Experimental and simulated spatiospectral interference trace (a: experimental, c: simulated) and spatiotemporal intensity reconstruction (b: experimental, d: simulated) of the interference between two crossing waves for 120-fs pulses.

Figure 4.12a shows the interference spectrum trace, which displays two different fringe patterns: first, the fringes in the spectral dimension corresponding to the spectral interferences between the test beam and a 2.0-ps delayed reference beam, and second the fringes in the spatial dimension (thirteen maxima and minima) arising from the spatial interference of the two crossing waves that form part of the test beam. In this case, we scanned 5 mm of the beam profile in $20\mu m$-steps (251 points). In the spatiotemporal intensity reconstruction (Fig. 4.12b) the two waves of the test beam had a delay of around zero and had slightly crossing pulse-fronts (relative tilt 36 fs for the 5 mm profile). The maxima and minima of the double wave reconstruction are due to the spatial interference of the beams. We performed the simulations using parameters (spectrum, angle and delay) extracted from the experimental conditions. The interference trace is shown in Fig. 4.12c, and the intensity reconstruction in Fig. 4.12d. The simulations and experiments are in good agreement, showing the same behavior.

We also implemented the previous experiment with the 35-fs-pulse duration laser, obtaining interferences in a spectral bandwidth of 70 nm. We created the double beam with the Mach-Zehnder interferometer and controlled the relative angle and delay between the beams. In this case the delay between the test and the reference beam was 2.0 ps. We then scanned $10000\mu m$ on a transverse axis of the beam in $20\mu m$-steps (501 points). The experimental results and the corresponding simulations are shown in Fig. 4.13. The spatially-resolved interference spectrum in Fig. 4.13a clearly shows the spectral interferences with the reference beam and the spatial interferences of the double wave forming the test pulse.

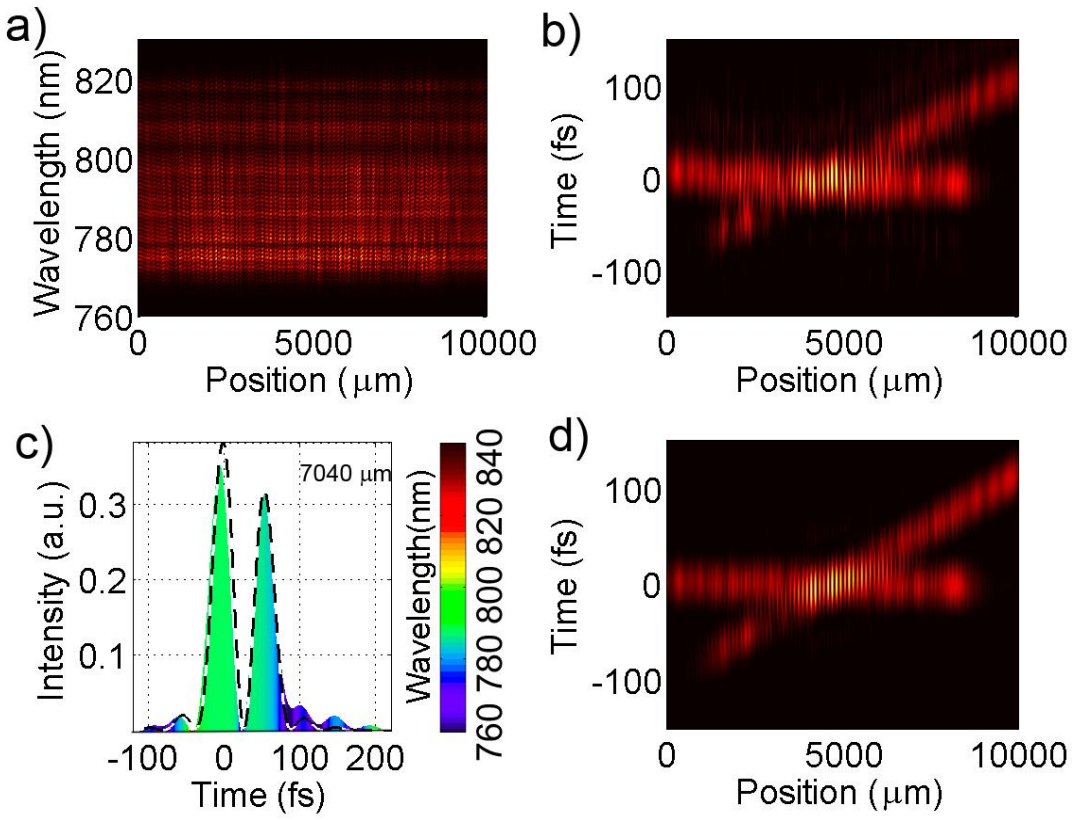


Fig. 4.13. (a) Experimental spatiospectral interference trace and spatiotemporal intensity reconstruction (b: experimental, d: simulation) of the interference of two crossing waves for 35-fs pulses. (d) Experimental temporal profile and instantaneous wavelength for the 7040 μm position in comparison with the simulated data (dashed line).

Reconstruction of the spatiotemporal intensity (Fig. 4.13b) reveals two relatively crossed plane waves. The intensity has the characteristic structure of maxima and minima due to the spatial interferences of the two beams. In this experiment, the angle between the beams was sufficiently high to have 100-fs-separated double pulses on both sides of the beam. In Fig. 4.13c, we show the temporal profile of the double pulse corresponding to position $7040\mu m$ colored with the instantaneous wavelength and compare with the simulated intensity (dashed line). Finally, we show the simulated spatiotemporal intensity (Fig. 4.13d) with the parameters involved in the experiment. The simulations match the experimental reconstruction very well.

In this case, the test pulse has two contributions (two plane waves) with different propagation direction. For this reason, the angle of incidence of each wave on the collecting fiber will be different. To evaluate the possible effect of the $NA$ of the fiber, we estimate the angle of incidence of the crossing plane wave. The total temporal shift is $T = 200\,fs$ over the whole spatial profile $x = 10000\,\mu m$. After converting time to space (through the speed of light, $z = cT$), the crossing angle will be given by $\tan\alpha = z/x$, which corresponds to $\alpha \approx 0.34^{o}$. This angle is too small to afflict the collection of the pulse. Finally, we have said that we have SI of two waves when they are collinear. In this case, they are not perfectly collinear (here, it is done deliberately), but thanks to the single-mode fiber coupler, the two contributions of the test pulse will interfere spectrally with the reference pulse.

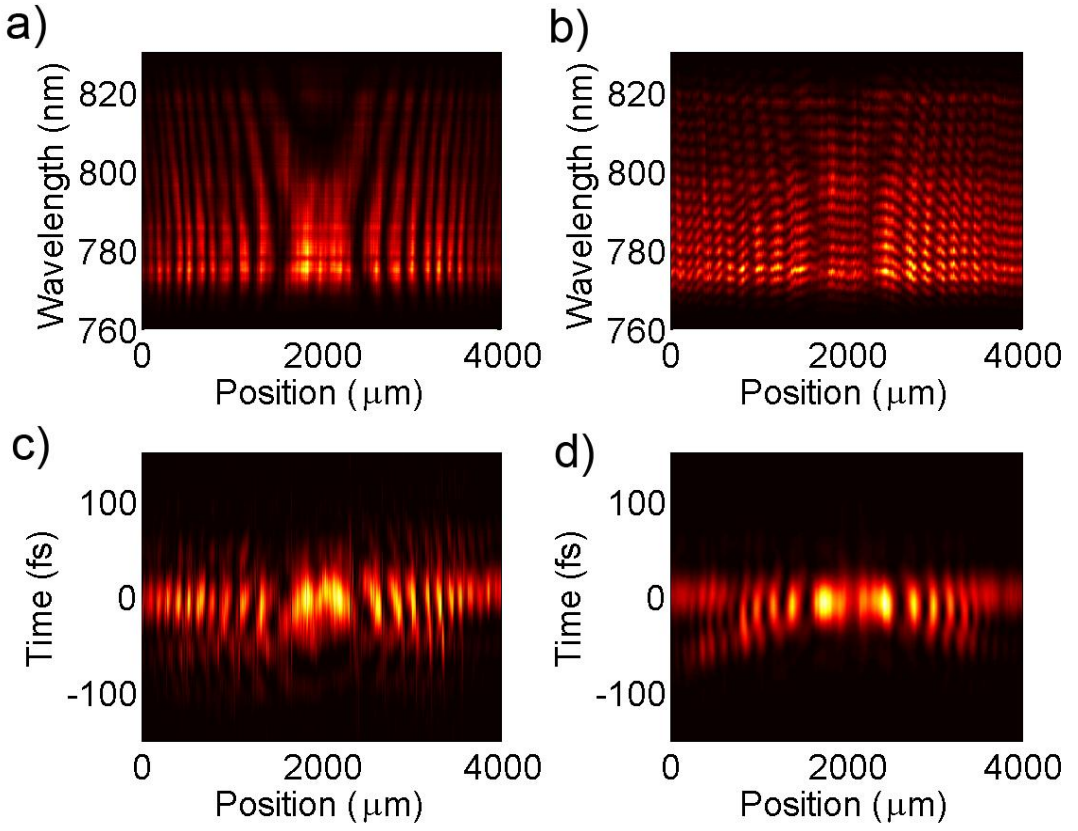


Fig. 4.14. Spherical and plane wave interference for 35-fs pulses. (a) Experimental spatiospectral test beam trace and (b) interference trace. (c) Experimental and (d) simulated spatiotemporal intensity reconstruction.

### *4.3.4. Interference of a plane and a spherical wave*

In Section 3.3.1 we simulated the spatiotemporal interference of a spherical and a plane wave. Here, we have created and reconstructed that pulse structure (Fig. 4.14). In this experiment, we used 35-fs laser pulses. We used a 50-cm focal lens in one arm of the Mach-Zehnder interferometer to obtain the spherical wave (a focusing beam), whereas the other arm controlled the delay between the spherical and the plane wave. The delay between the test and reference beams was 600 fs, whereas the spherical and plane waves overlapped in the central region. The spatiospectral interference pattern of the spherical and plane waves can be seen in Fig. 4.14a (the test beam trace, without

reference). We show the experimental interference spectral trace of the test and reference beams in Fig. 4.14b, where the quadratic variation of the spectral fringes position due to the curvature of the spherical beam contribution (convergent) can be seen. The transverse scan of 4 mm was performed with $8\mu m$-steps (501 points). The spatiotemporal intensity reconstruction (Fig. 4.14c) shows the interference of the spherical and plane waves: a convergent beam is retrieved with spatial modulations. The spacing of this modulation is larger in the central region than in the peripheral region, as corresponds to spherical and plane wave interference, and the same pattern was obtained in the simulation (Fig. 4.14d). The relative delay between the spherical and the plane beam was zero. We repeated this measurement for different relative delays between the plane and the spherical wave up to 100 fs (above and below), so that in the reconstruction we see how both beams separate in time and the spatial interferences decrease. We also tested this situation with higher delays between the test and the reference beam (1.0, 1.5 and 2.0 ps) and obtained the same intensity reconstructions.

Here, we would like to stress that we use amplified pulses, which typically present an inhomogeneous spatial profile and energy fluctuations. Also, we have used a Mach-Zehnder interferometer (which has inherent instability) to create the double-beam structure. In spite of this and that the technique is multi-shot, the experimental reconstructions describe with fidelity the expected structures. Moreover, we will see in the next section how the simplicity and compactness of the setup will be crucial to obtain fine structure of the pulse, such as the wavefront and the pulse-front.

## 4.4. Wavefront and pulse-front characterization: interferometer stability

The retrieval of the pulse-front with STARFISH is direct, since it characterizes the spatiotemporal coupling of the pulses. We will discuss here how the reconstruction of the wavefront is not trivial with multi-shot techniques due to the presence of interferometric instabilities. However, we will also see how the stability achieved by our interferometer (with the fiber coupler of STARFISH) allows us to perform the wavefront characterization. The fact that the wavefront of focused pulses can be retrieved thanks to the high spatial resolution is particularly promising, as is, too, that the full spatiospectral phase retrieval allows the measurement of chromatic wavefronts: those in which the wavefront is a function of the wavelength.

### *4.4.1. Phase fluctuations in the interferometer*

In general, interferometers are affected by small fluctuations due to system instabilities and, in particular, our setup (based on the fiber optic coupler) is indeed expected to exhibit a phase fluctuation (also referred to as phase drift). The origins of these fluctuations are mainly thermal variations (that induce a change on the refractive index), air-flow in the laboratory, vibrations and mechanical instabilities. The consequence is a variation in the relative phase term between the two interferometer arms. Since this variation is almost independent of the wavelength, this means a loss of the constant zero-order relative phase of the pulses, thus preventing precise knowledge of the pulse wavefront and introducing a small error in the pulse front. Recently, a

numerical iterative algorithm was proposed to overcome this drawback and to retrieve the wavefront from this kind of measurements [20].

In a first study of the stability of our interferometer, we analyzed the stability of the spectral interferences (see Fig. 4.15a) for a sequence of single-shot measurements (acquired continuously without averaging, that is, with an integration time of $100ms$ for $10Hz$ repetition rate) with 120 fs pulses, tracking the full spectral phase (Fig. 4.15b), the zero-order phase (Fig. 4.15c), the delay, and the width of the temporal intensity (Fig. 4.15d).

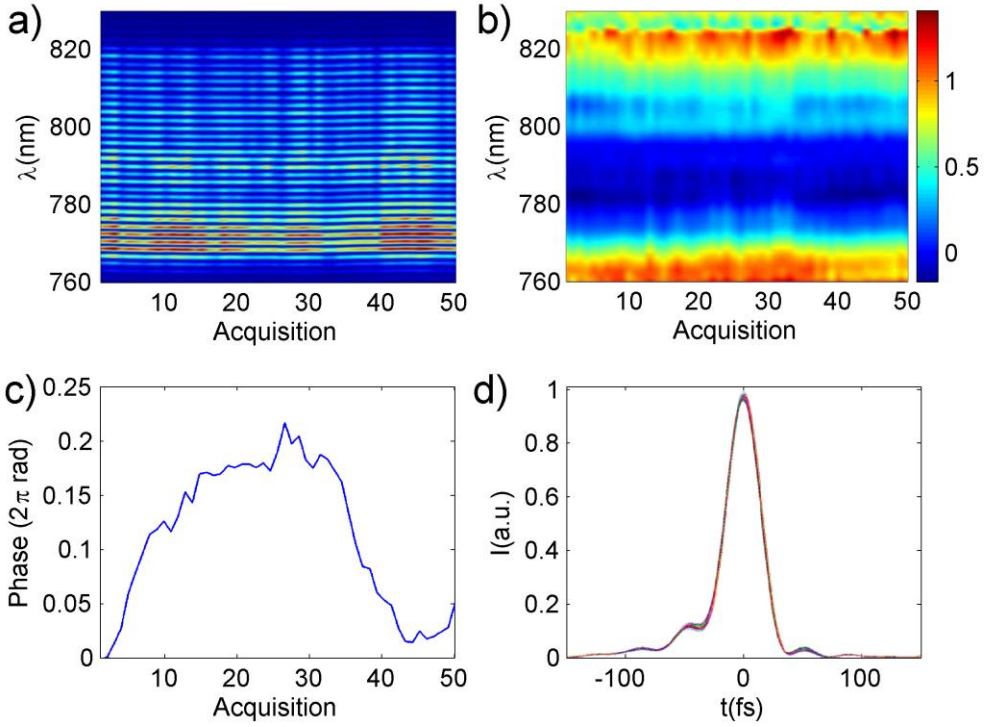


Fig. 4.15. Multiple acquisitions for the phase stability study: (a) spectral interferences, (b) retrieved spectral phase, (c) spectral phase for the central wavelength, and (d) temporal intensity retrieved for all the acquisitions.

We measured a zero-order phase drift in the interferometer of 1.4 rad (peak to peak) during the time usually taken for a measurement to be made (about 1 min). The maximum phase drift for the central wavelength ($0.225{\cdot}2\pi$, see Fig. 4.15c) slightly affected the pulse front, with the corresponding temporal shift thus being limited to 0.60 fs (0.225·T, with T being the laser period for the central wavelength). For the delay, we calculated a standard deviation of 0.40 fs, and for the time-width of the measured pulse we calculated 0.09 fs (the intensity reconstruction is almost invariant, as seen in Fig. 4.15d), whereas the whole spectral phase (Fig. 4.15b) was very stable between shots (except for the effect of the zero-order phase drift). We also studied stability for repeated multi-shot averaging measurements, for which we obtained blurry and reduced contrast interferences due to the shift of the fringes. As a result, poorer reconstructions were obtained owing to incorrect phase retrieval.

In a second analysis, we used the $1kHz$ repetition rate output of the $100\,fs$ laser system (Spectra Physics, Inc.). In this case, we measured 20 fixed spectral interferences during 30 seconds. By studying the stability during 30 seconds (a time larger than the

typical time of the measurement of a focused pulse), we ensured that the measurements were not affected by higher instabilities sources. For the zero-order phase drift: the maximum phase excursion was $0.35{\cdot}2\pi$ and the standard deviation $0.09{\cdot}2\pi$. As it will be seen in Chapter 6 [9] (where the corresponding plots are shown in Fig. 6.3), this phase drift is low enough to directly measure the wavefronts, although a small error of the order of the phase drift will be present in the retrieval.

Additionally, one should take into account that the wavefront is spatially sampled by the scan of the test beam with the fiber and that the phase is retrieved wrapped (between $-\pi$ and $\pi$) with that sampling. Therefore, the spatial scanning step must be small enough (depending on the wavefront curvature) to avoid discontinuities (artificial loss of multiples of $2\pi$) after numerically unwrapping the retrieved phase. For example, in the measurement of focused pulses we used a step of $1\mu m$. Although the resolution of the fiber is $4\mu m$, a smaller scanning step for the focus measurement is mandatory to obtain a smoother spatial profile of tightly focused pulses and to avoid the mentioned phase discontinuities.

### *4.4.2. Pulse-front and wavefront of a convergent wave*

We first demonstrated the pulse-front and wavefront measurement with STARFISH characterizing a convergent wave, created by focusing the beam with a 50-cm focal length lens (Fig. 4.16) [3,9]. The test beam was scanned transversely at a propagation distance of 31 cm after the lens, that is, before the focus. The input laser pulses had a duration of 35-fs and the reference pulse was calibrated with the SPIDER device. We scanned 4 mm of the beam profile in $20\mu m$-steps (201 points). The delay between the reference and the test beam was 550 fs. The spatially-resolved spectrum is represented in Fig. 4.16a, which have been integrated to obtain the spatial profile given in Fig. 4.16b. We show the spectral interference trace of the reference and test beam as a function of the wavelength and the transverse position in Fig. 4.16c. The evolution of the fringes with the position is quadratic, in agreement with the curvature of the wavefront and the pulse-front of the test beam. The spatiotemporal intensity reconstruction is shown in Fig. 4.16d, in which the convergence of the beam is observed: the peripheral region of the beam arrives before the central region at a certain propagation distance. We fitted the retrieved pulse-front curvature of the beam (see fit in blue dashed line in the figure) and obtained a value of 18.6 cm for the radius of curvature, in agreement with the expected value of 19 cm, if Gaussian beam propagation is assumed.

Since we used a terawatt laser, the beam profile was inhomogeneous and the pulse energy fluctuated. To remove the energy instability, we have averaged the test beam spectrum taken at each point in the measurements presented in this work. We checked that the spectral phase retrieved was not affected by this instability. The intensity reconstruction showed in Fig. 4.16d exhibits spatial modulations that can be explained in terms of the spatial inhomogeneity of the beam: the modulations are related to those present in the spatial profile: Fig. 4.16a and 4.16b. For further proof, we checked the reproducibility of the beam profile reconstruction (the retrieved profile was invariant for

multiple measurements), thus discarding SI or laser instability as being the origin of the inhomogeneity of the reconstructed profile.

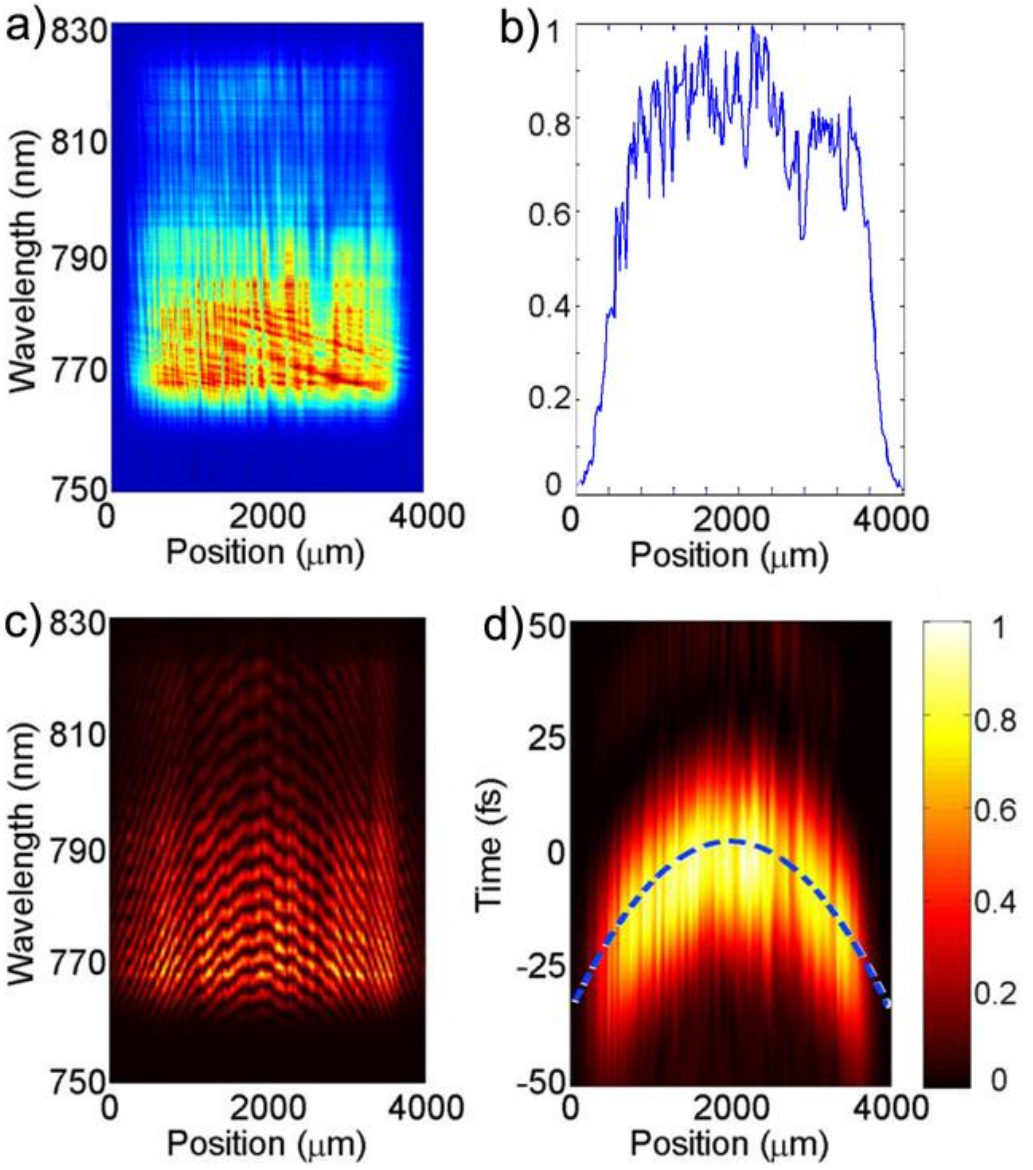


Fig. 4.16. (a) Spatially-resolved spectrum, (b) spatial profile, (c) spatiospectral interference trace and (d) spatiotemporal intensity reconstruction of a convergent wave (experimental, 35-fs pulses). The amplitude of the plots is in linear scale.

Then, we calculated the wavefront for the convergent beam. We retrieved the wavefront in one axis $\phi(x;\lambda=\lambda_j)$ for different wavelengths $\lambda_j$ of the pulse spectrum (see Fig. 4.17a). Note that, to depict each wavelength a different color has been used. The expected phase is quadratic, given by the expression $\phi(x;\lambda=\lambda_j)=-(\pi/\lambda_j R)x^2$. In agreement with the experiment, the shorter wavelengths correspond to the higher curvatures. Then, we calculated the coefficient of the quadratic term of the phase for each wavelength defined as $\kappa(\lambda_j)=-\pi/\lambda_j R$ (see blue solid line in Fig. 4.17b). From the linear regression of the data we obtained a value of $R=-189.8\pm1.7\,mm$, also in good agreement with the expected value ($R=-190\,mm$). The fit is represented as a dashed red line in Fig. 4.17b, where the gray shaded area stands for the uncertainty obtained directly from the fit.

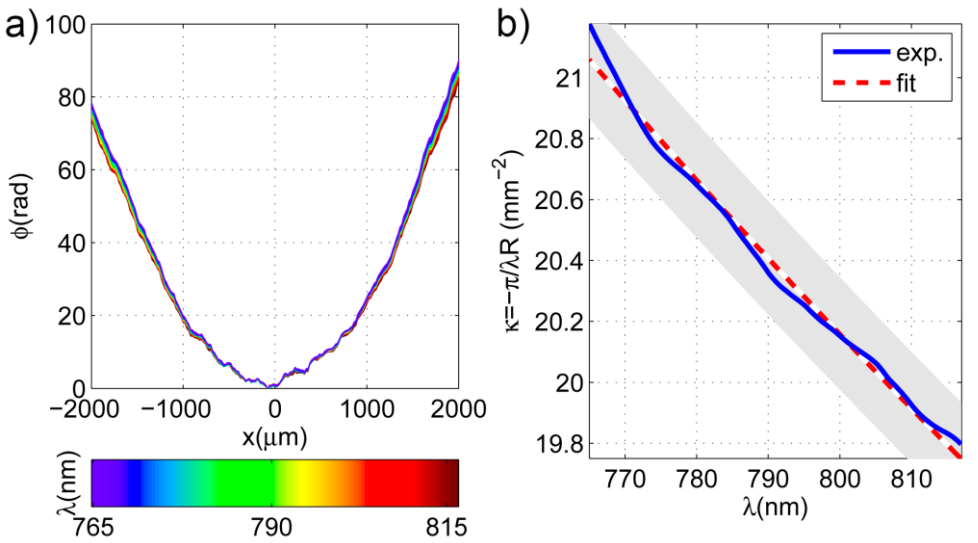


Fig. 4.17. (a) Wavefront as a function of the wavelength for a convergent wave. The wavefront for each wavelength is plotted in the color given by the colorbar. (b) Curvature of the wavefronts (solid blue line) and theoretical value (dashed red line).

### *4.4.3. Long-term high interferometric stability*

The magnitude of the phase fluctuations depends on the particular experimental conditions and the tolerance to those fluctuations of the interferometer also depends on the specific application. For this reason, the stability required for an experiment is not always the same and has to be studied and assured for each case, especially for experiments demanding high-precision. For example, when measuring few-cycle pulses, small pulse-front instabilities (e.g. of the order of a cycle) will be comparable to the pulse duration. The same applies to the wavefront. This led us to look actively for a stabilization of the interferometer. Note that the experiments presented up to now (and those in Chapter 6), were carried out without taking a special care on this.

In order to reduce the phase fluctuations, we firstly improved the mechanical performance of the setup: we used tight mounts and eliminated unnecessary unstable $x$-$y$ micrometric stages. Also, we isolated or switched off the vacuum pumps that were a cause of vibrations. Then, the air-flows were identified as the main source of fluctuations. Finally, we built a box comprising at least the whole interferometer, that is, from the beam splitter to the fiber inputs. At this point, we could observe long-term stability of the spectral fringes: shot-to-shot, the position of the fringes did not change visually. This only happened with the box closed. Even when the air conditioning switched off, the box was mandatory. Since other sources of instability (mainly mechanical) can be present during a spatial scan of STARFISH, we studied the stability during a long-time spatial scan of the pulse.

This experiment was performed with the laser output of a Ti:sapphire laser amplifier (Femtolasers Produktions GmbH) that delivers $25\,fs$ (FWHM of the Fourier-limit) pulses centered at around $800nm$ with a repetition rate of $1kHz$. The study was conducted at the Universidade do Porto (Porto, Portugal). It consisted in measuring the transverse profile of the amplifier across the horizontal axis along a section of $11000\mu m$ using $10\mu m$ steps, which means a sampling of 1101 points. We did the scan

twice and compared the pulse-front retrieved. The full scan took over 30 minutes and this is what we mean by long-term stability. The integration time was set to $2ms$ (the minimum allowed by the spectrometer).

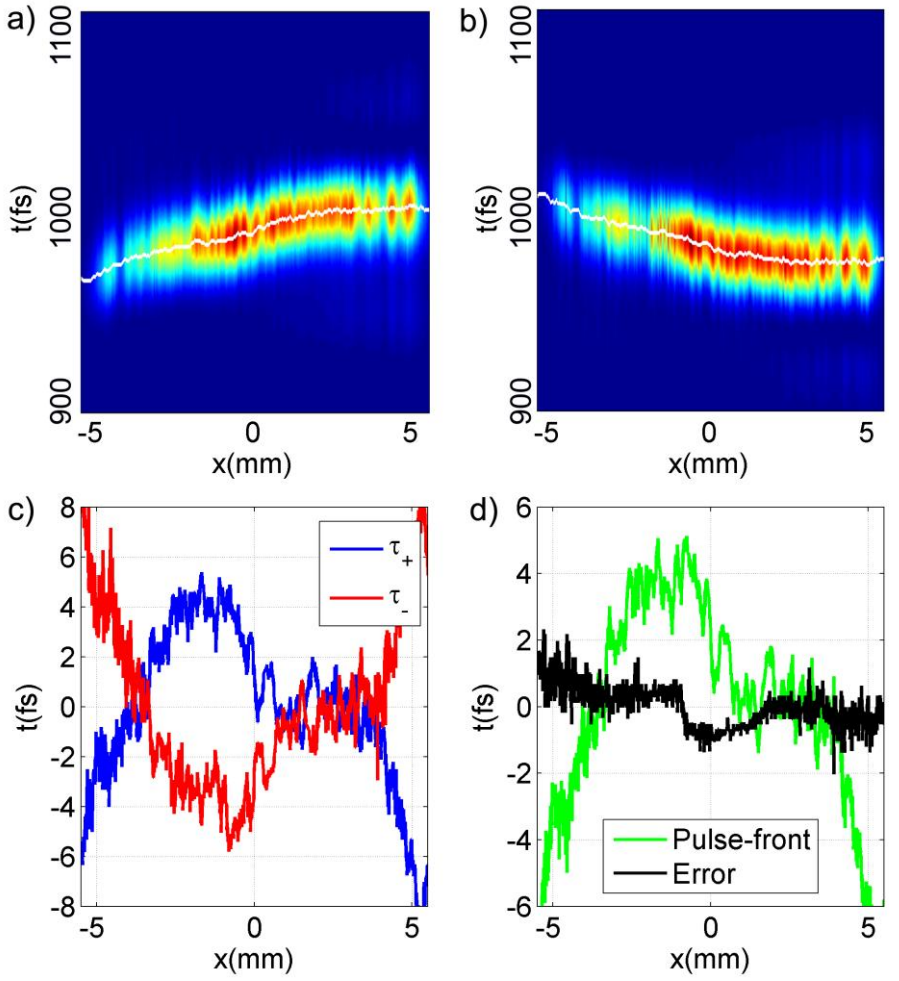


Fig. 4.18. Right-hand side-band peak after inverse Fourier-transform of the interferences, for the reference, (a) before and (b) after, the test pulse. (c) Pulse-front (blue line) and its conjugated (red line). (d). Mean (green line) and error (black line) of the pulse-front.

We did the spatial scan with the reference before the test pulse in the SI (this is the criterion that we usually follow) and with the reference after the test, for which we show the side-band peak of the inverse Fourier-transform of the SI centered at $t=+\tau$ in Fig. 4.18a and 4.18b, respectively. The evolution of the peak with respect to the spatial coordinate for the two cases is conjugated, as expected. The tilt of the side-band peaks is due to a scan not-perfectly transverse to the propagation direction. We assume that the amplified pulses do not present pulse-front tilt. This is consistent ─although not decisive─ with the absence of spatial chirp (typically associated to pulse-front tilt in these systems). Moreover, since we also measured the wavefront, we can obtain the propagation direction and correct the tilt of the scan. To retrieve the pulse-front, we have subtracted the linear tilt of the scan, which corresponds to a tilt of $35\,fs$ over the full spatial scan of $11\,mm$.

In Fig. 4.18c, we show the pulse-front (blue line) and its conjugated (red line) obtained for the case of reference before and after the test, respectively. By comparing

the two retrievals we can calculate their mean (green line) and the error associated to the measurement (black line), as shown in Fig 4.18d. Despite not being perfectly flat, the pulse-front structure is contained inside a $2\lambda$ deviation (excluding the tails of the spatial profile). It is clear that the two retrievals are quite similar and from the error curve that the pulse-front fluctuation is below $\pm 1 fs$ ($\sim 0.4\lambda$) for the long-term scan. Of course, faster acquisitions will present smaller fluctuations. In particular, using an ultrafast oscillator, we have achieved routinely (with the box closed) phase fluctuations below $\pm 0.06 rad$ ($\sim 0.01\lambda$) for 59 acquisitions during a total time of $20s$ with the test fiber fixed (that is, without spatially scanning). For the latter case, we show the spectral phase variation during the acquisition for three different wavelengths (Fig 4.19).

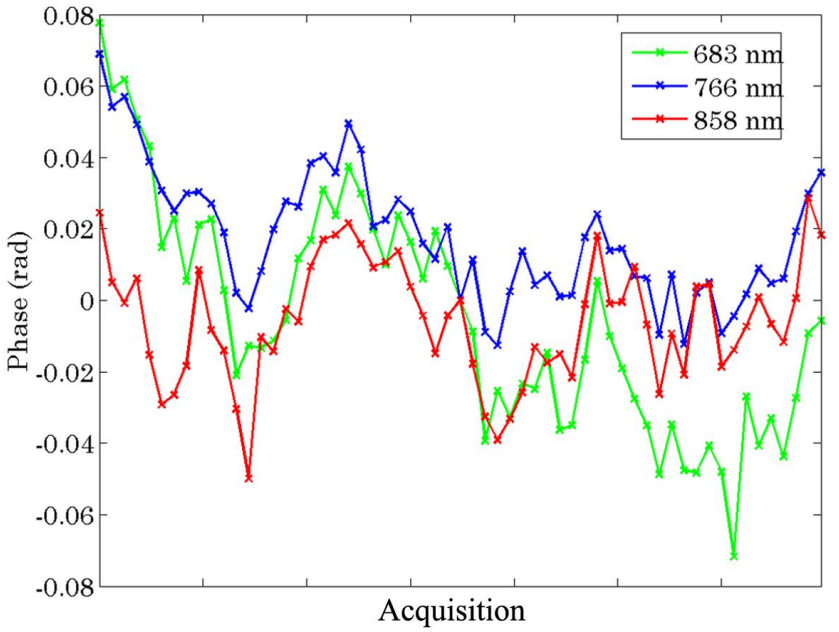


Fig. 4.19. Spectral phase variation during the acquisition for three different wavelengths.

These results are valuable, since they demonstrate that the phase fluctuations can be reduced to negligible values, preventing unacceptable errors in the measurements. The achievement is relevant for measurements of the wavefront, for few-cycle pulses and in general for phase measurements with SI. Also, in the case of measurements of the 2D spatial plane (x-y plane) the scans will take longer and a good stability is required.

## 4.5. Conclusions

We have proposed an innovative scheme for the spatiotemporal characterization of ultrashort laser pulses based on a fiber-optic coupler interferometer (STARFISH). The device has the advantages of its being alignment-free, its use of only one reference, and its simplicity: only a fiber coupler and a standard spectrometer are necessary. The optical elements are commercial and connected in a plug-and-play basis. The extension to other ranges of wavelengths just goes through the use of the appropriate elements and reference characterization. For example, an especially designed beam splitter will be required for the measurement of ultra-broadband pulses. The time direction is determined with this technique whenever it is known for the reference characterization, as in our case.

We have analyzed in detail the characteristics of the fiber coupler and have studied the applicability to the measurement of non-collimated beams (with $NA > 0$), to focused pulses and to ultra-broadband few-cycle pulses. We can conclude that the pulse measurement is limited to pulses of $NA \sim 0.1$. The spatial resolution of $\sim 4\mu m$ allows us to resolve pulse foci of diameter $\sim 10\mu m$ with a low relative error. In principle, the operating bandwidth of the coupler is limited to 550-1000 nm, and will depend on the pulse waveform, which allows us to measure pulses with a Fourier-transform limit $\sim 4\,fs$.

We have shown STARFISH to measure 1.3-ps long ($1/e^2$ width) negatively chirped pulses. According to the simulations, it could measure 1-ps FWHM unchirped pulses or, in the case of broadband chirped pulses, even longer ones. Moreover, the use of better resolution spectrometers would allow the measurement of much longer pulses, conserving the advantages of the fiber coupler since it is only necessary to connect the fiber output to the new spectrometer entrance. We applied the STARFISH not only to the characterization of a converging beam but also to more complex structures, such as measurement of the spatiotemporal interference of plane-plane and spherical-plane waves, with the results obtained being in agreement with the simulations. We reconstructed laser beams using two laser systems with different pulse durations (35 and 120 fs) and spectral bandwidths. We demonstrated the ability of our method to reconstruct complex pulses despite working with terawatt lasers, which are less stable, more inhomogeneous, and have lower repetition rate in benefit of higher pulse energy, and their characterization therefore being more difficult.

Finally, we have demonstrated the capabilities of the system to measure the pulse-front and the frequency-resolved wavefront. We have fixed the instability sources to overcome the phase fluctuations typically present in interferometric setups.

All these characteristics and results will allow us to apply STARFISH to many different situations. In the next chapters, we will present its applications to several experiments involving diffractive optics, nonlinear optics and few-cycle pulses. In the future, we expect a growing number of applications of the technique thanks to its simplicity and versatility.

## References

[1] P. Bowlan, P. Gabolde, and R. Trebino, "Directly measuring the spatiotemporal electric field of focusing ultrashort pulses," Opt. Express 15, 10219-10230 (2007).

[2] E. Rubino, D. Faccio, L. Tartara, P. K. Bates, O. Chalus, M. Clerici, F. Bonaretti, J. Biegert, and P. Di Trapani, "Spatiotemporal amplitude and phase retrieval of space-time coupled ultrashort pulses using the Shackled-FROG technique," Opt. Lett. 34, 3854-3856 (2009).

[3] B. Alonso, I. J. Sola, O. Varela, J. Hernández-Toro, C. Méndez, J. San Román, A. Zaïr, and L. Roso, "Spatiotemporal amplitude-and-phase reconstruction by Fourier-transform of interference spectra of high-complex-beams," J. Opt. Soc. Am. B. 27, 933-940 (2010).

[4] L. Lepetit, G. Cheriaux, and M. Joffre, "Linear techniques of phase measurement by femtosecond spectral interferometry for applications in spectroscopy," J. Opt. Soc. Am. B 12, 2467-74 (1995).

[5] Keigo Iizuka, Chapter 13: "Fiber Optical Communication" in *Engineering optics*, Springer Series in Optical Sciences, Springer (2008).

[6] Carlos Feio Gama Alegria, *All-Fibre Devices for WDM Optical Communications*, Ph.D. Thesis, University of Southampton (2001).

[7] J. M. Schmitt, "Optical coherence tomography (OCT): a review," IEEE Journal of Selected Topics in Quantum Electronics 5, 1205 (1999).

[8] B. Alonso, M. Miranda, I. J. Sola, and H. Crespo, "Spatiotemporal characterization of few-cycle laser pulses," Opt. Express, 20, 17880-17893 (2012).

[9] B. Alonso, R. Borrego-Varillas, O. Mendoza-Yero, I. J. Sola, J. San Román, G. Mínguez-Vega, and L. Roso, "Frequency resolved wavefront retrieval and dynamics of diffractive focused ultrashort pulses," J. Opt. Soc. Am. B 29, 1993-2000 (2012).

[10] B. Alonso, M. Miranda, F. Silva, V. Pervak, J. Rauschenberger, J. San Román, I. J. Sola, and H. Crespo, "Generation and spatiotemporal characterization of 4.5-fs pulses from a hollow-core fiber compressor," submitted (2012).

[11] O. Mendoza-Yero, B. Alonso, O. Varela, G. Mínguez-Vega, I. J. Sola, J. Lancis, V. Climent, and L. Roso, "Spatiotemporal characterization of ultrashort pulses diffracted by circularly symmetric hard-edge apertures: theory and experiment," Opt. Express 18, 20900–20911 (2010).

[12] O. Mendoza-Yero, B. Alonso, G. Mínguez-Vega, I. J. Sola, J. Lancis, and J. A. Monsoriu, "Synthesis of fractal light pulses by quasi-direct space-to-time pulse shaping," Opt. Lett. 37, 1145-1147 (2012).

[13] P. Bowlan, U. Fuchs, R. Trebino, and U. D. Zeitner, "Measuring the spatiotemporal electric field of tightly focused ultrashort pulses with sub-micron spatial resolution," Opt. Express 16, 13663-13675 (2008).

[14] Anthony E. Siegman, Chapter 17: "Physical properties of Gaussian beams" in *Lasers*, University Science Books (1986).

[15] J. Paye and A. Migus, "Space-time Wigner functions and their application to the analysis of a pulse shaper," J. Opt. Soc. Am. B 12, 1480-1490 (1995).

[16] E. Kim, H. Kim and J. Noh, "Measurement of the Spatial Wigner Distribution Function of Laser Light by Using a Sagnac Interferometer," J. Korean Phys. Soc. 46, 1342-1346 (2005).

[17] P. O'Shea, M. Kimmel, X. Gu, and R. Trebino, "Highly simplified device for ultrashort-pulse measurement," Opt. Lett. 26, 932-934 (2001).

[18] C. Iaconis and I. A. Walmsley, "Spectral phase interferometry for direct electric-field reconstruction of ultrashort optical pulses," Opt. Lett. 23, 792-794 (1998).

[19] E. B. Treacy, "Optical pulse compression with diffraction gratings," IEEE J. Quantum Electron. 5, 454–458 (1969).

[20] P. Bowlan and R. Trebino, "Using phase diversity for the measurement of the complete spatiotemporal electric field of ultrashort laser pulses," J. Opt. Soc. Am. B 29, 244-248 (2012).

# CHAPTER 5

# DIFFRACTION OF ULTRASHORT LASER PULSES BY A ZONE PLATE

**Contents**



*Some of the results in this chapter were originally presented in O. Mendoza-Yero et al., Opt. Express 18, 20900-20911 (2010).*

## 5.1. Interest and applications

Part II of this thesis is devoted to present the main results of the application of STARFISH to the field of diffractive optics, which has been carried out thanks to an intense collaboration with the Grup de Recerca d'Òptica de Castelló (GROC) of the Universitat Jaume I (UJI), Castellón, Spain. In addition, the numerical simulations presented in Chapters 5 and 7 were performed by researchers from the GROC-UJI.

Diffractive optical elements (DOEs) essentially consist of amplitude or phase masks that are designed to diffract the pulses in a desired way depending on their application. For example, Fresnel zone plates (binary amplitude concentric rings) can be used to focus a beam using diffraction [1], as an alternative to conventional lenses or curved mirrors based on refraction and reflection, respectively. In the same way, phase lenses known as kinoform diffractive lenses can also be used to focus the pulse with more efficiency than amplitude zone plates [2,3]. A broad theoretical background has been developed for the applications of DOEs, in particular for the manipulation of (broadband) ultrashort pulses [4-8], which is our field of interest. On the experimental side, the theory has been corroborated by measurements of the on-axis spectrum [9], or just by a spatial image of the profile. This point was limited by the possibilities of the characterization techniques. The temporal properties of the pulses have already been studied theoretically [10]. However, the pulses diffracted by DOEs often exhibit a strong spatiotemporal coupling and complex spatiospectral features that are relevant for the applications and require full characterization methods [4,5,11,12]. Nowadays, the development of spatiotemporal reconstruction techniques allows us to perform such characterization [13,14]. In Chapters 5, 6 and 7, we will present different applications of the technique STARFISH [14] (already detailed in Chapter 4) to the spatiotemporal measurement of the field diffracted by DOEs in linear regime.

The use of DOEs is widespread for applications both in linear and nonlinear regime. We will present how these elements can be designed to manipulate the electric field of ultrashort laser pulses and achieve the desired pulse shapes in the experiment [15-17]. For example, ultrashort laser pulse shaping [18-20] is of interest e.g. to control laser assisted chemical reactions [21,22] or to coherent quantum control of two-photon transitions [23]. Moreover, diffractive pulse shaping can be applied to pulses in different wavelengths, including X-rays [24,25] or the UV, which has interest in molecular processes [26]. DOEs have also been shown to tailor processes as second harmonic generation [27,28], supercontinuum generation [29], filamentation [30], high-harmonic generation [31] and many others. Recently, a diffraction-based dispersion compensating module has been experimentally applied to avoid the spatiotemporal spreading of the multiple foci generated by a diffraction grating [32].

In this chapter, the pulses will be analyzed after a zone plate consisting of several binary amplitude concentric rings. We will present the analytical expressions derived for the numerical simulations and then the experimental and theoretical results will be compared. We will show the results for the foci in the three regions after the DOE,

namely the near-field, Fresnel and far-field regions, and will also discuss the implications of the numerical aperture of the pulses and the detection [11].

## 5.2. Theory: analytical model

The numerical simulation of diffraction is in general computationally demanding. Here, we will introduce the derivation of the analytical expressions used to simulate the field diffracted by a circularly symmetric hard-edge aperture, for which the Rayleigh-Sommerfeld formulation of the diffraction has been considered. With this approach, the diffracted field can be fast and accurately described both in the spatiospectral and spatiotemporal domains. The full details of the derivation can be found in [11]. Both the model and the numerical simulations have been proposed and carried out by the group of the UJI (Castellón, Spain). We will validate the theoretical model by comparison with the experimental results.

We consider an ultrashort laser pulse and spatial plane wave illuminating the plate. Since there is cylindrical symmetry, we will use the polar coordinates $r,\theta$ in the plane of the aperture ─the input plane─ and $R,\phi$ in the observation plane at a propagation distance $z$. To work with broadband pulses, the diffracted field for each frequency component of the pulse spectrum will be calculated and then recomposed after the DOE.

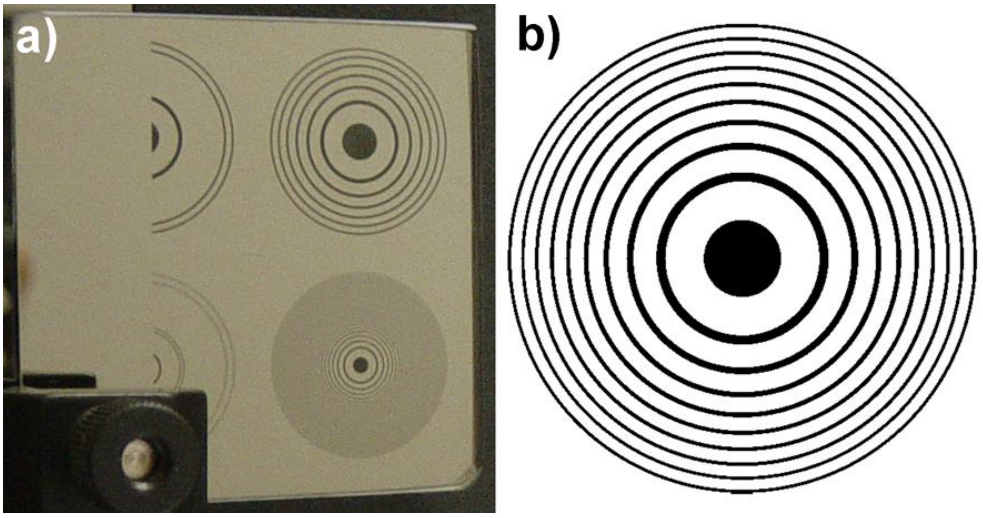


Fig. 5.1. (a) Picture of different diffractive optical elements registered in a quartz plate. (b) Example of a zone plate consisting of several amplitude concentric rings. The light after the plate is diffracted according to the distribution of the rings.

The aperture consists of $N$ transparent rings as shown in Fig. 5.1. The first Rayleigh-Sommerfeld diffraction integral gives an approximate analytical expression [9] for the field diffracted from the edge of the $m$-th ring that can be calculated as $U_m(z,R,\omega) \approx U_{im}(z,R,\omega) - U_{om}(z,R,\omega)$, where

$$U_{im/om}(z,R,\omega) = \frac{z \exp\left( i \frac{\omega}{c} \sqrt{z^2 + r_{im/om}^2} \right) J_0\left( \frac{\omega}{c} \frac{r_{im/om} R}{\sqrt{z^2 + r_{im/om}^2}} \right)}{\sqrt{z^2 + r_{im/om}^2}} \qquad (5.1)$$

and $r_{im}$ and $r_{om}$ are respectively the inner and outer radii of the $m$-th transparent ring, $c$ is the speed of light, $\omega$ is a frequency component of the pulse, and $J_0$ denotes the

Bessel function of the first kind of zero order. The Eq. 5.1 is a valid approximation in the vicinity of the propagation axis (several hundreds of microns) and it is exact on-axis, which allows us to determine the field at the different foci of the DOE. The total diffracted field for the frequency $\omega$ is calculated as the sum of the contributions from each transparent ring, that is, $U(z,R,\omega)=\sum_{m=1}^{N}U_m(z,R,\omega)$.

In order to calculate the spatiospectral distribution of the electric field $E_f(z,R,\omega)$, the expression for $U(z,R,\omega)$ has to be modified by the amplitude and phase of the input pulse in spectral domain, called $E_{f,in}(\omega)$. The input pulse $E_{f,in}(\omega)$ can be expressed in the temporal domain as $E_{t,in}(t)=\mathcal{F}^{-1}\{E_{f,in}(\omega)\}$. After the inverse Fourier-transform ($\mathcal{F}^{-1}$) of the pulse, one can obtain its spatiotemporal amplitude and phase

$$E_t(z,R,t)=\mathcal{F}^{-1}\{E_{f,in}(\omega)U(z,R,\omega)\} \tag{5.2}$$

From Eq. 5.2, the spatiotemporal field can be expressed as

$$E_t(z,R,t)=\sum_{m=1}^{N}\{F_{im}(z,R,t)-F_{om}(z,R,t)\}, \tag{5.3}$$

where the function $F_{im/om}(z,R,t)$ is given by the approximate analytical relation

$$F_{im/om}(z,R,t)\simeq\frac{z}{\sqrt{z^2+r_{im/om}^2}}\frac{1}{2\pi}\int_0^{2\pi}E_{t,in}\left(t-\frac{\sqrt{z^2+r_{im/om}^2}}{c}+\frac{r_{im/om}R\cos\theta}{c\sqrt{z^2+r_{im/om}^2}}\right)d\theta. \tag{5.4}$$

This expression is valid for points in the vicinity of the propagation axis, as it is corroborated at least up to a distance from the axis of $200\mu m$ by means of the agreement in the comparison between experiments and simulations. Since the paraxial approximation has not been considered, the expression is valid from near to far field. From the Eq. 5.3, the field $E_t(z,R,t)$ can be interpreted as the sum of the $2N$ boundary waves coming from the edges of the transparent rings. If we observe on-axis ($R=0$), it follows that these waves do not arrive at the same time, but with a propagation time $(z^2+r_{im/om}^2)^{1/2}/c$, which will account for the train of pulses observed in the near-field and Fresnel region. This arrival time comes directly from doing the $\mathcal{F}^{-1}$ of the exponential function in Eq. 5.1. In the case of off-axis points ($R\neq 0$), this arrival time is corrected up- or downwards by a term including the cosine of the azimuthal angle $\theta$ that covers the contribution of the whole input plane.

In the specific case of a Gaussian input pulse in temporal domain, it is given by the expression $E_{t,in}(t)=\exp\{-i\omega_0 t\}\exp\{-t^2/4\sigma^2\}$, where $\omega_0$ is the carrier frequency and $\sigma$ is the standard deviation width. The width $\sigma$ is related to the intensity FWHM (full-width at half maximum) of the pulse through the equation $\sigma=FWHM\Big/\left(2\sqrt{2\ln 2}\right)$. To fit the experimental parameters, we consider $\lambda_0=2\pi c/\omega_0=795nm$ and the pulse duration of FWHM = 30 fs. Substituting $E_{t,in}(t)$ in Eq. 5.4 gives

$$F_{im/om}(z,R,t)\simeq\frac{z\exp\left\{-i\omega_0\left(t-\frac{s_{im/om}}{c}\right)\right\}}{s_{im/om}}\exp\left\{-\frac{\left(t-\frac{s_{im/om}}{c}\right)^2}{4\sigma^2}\right\}J_0\left(\omega_0\frac{r_{im/om}R}{c\,s_{im/om}}\right), \tag{5.5}$$

where we define $s_{im/om} = \sqrt{z^2 + r_{im/om}^2}$. The approximation $1 + z^2 / r_{im/om}^2 >> R / r_{im/om} \cos\theta$ has been considered, which is consistent with our restriction of observation close to the propagation axis.

The rings of the DOE shown in Fig. 5.1 are periodic in the squared radial coordinate. The inner and outer radii of the rings are given by $r_{im} = [p(m-1)]^{1/2}$ and $r_{om} = [p(m-(1-1/\varepsilon))]^{1/2}$, respectively. If $\varepsilon = 2$ the areas of the opaque and transparent regions are equal, and this is the case of the Fresnel zone plate. In our case, the DOE parameters are $N = 10$, $\varepsilon = 2$ and $p = 3.2\,mm^2$. The parameter $p$ is related to the area of the rings, which is a constant given by $\pi(r_{om}^2 - r_{im}^2) = \pi p / \varepsilon = 2.51 mm^2$.

The parameters of the DOE define the difference of arrival time of the boundary waves —coming from the $2N$ hard edges— at a certain propagation distance $z$. There are two time differences: a) the difference between the edges of a ring $\Delta t_1$, and b) the difference between two neighboring apertures $\Delta t_2$. As the propagation distance increases, the time differences are reduced, which will define three regions with different behaviors: near-field, Fresnel and far-field region. In the near-field. the times $\Delta t_1$ and $\Delta t_2$ are larger than the pulse duration, so a train of pulses with sub-structure (double pulse due to the two edges of the ring) is observed. In the Fresnel region, the sub-structure is lost, whereas the train of pulses (coming from the N rings) is still present, since $\Delta t_2$ is larger than the pulse duration. Finally, in the far-field region all the boundary waves merge into a longer pulse, in which the sub-structure cannot be resolved in time. Following the criterion that each time difference has to be $\Delta t \geq 2\sigma$ in order to be resolved, the location of the regions in the longitudinal axis is: $z < 52.3 mm$ (near-field region), $52.3 mm \leq z \leq 157.0 mm$ (Fresnel region) and $z > 157.0 mm$ (far-field region) [11].In fact, the change of behavior between the frontiers of the regions will be gradual.

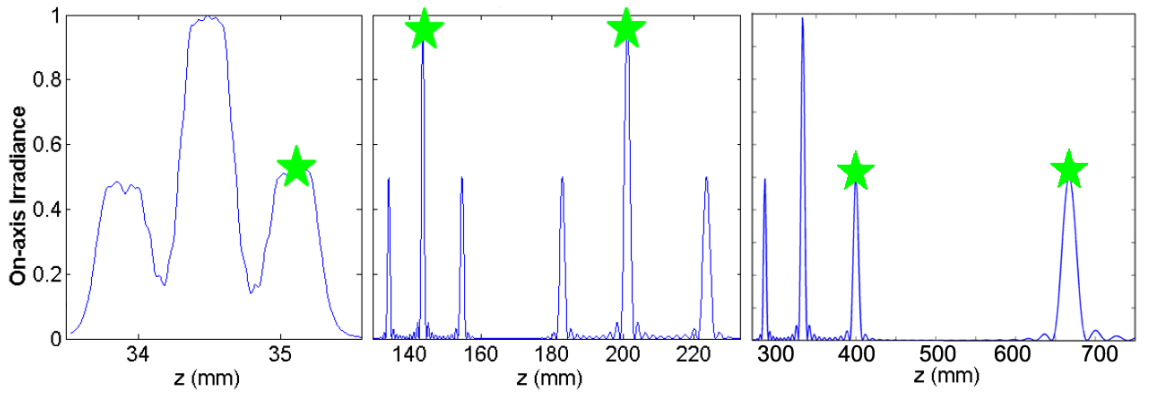


Fig. 5.2. Simulated on-axis irradiance pattern of the DOE for the central wavelength of the pulse. The green stars correspond approximately to the positions of the spatiotemporal reconstructed planes at z=35mm, z=141mm, z=203mm, z=405mm, and z=660mm shown in the next section, respectively.

The light diffracted by the DOE presents multiple foci along its propagation. We used the on-axis irradiance to analyze these foci. Although the exact distribution can be calculated by computing $\int_0^\infty |E_{f,in}(\omega) U(z, R=0, \omega)|^2 d\omega$, the estimation through the monochromatic wave case $\omega = \omega_0$ is a good evaluation of the distribution of such foci. Figure 5.2 shows different ranges of the theoretical on-axis irradiance, contained within

the near-field, Fresnel and far-field regions, respectively. Firstly, we performed the study of the spatiotemporal structure of three foci for propagation distances (namely, z = 35, 141 and 203 mm) corresponding to each one of the different regions. Then, we analyzed two subsequent planes in the far-field region, for z = 405 mm and z = 660 mm, respectively. The positions of these planes are highlighted in Fig. 5.2.

## 5.3. Spatiotemporal results on the foci

### *5.3.1. Experimental setup*

The experiments were carried out using a Ti:sapphire CPA laser (Amplitude Technologies) that delivers 30 fs (FWHM) pulses centered at 795 nm. In order to work in linear regime, we reduced the energy per pulse below 100 $\mu J$ by means of a variable attenuator. The pulse was spatiotemporally characterized at different propagation distances by means of STARFISH [14] (see Chapter 4).

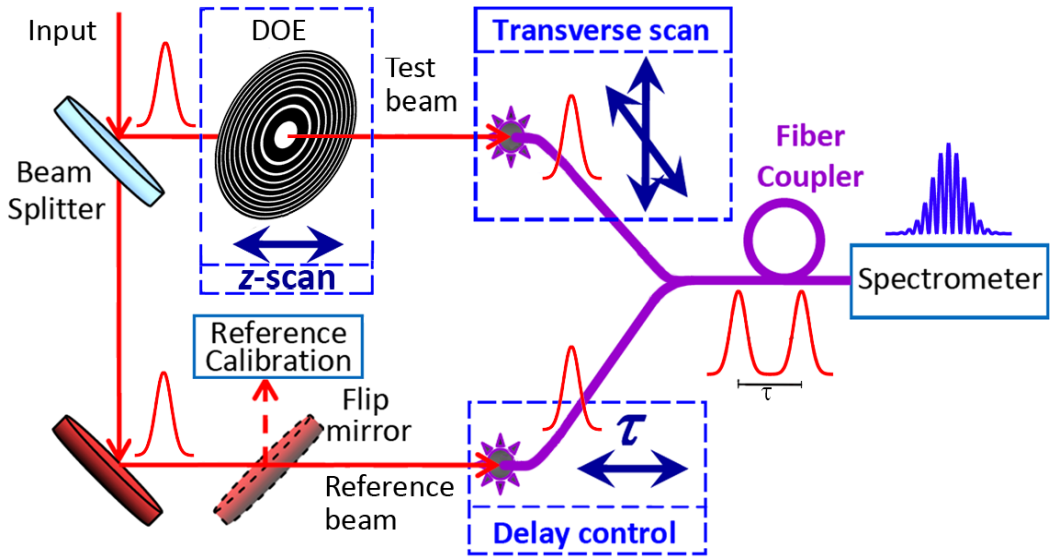


Fig. 5.3. Experimental setup: the beam is divided into two replicas, one part acting as the reference, whereas the replica illuminating the DOE acts as the test. The pulses are recombined inside the fiber optic coupler that also spatially scans the test pulse. The spectral interferences are recorded in the spectrometer.

The experimental setup is depicted in Fig. 5.3, and is the same setup than in other experiments. In this case, the DOE was translated along the optical axis of the system to allow us to observe different propagation distances and therefore different regions. We used a standard spectrometer with resolution of 0.1 nm (Avantes Inc.). The reference was calibrated by using a SPIDER (APE GmbH). For the present conditions, a delay of between 2 and 3 ps was used. Since the system presents cylindrical symmetry, we spatially scanned only one axis. The technique consists in measuring the spatially-resolved spectral interferometry and to apply Fourier-analysis [33] to the fringes in order to obtain the relative phase of the diffracted pulse with respect to a known reference pulse.

The spectrum of the experimental input pulses is given in Fig. 5.4a, which clearly differs from a Gaussian spectrum assumed in the analytical model. Also, the spatial

profile is not a plane wave, but more similar to a supergaussian function, although not being flat in the plateau, what is clear in the spatially-resolved spectrum (Fig. 5.4b). This spatial dependence present in our laser system is characteristic of amplified pulses delivered from CPA laser systems.

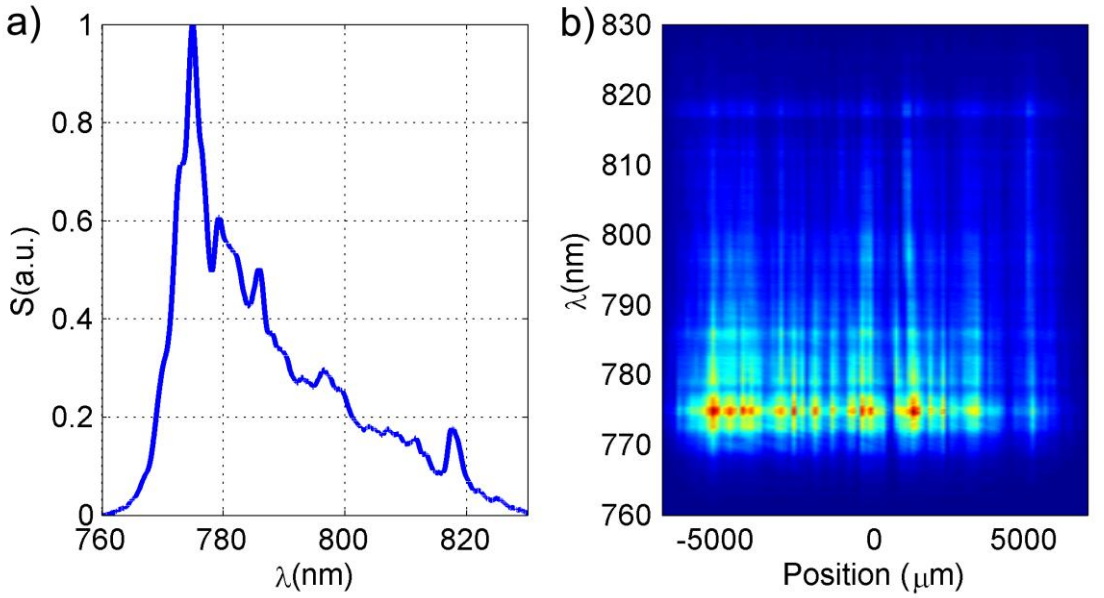


Fig. 5.4. Experimental (a) normalized input power spectral density and (b) input spatially-resolved spectrum.

### *5.3.2. Near-field, Fresnel and far-field region comparison*

In Figs. 5.6 to 5.9, the experimental results are shown and compared with the theoretical (analytical) simulations, corresponding to propagation distances 35, 141, 203, 405 and 660 mm. In all cases, the theoretical simulations of spatially resolved spectra are shown in subfigures (a), while the spatiotemporal structure of the pulses is shown in subfigures (b). These figures are compared with the corresponding experimental results given in subfigures (c) for experimental spatially resolved spectra, and in subfigures (d) for experimental time evolution of the pulses.

In particular, the spatiotemporal structure for the axial position z = 35 mm (near-field region) after the DOE is shown in Fig. 5.5. There is a very structured spectrum, presenting some sharp peaks (Fig. 5.5a). Its dependence on the transverse coordinate corresponds to a complex spatiotemporal distribution of the beam. In the spatiotemporal domain (Fig. 5.5b), a train of double pulses appears. The double pulse peaks are slightly separated (27 fs) and distinguished from the theoretical simulation (see inset in Fig. 5.5b, a zoom on the temporal intensity on-axis, for $x = 0$), and have an intensity FHWM of approximately 65 fs. Off-axis ($x \neq 0$), the double pulse structures are spatially separated and can be distinguished better. The 10 double pulses of the train are separated by 150 fs approximately. As mentioned at the end of Section 5.2, this is the expected behavior in the near field region. In the experiment, certain pairs of pulses are poorly visible and sometimes do not appear.

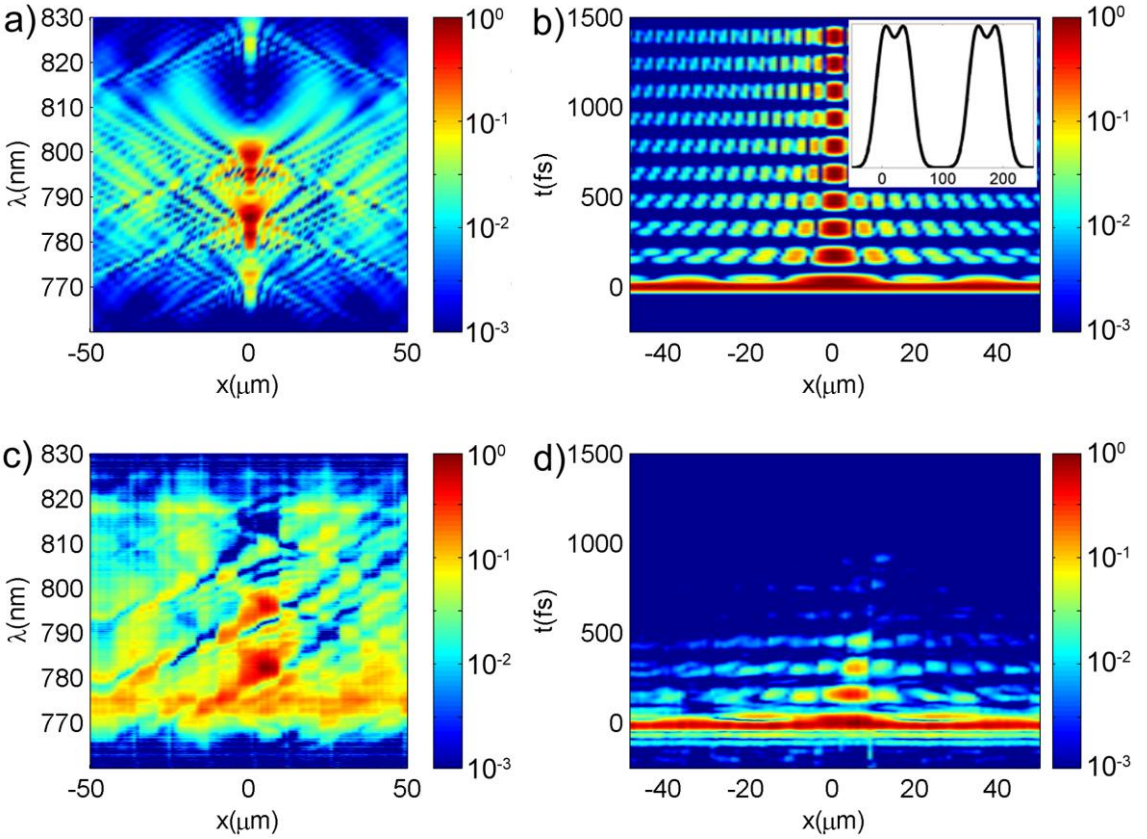


Fig. 5.5. Normalized simulated and experimental spatially resolved spectrum (a, c), and corresponding spatiotemporal intensity (b, d) for the propagation distance z=35mm in logarithmic scale. (b) Inset: Zoom of the temporal intensity on-axis showing the first two double pulses of the train.

The measurement at the plane z = 35 mm, which is very close to the DOE, poses some difficulties to be accomplished because of the low diffraction energy at the given focus and its small spatial width. In addition, it presents another problem: the numerical aperture ( *NA*) of the optical fiber limits the coupling of the light for tight-focusing conditions. In this case, taking into account the *NA* provided by the fiber's manufacturer ( $NA = 0.11 \pm 0.01$) and the design parameters of the DOE, it can be shown that the number of rings allowed by the NA condition is between 4 (for $NA = 0.10$) and 6 ( $NA = 0.12$). Accordingly, Fig. 5.5d clearly shows four axial pairs of pulses. Therefore, in the particular conditions given at the plane z = 35 mm, our measurement does not have enough *NA* to collect all pulses within the train. Note that those pulses propagating at angles larger than the *NA* of the fiber do not appear in Fig. 5.5d. Despite the abovementioned problem, it is possible to observe a reasonable good agreement between theory and experiment in the forward part of the spatiotemporal structure. Other discrepancies may arise from the assumption of plane-wave illumination and the use of an ideal Gaussian spectral distribution in the simulations. The inclusion of a Gaussian illumination or the experimental pulsed light spectrum into the theoretical model implies numerical calculus and therefore, no longer analytical solutions. In fact, as it has been shown in Fig. 5.4, the experimental input conditions do not correspond to a Gaussian spectrum or a spatial plane wave.

In Fig. 5.6, the complex structure observed in Fig. 5.5 remains when the focus at position z = 141 mm is analyzed. The measurements are very symmetric with respect to the center in the spatial scan. The spatially resolved theoretical and experimental spectra in Fig. 5.6a and 5.6c, respectively, show a maximum located within $10\mu m$ around the optical axis. The off-axis spectral contribution appears in a structured way. This is translated to the spatiotemporal field as a complex distribution (Fig. 5.6b, theoretical and 5.6d, experimental), presenting a train of 10 pulses (one per ring of the mask) of about 16 fs intensity FWHM and 38 fs from peak to peak. Note that in the Fresnel region the double pulse structure has disappeared from the pulses of the train. Off-axis, the different pulses forming the train after the main peak front exhibit a divergent structure. The agreement between simulation and theory is remarkable.

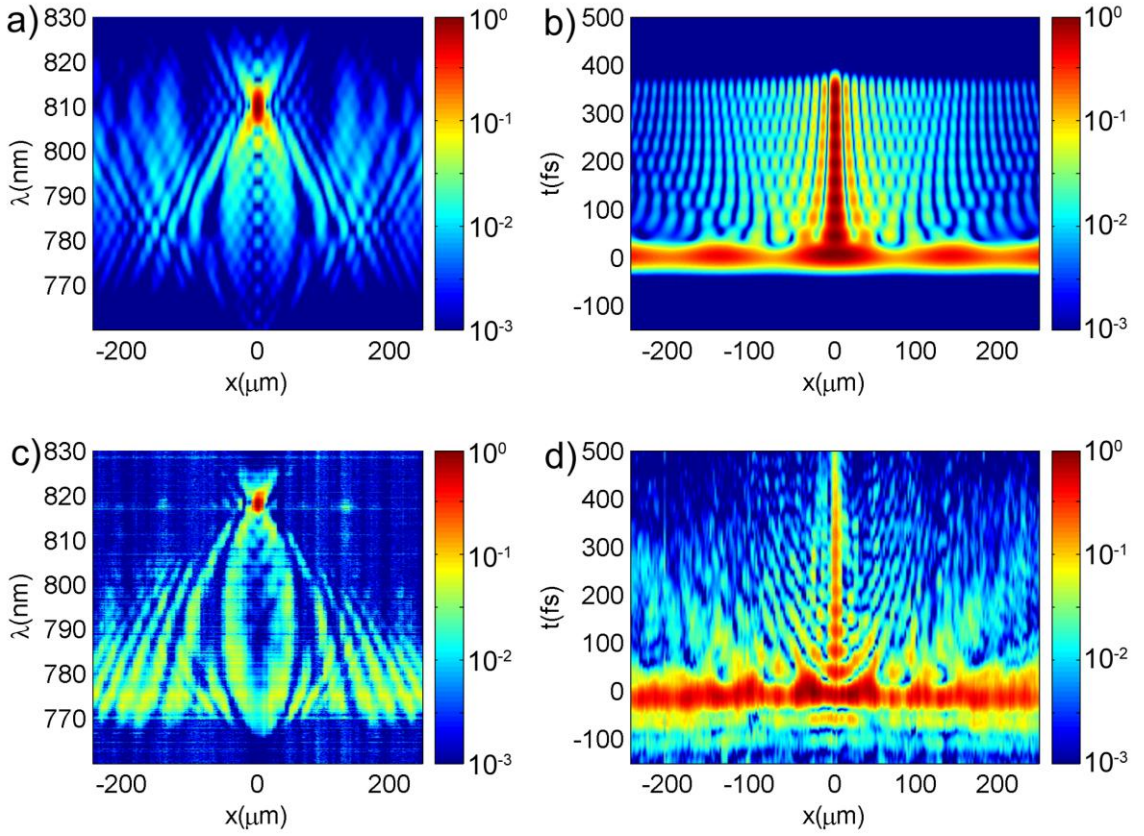


Fig. 5.6. Normalized simulated and experimental spatially resolved spectrum (a, c), corresponding spatiotemporal intensity (b, d) for the propagation distance z=141mm in logarithmic scale.

The characteristics of the pulse at the plane z = 203 mm are shown in Fig. 5.7. Here, some features observed for the plane z = 141 mm remain, while important differences appear. In the spatiospectral domain, a main central peak and the wings are still observed presenting x-shape, as seen in Fig. 5.7a and 5.7c. In the spatiotemporal domain shown in Fig. 5.7b and 5.7d, the pulses from the former train (see the corresponding plot in Fig. 5.5 and 5.6) now merge into a broad central pulse of 250 fs intensity FWHM, shorter than the former pulse train, but longer than the input pulse. This is the behavior expected in the far-field region, where the arrival time differences from the edges of the rings have decreased and are not sufficient to resolve in time the

boundary waves. Off-axis, it is possible to see a wing structure, still preserving a train pulse structure. This behavior is caused by the lower angle of the light converging to this longer focus, since the time difference between the central and outermost rings of the DOE is reduced.

Here, it should be pointed out that the spatiotemporal and spatiospectral focusing dynamics of DOEs is very rich. Depending on the region of observation, in the time domain it is possible to find a train of pulses with and without sub-structure, or a broadened pulse. In the spectral domain, spectral shaping is possible, and the focusing wavelength can be switched (by adjusting the plane of observation) within the spectral bandwidth of the input ultrashort pulse. This is very promising for applications in which temporal or spectral shaping is required. The theoretical simulations, in conjunction with the experimental diagnosis of STARFISH, predict and show this behavior.

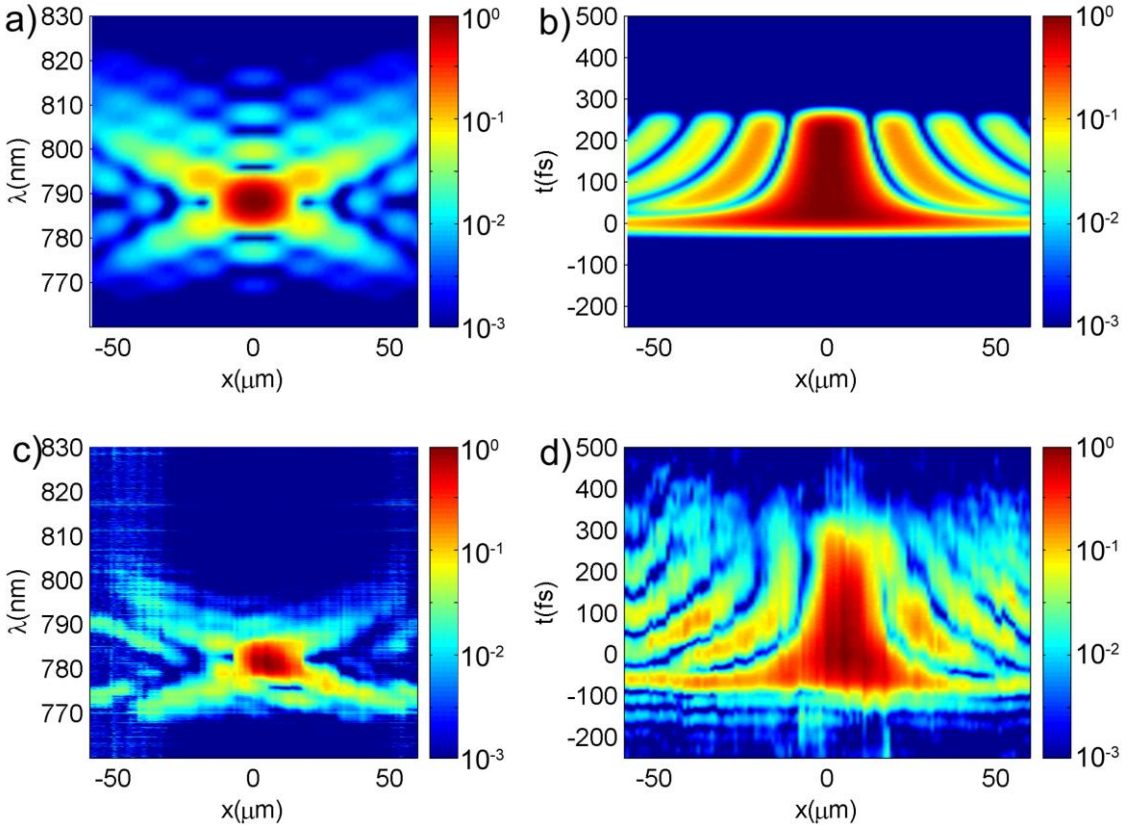


Fig. 5.7. Normalized simulated and experimental spatially resolved spectrum (a, c), corresponding spatiotemporal intensity (b, d) for the propagation distance z=203mm in logarithmic scale.

As the propagation distance increases inside the far-field region, the main structure of the focused pulses is preserved. We analyzed two additional foci of the DOE, the first of them at the propagation distance z = 405 mm. The spatially resolved spectrum (Fig. 5.8a and 5.8c) shows the x-shape already present for z = 203 mm. In the spatiotemporal intensity, the broadened pulse in the center of the spatial profile (x=0), surrounded by modulated wings, is also observed. In this case, the global temporal duration is reduced since the arrival time differences are smaller owing to the larger value of $z$. As expected for a longer focus, the focus width in the spatial domain is larger than for the case previously presented.

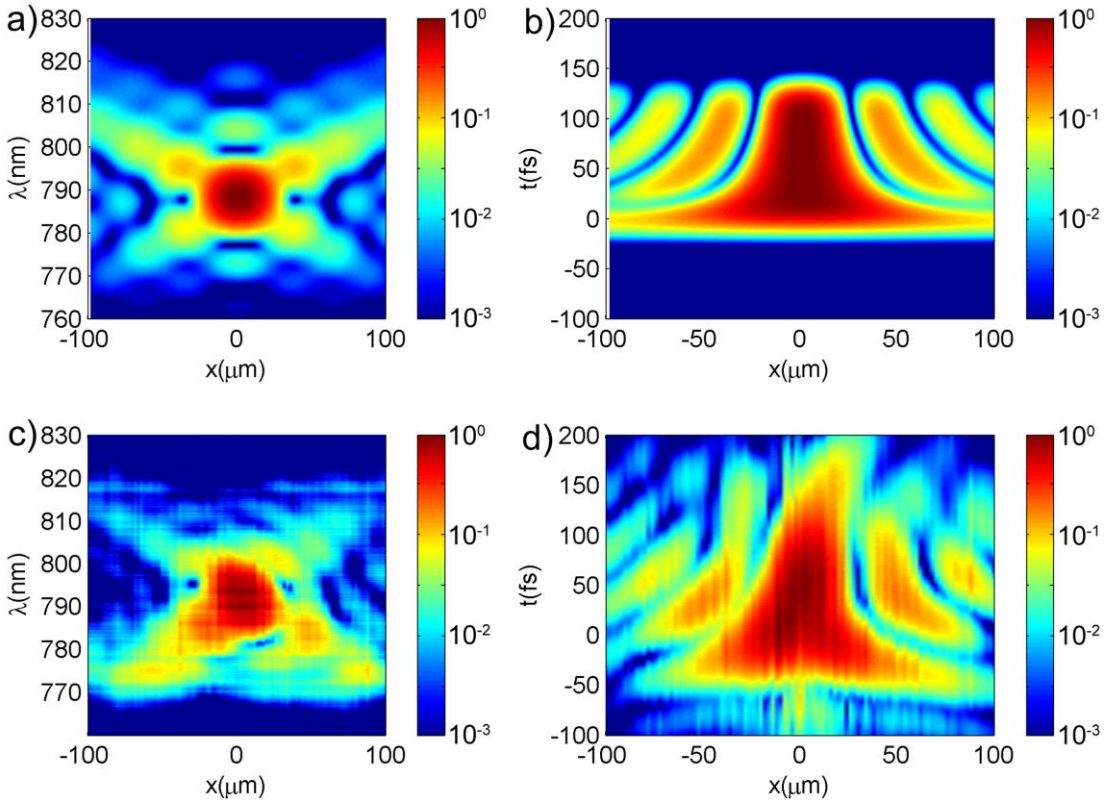


Fig. 5.8. Normalized simulated and experimental spatially resolved spectrum (a, c), corresponding spatiotemporal intensity (b, d) for the propagation distance z=405mm in logarithmic scale.

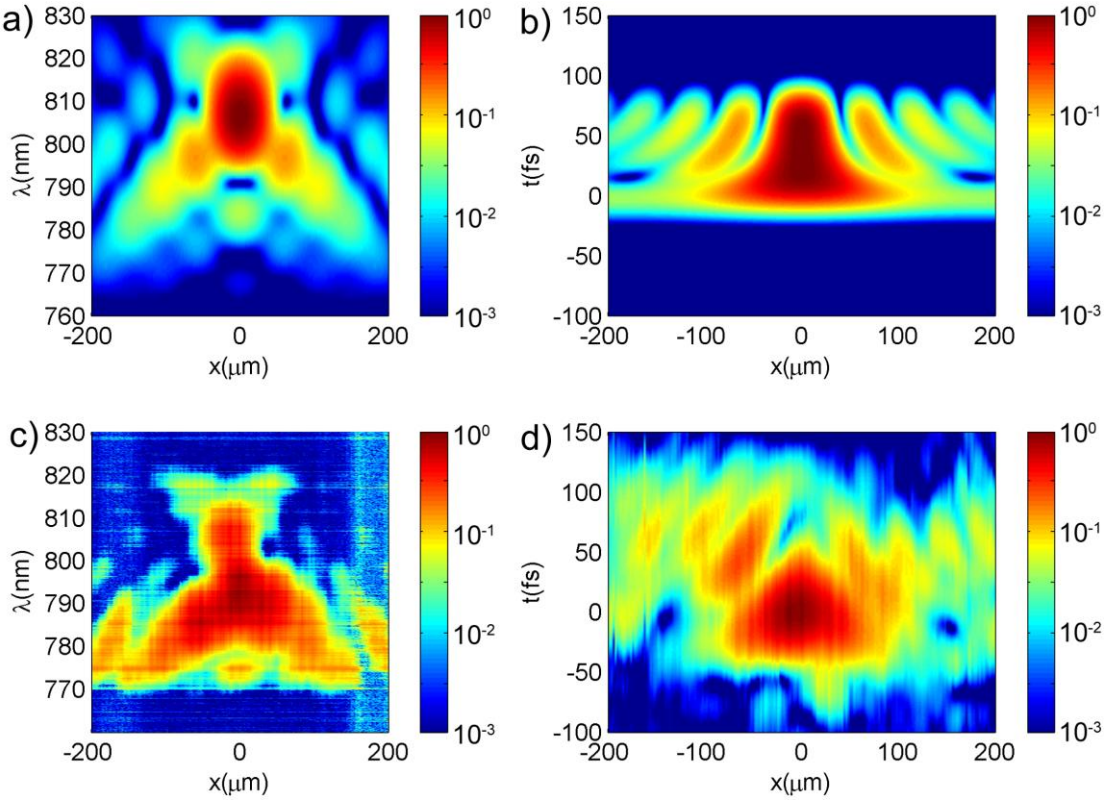


Fig. 5.9. Normalized simulated and experimental spatially resolved spectrum (a, c), corresponding spatiotemporal intensity (b, d) for the propagation distance z=660mm in logarithmic scale.

At the following focus (z = 660 mm), the behavior is quite similar to the previous position, as seen in Fig. 5.9. As expected, when increasing the distance of observation, the pulse duration is further reduced and the spatial width is increased. In this case, the x-shape is shifted towards the redder part of the spectrum, which may be originated by a measurement taken at a propagation distance slightly different from the focal position for the central wavelength. This fact leads to a slightly different spatiotemporal experimental intensity (Fig. 5.9d), while in qualitative agreement with the simulated pattern (Fig. 5.9b).

Finally, it should be pointed out that when comparing the spatiotemporal intensity (Fig. 5.5 to 5.9) for the theoretical distributions (subplots (b)) and the experimental results (subplots (d)), the latter show a slight temporal pulse broadening. We believe that this may be caused by dispersion of the short pulse while passing through the DOE material (quartz).

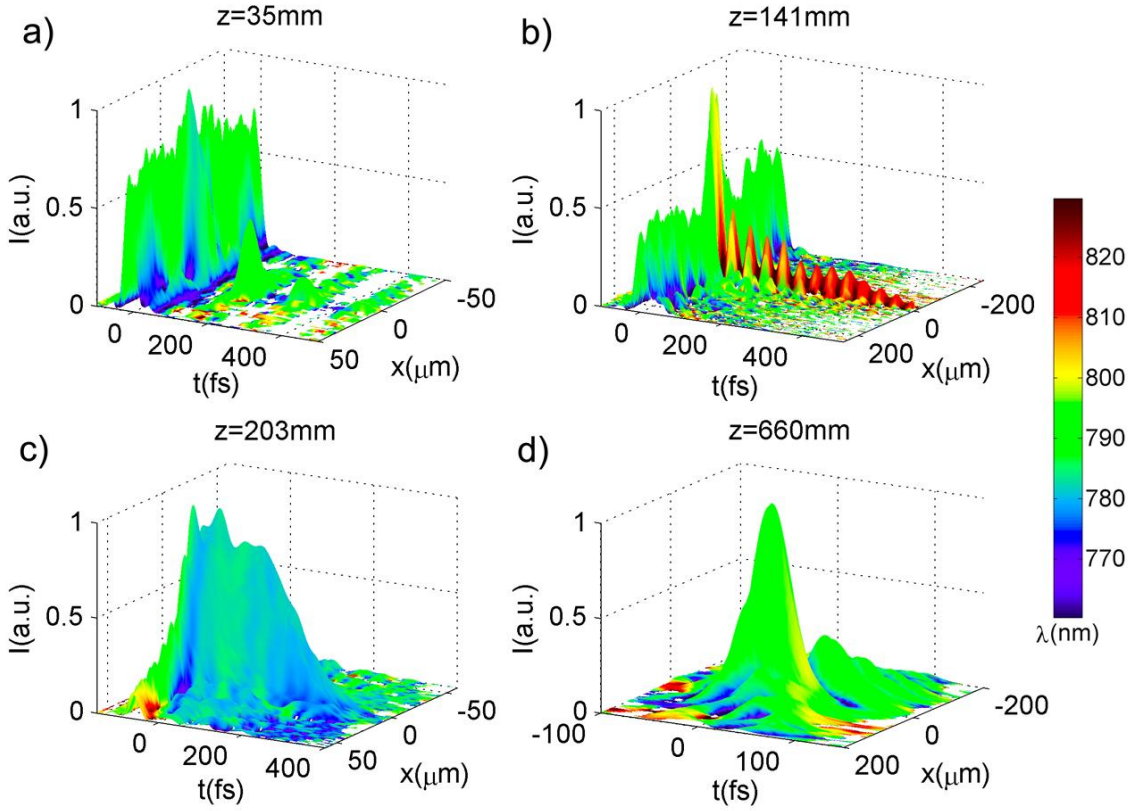


Fig. 5.10. Experimental normalized spatiotemporal intensity colored by the retrieved instantaneous wavelength as indicated in the colorbar (the same colorbar applies for the 4 subplots), for different propagation distances z.

### 5.3.3. Intensity and instantaneous wavelength maps

Additionally, the phase of the pulse is obtained in the spatiotemporal domain, which means that the intensity and phase information can be combined to have a deeper insight into the pulse structure. Many times the instantaneous wavelength —calculated from the inverse of the temporal phase derivative— of the pulse is rather more useful than its phase in illustrating the temporal chirp. Here, the spatiotemporal intensity is combined with the corresponding instantaneous wavelength $\lambda_t(x,t)$ by coloring the

intensity map with a color depending on the value of $\lambda_t$ at each point. This information is shown in Fig. 5.10 for different propagation distances. For example, in the Fresnel region, at the focus z = 141 mm (Fig. 5.10b), in the center of the spatial profile ($x = 0$) a main pulse with $\lambda_t$ around 800 nm is followed by a redder train of pulses. Off-axis ($x \neq 0$), the main pulse has a bluer $\lambda_t$ close to the central wavelength of the spectrum. This is in agreement with the spatially-resolved spectral distribution (Fig. 5.6c). However, the present information is much more complete, since it cannot be inferred from the spectral amplitude.

Similar analyses can be carried out for the other foci. In the near-field (Fig. 5.10a), on-axis, the main pulse is bluer and the rest of the pulses of the train are close to the central wavelength. The main pulse has a spatially modulated structure (see Fig. 5.5d). In Fig. 5.10a it can be seen that the broader temporal pulse (at $x \simeq \pm 40 \mu m$) is also associated with a bluer $\lambda_t$. In the far-field, the frequencies redistribution inside the spatiotemporal intensity is not so complex. In Fig. 5.10c and 5.10d, it is observed that the instantaneous wavelength is almost constant in the whole structure.

## 5.4. Conclusions

In this chapter, we have analyzed the structure of the multiple foci created by a DOE, a zone plate, consisting of a set of concentric transparent and opaque rings. The technique STARFISH has been utilized to measure the amplitude and phase of the focused ultrashort pulses in the spatiospectral and the spatiotemporal domains. The spatial resolution of the collecting fiber allows for the measurement of focused pulses, as shown in Section 4.2.3. As predicted by the numerical simulations, the spatiospectral and the spatiotemporal structure of the pulses exhibit a strong coupling that requires a full characterization method –in our case, STARFISH. The pulse distribution is analyzed for foci at different propagation distances, corresponding to the near-field, Fresnel and far-field regions. The pulse evolution is discussed from a theoretical point of view and is corroborated by the agreement with the experimental characterization. The limited numerical aperture of the fiber prevents an accurate collection of the light coming from the outer part of the DOE in the near-field region, which causes the differences observed between the experiments and the simulations in that case.

## References

[1] Eugene Hecht, Chapter 10: "Diffraction" in *Optics*, 4th Ed., Addison Wesley (2002).

[2] J. A. Jordan, Jr., P. M. Hirsch, L. B. Lesem, and D. L. Van Rooy, "Kinoform Lenses," Appl. Opt. 9, 1883-1887 (1970).

[3] V. Moreno, J. F. Román, and J. R. Salgueiro, "High efficiency diffractive lenses: Deduction of kinoform profile", Am. J. Phys. 65, 556-562 (1997).

[4] S. P. Veetil, C. Vijayan, D. K. Sharma, H. Schimmel, and F. Wyrowski, "Diffraction induced space-time splitting effects in ultra-short pulse propagation," J. Mod. Opt. 53, 1819–1828 (2006).

[5] S. P. Veetil, N. K. Viswanathan, C. Vijayan, and F. Wyrowski, "Spectral and temporal evolutions of ultrashort pulses diffracted through a slit near phase singularities," Appl. Phys. Lett. 89, 041119 (2006).

[6] Z. Jiang, R. Jacquemin, and W. Eberhardt, "Time dependence of Fresnel diffraction of ultrashort laser pulses by a circular aperture," Appl. Opt. 36, 4358–4361 (1997).

[7] H. Zhang, J. Li, D.W. Doerr, and D. R. Alexander, "Diffraction characteristics of a Fresnel zone plate illuminated by 10 fs laser pulses," Appl. Opt. 45, 8541–8546 (2006).

[8] O. Mendoza-Yero, G. Mínguez-Vega, J. Lancis, and V. Climent, "Focusing and spectral characteristics of periodic diffractive optical elements with circular symmetry under femtosecond pulsed illumination," J. Opt. Soc. Am. A 24, 3600-3605 (2007).

[9] O. Mendoza-Yero, G. Mínguez-Vega, J. Lancis, E. Tajahuerce, and V. Climent, "Spectral analysis of femtosecond pulse diffraction through binary diffractive optical elements: theory and experiment," Opt. Express 16, 2541-2546 (2008).

[10] O. Mendoza-Yero, G. Mínguez-Vega, J. Lancis, M. Fernández-Alonso, and V. Climent, "On-axis diffraction of an ultrashort light pulse by circularly symmetrical hard apertures," Opt. Express 15, 4546-4556 (2007).

[11] O. Mendoza-Yero, B. Alonso, O. Varela, G. Mínguez-Vega, I. J. Sola, J. Lancis, V. Climent, and L. Roso, "Spatio-temporal characterization of ultrashort pulses diffracted by circularly symmetric hard-edge apertures: theory and experiment", Opt. Express 18, 20900-20911 (2010).

[12] M. Lõhmus, P. Bowlan, P. Piksarv, H. Valtna-Lukner, R. Trebino, and P. Saari, "Diffraction of ultrashort optical pulses from circularly symmetric binary phase gratings," Opt. Lett. 37, 1238-1240 (2012).

[13] P. Bowlan, P. Gabolde, and R. Trebino, "Directly measuring the spatio-temporal electric field of focusing ultrashort pulses," Opt. Express 15, 10219-10230 (2007).

[14] B. Alonso, I. J. Sola, O. Varela, J. Hernández-Toro, C. Méndez, J. San Román, A. Zaïr, and L. Roso, "Spatiotemporal amplitude-and-phase reconstruction by Fourier-transform of interference spectra of high-complex-beams," J. Opt. Soc. Am. B 27, 933-940 (2010).

[15] G. Mínguez-Vega, O. Mendoza-Yero, J. Lancis, R. Gisbert, and P. Andrés, "Diffractive optics for quasi-direct space-to-time pulse shaping," Opt. Express 16, 16993-16998 (2008).

[16] O. Mendoza-Yero, B. Alonso, G. Mínguez-Vega, I. J. Sola, J. Lancis, and J. A. Monsoriu, "Synthesis of fractal light pulses by quasi-direct space-to-time pulse shaping," Opt. Lett. 37, 1145-1147 (2012).

[17] B. Alonso, R. Borrego-Varillas, O. Mendoza-Yero, I. J. Sola, J. San Román, G. Mínguez-Vega, and L. Roso, "Frequency resolved wavefront retrieval and dynamics of diffractive focused ultrashort pulses," J. Opt. Soc. Am. B 29, 1993-2000 (2012).

[18] A. Monmayrant, S. Weber and B. Chatel, "A newcomer's guide to ultrashort pulse shaping and characterization," J. Phys. B: At. Mol. Opt. Phys. 43, 103001 (2010).

[19] J. D. McKinney, D. E. Leaird, and A. M. Weiner, "Millimiter-wave arbitrary waveform generation with a direct space-to-time pulse shaper," Opt. Lett. 27, 1345-1347 (2002).

[20] A. M. Weiner, "Femtosecond pulse shaping using spatial light modulators," Rev. Sci. Instrum. 71, 1929 (2000).

[21] H. Rabitz, R. de Vivie-Riedle, M. Motzkus, and K. Kompa, "Whither the future of controlling quantum phenomena?," Science 288, 824-828 (2000).

[22] T. Hornung, R. Meier, D. Zeidler, K.-L. Kompa, D. Proch, and M. Motzkus, "Optimal control of one- and two-photon transitions with shaped femtosecond pulses and feedback," Appl. Phys. B 71, 277-284 (2000).

[23] D. Meshulach and Y. Silberberg, "Coherent quantum control of two-photon transitions by a femtosecond laser pulse," Nature 396, 239-242 (1998).

[24] Y. X. Wang, W. B. Yun, and C. Jacobsen, "Achromatic Fresnel optics for wideband extreme-ultraviolet and X-ray imaging," Nature 424, 50-53 (2003).

[25] C. David, S. Gorelick, S. Rutishauser, J. Krzywinski, J. Vila-Comamala, V. A. Guzenko, O. Bunk, E. Färm, M. Ritala, M. Cammarata, D. M. Fritz, R. Barrett, L. Samoylova, J. Grünert, and H. Sinn, "Nanofocusing of hard X-ray free electron laser pulses using diamond based Fresnel zone plates," Sci. Rep. 1, 57 (2011).

[26] B. J. Pearson and T. C. Weinacht, "Shaped ultrafast laser pulses in the deep ultraviolet," Opt. Express 15, 4385-4388 (2007).

[27] G. Mínguez-Vega, C. Romero, O. Mendoza-Yero, J. R. Vázquez de Aldana, R. Borrego-Varillas, C. Méndez, P. Andrés, J. Lancis, V. Climent, and L. Roso, "Wavelength tuning of femtosecond pulses generated in nonlinear crystals by using diffractive lenses," Opt. Lett. 35, 3694-3696 (2010).

[28] C. Yang, K. Shi, H. Li, Q. Xu, V. Gopalan, and Z. Liu, "Chromatic second harmonic imaging", Opt. Express 18, 23837-23843 (2010).

[29] C. Romero, R. Borrego-Varillas, A. Camino, G. Mínguez-Vega, O. Mendoza-Yero, J. Hernández-Toro, and J. R. Vázquez de Aldana, "Diffractive optics for spectral control of the supercontinuum generated in sapphire with femtosecond pulses," Opt. Express 19, 4977-4984 (2011).

[30] Y. Fu, H. Xiong, H. Xu, J. Yao, B. Zeng, W. Chu, Y. Cheng, Z. Xu, W. Liu, and S. L. Chin, "Generation of extended filaments of femtosecond pulses in air by use of a single-step phase plate", Opt. Lett. 34, 3752-3754 (2009).

[31] R. Bartels, S. Backus, E. Zeek, L. Misoguti, G. Vdovin, I. P. Christov, M. M. Murnane, and H. C. Kapteyn, "Shaped-pulse optimization of coherent emission of high-harmonic soft X-rays," Nature 406, 164-166 (2000).

[32] R. Martínez-Cuenca, O. Mendoza-Yero, B. Alonso, I. J. Sola, G. Mínguez-Vega, and J. Lancis, "Multibeam second-harmonic generation by spatiotemporal shaping of femtosecond pulses," Opt. Lett. 37, 957-959 (2012).

[33] L. Lepetit, G. Cheriaux, and M. Joffre, "Linear techniques of phase measurement by femtosecond spectral interferometry for applications in spectroscopy," J. Opt. Soc. Am. B 12, 2467-2474 (1995).

# CHAPTER 6

# FOCUSING DYNAMICS OF A KINOFORM DIFFRACTIVE LENS

**Contents**



*Some of the results of this chapter were presented in the original in B. Alonso et al., J. Opt. Soc. Am. B 29, 1933-2000 (2012)*

## 6.1. Interest of diffractive focusing and wavefront measurement

The focusing properties of diffractive lenses are a subject of high interest in nonlinear optics. Recently, they have been used with ultrashort laser pulses for applications such as tuning the central wavelength of the second-harmonic generation (SHG) [1,2] or the control of the supercontinuum generation structure and broadening [3].

These two applications are based on the chromatic dependence of the focus of a kinoform diffractive lens (KDL), whose focal length is given by the expression $f(\lambda) = f_c \lambda_c / \lambda$, where $\lambda$ denotes any wavelength of the pulse, $\lambda_c$ is the central wavelength of the pulse, and $f_c$ is the focal length for $\lambda_c$. KDL are especially designed and modified Fresnel zone plates, in which the opaque and transparent rings are substituted by a parabolic and transparent profile [4]. To improve the efficiency of the KDL, the parabolic profile is truncated every $2\pi$-shift owing to the material, as illustrated in Fig. 6.1, resulting in rings with a maximum phase amplitude of $2\pi$. The rings are closer off-axis owing to the parabolic dependence.

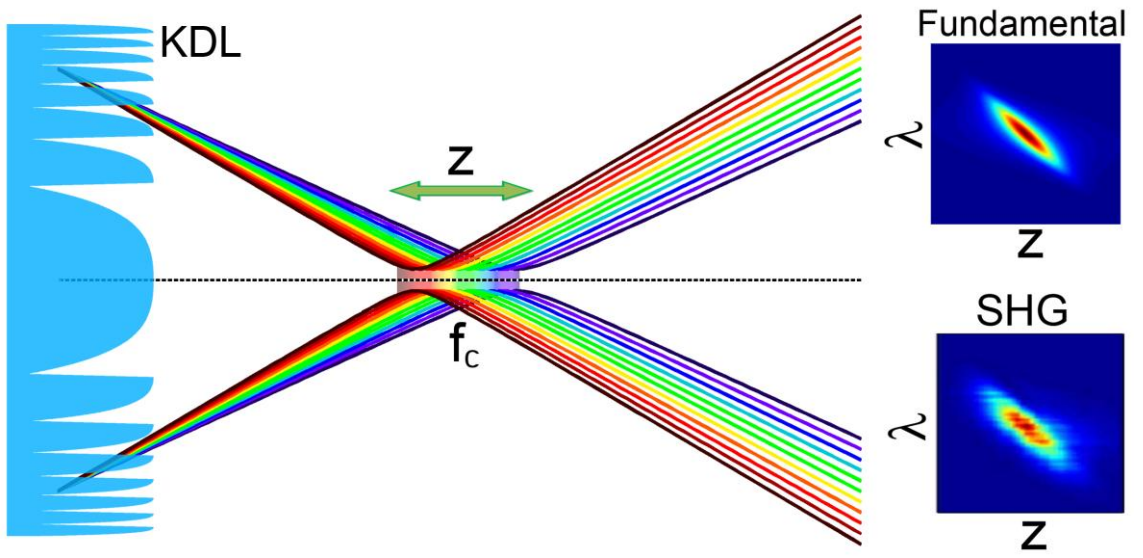


Fig. 6.1. Schematic diagram of a kinoform diffractive lens (KDL) that focuses an ultrashort laser pulse. Shorter (redder) wavelengths focus before longer (bluer) wavelengths. Thefundamental spectrum along the optical axis is shifted from red to blue, as well as the second-harmonic generation (SHG) in a nonlinear crystal scanning the focusing region (SHG trace from [1]).

The focal dependence on the wavelength, $f(\lambda) \propto \lambda^{-1}$, is responsible for a chromatic focusing. Given a collimated input beam focused by a KDL, longer wavelengths (redder) will focus before shorter wavelengths (bluer). In our case, ultrashort laser pulses have a considerable spectral bandwidth that will make this effect very noticeable. We illustrate this fact in Fig. 6.1, where we plot with different colors (to distinguish the wavelengths, from red to blue) the transverse size of the beam as a function of the propagation distance. As a consequence, the spectrum of the pulse along the optical axis will be shifted from redder to bluer wavelengths in the focusing region (denoted by the arrow). The simulated evolution of the spectrum is depicted in the trace labeled as

"fundamental". As previously discussed, this fact has been applied, for example, to tune the central wavelength of the SHG generated in a nonlinear crystal by shifting the crystal along the focusing region (see inset the experimental "SHG" trace extracted from the work of Mínguez-Vega et al. [1]). The correlation between the linear propagation dependence (in the fundamental trace) and the SHG trace is direct, and the whole spectrum of the pulse can be covered just by placing the crystal in the correct position. If KDL is compared to achromatic lens focusing, in the latter case the focus is not dependent on the wavelength and the spectrum is not modified, so wavelength tuning of the SHG is not possible.

In fact, the sum of the different contributions (from different wavelengths) off-axis (out of the optical axis) will not be as simple as the picture presented above. Since the whole pulse (in spatial terms) contributes to the process (e.g. SHG), this will be tailored by the evolution of the full spatiospectral and spatiotemporal features of the pulses along the focus of the KDL. Therefore, the full characterization of this evolution (not only on-axis) is important to give deeper insight into the pulse structure involved in the different processes.

Furthermore, the wavefront of the pulses is of huge importance for the phase-matching properties of the mentioned nonlinear processes. It is expected that, over the next years, diffractive optical elements (DOEs) will tailor nonlinear processes such as SHG [1,2], supercontinuum [3], filamentation [5] or high-order harmonic generation [6].

However, the full characterization of pulses with a strong spatiotemporal (and spatiospectral) coupling is not trivial. In Section 4.4, we demonstrated the capability of STARFISH [7] to be used as a wavefront sensor. The full spatiospectral phase can be retrieved, although a small phase noise is present owing to the instabilities during the spatial scan [8]. Moreover, it can be applied to focused pulses thanks to its high spatial resolution.

The possibility of measuring the wavefronts of ultrashort laser pulses as a function of their frequency content opens the way for multiple applications, e.g. the study of aberrations in optical systems [9] or the characterization of ultrashort pulses involved in nonlinear processes [1-3,5,6]. Since STARFISH has already been adapted to analyze the filamentation of light [10] (as we will present in Chapter 8), a possible application would be to examine the wavefront dynamics in this regime to study the energy-density flux involved in the process, via the calculation of the phase (wavefront) gradient as explained in [11].

In this chapter, we apply STARFISH to the study of pulses focused by a KDL [8], measuring their wavelength dependent wavefront. Additionally, a full spatiotemporal characterization of the amplitude and phase evolution of such pulses in the focusing region is given, offering a complete insight into its propagation dynamics. The numerical simulations that we performed are in excellent agreement with the experimental measurements [8]. In this case, we proposed and implemented a theoretical model based on Fresnel diffraction for the numerical simulations.

## 6.2. Experimental setup

The spatiotemporal characterization was carried out with STARFISH [7], already presented in Chapter 4. The scheme of the experimental setup is presented in Fig. 6.2. In this experiment, the test beam was focused by a KDL, whose focus was scanned in the transverse direction to the propagation axis with a spatial resolution of $4\mu m$ (given by the fiber diameter). The measurements were performed in different planes along the propagation axis, by changing the relative distance between the lens and the input fiber. Since the propagation distance explored was very short (4 mm), we shifted the collecting fiber along the optical axis to do the z-scan, instead of shifting the KDL (as opposed to what was done in Chapter 5 with the DOE).

For the experiments we used a Ti:sapphire CPA laser system (Spectra-Physics) that delivers 100 fs pulses (Fourier-transform limit) with central wavelength of 795 nm, 9 nm intensity full-width-half-maximum (FWHM) spectral bandwidth and 1 kHz repetition rate. The temporal characterization of the reference pulse was performed with a GRENOUILLE device (Swamp Optics) and the spectra were measured with a spectrometer of resolution 0.1 nm (Avantes Inc.). The delay between the reference pulse and the test pulse was 2 ps.

The KDL employed in the experiment (manufactured by the Institute of Automatics and Electrometry, Russia) had cylindrical symmetry and a focal length given by the expression $f(\lambda) = f_0\lambda_0 / \lambda$, where $\lambda$ denotes any wavelength of the pulse. The design parameters of the KDL where $f_0$ = 150 mm and $\lambda_0$ = 565.1 nm. In our case, for the central wavelength of the pulses $\lambda_c$ = 795 nm, the corresponding focal length is $f_c \equiv f(\lambda_c) = 106.6mm$. Since cylindrical symmetry was preserved in all the cases during our study, the measurements were just performed only along the $x$-axis.

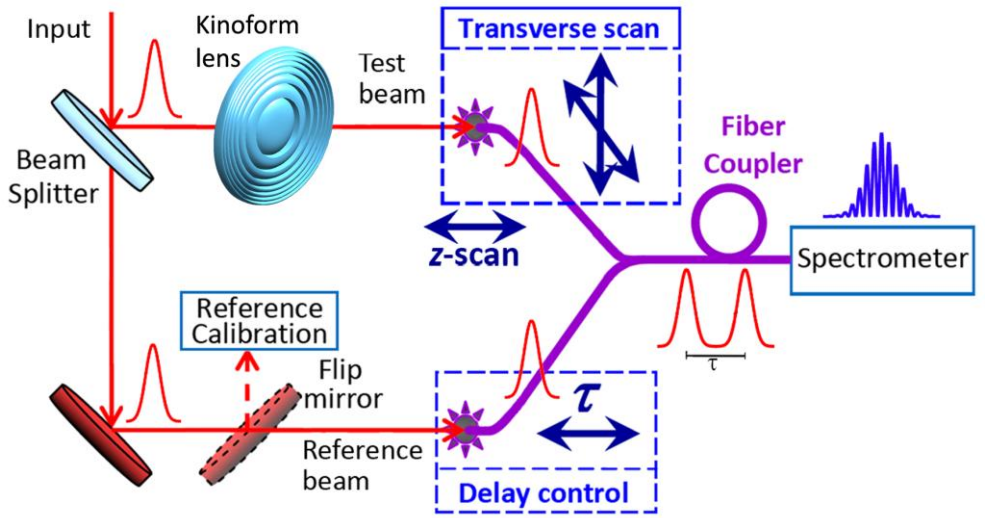


Fig. 6.2. Scheme of the experimental setup: one replica of the laser pulse is used as the reference and the other replica is focused by a KDL. The pulses are collected by the fibers; the fiber in the reference arm controls the relative delay, whereas the fiber in the test arm spatially scans the unknown beam. The spatially resolved spectral interferometry is measured after the fiber coupler in the spectrometer. The position of the lens with respect to the fiber allows for the exploration of different propagation distances.

The algorithm for the retrieval of the amplitude and phase of the pulses is detailed in Sections 2.2 (Fourier analysis of the spectral fringes) and 4.2.1 (extension to the spatiotemporal domain). STARFISH directly yields the spatiospectral phase of the pulses $\phi(x,\lambda)$. The different phase curves for each wavelength $\lambda_j$ are what we call the frequency-resolved wavefronts $\phi(x;\lambda_j)$.

As discussed in Section 4.4, the phase stability of the interferometer is vital to obtaining the wavefront. Shot-to-shot fluctuations lead to a phase noise in the measurement. The more stable the interferometer is, the less noise is introduced. The amount of noise will depend on the experimental configuration (optical path, mounts, air and thermal effects). The spectral interferences and the fluctuation of the spectral phase for the central wavelength are shown in Fig 6.3a and 6.3b, respectively. In general, we have checked that our stability is sub-wavelength. In this case, it was found that the fluctuation was $0.35{\cdot}2\pi\,rad$. Consequently, larger phase variations will be measured and will allow us to study the chromatic properties of the KDL focus.

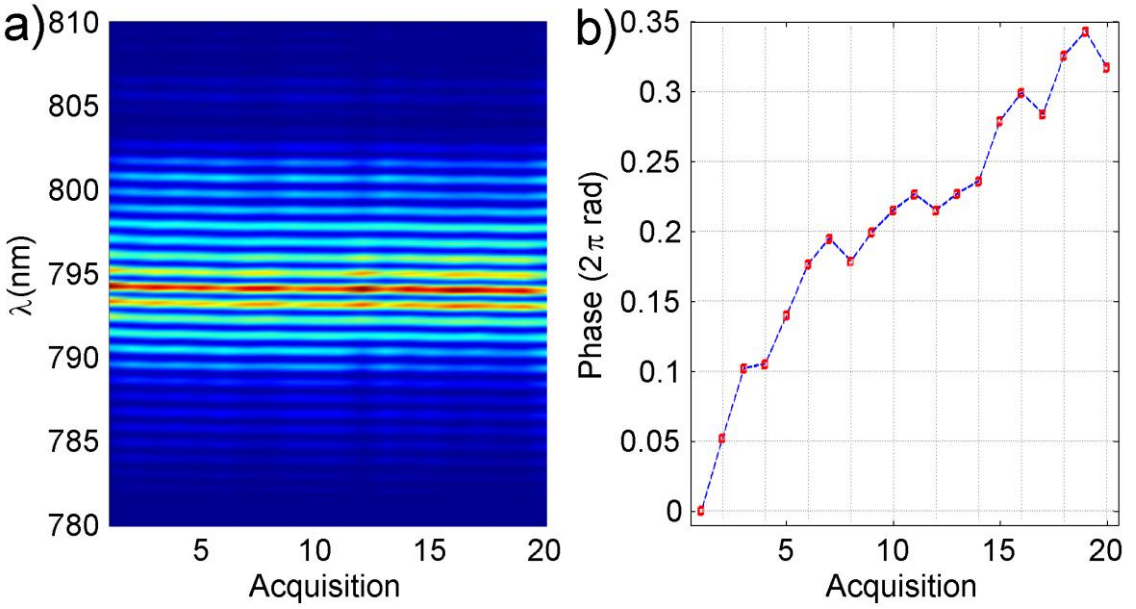


Fig. 6.3. Multiple acquisition for the phase stability study: (a) spectral interferences and (b) spectral phase drift for the central wavelength.

## 6.3. Theoretical model for the numerical simulations

In order to predict the focusing dynamics of the pulses after the KDL and to validate the experimental measurements, we numerically simulated the propagation of such pulses. For this purpose, we calculated the electric field diffracted by the KDL using the theory of Fresnel diffraction. To model the lens, one should take into account the kinoform profile of the lens as detailed in [4] (rings constituted by sections of a parabola with $2\pi$ phase amplitude). However, this exact approach requires a very computationally demanding sampling in the spatial domain. Instead, for the calculations one can model the effect of the KDL as the phase introduced by a thin lens with a variable focal length given by the expression $f(\lambda) = f_0\lambda_0 / \lambda$.

To calculate the diffracted electric field $U_2$ at the focus from the electric field $U_1$ that illuminates the KDL, we take advantage of the system's cylindrical symmetry and express the equations as a function of the radial coordinates $r_1$ and $r_2$ in the input and output planes, respectively. Under the paraxial approximation, Fresnel diffraction can be expressed as follows [12]

$$U_2(r_2,\lambda) = i\frac{2\pi}{\lambda z}\exp\left(-\frac{ikr_2^2}{2z}\right)\int_0^\infty U_1(r_1,\lambda)\exp\left(-\frac{ikr_1^2}{2z}\right)J_0\left(\frac{kr_1r_2}{z}\right)r_1\,\mathrm{d}r_1, \qquad (6.1)$$

where $\lambda$ is the wavelength, $z$ is the propagation distance, $k$ is the wave vector, and $J_0$ is the Bessel function of the first kind of zero order. The input electric field $U_1$ in the spatial domain is a Gaussian profile with a full-width at $1/e^2$ in intensity of 7 mm, which agrees very well with the experimental conditions. In the same way, the experimental spectrum was also included (FWHM of 9 nm in intensity). Finally, to model the KDL, we introduced it as the phase of a lens of variable focal length $\exp\{ikr^2/2f(\lambda)\}$.

Therefore, the spatiospectral amplitude and phase of the electric field $U_2(r_2,\lambda)$ were calculated for different propagation distances $z$ in the vicinity of the focus using Eq. (6.1). Then, the corresponding amplitude and phase in spatiotemporal domain were obtained by inverse Fourier-transform. Note that in Eq. (6.1) the contribution of the phase $\exp\{-ikz\}$ has been removed (in comparison to the equation given in [12]), since we have applied the temporal translation $t \to t - z/v_g$ (being $v_g$ the group velocity) to freeze the temporal axis during the propagation (so the pulse is always centered around zero).

We wish to emphasize that we have adapted a classical equation in optics (Fresnel diffraction) to model the propagation of ultrashort laser pulses. The propagation is simply calculated as the superposition of the "diffraction" in the input plane (in this case, the KDL) for different wavelengths. Surprisingly, this approach is sufficient to describe the propagated pulse both in the spatiospectral (including the wavefront) and the spatiotemporal domains (retrieving the correct pulse-front, as well as the intensity and chirp of the pulses). Before applying it to the focus of the KDL, we tested it by comparing the calculations with additional simulations that we implemented using analytical expressions for Gaussian beam propagation. Moreover, we checked the correct focal spot size dependence as a function of the input spatial profile, and we also checked the diffraction of an input plane wave (instead of Gaussian profile) by a circular aperture. Finally, the good agreement between the simulations and the measurements confirms the validity of the model.

## 6.4. Experimental measurements and comparison with simulations

### *6.4.1 Evolution of the wavefront and the spectrum*

The propagation of the pulses focused by the KDL (described in Section 6.1 and illustrated in Fig. 6.1) has a strong dependence on the wavelength. For this reason, the wavefront of the pulses, the spatially-resolved spectrum and the spatiotemporal intensity

will also be dependent on the wavelength. The results presented in this section (for the KDL) can be compared to achromatic focusing, where no spectral or temporal distortion exists. An example showing this behavior is given in Section 4.2.3 (Fig. 4.5), where we used an achromatic doublet lens with a similar focal length (100 mm).

To track the evolution of the pulse around the focus of the KDL ($f_c$) and test the influence of the phase shift on the measurement, we measured the full spatiotemporal amplitude and phase at the following propagation distances (z): $f_c$-2 mm, $f_c$-1 mm, $f_c$, $f_c$+1 mm and $f_c$+2 mm ($f_c$=106.6 mm). For the three central positions, we scanned 100 μm of the transverse profile with 1 μm steps. For the two external positions, we scanned 200 μm of the transverse profile in 2 μm steps.

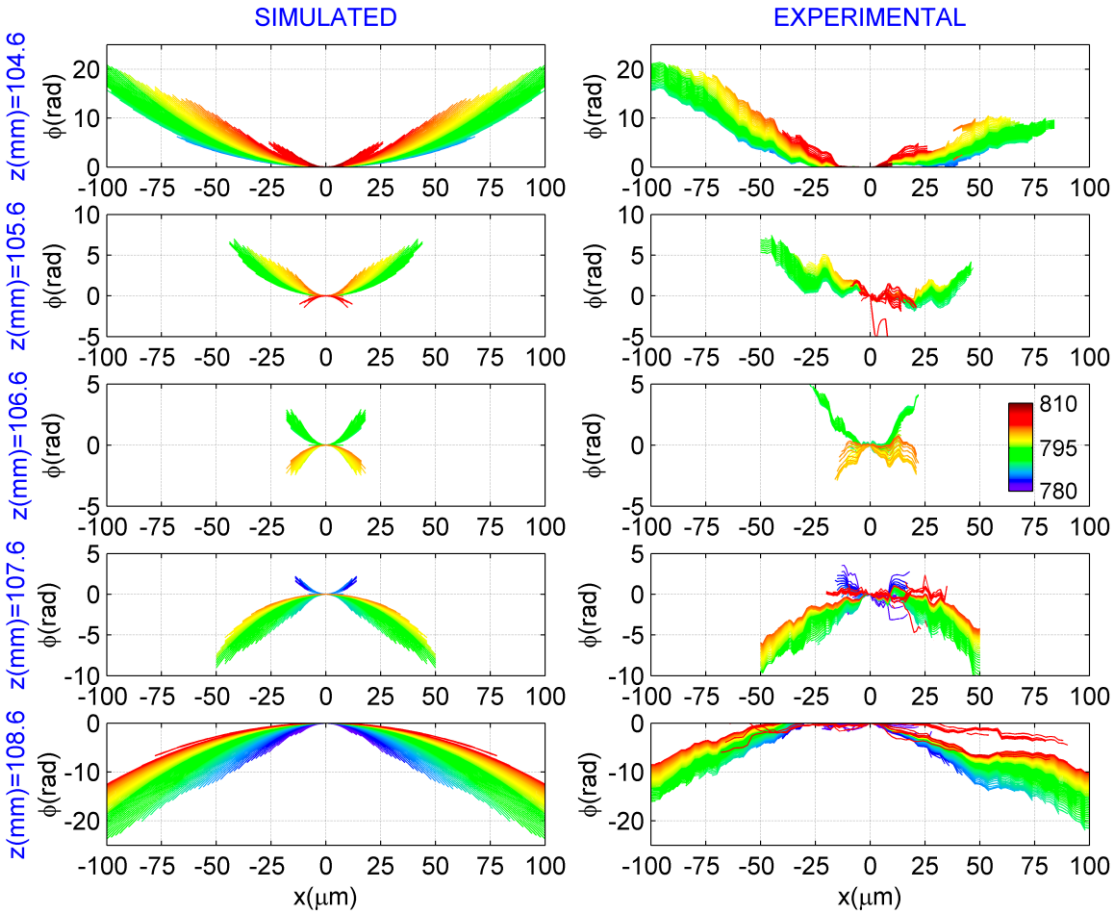


Fig. 6.4. Simulated (left) and experimental (right): wavefront as a function of the wavelength before and after the focus of the KDL. The wavefront for each wavelength is plotted in the color given by the colorbar inset (the same colorbar applies to all subplots in the figure).

In Fig. 6.4, the line-outs of the wavefronts $\phi(x;\lambda_j)$ are given for the different wavelengths $\lambda_j$ of the pulse spectrum. Each wavelength corresponds to a color given by the colorbar inset in Fig. 6.4. The results are presented for the propagation distances labeled in the left. The left column shows the simulation, whereas the right column shows the experimental results. The resulted wavefronts clearly show the chromatic dependence due to the focal length f(λ). For the first position, $z_{-2}$= $f_c$-2 mm, the redder wavelength ~808 nm is just arriving at its focus, so all the wavefronts have positive curvature (converging). As expected for a Gaussian beam around the focus, the higher

curvature corresponds to the bluer wavelengths. At longer propagation distances, the focus moves towards shorter wavelengths. For instance, at $z_{-1}= f_c-1$ mm, the wavelength ~802 nm is focused: longer wavelengths are after the focus, thus showing negative curvature (diverging), while the remaining wavelengths are still focusing (converging). At the position of the focus for the central wavelength 795 nm, i.e. $z_0= f_c$ (mm), half of the spectrum is before the focus (the bluer), while the other half (the redder) is after the focus. This yields positive and negative wavefront curvatures respectively. As we move apart from the distance $z_0$, the shorter wavelengths are focused. For instance, at $z_{+1}= f_c+1$ mm, the focusing wavelength corresponds to ~786 nm. At the last position, $z_{+2}= f_c+2$ mm, the bluer wavelength ~781 nm is focused and the whole pulse is after the focus, exhibiting negative curvature in the wavefront (thus diverging).

The agreement between the experiment and the theory is quite good, showing an almost negligible effect of the phase drift error. Note that this error affects more the central positions because the curvature is smaller, and thus comparable with the error. Also, the retrieved wavefront is noisy and not reliable for the wavelengths where the spectral amplitude is small and there is too low a signal (see the corresponding Fig. 6.5). Finally, the slight spatial asymmetry (x-axis) in the experimental data shown in Fig. 6.4 could be originated by a misalignment of the setup, in particular in the case of a scan not perfectly perpendicular to the z-axis.

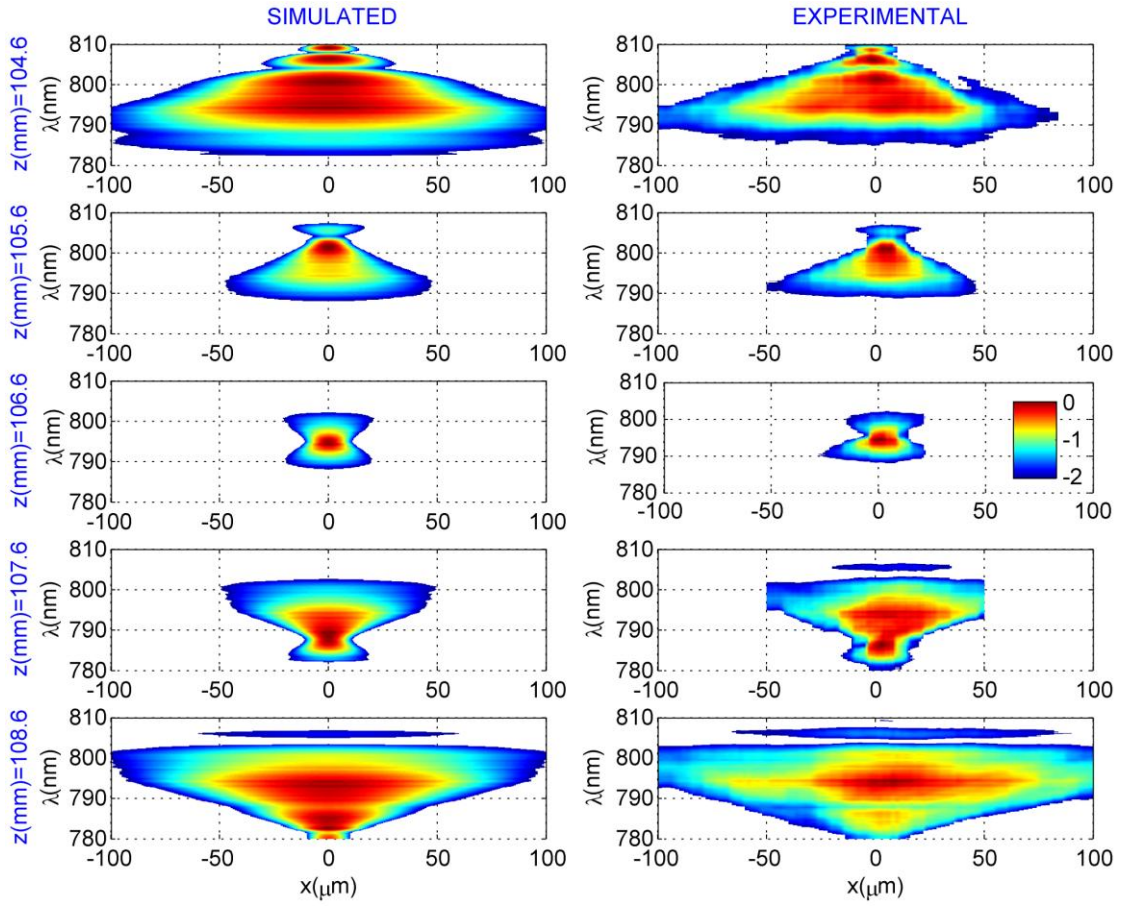


Fig. 6.5. Simulated (left) and experimental (right): spatially resolved spectrum before and after the focus of the KDL. The logarithmic scale comprises two orders of magnitude (see colorbar inset).

### 6.4.2 Spatiotemporal dynamics

To gain a deeper insight into the dynamics of the processes involved in the focusing of ultrashort pulses by a KDL, a complete spatiotemporal study is mandatory. In such cases, knowing the structure of the pulse on-axis is not enough because the whole spatial profile is involved in the process. The spatiotemporal reconstructions made by STARFISH are in very good agreement with the simulations, which are shown for different propagation distances in Fig. 6.6. for the focus position ($z=z_0$), the spatiotemporal intensity corresponds to the far-field structure, already presented in Chapter 5 for a DOE, with a main broadened central peak, and a train of pulses in the wings.

We observe that the pulse-front curvature is the same at both sides of the focus. The measurements of the wavefront (phase front) and the pulse-front are in agreement with the predictions presented in the work [13] for chromatic elements. In that work, Bor found out that the wavefront (the phase-front) is symmetrical with respect to the focus, being flat for the central wavelength at its focus (as we have measured and simulated). In the case of chromatic aberration of lenses (bluer wavelengths focus before, the opposite of our case), the pulse-front curvature goes ahead with respect to the phase-front curvature a quantity proportional to the squared radial coordinate, independently from the propagation distance.

In our case, the sign of the chromatic aberration is the opposite ( $f(\lambda) \propto \lambda^{-1}$ for the KDL), so we could interpret that the pulse-front goes behind off-axis with respect to the axis (x=0). Since the curvature of the wavefront is relatively low in the focusing region (up to $\sim 3.5\lambda$), the pulse-front curvature is the same as that of a divergent beam and is approximately invariant before and after the focus. In fact, the pulse-front is expected to be slightly flatter before than after the focus due to the conjugation with the curvature of the wave-front. This difference is limited to ~3.5 T ($<10\,fs$, T being the duration of the optical cycle) from the axis to the periphery, so it is hard to observe in the experiment. For this reason, we have corroborated this behavior by carefully analyzing the simulations.

For the focus position ($z=z_0$), the spatiotemporal intensity corresponds to the far-field structure, already observed in [14] (Chapter 5), with a broadened central peak, and a train of pulses in the wings. Furthermore, the spatiotemporal structure is quite similar to the focus ($z=f_c$). The slight asymmetry observed in the simulations is due to the non-symmetric input spectrum. To ensure it was so, we carried out the simulations using a 9-nm FWHM Gaussian input spectrum and obtained symmetrical structures. On the other hand, the spatiotemporal phase is not symmetrical with respect to the focus. As we will present in Fig. 6.7, the chirp on-axis goes from negative to positive, respectively before and after the focus. Also, the periphery (off-axis) is bluer before focus and redder after focus, because of the wavelength-dependent focal spot size as a function of the propagation distance for the KDL. Consequently, before and after focus the spatiotemporal intensity is the same, but the spectral distribution (the chirp) is reverted

with respect to the central wavelength. This explains that for quasi-symmetrical spectra (e.g., close to Gaussian shape) the symmetry is slightly broken.

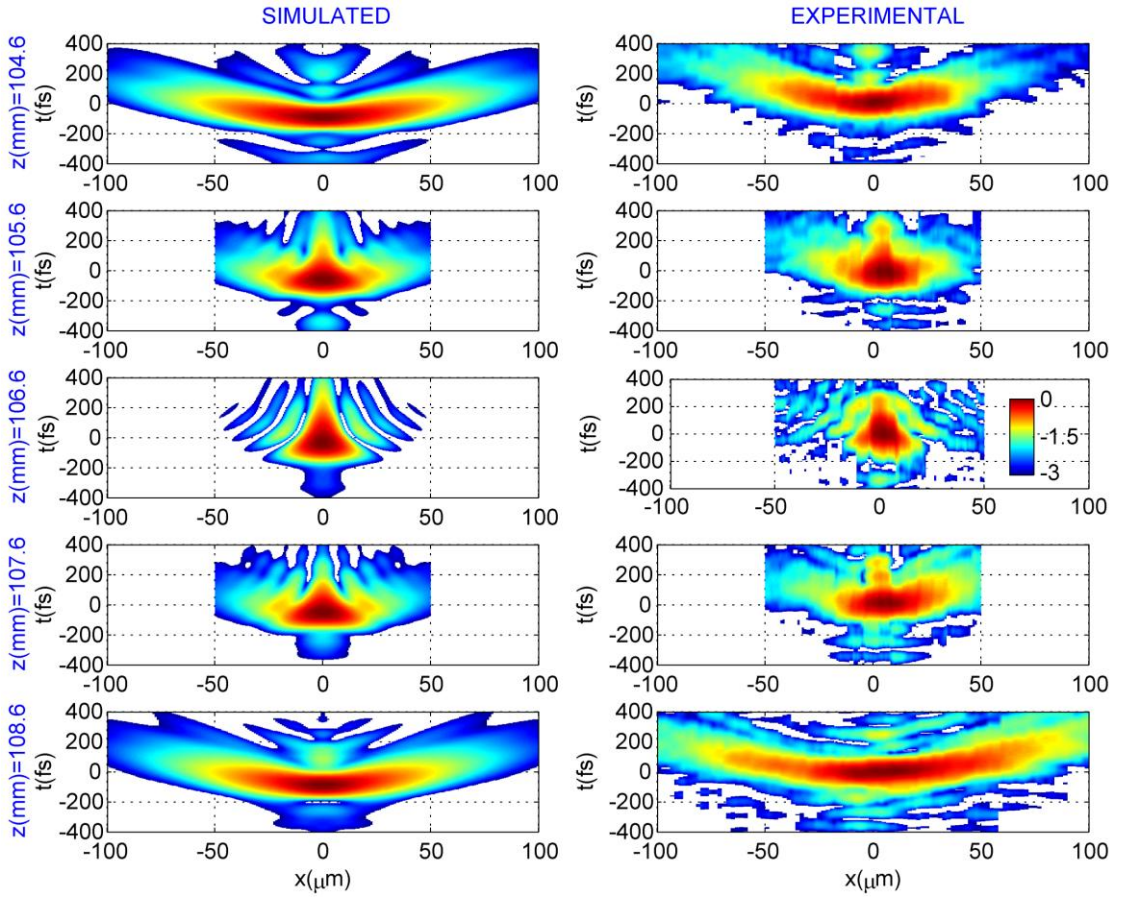


Fig. 6.6. Simulated (left) and experimental (right): spatiotemporal intensity before and after the focus of the KDL. The logarithmic scale comprises three orders of magnitude (see colorbar inset).

### *6.4.3 Temporal and spectral results on-axis*

To complete the analysis, it is very helpful to observe directly the pulse on-axis in spectral and temporal domain. The simulated and experimental results are shown in Fig. 6.7 for the different propagation distances. The information of Fig. 6.7 is completed with Table 6.1, where we give the values associated with the pulses (both simulated and experimental): gravity center of the spectrum, instantaneous wavelength of the pulse at its maximum and FWHM in the temporal domain.

The effect of the variable focal length makes the spectrum narrower in the focus ( $z = z_0$ ), which corresponds to a longer pulse on axis with an instantaneous wavelength close to the central wavelength of the pulse. This narrowing in the spectrum comes from the fact that the other wavelengths are out of focus, yielding a higher ratio between the spectral intensity of the central wavelength and that of the remaining wavelengths. In contrast, out of the nominal focus $f_c$, the tails of the spectrum are enhanced, which corresponds to a broader (flatter) spectrum and therefore shorter pulses on-axis. As said above, the behavior is quite similar with respect to the focus ($f_c$) and the spectrum: the role played by redder and bluer wavelengths is inverted before and after the focus (both

in the temporal and spectral domains), respectively, for example going from negative to positive chirp. Similar results are obtained for the experiments and the simulations.

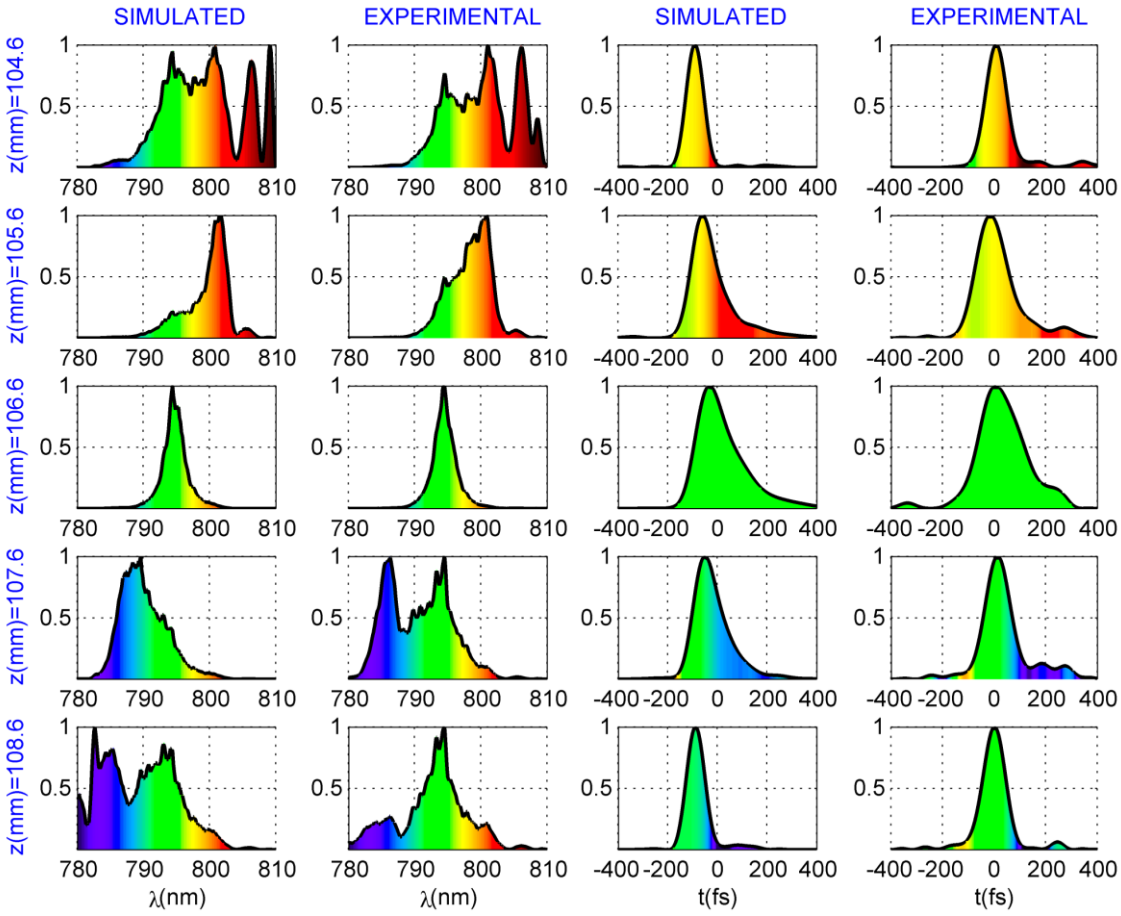


Fig. 6.7. On-axis normalized simulated spectrum (first column) and experimental spectrum (second column), simulated intensity (third column) and experimental intensity (forth column), as a function of the propagation distance (see labels on the left). The spectra are colored by their wavelengths. The same color scale applies to represent the instantaneous wavelength in the temporal intensity plots.

Some discrepancies appear in the spectrum for the last two propagation distances ($z_{+1}$ and $z_{+2}$) in the bluer part of the spectrum. The experimental spectrum used in the simulations was taken from a direct measurement of the pulse on-axis before the KDL (before focusing). The difference observed may be originated by an inhomogeneous spatial profile of the laser beam used in the simulations, which shows up the importance of the quality of the pulses used for certain applications.

Regarding the results of Table 6.1, the central wavelength of the pulses, calculated both as the gravity center of the spectrum and as the instantaneous wavelength of the pulse at its maximum, exhibits a tendency from redder to bluer wavelengths along the optical axis. This behavior tends to saturate at the extremes of the focusing region, since there is no more spectral content beyond the tails of the spectrum of the input pulse. As said before, the pulse duration on-axis at the focus is longer than for the input pulse due to spectral narrowing, whereas in the first and last positions the pulse is shorter because of spectral flattening. These behaviors are explained by the dependence on the wavelength of the focal length of the KDL.

| | Gravity center (nm) | | $\lambda_{inst}$ (nm) | | Time FWHM (fs) | |
|---|---|---|---|---|---|---|
| z(mm) | Simul. | Exper. | Simul. | Exper. | Simul. | Exper. |
| 104.6 | 799.2 | 800.0 | 797.9 | 798.5 | 82.6 | 96.0 |
| 105.6 | 799.4 | 798.3 | 798.0 | 797.1 | 122.4 | 141.3 |
| 106.6 | 794.8 | 794.5 | 794.8 | 794.2 | 165.4 | 187.4 |
| 107.6 | 790.1 | 790.7 | 790.8 | 791.9 | 129.4 | 113.6 |
| 108.6 | 789.5 | 792.8 | 790.7 | 793.1 | 85.5 | 100.7 |

Table 6.1. Spectral and temporal parameters of the pulse measured on axis. $\lambda_{inst}$ stands for the instantaneous wavelength of the pulse at its maximum.

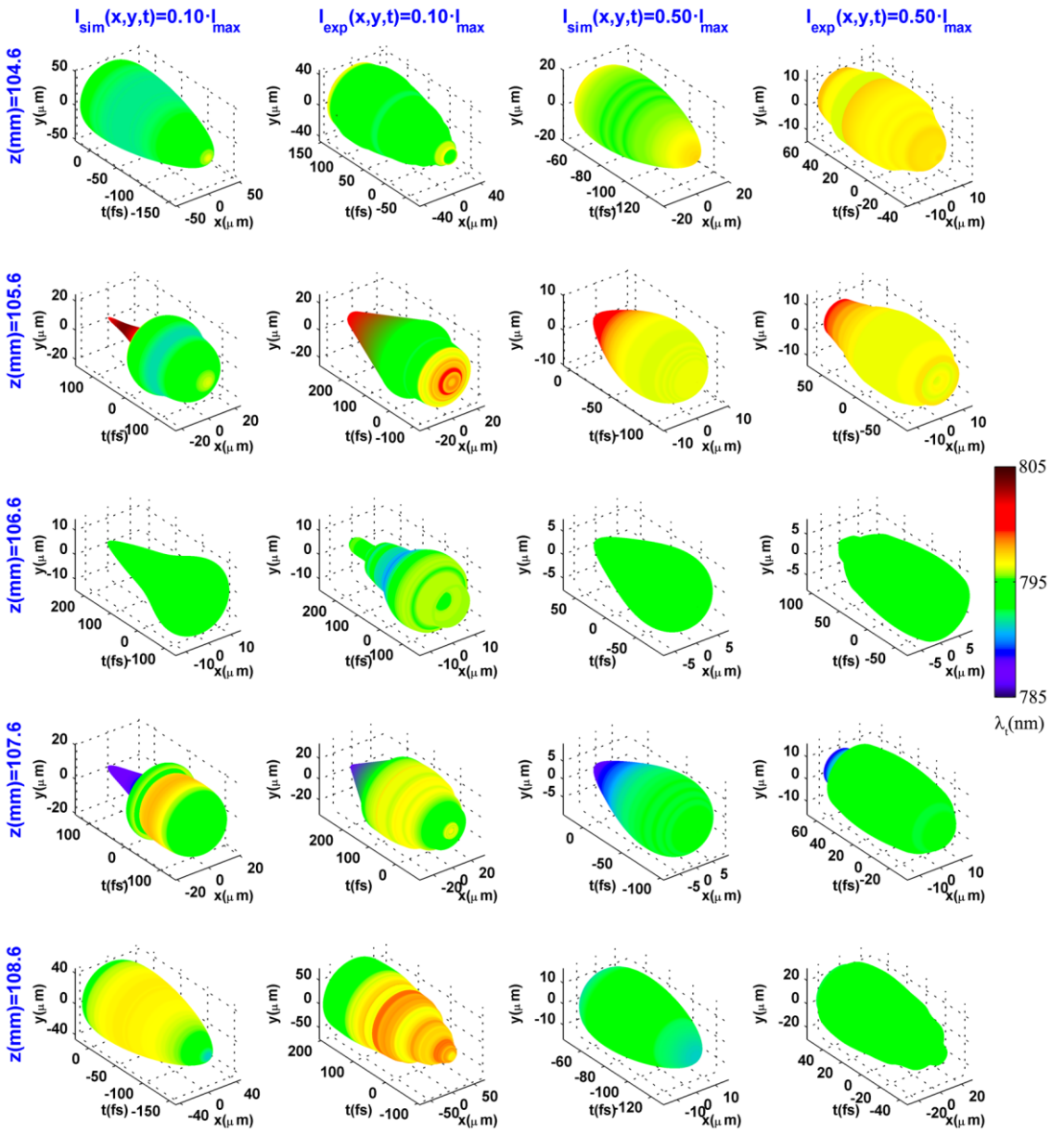


Fig. 6.8. Iso-intensity surfaces $I(x,y,t)=\alpha \cdot I_{max}$, colored by the corresponding instantaneous wavelength (see the colorbar), before and after the focus of the KDL. The results for $\alpha$=0.1 (simulation, 1st column; experiment, 2nd column) and $\alpha$=0.5 (simulation, 3rd column; experiment, 4th column) are shown. Cylindrical symmetry is assumed to obtain the plot.

### *6.4.4 Comparison of the results at different levels of intensity*

Taking advantage of all the information obtained with STARFISH and the cylindrical symmetry of the system, it is possible to depict a representation of the amplitude and phase of the pulse in the spatiotemporal domain. The amplitude is represented as an iso-intensity surface, i.e. $I(x,y,t)=\alpha\cdot I_{max}$ ($\alpha$ being a constant), where cylindrical symmetry has been assumed to extend the results to the spatial variable $y$. The phase is represented by coloring that intensity with the instantaneous wavelength evaluated at the surface $I(x,y,t)$. Each instantaneous wavelength is represented by a color. In Fig. 6.8, the simulated and experimental results for the different propagation distances are compared for the values $\alpha$=0.1 and $\alpha$=0.5. This information gives an idea of the pulse structure and the chirp at different levels of intensity, and may be helpful to understand the pulse dynamics, as well as to predict the output in certain applications without losing the spatial information.

## 6.5. Conclusions

The wavefront reconstruction obtained with STARFISH allows for resolving its wavelength dependence, which is of high interest in many situations, as highlighted in the introduction. In contrast to standard wavefront sensing techniques, our high spatial resolution allows for applying STARFISH to focused beams. We should also emphasize here that STARFISH retrieves the spatiotemporal and spatiospectral amplitude and phases, and constitutes a complete tool for the experimental description of the pulse dynamics. We found that an intrinsic phase drift error exists in the measurements, but its low value (in this case $0.35\cdot 2\pi\, rad$) allows us to reconstruct the wavefronts of the pulses.

We have applied the method for the characterization of DOEs, which is a highly interesting topic nowadays. The wavefront retrieval and the complete study of the pulse dynamics in the focusing region of a KDL were performed. In this context, we studied the frequency resolved wavefronts in the vicinity of the focus, which are responsible for the phase-matching in many nonlinear processes. The spatiotemporal, spatiospectral and on-axis results are also helpful to understand these processes, e.g., the SHG tuning, explained by the spectral waveform modulation due to the focal length dependent on wavelength. In the time domain, the on-axis pulse is longer at the focus because of the spectral narrowing, whereas owing to the opposite effect it is shortened before and after focus.

The experimental results presented in this paper were compared with numerical simulations of the diffracted electric field, presenting an excellent agreement.

## References

[1] G. Mínguez-Vega, C. Romero, O. Mendoza-Yero, J. R. Vázquez de Aldana, R. Borrego-Varillas, C. Méndez, P. Andrés, J. Lancis, V. Climent, and L. Roso, "Wavelength tuning of femtosecond pulses generated in nonlinear crystals by using diffractive lenses," Opt. Lett. 35, 3694-3696 (2010).

[2] C. Yang, K. Shi, H. Li, Q. Xu, V. Gopalan, and Z. Liu, "Chromatic second harmonic imaging," Opt. Express 18, 23837-23843 (2010).

[3] C. Romero, R. Borrego-Varillas, A. Camino, G. Mínguez-Vega, O. Mendoza-Yero, J. Hernández-Toro, and J. R. Vázquez de Aldana, "Diffractive optics for spectral control of the supercontinuum generated in sapphire with femtosecond pulses," Opt. Express 19, 4977-4984 (2011).

[4] V. Moreno, J. F. Román, and J. R. Salgueiro, "High efficiency diffractive lenses: Deduction of kinoform profile," Am. J. Phys. 65, 556-562 (1997).

[5] Y. Fu, H. Xiong, H. Xu, J. Yao, B. Zeng, W. Chu, Y. Cheng, Z. Xu, W. Liu, and S. L. Chin, "Generation of extended filaments of femtosecond pulses in air by use of a single-step phase plate," Opt. Lett. 34, 3752-3754 (2009).

[6] L. Van Dao, K. Ba Dinh, and P. Hannaford, "Generation of extreme ultraviolet radiation with a Bessel-Gaussian beam," Appl. Phys. Lett. 95, 131114 (2009).

[7] B. Alonso, I. J. Sola, O. Varela, J. Hernández-Toro, C. Méndez, J. San Román, A. Zaïr, and L. Roso, "Spatiotemporal amplitude-and-phase reconstruction by Fourier-transform of interference spectra of high-complex-beams," J. Opt. Soc. Am. B. 27, 933-940 (2010).

[8] B. Alonso, R. Borrego-Varillas, O. Mendoza-Yero, I. J. Sola, J. San Román, G. Mínguez-Vega and L. Roso "Frequency resolved wavefront retrieval and dynamics of diffractive focused ultrashort pulses," J. Opt. Soc. Am. B. 29, 1933-2000 (2012).

[9] J. Jasapara and W. Rudolph, "Characterization of sub-10-fs pulse focusing with high-numerical-aperture microscope objectives," Opt. Lett. 24, 777-779 (1999).

[10] B. Alonso, I. J. Sola, J. San Román, Ó. Varela, and L. Roso, "Spatiotemporal evolution of light during propagation in filamentation regime," J. Opt. Soc. Am. B 28, 1807-1816 (2011).

[11] D. Faccio, A. Lotti, A. Matijosius, F. Bragheri, V. Degiorgio, A. Couairon, and P. Di Trapani, "Experimental energy-density flux characterization of ultrashort laser pulse filaments," Opt. Express 17, 8193-8200 (2009).

[12] Min Gu (editor), Chapter 2: "Diffraction Theory" in *Advanced optical imaging theory*, Springer-Verlag (1999).

[13] Z. Bor, "Distortion of femtosecond laser pulses in lenses," Opt. Lett. 14, 119-121 (1989).

[14] O. Mendoza-Yero, B. Alonso, O. Varela, G. Mínguez-Vega, I. J. Sola, J. Lancis, V. Climent, and L. Roso, "Spatio-temporal characterization of ultrashort pulses diffracted by circularly symmetric hard-edge apertures: theory and experiment," Opt. Express 18, 20900-20911 (2010).

# CHAPTER 7

# FRACTAL PULSES AND DISPERSION CORRECTED GRATING

**Contents**



*Some of the results in this chapter were originally presented in O. Mendoza-Yero et al., Opt. Lett. 37, 1145-1147 (2012) and R. Martínez-Cuenca et al., Opt. Lett. 37, 957-959 (2012).*

## 7.1. Introduction

As it has been mentioned in Chapters 5 and 6, diffractive optical elements (DOEs) possess many applications. However, when dealing with femtosecond pulses, their large bandwidth many times destroys the desired effect of the DOE. Since diffraction is a process that inherently depends on the wavelength, the broadband pulses will be afflicted of strong chromatic aberration, dispersive effects or spatial chirp. On the one hand, this effect sometimes acts in favor of the application. For example, the wavelength dependent focal length of a kinoform diffractive lens (KDL) ─seen in detail in Chapter 6─ is the responsible for a strongly chromatic focusing that can be used to tune nonlinear processes as second-harmonic generation (SHG) [1] or supercontinuum generation [2]. On the other hand, the consequences of the wavelength dependence are sometimes negative for the desired application. Since ultrashort laser pulses have a broadband spectrum, in these cases is necessary to design strategies to correct the chromatic distortion of the DOEs.

This way, current femtosecond laser systems provide pulse energies far exceeding the energy required for many of their applications. This fact has motivated the generation of multiple beams ("multibeams") from the same laser beam in order to be used in parallel. For this purpose, DOEs and microlens arrays and have been used for applications of multibeams in material processing [3-5] and multiphoton microscopy [6-8], for example. In the case of DOEs, diffraction grating before the focusing lens can be used to generate multibeams. However, spatial chirp induced by wavelength-dependent diffraction produces spatiotemporal spreading of the multiple foci with a subsequent reduction of peak intensity. To compensate for the chromatic response when using femtosecond pulses, a dispersion compensating module was proposed by the group of GROC-UJI (Castellón, Spain) [9]. In collaboration with that group, we have applied STARFISH (Chapter 4, [10]) for the characterization of the multibeam foci with and without compensation of the dispersion, which subsequently they have applied to multibeam SHG [11]. The experiments presented in this chapter were performed in the laboratory of the GROC-UJI.

Moreover, the application of DOEs for pulse-shaping of ultrashort laser pulses based on the self-similarity of the light will also be presented. Here, the term self-similarity refers to the fact that in some situations a direct correspondence exists between the shape of the pulses in the spatial domain and the temporal or frequency domains, which can be caused by different reasons both in linear and nonlinear regimes. This correspondence can be used to generate fractal light pulses [12] that have a growing number of applications, e.g. for microwave antennas [13] and photonic crystals [14]. In this chapter, we will demonstrate the application of quasi-direct space-to-time (QDST) shaping [15,16] for the synthesis of fractal pulses using a fractal plate [17]. The expression "quasi-direct" is used to illustrate that the transformation is made between the squared radial coordinate and time (instead of being directly from the spatial coordinate). In [16], the authors used spatially-resolved cross-correlation to experimentally demonstrate the operation of the QDST.

In the two applications presented in this chapter ─fractal pulses [17] and dispersion compensated multibeams [11]─ the theoretical design of the optical systems and the numerical simulations were carried out by the GROC-UJI. We applied the STARFISH technique in the experiments to corroborate the response predicted by the theory. The spatiotemporal characterization of the diffracted pulses gives the ultimate validation of the proposal and can be used as feedback in the process of design. Finally, we will briefly present the optical schemes and then we will focus on the characterization of the pulses.

## 7.2. Synthesis of fractal pulses by quasi-direct space-to-time shaping

### *7.2.1. Theory and design of fractal pulses*

One of the first studies on geometric self-similarities was the pioneering work of Mandelbrot about the fractal geometry of nature [18]. For example, self-similarity is present in the propagation of light in high power laser cavities [19]. In the field of optics, the first contributions on self-similarity addressed the analysis of light scattered and diffracted by fractal structures usually known as diffractals [20-22]. Diffractals are beams that have gone through a fractal aperture [20]. Their propagation in space and time produces the diffraction pattern of the fractal aperture [23].

More recently, a family of diffracting apertures known as fractal zone plates (FZPs) has been introduced [24], with applications, for example, in the generation of optical vortices [25]. FZPs are sets of circularly symmetric apertures with spatial self-similar distribution in $r^2$, where $r$ is the radial coordinate. Fractal generalized zone plates (FraGZPs) have been shown to produce self-similar irradiance patterns along the optical axis [26]. To our knowledge, reports of the self-similar behavior of fractal plates have been limited to the spatial or spectral domains, with no mention of similar effects in the time domain. Here, we demonstrate that a KDL can be used to generate self-similar light pulses from any set of circularly symmetric fractal plates (i.e., FZPs or FraGZPs) [17].

The proposal is based on the use of a diffractive pulse shaper that was introduced theoretically in [15]. The QDST shaper is composed of a FZP and a KDL, which are located together. The shaper is illuminated with a spatially plane wave and temporally ultrashort pulsed light. Its output is located at the focal point of the KDL ( $z = z_0$ ) for the central wavelength of the pulse $\lambda_0$, where the light distribution is both temporally shaped and spatially focused. Under few-cycle pulses illumination, the spatial features of plates are mapped into the time domain [15]. FZPs are constructed from the fractal structures known as the Cantor set. The construction process is controlled by two parameters: the generator $N$ and the stage of growth $S$ (the definition can be found in Eq. 2 of reference [15]). In this work, we used FZPs with $N = 2$ and $S = 0,1,2$. The maximum extension of the FZP is $4.33mm$. The details of the FZPs transmittance function and fabrication can be found in [17]. In Fig. 7.3, the three FZPs used in the experiments can be seen.

The optical setup for the generation and characterization of the fractal pulses is shown in Fig. 7.1. We used STARFISH [10] for the spatiotemporal diagnostic of the temporally shaped, spatially focused output pulses. We used a Ti:sapphire laser source that delivers $\sim 35\,fs$ intensity full-width at half maximum (FWHM) pulses with central wavelength $795nm$ and a repetition rate of $1kHz$. The laser is split into two beams: the reference beam and the test beam. The test beam is spatially expanded with a $4\times$ all-mirrors beam expander before the shaper. At the focus of the KDL, the optical fiber of the test arm spatially scans the pulse in the transverse direction to its propagation axis.

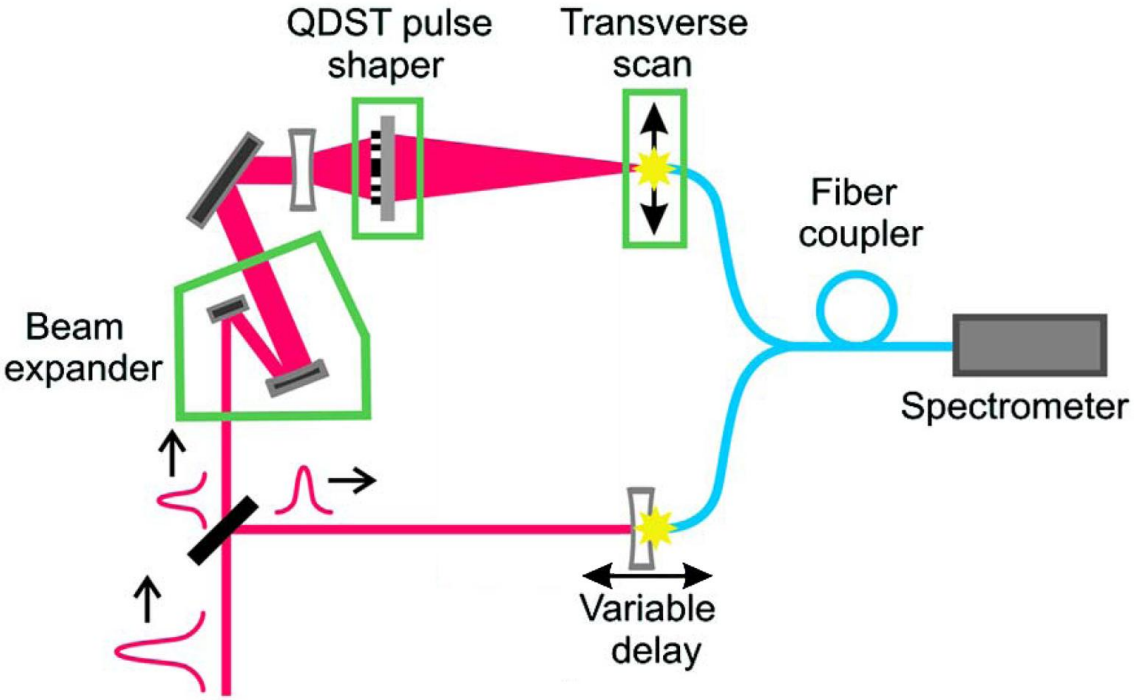


Fig. 7.1. Experimental setup for the production and measurement of temporally shaped self-similar ultrashort pulses. The quasi-direct space-to-time (QDST) shaper consists of a fractal zone plate and a kinoform diffractive lens.

For our experiment, the KDL has a focal length of $z_0 = 50mm$ for the central wavelength of the pulse ($\lambda_0 = 800nm$). Hence, the numerical aperture ($NA$) at the focal plane $z = z_0$ is $NA = 0.087$, which is slightly lower than the $NA$ provided by the fiber's manufacturer ($NA = 0.11 \pm 0.01$). To achieve a better coupling of light into the optical fiber, the $NA$ of the system was further reduced by including a divergent lens ($f = -40mm$) a few millimeters before the entrance of the shaper (see Fig. 7.1). By doing so, the output plane of the optical system was increased until the value $z = 200mm$ resulting in $NA = 0.02$, which prevented distortion of the light coming from the outer rings.

The dispersion introduced by the divergent lens material is pre-compensated by using the prisms compressor of the laser system. Because this compensation also affects the light at the reference arm, we added an equal lens just before the entrance of the corresponding optical fiber. In our experiment, the spectral phase of the reference pulse is obtained on-axis by means of a SPIDER measurement with a commercial device (LX Spider, Ape GmbH). The amplitude and phase of the reference pulse characterized in

the spectral and the temporal domain are shown in Fig. 7.2a and 7.2b, respectively. The temporal reconstruction of the SPIDER had an intensity FWHM of 33 fs. The spectral amplitude was measured directly with the spectrometer used for STARFISH.

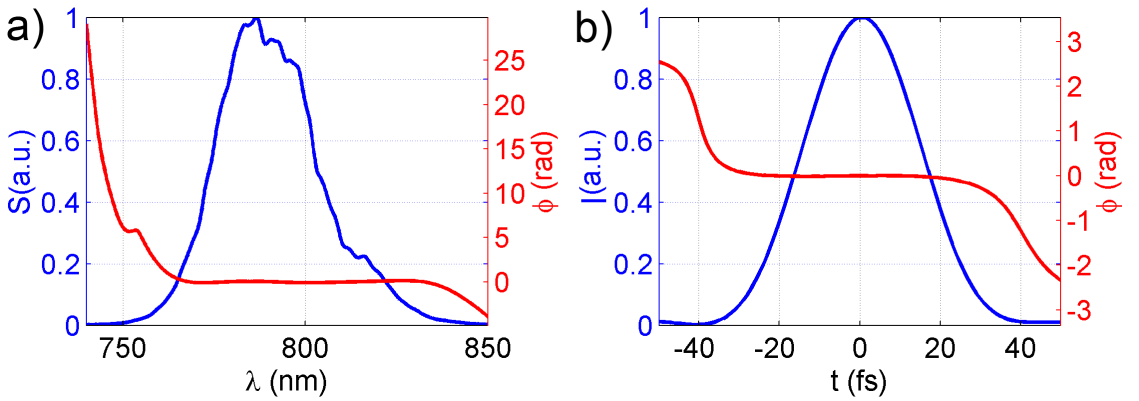


Fig. 7.2. Characterization of the reference pulse in the (a) spectral and (b) temporal domains.

### *7.2.2. Experimental and theoretical results: discussion*

The FZPs considered for the experiments are given in the left column of Fig. 7.3, with $S = 0,1,2$ respectively. The normalized spatiotemporal intensity for the numerical simulations and for the experiments is compared. The results are presented in logarithmic scale to highlight the details. The simulations were determined in the frequency-domain by means of the generalized Huygens-Fresnel integral for each frequency component of the pulse, followed by Fourier transforming to obtain the temporal domain.

For the first plate (S=0), the spatiotemporal is similar to the focus of the DOEs that we have already characterized in Chapters 5 and 6. For the FZPs with S=1 and S=2, a temporal modulation with respect to the spatiotemporal intensity for S=0 reveals a clear mapping between the squared radial coordinate in the FZP and the temporal coordinate in the focus of the pulse. From Fig. 7.3, it can be seen that the fractal behavior of the light is mainly concentrated within the spatial interval from $-10\mu m$ to $10\mu m$. This is consistent with the fact that the working zone of the shaper is expected for points in the close vicinity of the optical axis [15], where the previous analysis holds.

The experimental spatiotemporal electric fields are in agreement with the theoretical results. We believe that the small discrepancies observed in Fig. 7.3 are mainly caused by the deviations of the real pulse from the ideally assumed plane-wave and few-cycle incident pulse, since the effect of the numerical aperture is discarded. In addition, the convolution of the incident electric field amplitude (having a finite temporal width) with the transmittance function of the mask causes the synthesized pulses to suffer from temporal stretching (when comparing to the input pulses similar to the reference characterization of Fig. 7.2b). As a result, the pulses in the vicinity of the axis are no longer square but temporally Gaussian-like pulses, specially for $S = 2$.

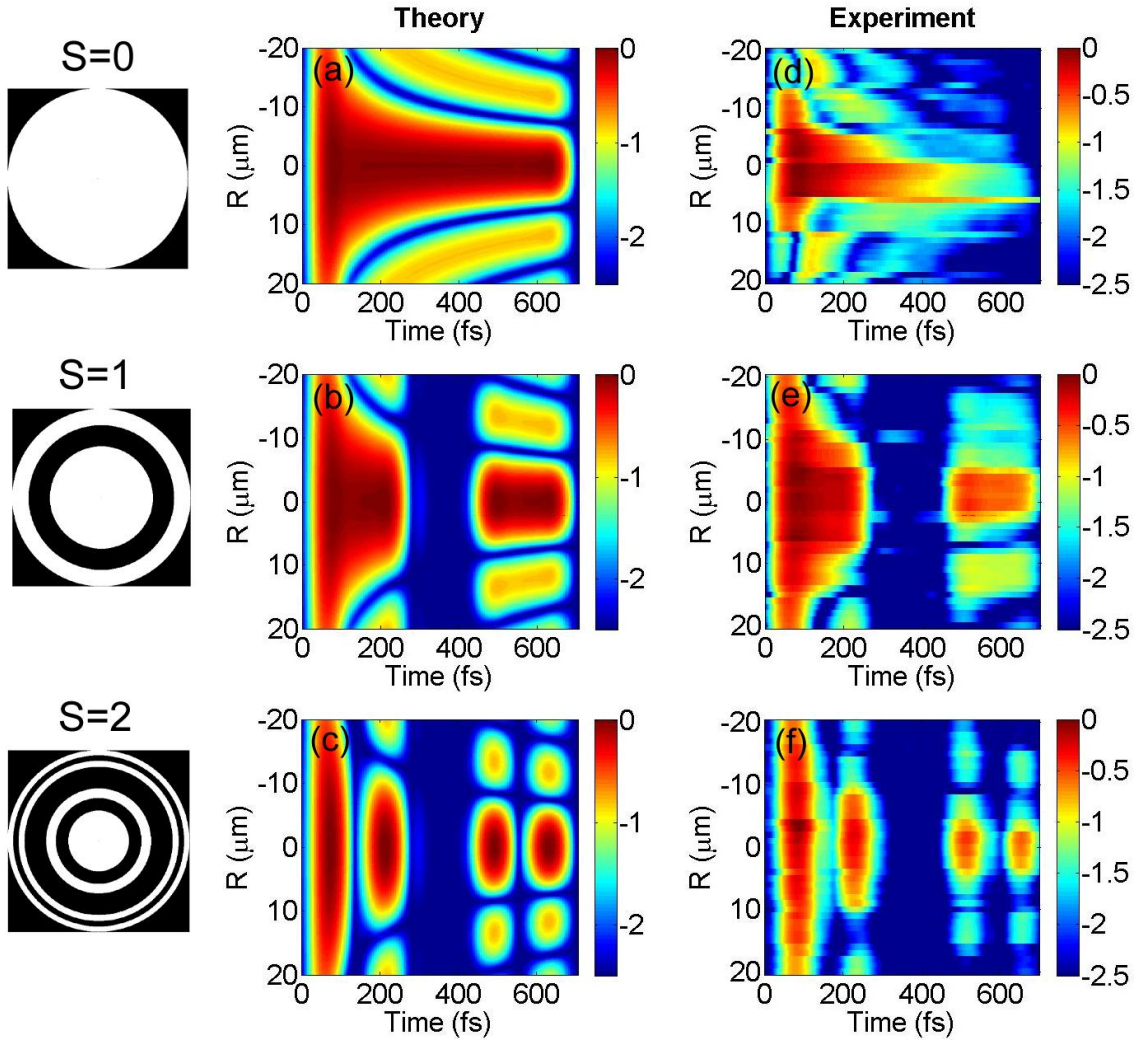


Fig. 7.3. Spatiotemporal characteristics of the synthesized ultrashort fractal pulses. Numerical simulations (a-c) and corresponding experimental results (d-f).The FZPs are included in the left-column.

The spatially-resolved spectrum for the same cases is represented in Fig. 7.4 (first column). For the first plate (S=0), the spatiospectral distribution presents an x-shape (Fig. 7.4a), which is again characteristic of a DOE focus. For S=1 and 2, it can be seen that the spectrum presents a modulation inherited from the structure of the transmittance function of the FZPs (Fig. 7.4d and 7.4g). As said before, when far from the axis (that is, for $R \gg 0$), the fractal structure is lost. The spectrum on axis is shown in Fig. 7.4 (second column), in order for the modulation of axis to be seen more clearly. The corresponding on-axis intensities are plotted in Fig. 7.4 (third column). The effect of the contribution of the zones of the different FZPs can be distinguished in the on-axis spectrum and intensity. For example, from Fig. 7.4f and 7.4i (S=1 and 2), it can be seen that the fractal structure is the same, except for the double pulse structure for S=2 compared to S=1. This is clear evidence of the space-to-time mapping from the respective FZPs (see the transmittance of the zone plates in Fig. 7.3).

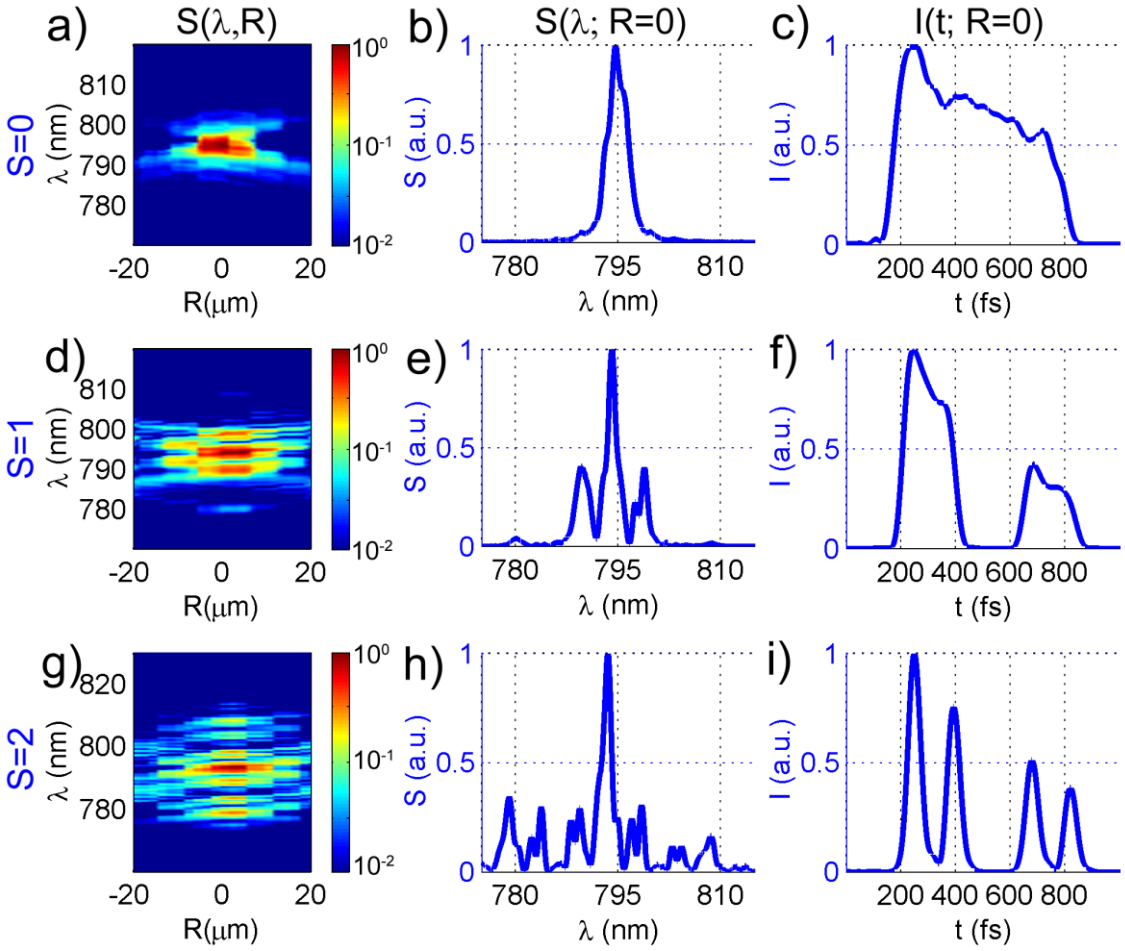


Fig. 7.4. Spatiospectral distribution (first column: a,d,g), on-axis spectrum (second column: b,e,h) and on-axis intensity (third column: c,f,i) for the same set of FZPs than in Fig. 7.3 (S=0 first row, S=1 second row, S=2 third row).

There is a noticeable difference between the theoretical and the experimental amplitude of the train of fractal pulses. In the simulation, the amplitude of the pulses is the same (on axis, for $R = 0$), whereas in the experiment the amplitude decreases as a function of time. In fact, the envelope of the train of pulses for S=1 and S=2 (Fig. 7.4f and 7.4i) is the pulse measured for S=0 (Fig. 7.4c), that is, with the "empty" mask. For this reason, we conclude that the origin is not to be with the FZPs. Different hypotheses could explain this difference. In fact, we believe all of these hypotheses contribute to the experimental observation. Firstly, despite using a beam expander, the beam illuminating the QDST shaper is not perfectly a plane wave (in spatial terms). This fact is combined with the efficiency of the KDL, which is lower off-axis compared to the center owing to the design for the manufacturing process. Additionally, the numerical aperture of the fiber coupler is less efficient in collecting the light with oblique incidence. Because of the space-to-time mapping, it contributes to reduce gradually the amplitude of the pulses coming from the outer part of the shaper, which are the rear pulses. Furthermore, we had another hypothesis, related to the Fourier-transform (FT) and the delay. We wondered if the different delay of each pulse of the train with respect to the reference pulse, as well as the FT algorithm, could induce a temporal modulation of the amplitude of the pulse train. For this reason, we measured the spectral interferences with the

reference pulse before (as usual) and after the test pulse (for S=2 on-axis). In Fig. 7.5a and 7.5b, a zoom is plotted on the right-hand peak of the inverse FT (IFT) of the interferences for the reference before and after, respectively. Owing to the exchange of positions between the reference and the test pulse, a subsequent flip of the IFT signal (in the time axis) appears, as it is observed. Since the signal is simply time reversed, but the amplitudes are preserved, we concluded that the FT algorithm and the delay have no effect on this.

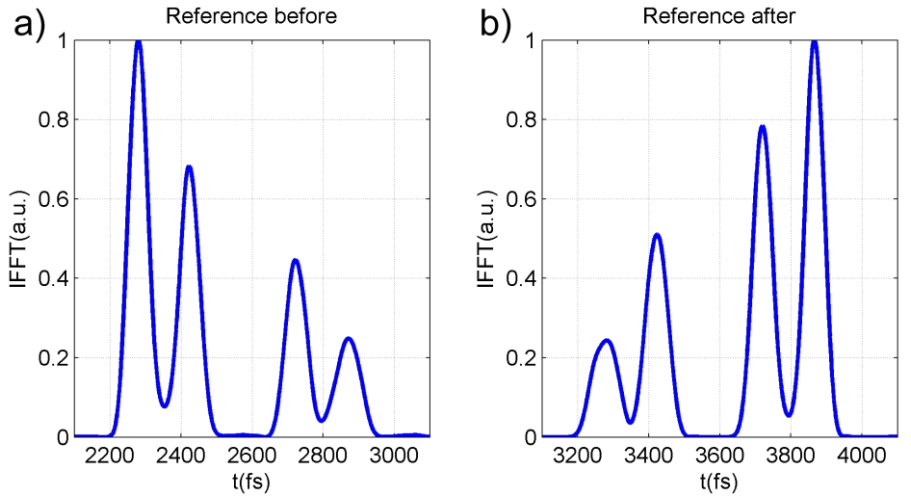


Fig. 7.5. Zoom of the right-hand side peak of the inverse Fourier-transform (IFT) of the spectral interferences of the reference and test pulse (S=2, on-axis R=0), with the reference pulse (a) before and (b) after the test pulse.

## 7.3. Dispersion corrected diffraction grating

As explained in Section 7.1, the bandwidth limitation is a characteristic of all diffractive optics when used with a broadband source, such as ultrashort laser pulses. An approach to the creation of multiple focused beams from a single laser input consists in the use of a diffraction grating that splits the laser beam into several diffracted beamlets, which are focused by an achromatic objective to produce an array of focal spots as illustrated in Fig. 7.6a.

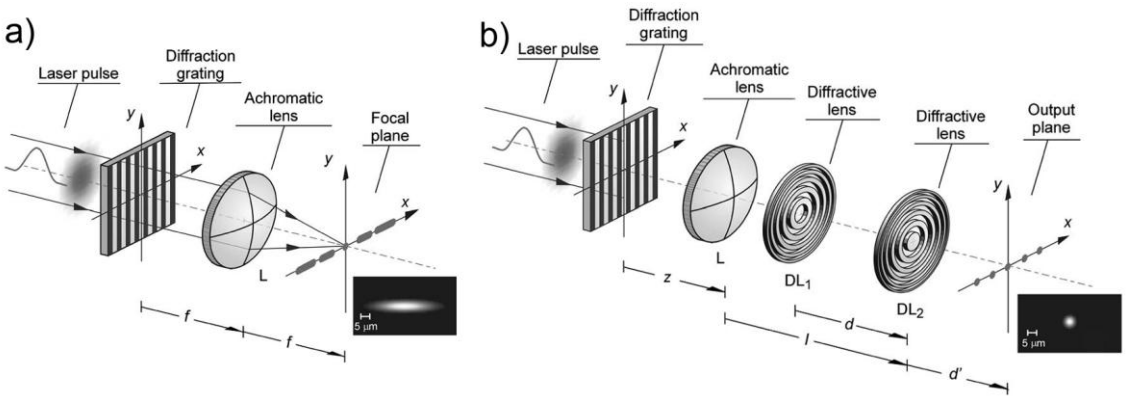


Fig. 7.6. (a) Conventional diffraction-grating-based multifocal generation. Inset, chromatic elongated fifth-order diffraction spot. (b) Dispersion compensated module for diffraction-grating-based multifocal generation with femtosecond pulses. Inset, compensated fifth-order diffraction spot. Figures extracted from [9].

Owing to the angular dispersion of the grating, each wavelength is focused at a different transverse position, which results in an elongated light spot, except for the zero-order (Fig. 7.6a). Also, the spots will be afflicted by the temporal stretching. Different solutions have been proposed to compensate for the chromatic distortion [9,27,28].

Here, the use of a diffractive lens pair [9] for the compensation (Fig. 7.6b) is experimentally demonstrated and then is applied to multibeam SHG [11]. We will measure different diffraction orders from DOE with and without the compensation of the dispersion. The multiple focal spots will be characterized in the spatiotemporal domain by means of STARFISH [10] to be compared.

We used ultrashort laser pulses from a mode-locked Ti:sapphire laser (Femtosource, Femtolaser) with pulse durations of 28 fs (amplitude FWHM), central wavelength $\lambda_0 = 800nm$, a bandwidth of approximately $80nm$, $1kHz$ repetition rate and maximum energy per pulse of $0.8mJ$. The energy per pulse was controlled by means of a variable attenuator composed of a half-wave plate and a polarizer and the beam width was fixed after a reflective beam expander. A pair of fused silica Brewster prisms pre-compensated the group delay dispersion (GDD) in the beam delivery path until the observation plane. Fig. 7.7 shows the experimental setup. The laser pulses after the DOE ─by virtue of the beam delivery optics (inside the dashed box)─ generate multiple foci onto its back focal plane (FP).

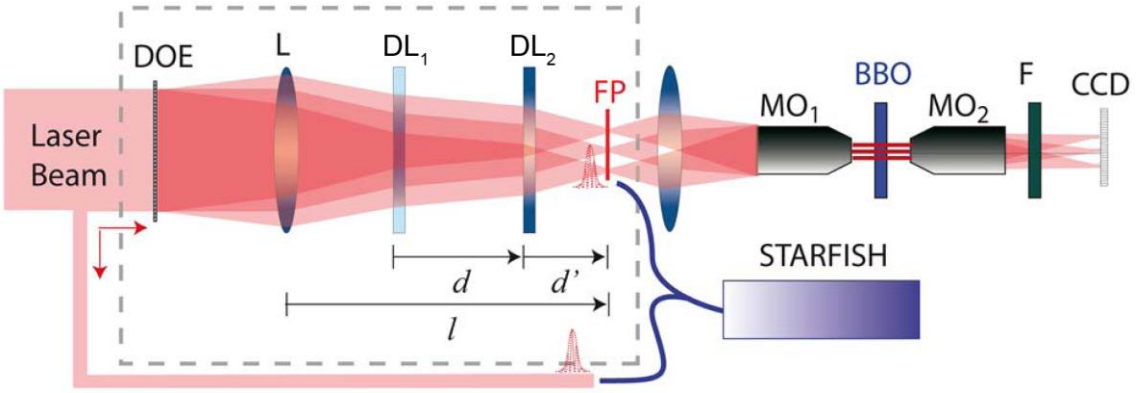


Fig. 7.7. Experimental setup with the module for the chromatic dispersion compensation, the characterization with the STARFISH technique, and the generation of arbitrary patterns of second-harmonic generation (SHG) in a nonlinear crystal (BBO). DOE = diffractive optical element, L = achromatic lens, DL = diffractive lenses, FP = focal plane, MO = microscope objectives, F = blue filter.

The beam delivery is carried out by means of an achromatic lens $L$ (with focal length $f$) coupled to a diffractive lens pair ($DL_1$, $DL_2$) as was introduced in [9]. The focal lengths of $DL_1$ and $DL_2$ for the central wavelength $\lambda_0$ are denoted by $f_{o1}$ and $f_{o2}$, respectively. Firstly, the system acted as a Fourier transformer for $\lambda_0$, i.e. the field at FP is the Fourier-transform of the field in the DOE plane for $\lambda_0$. In a second step, it was designed to avoid the spatial chirp (the spatial spreading) at every diffraction order and that all the rays coming from the DOE have the same arrival time at FP. Although exact compensation is not possible, the imposition of first-order or achromatic correction led to the geometrical constraints, $l = f$, $d^2 = -f_{o1} f_{o2}$, and $d' = -d^2/(d + 2f_{o1})$. The

derivation of these relations is done by cancelling the first-order dispersion of the transformation matrix from the DOE to the FP, as well as the first-order temporal stretching of the pulse (see the details in [9]). As a result, the actual foci provided by the dispersion compensating module shows a slight spatial and temporal stretching with respect to the ideal transform-limited spots. To compare the optical features of our proposal with the uncompensated case, we simply removed the diffractive lens pair, and displaced the achromatic lens $L$ just to locate its back focal plane at FP. The multiple foci were created with a Ronchi grating acting as a DOE, which distributed the incident radiation in different diffraction orders at the output FP. A Ronchi grating is a specific grating with $a = 2b$, $a$ being the spacing of the grating and $b$ the width of the slit. The position of the diffracted orders is determined by the period of the grating. For STARFISH, the spectral phase of the reference pulse was obtained on-axis by means of an interferometry measurement with a SPIDER device. The relative delay between the test and reference pulses was between 2-3 ps.

For the experimental implementation we constructed the optical setup shown in Fig. 7.7, where the parameters are $f = 200mm$, $f_{o1} = -150mm$, $f_{o2} = 150mm$ and numerical aperture $NA = 0.02$, and we used a Ronchi grating with fundamental frequency $\nu_s = 11.8\, grooves/mm$.

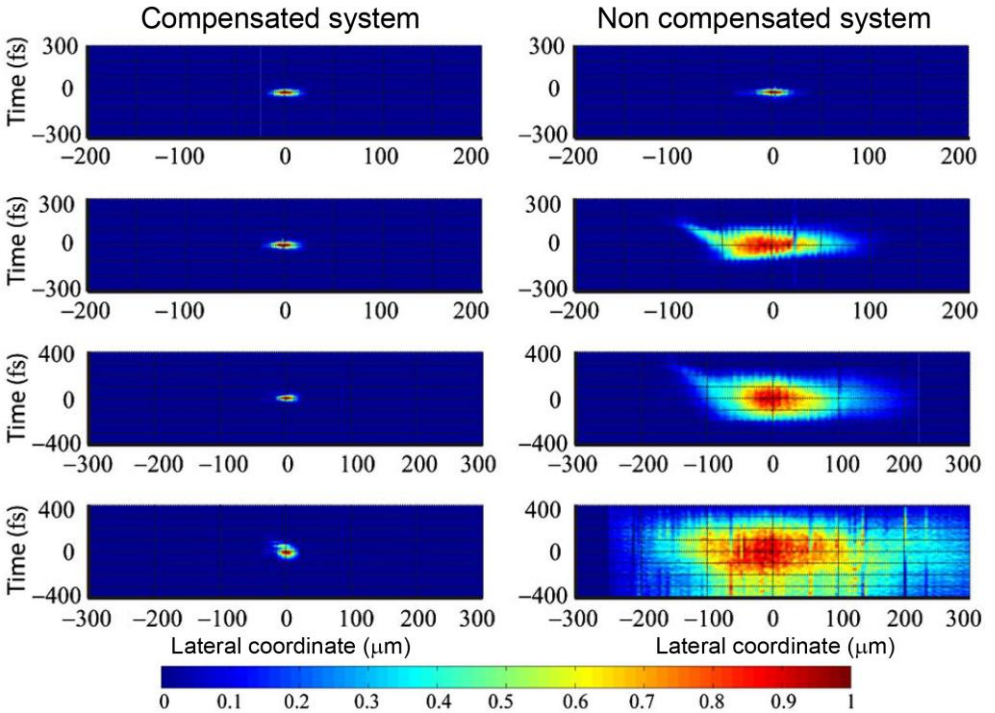


Fig. 7.8. Normalized spatiotemporal light intensity after low NA focusing of the beamlets coming from a DOE (m=0, +1, +2, and +3 diffraction orders from top to bottom) with (left column) and without (right column) dispersion compensating module. The maximum frequency component, for the 3rd diffraction order, is 35.4 gr/mm.

The spatiotemporal intensity of the different orders at the output plane FP, measured with STARFISH, is shown in Fig. 7.8. Since dispersion occurs in the horizontal axis, we spatially scanned only the horizontal axis ($x$-axis) in the output plane. The scan was performed through the line with the maximum irradiance for the

diffractive foci. We checked that in the vertical axis ( $y$ -axis) there was translational symmetry, except for amplitude decay. In the present measurements there is an indetermination in the pulse front tilt, since we are not able to assure that the spatial scan was done perfectly perpendicular to the optical axis. Left and right columns show the normalized spatiotemporal light distribution corresponding to the m=0, +1, +2, and +3 diffraction orders with and without dispersion compensating module, respectively. The capability of the dispersion compensating module to compensate dispersive stretching is noticeable at increasing frequency components of the grating that are located at outer regions of FP. The root-mean-square (RMS) widths for both spatial and temporal coordinates of the compensated foci (left column) are $2\sigma_x = 18.0\mu m$ and $2\sigma_t = 26.8\, fs$ (m=0), $2\sigma_x = 18.6\mu m$ and $2\sigma_t = 27.5\, fs$ (m=+1), $2\sigma_x = 18.7\mu m$ and $2\sigma_t = 31.9\, fs$ (m=+2) and $2\sigma_x = 19.3\mu m$ and $2\sigma_t = 63.2\, fs$ (m=+3). The widths remain nearly constant up to frequency components of about 30 gr/mm. Some ripples can be noticed in the temporal profile and are due to non-compensated third-order dispersion (TOD) in the glass components. Also radial GDD effects are apparent for the higher spatial frequencies [9]. The foci generated without dispersion compensating module suffer from a higher spatiotemporal stretching (even one order of magnitude for the higher spatial frequencies). Specifically only 10%, 2.5%, and 0.5% of the peak-power for the compensated foci are available for the spatiotemporal stretched diffraction orders m=+1, +2, and +3 in the non-compensated case, respectively. This fact limits the capability to generate simultaneous SHG with the DOE.

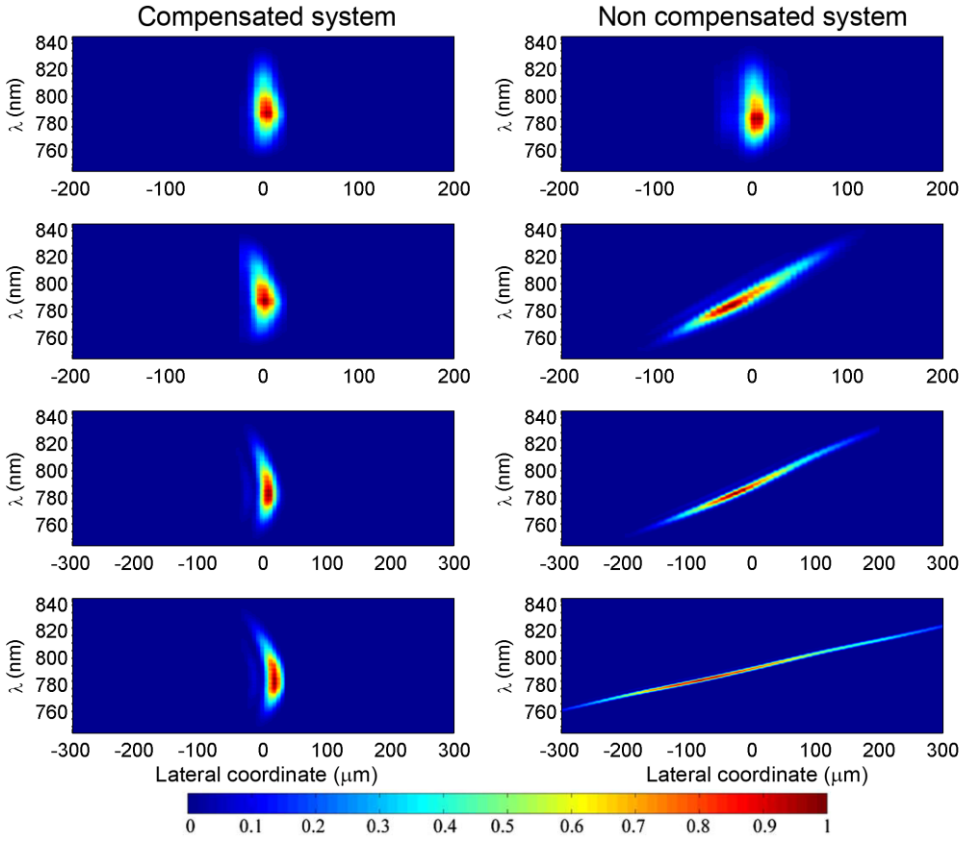


Fig. 7.9. Normalized spatially-resolved spectrum after low NA focusing of the beamlets coming from a DOE (m=0, +1, +2, and +3 diffraction orders from top to bottom) with (left column) and without (right column) dispersion compensating module.

The spatiotemporal distributions previously presented have also a manifestation in the spatiospectral domain (Fig. 7.9). The spatial chirp for the different orders without dispersion compensation is strongly noticeable as the diffraction order m increases (right column). For the compensated case, the spatial width is preserved up to m=+3 and the spectrum distortion is minimized (left column). In Fig. 7.9, it can be observed that even for the compensated case (left column) the chromatic compensation achieved grows worse as the diffraction order increases.

By way of an example, we present the application of the compensation system presented above to produce arbitrary irradiance patterns of SHG, which was done by researchers of the GROC-UJI. After the output plane (FP), an additional lens was used to cover the full aperture of a 10× microscope objective $MO_1$ (conjugated at 160 mm, NA=0.25), in order to make a reduced image of the diffractive foci at the sample, in our case a BBO crystal with a thickness of $20\mu m$ (see Fig. 7.7). Additional optics introduces extra GDD and TOD. Although GDD was compensated by tuning the prism pair to maximize the SHG yield, TOD prevents from achieving a transform-limited 28 fs (amplitude FWHM) pulse at the sample. The spatial resolution is fixed by the numerical aperture of the microscope and is estimated at $1.53mm$.

To observe the SHG signal, the BBO crystal is imaged onto a conventional CCD sensor (Ueye UI-1540M) by means of a 10× microscope objective $MO_2$ also conjugated at 160 mm. A suited filter F (BG39-Schott crystal) was placed before the CCD camera to absorb the remaining infrared radiation (not up-converted) coming directly from the laser. A Fourier DOE was utilized in which the complex Fourier transform of a "smiling face" was encoded in amplitude as an off-axis binary computer generated hologram. The computer reconstruction of the Fourier DOE shows a set of more than 100 diffractive foci. The spatial spectrum of the sample spreads from around 5 gr/mm to about 40 gr/mm. Irradiance uniformity of the foci is estimated at 65%. Results of the recorded SH signal are shown in Fig. 7.10 without (Fig. 7.10a) and with (Fig. 7.10b) the dispersion compensating module. For the uncompensated system, only the lower spatial frequencies are able to excite SHG signal for the present input energy.

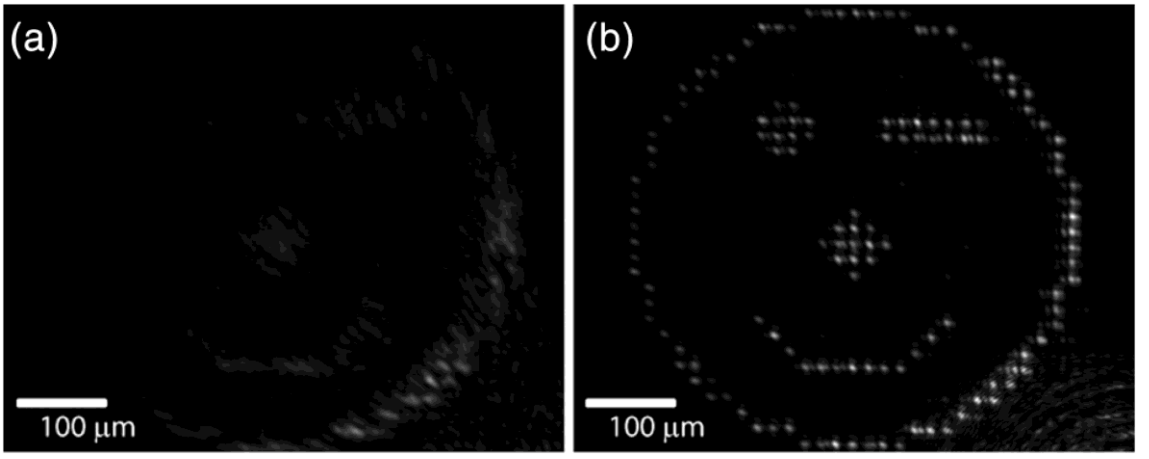


Fig. 7.10. SHG signal from a BBO crystal illuminated with a multispot pattern originated from a DOE without (a) and with (b) the dispersion compensating module.

## 7.4. Conclusions

Firstly, we demonstrate that DOEs can be used for shaping ultrashort laser pulses. The output pulses are characterized in the spatiotemporal domain with STARFISH and numerically simulated with Huygens-Fresnel diffraction, and present good agreement between them. We propose the use of fractal zone plates to generate fractal pulses in the spatiotemporal domain from quasi-direct space to time mapping thanks to self-similarity. Fractal pulses are generated with different masks combined with a KDL. This can be used to originate different fractal pulses.

Secondly, we compensate the dispersion of a DOE consisting of a Ronchi diffraction grating when using ultrashort pulses. The chromatic compensation is achieved with a pair of diffractive lenses. We corroborate experimentally that spatiotemporal stretching of the diffraction orders $m \neq 0$ is prevented with this system. This way, multiple foci can be generated without a severe loss of peak irradiance. GROC-UJI has applied it to create an arbitrary irradiance pattern of SHG with multiple beams produced from intense ultrashort pulses delivered by a Ti:sapphire amplifier.

We expect that DOEs can continue to be used in applications with ultrashort laser pulses. In general, the spatiotemporal distribution of the pulses has a complex space-time structure and coupling, so a full experimental characterization is very helpful to evaluate the process or to assist in its design.

## References

[1] G. Mínguez-Vega, C. Romero, O. Mendoza-Yero, J. R. Vázquez de Aldana, R. Borrego-Varillas, C. Méndez, P. Andrés, J. Lancis, V. Climent, and L. Roso, "Wavelength tuning of femtosecond pulses generated in nonlinear crystals by using diffractive lenses," Opt. Lett. 35, 3694-3696 (2010).

[2] C. Romero, R. Borrego-Varillas, A. Camino, G. Mínguez-Vega, O. Mendoza-Yero, J. Hernández-Toro, and J. R. Vázquez de Aldana, "Diffractive optics for spectral control of the supercontinuum generated in sapphire with femtosecond pulses," Opt. Express 19, 4977-4984 (2011).

[3] Y. Kuroiwa, N. Takeshima, Y. Narita, S. Tanaka, and K. Hirao, "Arbitrary micropatterning method in femtosecond laser microprocessing using diffractive optical elements," Opt. Express 12, 1908-1915 (2004).

[4] Z. Kuang, W. Perrie, J. Leach, M. Sharp, S. P. Edwardson, M. Padgett, G. Dearden, and K. G. Watkins, "High throughput diffractive multi-beam femtosecond laser processing using a spatial light modulator," Appl Surf. Sci. 255, 2284-2289 (2008).

[5] K. Obata, J. Koch, U. Hinze, B. N. Chichkov, "Multi-focus two-photon polymerization technique based on individually controlled phase modulation," Opt. Express 18, 17193-17200 (2010).

[6] A. H. Buist, M. Müller, J. Squer, and G. J. Brakenhoff, "Real time two-photon absorption microscopy using multi point excitation," J. Microsc. 192, 217-226 (1998).

[7] L. Sacconi, E. Froner, R. Antolini, M. R. Taghizadeh, A. Choudhury, and F. S. Pavone, "Multiphoton multifocal microscopy exploiting a diffractive optical element," Opt. Lett. 28, 1918-1920 (2003).

[8] N. Ji, J. C. Magee, and E. Betzig, "High-speed, low-photodamage nonlinear imaging using passive pulse splitters," Nat. Meth. 5, 197-202 (2008).

[9] G. Mínguez-Vega, J. Lancis, J. Caraquitena, V. Torres-Company, and P. Andrés, "High spatiotemporal resolution in multifocal processing with femtosecond laser pulses," Opt. Lett. 31, 2631-2633 (2006).

[10] B. Alonso, I. J. Sola, O. Varela, J. Hernández-Toro, C. Méndez, J. San Román, A. Zaïr, and L. Roso, "Spatiotemporal amplitude-and-phase reconstruction by Fourier-transform of interference spectra of highcomplex-beams," J. Opt. Soc. Am. B 27, 933–940 (2010).

[11] R. Martínez-Cuenca, O. Mendoza-Yero, B. Alonso, I. J. Sola, G.Mínguez-Vega, and J. Lancis, "Multibeam second-harmonic generation by spatiotemporal shaping of femtosecond pulses," Opt. Lett. 37, 957-959 (2012).

[12] M. Segev, M. Soljačić, and J. M. Dudley, "Fractal optics and beyond," Nature Photon. 6, 209-210 (2012).

[13] K. J. Vinoy, K.A. Jose, K. K. Varadan, and V. V. Varadan, "Hilbert curve fractal antenna: a small resonant antenna for VHF/UHF applications," Microwave Opt. Technol. Lett. 29, 215-19 (2001).

[14] S. W. Wang, X. Chen, W. Lu, M. Li, and H. Wang, "Fractal independently tunable multichannel filters," Appl. Phys. Lett. 90, 211113 (2007).

[15] G. Mínguez-Vega, O. Mendoza-Yero, J. Lancis, R. Gisbert, and P. Andrés, "Diffractive optics for quasi-direct space-to-time pulse shaping," Opt. Express 16, 16993-16998 (2008).

[16] V. Loriot, O. Mendoza-Yero, G. Mínguez-Vega, L. Bañares, and R. de Nalda, "Experimental Demonstration of the Quasi-Direct Space-to-Time Pulse Shaping Principle", IEEE Photonics Technology Letters 24, 273-275 (2012).

[17] O. Mendoza-Yero, B. Alonso, G. Mínguez-Vega, I. J. Sola, J. Lancis, and J. A. Monsoriu, "Synthesis of fractal light pulses by quasi-direct space-to-time pulse shaping," Opt. Lett. 37, 1145-1147 (2012).

[18] B. B. Mandelbrot, "The Fractal Geometry of Nature," 2nd ed. (Freeman, New York, 1982).

[19] J. M. Dudley, C. Finot, D. J. Richardson, and G. Millot, "Self-similarity in ultrafast nonlinear optics," Nat. Phys. 3, 597-603 (2007).

[20] M. V. Berry, "Diffractals," J. Phys. A 12, 781-797 (1979).

[21] C. Allain and M. Cloitre, "Spatial spectrum of a general family of self-similar arrays," Phys. Rev. A. 36, 5751-5757 (1987).

[22] D. A. Hamburger-Lidar, "Elastic scattering by deterministic and random fractals: Self-affinity of the diffraction spectrum," Phys. Rev. E 54, 354-370 (1996).

[23] R. Verma, V. Banerjee, and P. Senthilkumaran, "Redundancy in Cantor Diffractals," Opt. Express 20, 8250-8255 (2012).

[24] G. Saavedra, W. D. Furlan, and J. A. Monsoriu, "Fractal zone plates," Opt. Lett. 28, 971-973 (2003).

[25] W. D. Furlan, F. Giménez, A. Calatayud, and J. A. Monsoriu, "Devil's vortex-lenses," Opt. Express, 17, 21891-21896 (2009).

[26] O. Mendoza-Yero, M. Fernández-Alonso, G. Mínguez-Vega, J. Lancis, V. Climent, and J. A. Monsoriu, "Fractal generalized zone plates," J. Opt. Soc. Am. A. 26, 1161-1166 (2009).

[27] G. Mínguez-Vega, E. Tajahuerce, M. Fernández-Alonso, V. Climent, J. Lancis, J. Caraquitena, and P. Andrés, "Dispersion-compensated beam-splitting of femtosecond light pulses: Wave optics analysis," Opt. Express 15, 278-288 (2007).

[28] J. Amako, K. Nagasaka, and N. Kazuhiro, "Chromatic-distortion compensation in splitting and focusing of femtosecond pulses by use of a pair of diffractive optical elements," Opt. Lett. 27, 969-971 (2002).

# CHAPTER 8

# NONLINEAR DYNAMICS OF FILAMENTATION PROPAGATION

**Contents**



*Some of the results in this chapter were originally presented in B. Alonso et al., J. Opt. Soc. Am. B 28, 1807-1816 (2011).*

## 8.1. Introduction

The advent of high-power pulsed lasers in the last decades has made possible the study of the propagation of light in nonlinear regime. Several different behaviors have been observed; among others, the modified interference pattern of light in the two-slit experiment [1] and the self-guiding propagation of light when diffraction and the Kerr effect compete, with no ionization of the medium [2-4]. However, the process attracting the most attention in the past few years is the filamentation of light, which will be studied in this chapter.

In the filamentation regime [5], two physical processes compete in the propagation of the beam. Firstly, an intense electric field modifies the refractive index $n$ of a nonlinear medium, accordingly to the optical Kerr effect, $n = n_0 + n_2 I$, $I$ being the intensity, and $n_0$ and $n_2$ the linear and nonlinear components of the refractive index, respectively. Since a laser beam is typically more intense in the center (as illustrated with the red line in Fig. 8.1a), the dependence $I = I(r)$ increases the refractive index in the center of the beam (see the increment denoted as $\Delta n$ and plotted in blue). This effect creates the so-called "Kerr-lens" (illustrated in green) and is responsible for the self-focusing of an intense beam (plotted in orange). Ideally, this process would lead to the collapse of the beam in a singularity beyond the diffraction limit. The minimum power required for this process is known as the critical power for self-focusing, $P_{cr} = \alpha \lambda^2 / 4\pi n_0 n_2$, where $\alpha$ is a constant that depends on the beam characteristics. The value of the critical power is of few GW in air and few MW in solid media (with higher nonlinearity) as for example fused silica.

However, the beam collapse does not occur in practice. As the intensity of the pulse increases due to self-focusing, the ionization of the medium creates a weak plasma with density proportional to the intensity $I(r)$. Therefore, it introduces a negative contribution from the plasma to the refractive index and more intense in the optical axis (shown in blue in Fig. 8.1b), which has the same effect as a divergent lens (green): defocusing of the beam [5].

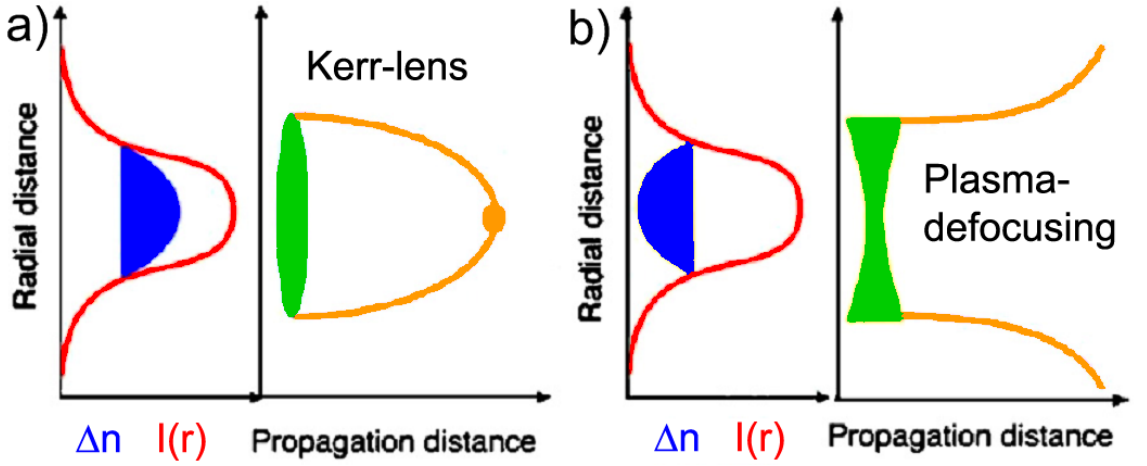


Fig. 8.1. (a) Representation of the Kerr-effect due to the nonlinearity of the medium, which produces the beam self-focusing. (b) The plasma produced by the ionization has the effect of a defocusing divergent lens. Figure extracted from [5].

The filamentation is the regime of nonlinear propagation where an equilibrium exists between the self-focusing process, caused by the Kerr effect, and the self-defocusing process, induced by the presence of weak plasma generated by the pulse. This equilibrium leads to the self-guiding of the light [5-7] along distances considerably larger than the Rayleigh length. During the light filament, the beam undergoes focusing-defocusing cycles, creating what is called a filament channel (Fig. 8.2). This phenomenon has been applied for example to pulse post-compression [8], atmospheric analysis [9,10], remote laser-induced breakdown spectroscopy (LIBS) [11], and the generation of sub-terahertz radiation [12].

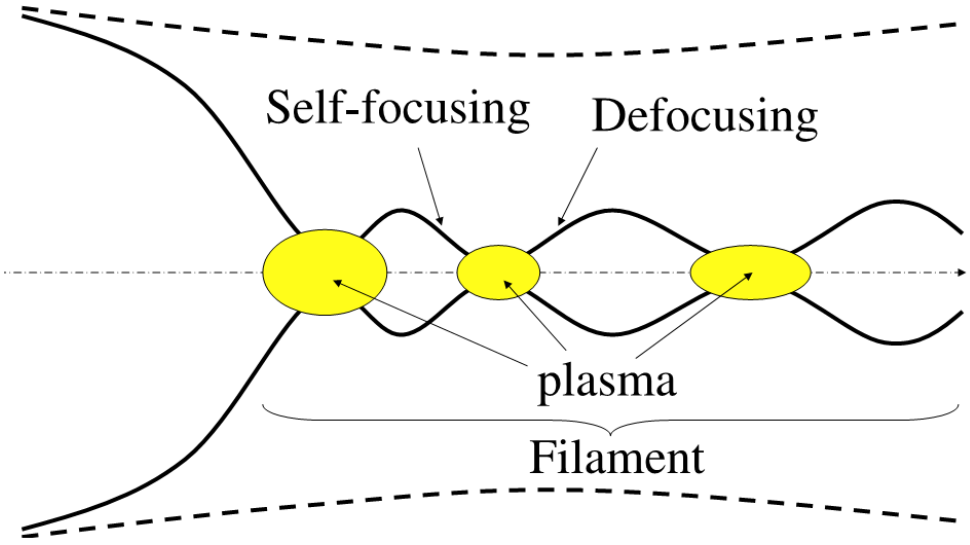


Fig. 8.2. Equilibrium between focusing-defocusing cycles (due to Kerr and plasma effect, respectively) leads to the self-guiding of a light filament. Figure extracted from [5].

Our research group, the Grupo de Investigación en Óptica Extrema (GIOE), was interested in the post-compression of the pulses by means of filamentation. The nonlinear propagation during filamentation leads to the generation of new frequencies mainly due to the processes of self-phase modulation (SPM), self-steepening and ionization [5]. Given an input intense pulse, the post-compression is based on the spectral broadening during the filamentation, followed by the compensation of the phase (e.g., with chirped-mirrors, grating-pair or prism-pair compressor) [8]. Since the GIOE is equipped with terawatt-class (high-power) chirped pulse amplification (CPA) Ti:sapphire lasers, we were interested in the study of the process to apply filamentation to high-energy pulses. An alternative to filamentation is post-compression in hollow-core fibers, where the beam is guided by geometrical constraints [13]. One of the drawbacks of hollow-fiber and filamentation post-compression is the limited input (and consequently output) energy per pulse derived from ionization and multi-filamentation issues, respectively. In filamentation, when the input power exceeds many times the critical power for self-focusing, the beam breaks up in multiple filaments. Therefore, we studied different approaches to scale-up the output energy after post-compression through stable single-filaments.

Through high-energy filament post-compression, we have shown how the use of input circularly polarized pulses [14], chirped pulses [15] and astigmatic phases [16]

allows us to increase the throughput energy. These results are possible thanks to the increase of critical power [14,16] and, alternatively, thanks to the reduction of the input power [15]. Therefore, we were interested to understand the filament dynamics to be able to control it in our favor. For example, we studied the self-compression through filamentation with negatively and positively chirped pulses [17]. Self-compression is a particular case of filamentation in which the spectral phase of the pulses is self-compensated without the need of any additional compressor (e.g. chirped mirrors). Consequently, the pulses are directly compressed and their duration is shorter than the input pulse.

Nevertheless, the propagation under filamentation regime is a rich process. This was indeed the reason why we developed the technique STARFISH (Chapter 4, [18]) for the measurement of the amplitude and phase of the pulses in the spatiotemporal domain. The aim of the work presented in this chapter is to achieve a full spatiotemporal characterization of the electric field of a filament at different planes along its propagation [19]. This will give a more complete understanding of the splitting and self-compression dynamics, since it will describe the evolution of the pulse-fronts, the spatiospectral and spatiotemporal distribution, and the time-space coupling effects.

Over the last two decades, the filamentation regime has been extensively studied by means of theoretical simulations considering different media, and showing the high degree of complexity of the electric field behavior in the spatiotemporal domain [5,20,21]. The experimental observation of these dynamics and the total understanding of the phenomena remain unsolved problems [22]. An important amount of work and effort has been devoted to further experimental comprehension of the different nonlinear phenomena. Several methods have been used to obtain further information about the filamentation process, such as measurement of the electric conductivity of the medium [23] or spectroscopy of the plasma emission for analyzing the electronic density and the temperature of the plasma [24], measurements of the high orders of the nonlinear refraction index [25], and reconstruction of the pulses at different points of the transverse plane to obtain the local temporal structure [26].

The work of Loriot and co-workers [25] opened a huge discussion within the filamentation community. The "standard model" described above, which relies on the balance of Kerr focusing and plasma defocusing, was called into question. The expansion of the Kerr refractive index in higher orders of the intensity, that is to say,

$$n_{Kerr} = n_2 I + n_4 I^2 + n_6 I^3 + n_8 I^4 + n_{10} I^5, \qquad (8.1)$$

opened a new interpretation of the filamentation process. In this higher-order Kerr model, or "HOKE model", when the intensity increases owing to self-focusing, the contribution of the Kerr effect can become negative without needing the presence of plasma [25,27]. Therefore, the HOKE model can explain the filamentation by means of the Kerr effect itself, which would self-balance the focusing-defocusing with the intensity modulation during the propagation [28]. The validity of each model is still under discussion and has led to many theoretical and experimental studies.

To date, the experimental evidence and studies of pulse dynamics have come from techniques that partially describe the pulse propagation. Minardi and co-workers used the shadowgraphy technique, obtaining the refractive index and the absorption of the medium when the probe pulse passed through the filament [28]. From these results it was possible to observe some features of the pulse propagation dynamics, such as the separation velocity of the two split pulses. Another observation of the spatiotemporal dynamics, obtaining experimental evidence of the pulse splitting, was achieved by using femtosecond time-resolved optical polarigraphy [29]. This technique uses a probe pulse to detect the birefringence generated by a filament acting as a pump. In addition, some traces of asymmetrical pulse splitting could be observed. Recent work evaluates the temporal duration of pulses undergoing filamentation propagation through transient-grating cross-correlation frequency-resolved optical gating (FROG) [30]. In [31], the authors investigate experimentally the dynamics of the wavefronts inside a filament, based on a spectral interferometry reconstruction setup.

Furthermore, the spatiotemporal reconstruction of light pulses has been notably developed in the past few years by the introduction of several techniques [32-36]. Therefore, the tools for the experimental study of the spatiotemporal structure of the pulse propagating nonlinearly are already available. The first important approach for the spatiotemporal reconstruction of nonlinearly propagated pulses was performed by using spatially resolved cross-correlation [32-34], which consisted in the spatially resolved temporal cross-correlation of the spatiotemporal intensity. The information obtained by this technique is very valuable, as it shows general features of the nonlinear generation of X-type waves during the propagation of a femtosecond pulse along a nonlinear crystal [32] or the pulse splitting dynamics when propagating a femtosecond pulse through water [33]. However, the spectral phase remained unknown, and so the information was still partial.

In previous chapters, we have used STARFISH with pulses delivered by a terawatt CPA laser system with a repetition rate of 10 Hz, which are considerably more difficult to be characterized than lower energy laser sources (e.g., ultrafast oscillators), mainly due to the instability in the outcome energy, the much lower repetition rate and the amplified spontaneous emission (ASE) that is present. Up to now, we have presented pulses propagating in linear regime. When applying these lasers to nonlinear processes, such as the filamentation propagation, the difficulty grows again. Now, the instability increases due to the dependence of the process on the input intensity. Note that STARFISH is a multi-shot technique and that we planned to measure the pulse at different propagation distances. Moreover, these processes are usually related to a spectral broadening of the pulses. Since STARFISH is based on spectral interferometry, we need a reference pulse with at least the same bandwidth than the pulse to be characterized. For this reason, we decided to implement a second and independent line of post-compression in a hollow-core fiber to be used as the reference pulse. Finally, the high intensities involved inside the filament may damage any material used to measure it. Our choice consisted in using a sampling plate that picked a small reflection of the pulse. For these experiments, we kept a regime with a moderate input energy and

spectral broadening, to avoid too much instability and damage to the surface of the plate. We found that using 0.7 mJ and 100 fs input pulses was a good trade-off to be in a conservative regime and still observe the filament evolution. In the next section we detail how we have overcome experimentally these issues in order to retrieve the filament dynamics.

## 8.2. Experimental setup

All the experimental results presented in this chapter were obtained with a CPA Ti:sapphire laser (Spectra-Physics), delivering 100 fs pulses (central wavelength of 795 nm, 10 nm FWHM), 10 Hz repetition rate, and 9 mm diameter beam. In order to study the filamentation process in air, the spatiotemporal structure of the pulse at different propagation distances was reconstructed using the STARFISH characterization technique [18] that was presented in Chapter 4.

The experimental implementation for the spatiotemporal characterization of the filament is shown in Fig. 8.3. As said before, the filament undergoes spectral broadening. As discussed in Chapter 2, spectral interferometry requires a spectral distribution of the reference pulse at least covering the test pulse spectrum. Otherwise, the information corresponding to the non-interfering parts of the spectrum will be lost. For this reason, we needed a hollow-core fiber post-compression in the reference arm in parallel to the filamentation experiment that we wished to characterize. The pulse coming from a CPA laser system was divided with a beam splitter to generate the reference pulse and the filament (the test pulse). To create an adequate reference pulse (in terms of spectral content), the beam transmitted through the beam splitter passed through a 1.5 m focal length lens, and it was coupled into a hollow-core fiber ($300\mu m$ inner diameter, 40 cm long) filled with air at atmospheric pressure. The beam was guided into the hollow-core fiber, where it experienced nonlinear spectral broadening due to SPM. An iris placed just before the focusing lens was used to optimize the beam coupling into the hollow fiber. The spectral broadening can be controlled by modifying the input pulse energy and chirp (in our particular case the chirp control was done with the compressor before the interferometer, so it afflicts simultaneously to the reference and test pulses). This can be used to adjust the reference spectrum to the test pulse spectrum (to attain the overlap in the whole test spectrum). Once the filamentation and the hollow-fiber are optimized, those parameters are fixed. Therefore, we focused on having a stable reference pulse whose spectrum fully covered the spectrum corresponding to that of the test pulse instead of obtaining the shortest pulse possible with this setup. Then, the reference pulse coming out of the hollow fiber was collimated by a 40 cm lens and passed through a transmission pair-of-grating pulse compressor to compensate the residual phase of the pulses. By means of a flip mirror, the beam can be driven into a GRENOUILLE [37] device (Swamp Optics), to obtain the temporal reconstruction of the pulse. The GRENOUILLE consists in a single-shot implementation of the second harmonic generation (SHG) frequency-resolved optical gating (FROG) (both techniques were already presented in Chapter 1). The spectral phase compensation was used mainly to achieve pulse durations within the time range

of the GRENOUILLE. In Section 8.5 (Fig. 8.7) the reference characterization is provided. The ambiguity concerning the time direction in the SHG FROG was solved by means of additional measurements just introducing windows with known dispersion. The reference pulse created in this way was spatially homogeneous, which is a requirement of the GRENOUILLE technique. Once the pulse was known, the mirror mentioned before was flipped down and the pulse was directed into one of the two inputs of the fiber coupler. This input was located at a fixed position, providing a constant reference.

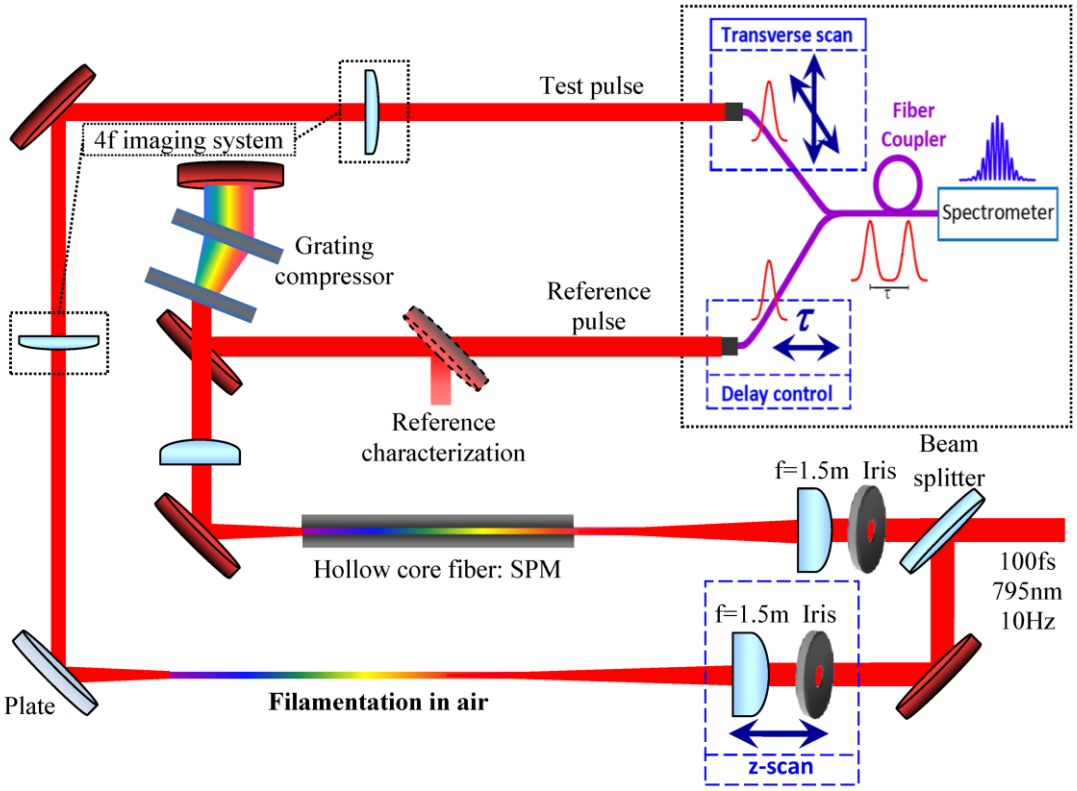


Fig. 8.3. Experimental setup used for the spatiotemporal study of the filamentation process. The input laser is divided into two beams. The first pulse spectrum is broadened into a hollow-core fiber. Then, it is compressed and characterized. The second pulse produces filamentation in air that is sampled by a reflective plate and imaged into the detection. The filament is characterized by the STARFISH technique: an optical fiber coupler collects both pulses to perform spectral interferometry. The propagation of the filament is tracked in a z-scan by moving the lens and iris along the optical axis.

The second arm of the interferometer, which comes from the light reflected by the beam splitter, was used to create the experiment under study (the test pulse). In our case, the beam was also focused by a 1.5 m focal length lens to generate a filament in air. An iris just before the focusing lens was used to control the filamentation process (e.g., obtaining a good central mode). After the iris, fixed to a 4-mm diameter during the whole experiment, the energy of the pulse was 0.7 mJ. The analysis of the beam at a given propagation distance from the lens, z, was performed by sending into the STARFISH the reflection of a small fraction of the energy of the beam on a plate at that position. We have checked that, while the part of the pulse transmitted inside the plate damaged the bulk, the plate surface remained undamaged (preserving its reflection and

flatness) even for the higher intensities used in these experiments. Also, the energy of the reflected pulse used in the measurement is very low, so the nonlinear propagation is truncated at this point. The beam sampled at the plate was imaged by a 4f optical system (f = 20 cm) into the fiber of the STARFISH devoted to taking the test signal. We used 4f-imaging because in this system the first lens acts as a Fourier-transform, whereas the second lens (with the same focal length) acts as an inverse Fourier-transform, so their combination provides a non-distorted image of the pulse (actually, the axes are inverted). The fiber coupler recombined the test spectrum with the reference spectrum and, after selecting a correct delay between both pulses (just moving the reference optical fiber back or forward), it was possible to obtain the spectral interference of the test and reference pulses. By simply moving the second optical fiber within the image plane (this does the spatial transverse scan), it was then possible to obtain the complete spatiotemporal reconstruction of the test pulse at a certain $z$. If the physical system under study presents cylindrical symmetry (which is the case of the measurements presented in this work), a radial scan is sufficient.

In order to study the filament propagation dynamics, the lens and the iris of the test arm were moved along the propagation direction, thus changing the position under analysis while maintaining the relative delay between both arms.

Since the measurement process is multi-shot, owing to both the propagation and the transverse scans, the stability of the physical system and the reconstruction setup is a key point. Therefore, we made sure that the reference and test pulse were stable by checking that the reference pulse and the spatiotemporal reconstruction of the filament did not vary shot to shot. Concerning the test pulse, we averaged 20 shots of the spectral amplitude in order to reduce the noise of the reconstructions. For the same purpose, we recorded 20 shots of spectral interferences at each spatial transverse position and averaged the phase retrieval for each shot, verifying that the spatiotemporal structure of the filament was maintained shot to shot and when doing the average. In Section 8.5 we will present the detailed study of the reference and test pulses, demonstrating the required stability.

## 8.3. Theoretical model for filamentation

In order to complete the study, we compared the experimental results with numerical simulations. The GIOE has implemented a code to study the nonlinear propagation of ultrashort laser pulses, which can be applied to the theoretical study of the filamentation. The simulations presented in this chapter were done by the GIOE. Here, we will just introduce the theoretical model used to understand the filamentation (more details can be found in [19]). The model implemented is known as the "standard model" of the filamentation, already mentioned in Section 8.1. It consists in the numerical calculation of the extended nonlinear propagation equation for the envelope of the pulse $\varepsilon$ [38,39]:

$$\frac{\partial \varepsilon}{\partial z} = \frac{i}{2k_0}\left(1+\frac{i}{\omega_0}\frac{\partial}{\partial t}\right)^{-1}\left(\frac{\partial^2}{\partial r^2}+\frac{1}{r}\frac{\partial}{\partial r}\right)\varepsilon + \sum_{n=2}^{\infty}\frac{i^{n+1}}{n!}\left(\frac{\partial^n k}{\partial \omega^n}\right)_{\omega_0}\frac{\partial^n \varepsilon}{\partial t^n} + T_{NL}(\varepsilon), \qquad (8.2)$$

where $k_0$ is the wave number associated with the central frequency of the pulse $\omega_0$, $z$ is the propagation distance, $r$ is the radial coordinate, and $t$ represents the retarded time variable. The first term of the right-hand side of Eq. (8.2) represents the diffraction, including also the space-time coupling term with the presence of the temporal derivative. The second term represents the dispersion, while the third term includes the principal nonlinear terms that affect the propagation of the pulse, $T_{NL}(\varepsilon)=K(\varepsilon)+I(\varepsilon)+A(\varepsilon)$, where $K(\varepsilon)$ corresponds to the Kerr effect (including both the instantaneous Kerr and the retarded Raman response), $I(\varepsilon)$ corresponds to the ionization of the medium (only multiphoton ionization is considered [5,40], and the temporal effect is included), and $A(\varepsilon)$ corresponds to the nonlinear absorption.

The envelope that we have used in the model as the input pulse is a supergaussian radial profile with an experimental temporal profile, $f(t)$, which we obtained from experimental characterization of the input conditions:

$$\varepsilon(r,t,z=0)=E_0\exp\left\{-\left(\frac{r}{w_0}\right)^4\right\}\exp\left\{-i\frac{kr^2}{2f'}\right\}f(t). \qquad (8.3)$$

The supergaussian spatial profile was used in order to be close to the experimental observation of the spatial distribution and width of the beam. The temporal characterization of the input pulse was done using spectral interferometry with the same setup given in Fig. 8.3, but removing the focusing lens to be in linear regime. The moderate spectral bandwidth and the soft focusing induced by the aperture allow the use of the focusing phase factor as shown in Eq. (8.3), instead of a more accurate description as in [41], without appearance of artificial effects.

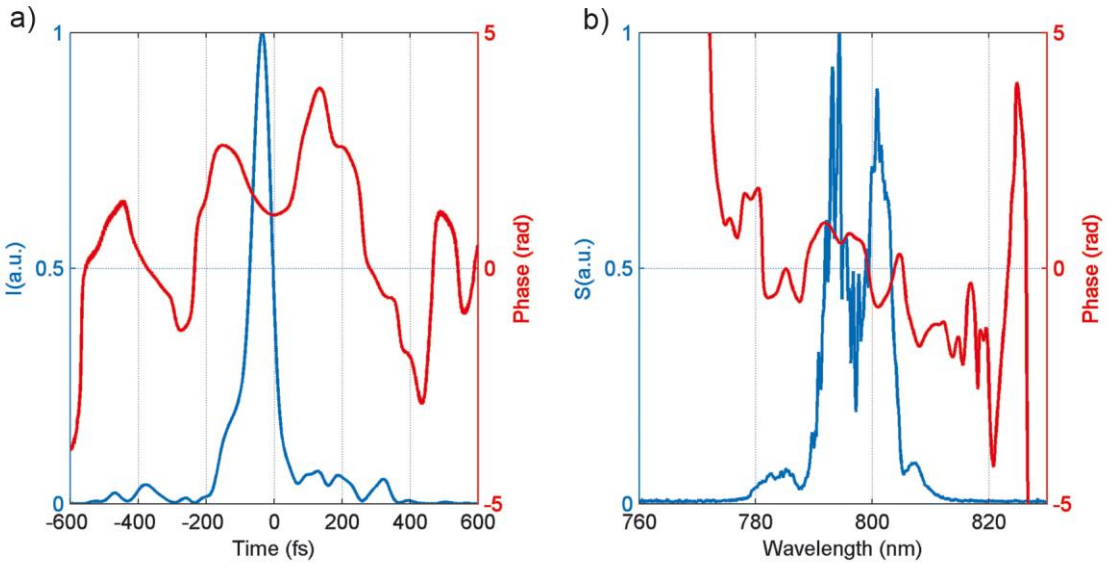


Fig. 8.4. Temporal (a) and spectral (b) structure of the input pulse used in the simulations. In both plots the blue curve represents the intensity of the envelope, while the red one corresponds to the phase. This particular temporal shape comes from the fact that the pulse shows a slight nonlinear propagation while going from the compressor to the experimentation table.

The parameters that we have used for the simulations are the following: the beam input spatial radius, $w_0$, is 2 mm; the pulse is focused with a 1.5 m focal length lens; its spectrum is centered at 795 nm; and it has an input energy of 0.7 mJ. The characterization of the temporal envelope used in the simulations is shown in Fig. 8.4. The medium where the pulse propagates is air, and to describe it we have used the dependence of the refractive index, $n(\lambda)$, calculated in [42].

## 8.4. Experimental results and comparison with simulations

The spatiotemporal reconstruction of the beam at different propagation distances is presented in Fig. 8.5, where we show different snapshots of the beam during its propagation after the lens. In the first column, labeled "A", we present the experimental pulse spectra at different transverse positions (x-axis) and at a given propagation position from the focusing lens (z), indicated on the left side of Fig. 8.5. In the second column, labeled "B," we show the corresponding spatiospectral distributions obtained from simulations. The experimental spatiotemporal reconstructions of the pulse-front at the corresponding propagation position are presented in the third column ("C"), while the theoretical spatiotemporal distributions are shown in the fourth column ("D"). For the sake of clarity, we refer to each subplot by its column label (from A to D) and its z coordinate (e.g., the experimental spatiotemporal reconstruction contained in column C at z = 160 cm after the focusing lens will be denoted "C-160 cm"). We have plotted the figures in logarithmic scale in order for the different structures (e.g., core part, wings, pre- and post-pulses, etc.) to be properly observed.

In order to explore the pulse splitting dynamics, we have plotted in Fig. 8.6 the on-axis pulse reconstruction, $E(t, x = 0)$, for each of the analyzed propagation positions z. The instantaneous frequency, obtained from the first derivative of the field phase on the time domain, is shown in the color-filled intensity profile.

First, before the nominal focus, at z = 120 cm after the lens, the beam starts to present some signals related to the nonlinear propagation that has taken place until that position is reached. The spectrum shows some broadening in the central part of the beam (Fig. 8.5, subplots A-120 cm and B-120 cm) and the pulse-front basically shows some structure of a train of pre- and post-pulses, which mainly results from the input temporal structure (Fig. 8.5, subplots C-120 cm and D-120 cm). In its on-axis reconstruction (Fig. 8.6), the input pulse main structures remain without relevant changes.

Some differences between the experimental and the theoretical data can already be observed at z = 120 cm. The main difference is the spatial size of the pulse, which is larger in the experiment. Several reasons could be the origin of this effect. One may be the presence of some wavefront aberrations in the experimental case, especially a slight astigmatism observed when analyzing the beam with a commercial wavefront sensor (SID4-HR, Phasics S.A.). The presence of the astigmatism, which was not included in the simulations to avoid breaking the cylindrical symmetry, is consistent with the fact that the beam size evolution within the studied propagation region is slightly smoother

in the experimental results than in the simulations. This is understood by the softer linear focusing of a propagating astigmatic beam and the related increase of critical power for self-focusing in a nonlinear regime as is our case [43]. In addition, the input beam presents $M^2 = 1.2$ (obtained from experimental characterization), so the linear focus would be greater than the focus corresponding to the ideal case. As a consequence of the more intense collapse achieved in the simulations, the spectral broadening and also the divergence obtained at larger distances are larger than in the experiments.

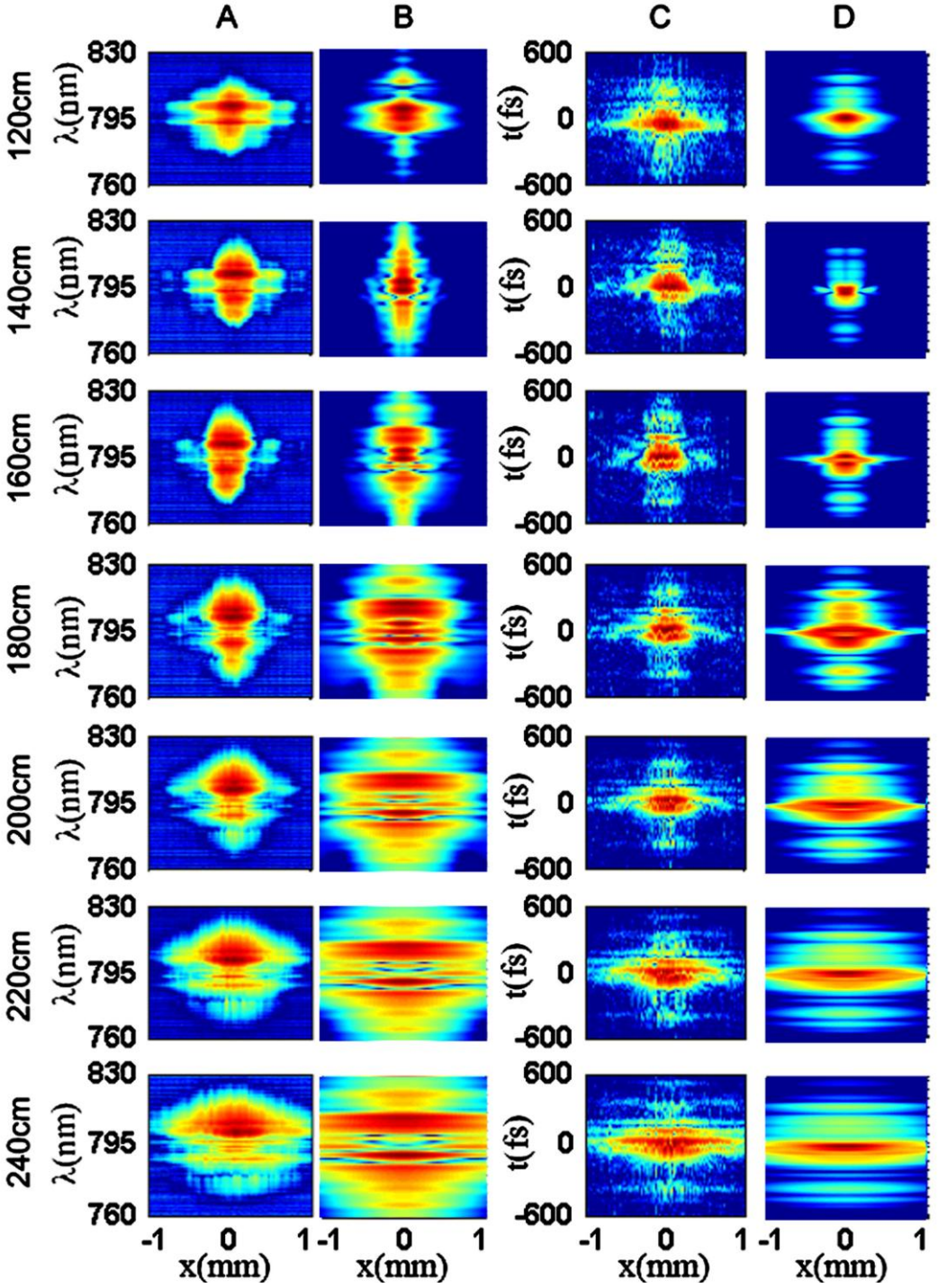


Fig. 8.5. Experimental (A) and simulated (B) spatially resolved spectrum; and experimental (C) and simulated (D) spatiotemporal intensity distribution, for different propagation distances after the focusing lens, given in the left column. The color scale for the logarithmic plots comprises three decades.

Just before the nominal focus, at z = 140 cm, the beam begins to show the main changes. The spectrum presents the largest broadening, as is shown in Fig. 8.5, subplots A-140 cm and B-140 cm. Together with this spectral broadening, an incipient temporal pulse splitting appears in the central part of the beam, while some structures become visible in the outer part of the beam (see Fig. 8.5, subplots C-140 cm and D-140 cm). At this stage, a self-compression process is observed. When the beam has passed the nominal focus, at z = 160 cm, we can observe that the maximum spectral broadening is almost achieved, and minor changes can be observed in the spectra. In contrast, the spatiotemporal structure is gaining a lot of complexity, showing a clear temporal pulse splitting at the center of the beam, while the spatial wings of the pulse exhibit temporal modulations (see Fig. 8.5, subplots C-160 cm and D-160 cm).

At distances further than z = 160 cm, the beam starts to diverge, showing an increase in size while increasing the propagation distance. Meanwhile, the spectra, which present a quite modulated structure, show some changes in the structure of the different maxima that are present in the central spatial part. Leaving aside these details, the experimental and theoretical data show the general structure of the (very modulated) spectra that can be explained by taking into account that the Kerr effects (the instantaneous and the retarded) are active during a much longer period of the propagation than the ionization, thus dominating the process.

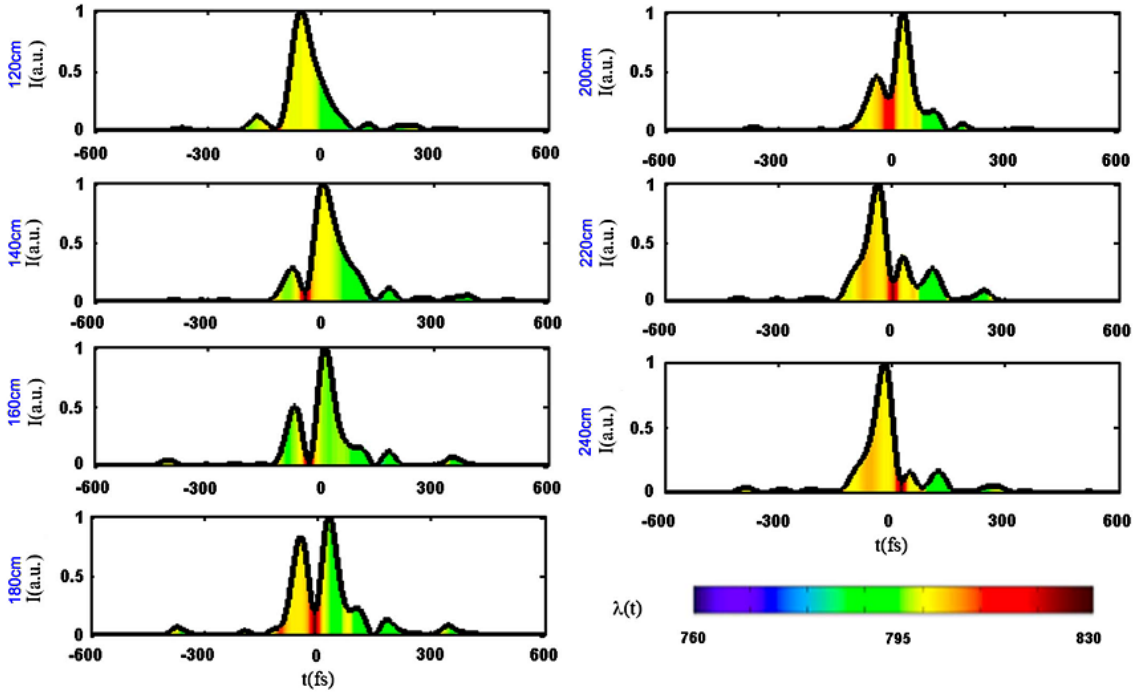


Fig. 8.6. Experimental on-axis pulse reconstruction for different propagation distances after the focusing lens (indicated on the left part of the figure). Color filling stands for the instantaneous wavelength.

As mentioned previously, some of the temporal dynamics of the propagation are shown more clearly in the on-axis reconstruction plots shown in Fig. 8.6. The general evolution presents a temporal pulse splitting and its subsequent evolution. Once the pulse splitting occurs, a competition dynamics intervenes between the two main split

pulses. When the beam propagates further (from z = 180 cm in the simulations, from z = 220 cm in the experiments) one of the split pulses, apparently the first one (the redder), fades out until becoming a hump in the main pulse.

In general, the simulations and the experimental results present a reasonably good qualitative agreement, despite the approximations made in the model and despite the fact that it is not possible to include all the experimental parameters in the theoretical analysis (e.g., slight astigmatism, etc.). The structure and propagation evolution of the pulse-front (r-t reconstruction) are very similar, with the exception of the size of the beam, especially at the focalization region, where the simulation overestimates the beam collapse. From the spectral point of view, and related to the beam size difference, the simulation shows more broadened spectra than the experiments. Concerning the quantitative discrepancies between experiments and theory, very recently Kolesik and co-workers [44] have shown some disagreements between experimental observations and theoretical model predictions. According to their report, the experimental results presented larger filament beam dimensions (around a factor of 2) than the results calculated by the theoretical models, which induced a theoretical overestimation of the filamentation effect, showing a remarkably lower filament creation threshold than that observed in the experiments. These observations match quite well our results. Nevertheless, these differences do not prevent us from observing the main features of the nonlinear spatiotemporal dynamics by comparing experimental and theoretical data, gaining an insight into the propagation dynamics within the filamentation regime, which is the aim of this work.

Therefore, from the experimental measurements, the filament dynamics can be better understood. Pulse splitting and pulse competition occurring during the filament propagation can be observed. An ambiguity exists in the present measurements regarding the time axis offset when comparing measurements at different propagation distances, caused by the readjustment of the delay for each spatiotemporal measurement. In spite of this, the measurements are very promising in the sense to provide more information to the discussion regarding the standard model and the HOKE model. For example, we have observed discrepancies between theory and model concerning the collapse and the spatial width, which had already been reported in the literature. Consequently, we think that some questions remain unanswered (e.g., models, pulse competition…), for which further experiments, in particular using spatiotemporal reconstruction techniques, would provide useful information.

## 8.5. Study of the stability of the nonlinearly propagated pulses

Here, we will show the study of the stability of the pulses (reference and test) involved in the characterization, demonstrating that the stability required is fulfilled. The spectral broadening both inside the hollow fiber and in the filamentation propagation is a highly nonlinear process. This nonlinear nature, combined with energy fluctuations between consecutive pulses, could lead to shot-to-shot fluctuation of the output pulses that would affect the pulse amplitude and phase. Since we are applying a multi-shot technique (note the spatial scan), this would be a problem. Firstly, the

reference has to be stable, as it is assumed to be constant during the whole scan (x-scan and z-scan). Secondly, the filament itself should also be stable in order to characterize the same pulse always and not sample slices of different unstable pulses.

For this reason, we took special care in this issue. We worked at a regime where stability was assured: we decided to work at conditions with moderated spectral broadening and pulse energy, in order to maintain the stability. We checked the repeatability of both, reference pulse and test pulse, shot-to-shot. We have not only averaged pulses, but also checked their fluctuation. The averaging gave us slightly less noisy spatiotemporal and spatiospectral figures, but the structure was always the same.

Regarding the reference stability, we first ensured a stable output spectrum and then we performed 30 consecutive single-shot temporal measurements of the pulse with our GRENOUILLE device. In Fig. 8.7 the spectral and temporal amplitude and phase are presented for the 30 shots. As a conclusion, the stability of the reference pulse compressed in the hollow-core fiber is shown.

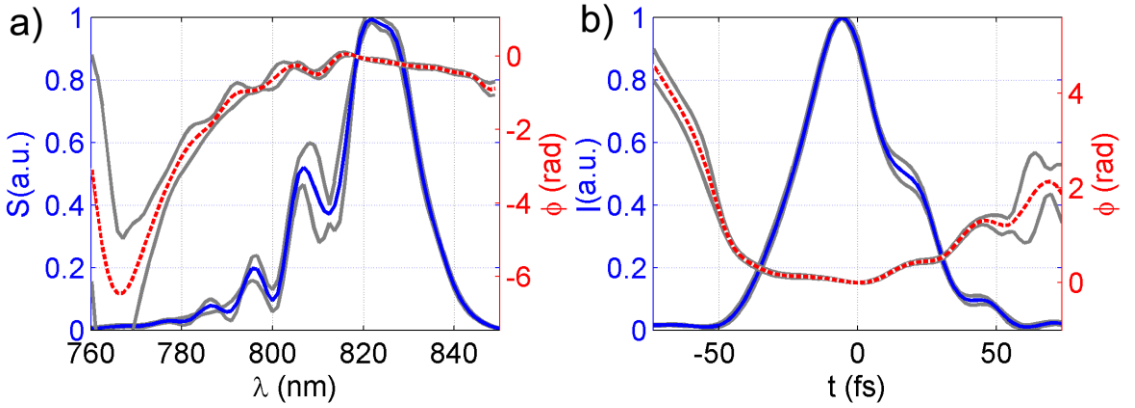


Fig. 8.7. (a) Spectral and (b) temporal amplitude (solid blue) and phase (dashed red) of the reference pulses compressed in the hollow fiber for 30 single-shot measurements with the GRENOUILLE. Gray curves represent the respective standard deviations.

Since we demonstrated that the reference is stable, we do not need further in situ characterization to combine with each shot of the spectral interferometry in the transverse scan of the spatial reconstruction of the filament. Conversely, the reference is characterized once before the $x-$ and $z-$scan and it is checked at the end to ensure that it has been preserved during the scans.

The filament is also nonlinear and could be instable. Moreover, the $x-$ and $z-$scan necessarily require a characterization in a multi-shot basis. Although it has already been indicated, we wish to stress that we worked in a moderate regime for stable filamentation, in which the spectral broadening was not too large, although the desired dynamics of the filament can still be observed.

Then, we did additional measurements to study the stability of the filament reconstruction. In this case, we averaged 20 shots of the test pulse spectrum for the spectral amplitude. We also averaged 20 phase retrievals from 20 different shots (single-shots) of spectral interferences. We combined this information to obtain the complete characterization of the test pulses.

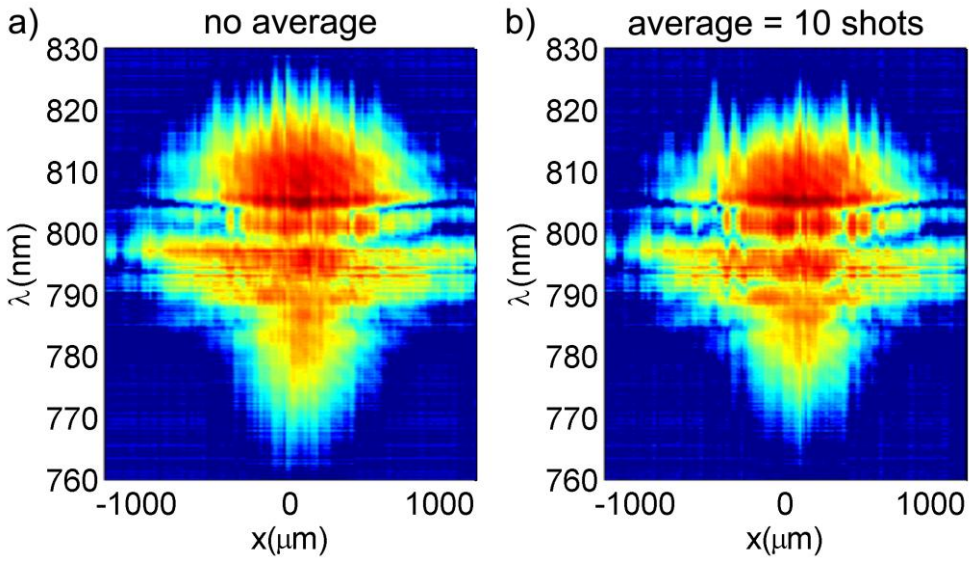


Fig. 8.8. Spatially-resolved spectrum (in logarithmic scale) after filamentation propagation, comparing the acquisition (a) without average (1 shot) and (b) with average (10 shots).

Regarding the spectral amplitude average, we present here the spatially resolved spectrum of the filament for z = 238 cm after the focusing lens (f = 150 cm), doing a comparison without averaging (for 1 shot per point acquisition, in Fig. 8.8a) and averaging 10 shots per point (Fig. 8.8b). As can be seen, the structure of the spatially resolved spectrum is the same for non-averaged than for averaged cases.

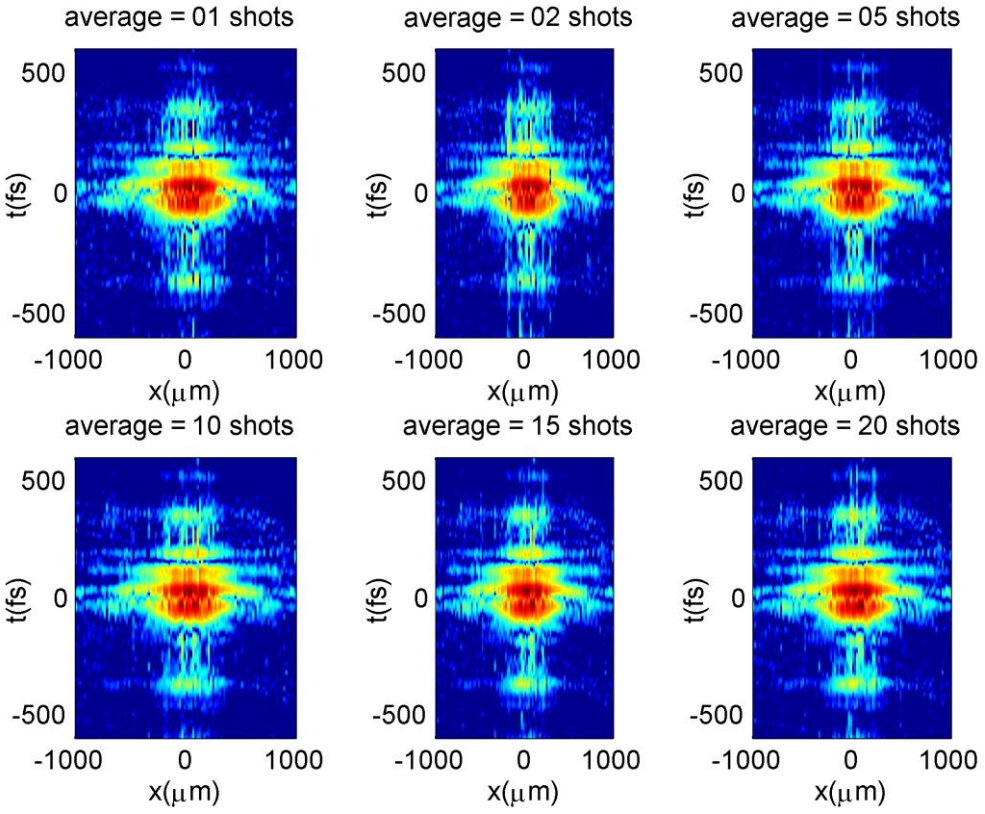


Fig. 8.9. Experimental spatiotemporal intensity distribution for different number of shots averaged (1, 2, 5, 10, 15 and 20 shots, respectively) for a propagation distance of 220 cm (f = 150 cm).

For the stability of the reconstruction in the spatiotemporal domain, we checked that the spatiotemporal intensity of the pulses was the same shot-to-shot for different single-shot acquisitions. In Fig. 8.9, we present the spatiotemporal reconstruction of the intensity of the pulse for $z = 220cm$ propagation distance (corresponding to the results in Fig. 8.5 C-220) calculated using the phase average of different number of shots of spectral interferences: 1, 2, 5, 10, 15 and 20, respectively. The spectral amplitude used in this comparison was always the same: an average of 20 shots of the test pulse spectrum. From the comparison in Fig. 8.9, it is demonstrated that the filament dynamics was stable in order to be characterized with a multi-shot technique.

Finally, we would like to point out that we tried different ways to average the pulses in the spectral amplitude. Given that the electric field is expressed as a complex number, it can be chosen either a Cartesian representation (real and imaginary parts) or a polar representation (module and phase). Owing to the possible zero-order phase instability shot-to-shot, averaging in the Cartesian representation may lead to a considerable error, whereas in the polar representation the phase fluctuations (from shot-to-shot) will be simply averaged. Since these phase fluctuations prevented us from retrieving the wavefront, we removed the zero-order phase and compared the average in Cartesian and polar representation. In this case, we found that the Cartesian average provided better results.

## 8.6. Conclusions

We have adapted the STARFISH technique for the measurement of nonlinear propagating light pulses. The instability of the process, the high intensities involved and the spectral broadening occurring during the propagation are the main critical points for this adaptation. We have fixed them by keeping a moderate regime of input power, using a sampling reflective plate and spectrally broadening the reference through self-phase modulation in an air-filled hollow-fiber. For more extreme cases with higher pulse energy or shorter focusing lenses, the instabilities or the plate damage threshold will prevent the use of STARFISH in the present configuration.

The nonlinear propagation of the pulse in the self-guiding regime of filamentation is described, presenting the complex evolution of the pulse-front and showing good agreement with theoretical simulations and previous works. The pulse splitting process and the subsequent dynamics of the pulses are discussed and shown, in qualitative agreement with the simulations. We believe that this kind of reconstruction opens the door to a full understanding of the underlying physics in a broad range of nonlinear optics phenomena, obtaining intimate information about the field evolution.

Future perspectives include studying the pulse-splitting in more detail and studying the output pulses under different conditions, e.g. astigmatic focusing or with chirped input pulses. Also, it would be interesting to study the alternative for post-compression based on a hollow-core fiber, for which the characterization of the spatiotemporal and spatiospectral properties of the compressed pulses will be presented in Chapter 10.

## References


[1] J. San Roman, C. Ruiz, J. A. Pérez, D. Delgado, C. Mendez, L. Plaja, and L. Roso, "Nonlinear Young's double-slit experiment," Opt. Express 14, 2817-2824 (2006).

[2] K. D. Moll, A. L. Gaeta, and G. Fibich, "Self-similar optical wave collapse: observation of the Townes profile," Phys. Rev. Lett. 90, 203902 (2003).

[3] C. Ruiz, J. San Roman, C. Mendez, V. Diaz, L. Plaja, I. Arias, and L. Roso, "Observation of spontaneous self-channeling of light in air below the collapse threshold," Phys. Rev. Lett. 95, 053905 (2005).

[4] S. L. Chin, S. A. Hosseini, W. Liu, Q. Luo, F. Théberge, N. Aközbek, A. Becker, V. P. Kandidov, O. G. Kosareva, and H. Schroeder, "Propagation of powerful femtosecond laser pulses in optical media: physics, applications, and new challenges," Can. J. Phys. 83, 863-905 (2005)

[5] A. Couairon and A. Mysyrowicz, "Femtosecond filamentation in transparent media," Phys. Rep. 441, 47-189 (2007).

[6] A. Braun, G. Korn, X. Liu, D. Du, J. Squier, and G. Mourou, "Selfchanneling of high-peak-power femtosecond laser pulses in air," Opt. Lett. 20, 73-75 (1995).

[7] L. Bergé, S. Skupin, R. Nuter, J. Kasparian, and J.-P. Wolf, "Ultrashort filaments of light in weakly ionized, optically transparent media," Rep. Prog. Phys. 70, 1633-1713 (2007).

[8] C. P. Hauri, W. Kornelis, F. W. Helbing, A. Heinrich, A. Couairon, A. Mysyrowicz, J. Biegert, and U. Keller, "Generation of intense, carrier-envelope phase-locked few-cycle laser pulses through filamentation," Appl. Phys. B 79, 673-677 (2004).

[9] J. Kasparian, M. Rodríguez, G. Méjean, J. Yu, E. Salmon, H. Wille, R. Bourayou, S. Frey, Y.-B. André, A. Mysyrowicz, R. Sauerbrey, J.-P. Wolf, and L. Wöste, "White-light filaments for atmospheric analysis," Science 301, 61-64 (2003).

[10] J. Kasparian and J. P. Wolf, "Physics and applications of atmospheric nonlinear optics and filamentation," Opt. Express 16, 466-493 (2008).

[11] K. Stelmaszczyk, P. Rohwetter, G. Méjean, J. Yu, E. Salmon, J. Kasparian, R. Ackermann, J.-P. Wolf, and L. Wöste, "Longdistance remote laser-induced breakdown spectroscopy using filamentation in air," Appl. Phys. Lett. 85, 3977-3979 (2004).

[12] S. Tzortzakis, G. Méchain, G. Patalano, Y.-B. André, B. Prade, M. Franco, A. Mysyrowicz, J.-M. Munier, M. Gheudin, G. Beaudin, and P. Encrenaz, "Coherent subterahertz radiation from femtosecond infrared filaments in air," Opt. Lett. 27, 1944-1946 (2002).

[13] M. Nisoli, S. De Silvestri, O. Svelto, R. Szipöcs, K. Ferencz, Ch. Spielmann, S. Sartania, and F. Krausz, "Compression of high-energy laser pulses below 5 fs," Opt. Lett. 22, 522-524 (1997).

[14] O. Varela, A. Zaïr, J. San Román, B. Alonso, I. J. Sola, C. Prieto, and L. Roso, "Above-millijoule super-continuum generation using polarisation dependent filamentation in atoms and molecules," Opt. Express 17, 3630-3639 (2009).

[15] B. Alonso, O. Varela, I. J. Sola, J. San Román, A. Zaïr, C. Méndez and L. Roso, "Energy scaling-up of stable single filament," Appl. Phys. B 101, 15-22 (2010).

[16] B. Alonso, R. Borrego-Varillas, Í. J. Sola, Ó. Varela, A. Villamarín, M. V. Collados, J. San Román, J. M. Bueno, and L. Roso, "Enhancement of filamentation postcompression by astigmatic focusing," Opt. Lett. 36, 3867-3869 (2011).

[17] O. Varela, B. Alonso, I. J. Sola, J. San Román, A. Zaïr, C. Méndez, and L. Roso, "Self-Compression controlled by the chirp of the input pulse," Opt. Lett. 35, 3649-3652 (2010).

[18] B. Alonso, I. J. Sola, O. Varela, J. Hernández-Toro, C. Méndez, J. San Román, A. Zaïr, and L. Roso, "Spatiotemporal amplitudeand-phase reconstruction by Fourier-transform of interference spectra of high-complex beams," J. Opt. Soc. Am. B 27, 933-940 (2010).

[19] B. Alonso, I. J. Sola, J. San Román, O. Varela, and L. Roso, "Spatiotemporal evolution of light during propagation in filamentation regime", J. Opt. Soc. Am. B 28, 1807-1816 (2011).

[20] K. Ishikawa, H. Kumagai, and K. Midorikawa, "High-power regime of femtosecond-laser pulse propagation in silica: multiple cone formation," Phys. Rev. E 66, 056608 (2002).

[21] A. Couairon, M. Franco, G. Méchain, T. Olivier, B. Prade, and A. Mysyrowicz, "Femtosecond filamentation in air at low pressures: Part I: theory and numerical simulations," Opt. Commun. 259, 265-273 (2006).

[22] S. Champeaux, L. Bergé, D. Gordon, A. Ting, J. Peñano, and P. Sprangle, "(3 þ 1)-dimensional numerical simulations of femtosecond laser filaments in air: toward a quantitative agreement with experiments," Phys. Rev. E 77, 036406 (2008).

[23] H. Schillinger and R. Sauerbrey, "Electrical conductivity of long plasma channels in air generated by self-guided femtosecond la-ser pulses," Appl. Phys. B 68, 753-756 (1999).

[24] J. Bernhardt, W. Liu, F. Théberge, H. L. Xu, J. F. Daigle, M. Châteauneuf, J. Dubois, and S. L. Chin, "Spectroscopic analysis of femtosecond laser plasma filament in air," Opt. Commun. 281, 1268-1274 (2008).

[25] V. Loriot, E. Hertz, O. Faucher, and B. Lavorel, "Measurement of high order Kerr refractive index major air components," Opt. Express 17, 13429-13434 (2009).

[26] A. Zaïr, A. Guandalini, F. Schapper, M. Holler, J. Biegert, L. Gallmann, A. Couairon, M. Franco, A. Mysyrowicz, and U. Keller, "Spatiotemporal characterization of few-cycle pulses obtained by filamentation," Opt. Express 15, 5394-5404 (2007).

[27] P. Bejot, J. Kasparian, S. Henin, V. Loriot, T. Vieillard, E. Hertz, O. Faucher, B. Lavorel, and J.-P. Wolf, "Higher-Order Kerr terms allow ionization-free filamentation in gases," Phys. Rev. Lett. 104, 103903 (2010).

[28] S. Minardi, A. Gopal, A. Couairon, G. Tamoašuskas, R. Piskarskas, A. Dubietis, and P. Di Trapani, "Accurate retrieval of pulse-splitting dynamics of a femtosecond filament in water by time-resolved shadowgraphy," Opt. Lett. 34, 3020-3022 (2009).

[29] J. Odhner and R. J. Levis, "Direct phase and amplitude characterization of femtosecond laser pulses undergoing filamentation in air," Opt. Lett. 37, 1775-1777 (2012).

[30] I. Blonskyi, V. Kadan, O. Shpotyuk, and I. Dmituk, "Manifestations of sub-and superluminality in filamented femtosecond laser pulse in fused silica," Opt. Commun. 282, 1913-1917 (2009).

[31] C. G. Durfee, D. E. Adams, and J. A. Squier, "Spatiotemporal characterization of ionizing wavefronts in a filament," presented at Third International Symposium on Filamentation, Crete, Greece, 31 May-5 June 2010.

[32] J. Trull, O. Jedrkiewicz, P. Di Trapani, A. Matijošius, A. Varanavičius, G. Valiulis, R. Danielius, E. Kucinskas, A. Piskarskas, and S. Trillo, "Spatiotemporal three-dimensional mapping of nonlinear X waves," Phys. Rev. E 69, 026607 (2004).

[33] A. Matijošius, J. Trull, P. Di Trapani, A. Dubietis, R. Piskarskas, A. Varanavičius, and A. Piskarskas, "Nonlinear space-time dynamics of ultrashort wave packets in water," Opt. Lett. 29, 1123-1125 (2004).

[34] S. Minardi, M. A. C. Potenza, and J. Trull, "Intensity mapping of three-dimensional optical wave packet: holographic properties and applications," in Trends in Laser and Electro-optical Research, W. T. Arkin, ed. (2006), pp. 151-182.

[35] C. Dorrer, E. M. Kosik, and I. A. Walmsley, "Spatiotemporal characterization of the electric field of ultrashort optical pulses using two-dimensional shearing interferometry," Appl. Phys. B 74, S209-S217 (2002).

[36] C. Dorrer, E. M. Kosik, and I. A. Walmsley, "Direct space-time characterization of the electric fields of ultrashort optical pulses," Opt. Lett. 27, 548-550 (2002).

[37] P. O'Shea, M. Kimmel, X. Gu, and R. Trebino, "Highly simplified device for ultrashort-pulse measurement," Opt. Lett. 26, 932-934 (2001).

[38] T. Brabec and F. Krausz, "Nonlinear optical pulse propagation in the single-cycle regime," Phys. Rev. Lett. 78, 3282-3285 (1997).

[39] A. Couairon, S. Tzortzakis, L. Berge, M. Franco, B. Prade, and A. Mysyrowicz, "Infrared femtosecond light filaments in air: simulations and experiments," J. Opt. Soc. Am. B 19, 1117-1131 (2002).

[40] L. Berge and A. Couairon, "Gas-induced solitons," Phys. Rev. Lett. 86, 1003-1006 (2001).

[41] L. Bergé, S. Skupin, and G. Steinmeyer, "Self-recompression of laser filaments exiting a gas cell," Phys. Rev. A 79, 033838 (2009).

[42] J. Zhang, Z. H. Lu, and L. J. Wang, "Precision refractive index measurements of air, $N_2$,$O_2$, Ar, and $CO_2$ with a frequency comb," Appl. Opt. 47, 3143-3151 (2008).

[43] C. R. Giuliano, J. H. Marburger, and A. Yariv, Appl. Phys. Lett. 21, 58-60 (1972).

[44] M. Kolesik, D. Mirell, J.-C. Diels, and J. V. Moloney, "On the higher-order Kerr effect in femtosecond filaments," Opt. Lett. 35, 3685-3687 (2010).

# CHAPTER 9

# FEW-CYCLE PULSES IN THE SPATIOTEMPORAL DOMAIN

**Contents**



*Some of the results in this chapter were originally presented in B. Alonso et al., Opt. Express 20, 17880-17893 (2012).*

## 9.1. Interest and state of the art

The field of ultrashort laser pulses is rapidly evolving both from the point of view of the development of laser sources and from their applications. As a result, the techniques for the characterization of such pulses are also in constant development.

Regarding the duration of the pulses, currently available technology routinely provides few-cycle near-infrared ultrafast laser pulses (with durations below 10 fs) either using post-compression schemes or directly from broadband and octave-spanning Ti:sapphire laser oscillators (see, e.g., [1,2]). Octave-spanning oscillators have many applications, for example, in optical frequency metrology and high-precision optical spectroscopy [3]. Moreover, the production of high-energy few-cycle laser pulses has also been recently achieved through direct chirped pulse amplification [4] as well as in post-compression schemes based on hollow-core fibers [5] and filamentation [6,7]. Intense few-cycle pulses can be used in atto-science [8], which we will discuss in greater detail in the next chapter.

In Chapter 8, we studied the light propagation undergoing filamentation in a moderate regime of pulse energy and spectral broadening [9]. In Chapter 10 we will present the spatiotemporal properties of pulses post-compressed in a gas-filled hollow-fiber, analyzing the spatial chirp, the pulse-front and wavefront curvatures, and the focusability of the pulses [10]. The spatiotemporal characterization of few-cycle pulses can provide very useful information for their applications, for example of light-matter interaction. Often, the pulses are tightly focused to achieve higher intensities. However, the ultra-broad spectral bandwidth makes these pulses very sensitive to chromatic aberrations. In this chapter, we study the propagation of low-energy few-cycle pulses from an ultrafast oscillator along the focusing region of an off-axis parabolic (OAP) mirror, in order to explore possible pulse distortions [11]. We characterized the oscillator pulses first because it is easier than for post-compressed pulses owing to their lower energy, high-repetition rate and higher stability. Moreover, we use the experimental spatiotemporal irradiance pattern to estimate the peak irradiance of the focused pulses, which is of interest for most applications.

As we have already seen in Chapter 1, the temporal characterization of ultrashort pulses ($>10\,fs$) is a well-established field, with several techniques allowing for the retrieval of the pulse amplitude and phase in the temporal domain [12]. The characterization of few-cycle pulses, which have ultra-broad bandwidths, is very demanding for common techniques as FROG [13] or SPIDER [14]. Many efforts have been made in adapting these techniques to this regime, where very thin nonlinear crystals and second-harmonic-generation (SHG) spectral signal calibration are required. For example, spatially encoded arrangement of SPIDER (SEA-SPIDER) [15] and two-dimensional spectral shearing interferometry [16] have been applied to the measurement of few-cycle pulses. Also, careful calibration of SHG-FROG [17-19] and the use of interferometric FROG [20] have been demonstrated in the few-cycle regime. A comparison of the experimental results for these techniques is given in [21]. Recently a new technique known as d-scan (dispersion-scan) has been introduced [22,23], and will

be presented in Section 9.2. It achieves the compression and characterization of the pulses by tracking the spectrum of the SHG signal during a continuous insertion of dispersion (from negative to positive chirp) and applying an iterative retrieval procedure. The SHG signal can be self-calibrated and the up-converted bandwidth requirements are more relaxed compared to other techniques.

The adaptation of those techniques for pulse characterization in the spatiotemporal domain is also a challenge. SEA-SPIDER has been recently shown to provide space-time information (excluding the pulse-front tilt) of 10.2 fs pulses [24]. In this chapter, we use the technique STARFISH [25] to measure the spatiotemporal structure of focused few-cycle pulses delivered by an oscillator. The phase of the test pulse can be extracted by using spectral interferometry (SI) with a known reference pulse. Here, we use the d-scan technique [22,23] to measure the spectral phase of the reference pulse. The experiments presented in this chapter were carried out in the laboratory of few-cycle pulses of the Universidade do Porto (Portugal).

Owing to the large bandwidth of the pulses (extending from 630 to 980 nm), the operating bandwidth of the detection is very relevant, as well as the calibration of the spectral response of the fiber optic coupler and the spectrometer with a reference white-light calibration lamp (LS1-CAL, Ocean Optics Inc.). The calibration of the spectral transmission of the fiber coupler (with a full-width at half-maximum, FWHM, of 250 nm) was presented in Section 4.2.4. Therefore, the spectral amplitude and phase retrieved by SI was corrected with this calibration. Since we are measuring focused pulses, the possible effect of the numerical aperture of the fiber (see Section 4.2.5) will also be taken into account.

## 9.2. The d-scan technique: measurement of the reference pulse

As we have said before, the reference pulse was characterized using the d-scan technique [22,23]. Because of the novelty of the technique, we will present it here. The technique has been developed by the Universidade do Porto (Portugal) in collaboration with the University of Lund (Sweden) as part of the PhD Thesis of Miguel Miranda. The objective of the d-scan is the compression and characterization of few-cycle pulses. The experimental setup is very simple (Fig. 9.1), it relies on the same optical elements already required for the compression of the pulses: a pair of glass wedges and a set of chirped mirrors optimize their spectral phase. Additionally, an auxiliary line for the measurement of the SHG of the pulse is required. However, the phase-matching bandwidth of the nonlinear crystal (for SHG) is not very demanding, as we will discuss below.

In the d-scan, the spectral phase of the pulses is compensated by negative dispersion chirped mirrors (we will explain how they work in the next section) and positive dispersion glass wedges. The dispersion of the pulse can be modified (scanned) in a continuous way by changing the insertion of a glass wedges. The compressor (wedges and chirped mirrors) is implemented in order to have the optimum pulse compression within the dispersion scan. Therefore, from lower to higher glass insertion, the pulse chirp is changed from negative to positive, respectively. The SHG spectrum is measured

as a function of the glass insertion, which is referred to as an experimental 'd-scan trace' (for example, see Fig. 9.2a).

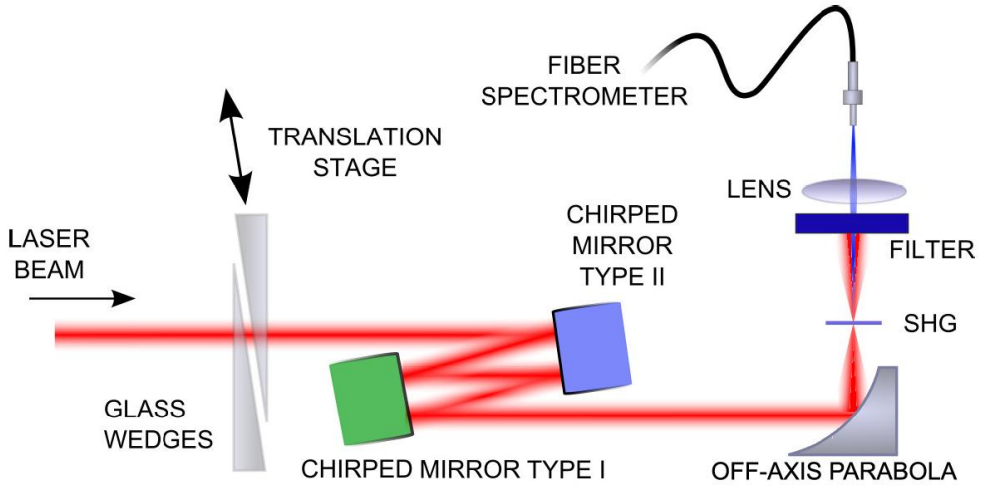


Fig. 9.1. Experimental setup for the d-scan technique: a pair of glass wedges (introducing positive dispersion in a continuous way) is combined with negative dispersion chirped mirrors to compress the pulse. The spectrum of the second-harmonic generation (SHG) of the pulse focused in a nonlinear crystal is measured as a function of the dispersion by modifying the glass insertion. Figure extracted from [23].

One of the key points is that the d-scan trace is directly related to the spectral phase $\phi(\omega)$ of the pulse, $E_f(\omega) = |E_f(\omega)|e^{i\phi(\omega)}$, that is going to be compressed and characterized. The d-scan trace is given by the expression

$$S_{dscan}(\omega, d) = |\mathcal{F}\{[\mathcal{F}^{-1}\{E_f(\omega)e^{id\cdot k(\omega)}\}]^2\}|^2, \tag{9.1}$$

where $\mathcal{F}$ and $\mathcal{F}^{-1}$ denote the Fourier-transform and its inverse (respectively), $d$ is the glass insertion (thickness), and $k(\omega)$ is the glass wave number. The dispersion introduced during the scan is calculated from the refractive index (e.g. using Sellmeier equations) of the wedges material and the thickness introduced during the wedge translation. The pulse, $E_f(\omega)$, is modified by the dispersion of the wedges, $\exp\{id\cdot k(\omega)\}$, and then it is up-converted in the nonlinear crystal. The SHG is calculated as the square of the electric field in time (after $\mathcal{F}^{-1}$), which assumes an instantaneous and wavelength-independent nonlinearity [22]. After squaring, an additional $\mathcal{F}$ provides the SHG in the frequency domain, whose squared amplitude is measured in the spectrometer as a function of the glass insertion.

The spectral amplitude of the fundamental pulse is measured directly with an spectrometer, that is, $S(\omega) = |E_f(\omega)|^2$. To retrieve the phase of the pulse $\phi(\omega)$, a guess phase is expressed in a certain basis (e.g. Fourier or Taylor series), its simulated d-scan trace is calculated according to Eq. (9.1), and the coefficients in that basis are calculated by numerically optimizing (using an iterative algorithm) the simulated trace (Fig. 9.2b) with respect to the experimental trace. The optimization is done using the Nelder-Mead (or downhill simplex) algorithm, where the minimized merit function is the comparison between the experimental and the simulated traces [26]. Therefore, the spectral phase of the pulse is fully determined and, together with the spectral amplitude, the pulse is calculated in the temporal domain. Since there is a coupling between all the

fundamental wavelengths and all the up-converted wavelengths [22,23], this technique makes it possible to relax the requirements on the bandwidth of the nonlinear crystal, and therefore relatively thick crystals can be used taking into account the large bandwidth of the fundamental spectrum. Moreover, the frequency marginal of the d-scan trace, $M(\omega)=\int_{-\infty}^{\infty} S_{dscan}(\omega,z)\,dz$, is an invariant and can be used to calibrate the trace, thus avoiding the calibration of the SHG spectral amplitude [22] (in Section 1.3.1, we commented how the marginals of the FROG trace are useful since they provide the autocorrelation and the spectrum). The duration of the iterative retrieval algorithm will depend on the complexity of the trace, which is linked to the complexity of the spectral phase. For example, a phase with fast oscillations or jumps will require a basis with more elements to be described, and therefore the calculation will be longer.

Once the spectral phase is retrieved for the "zero" glass insertion (a certain position of the wedge), it can be calculated for any other value of the wedge insertion (the glass dispersion is known). The optimum compression will correspond to the wedge position that provides the shortest pulse.

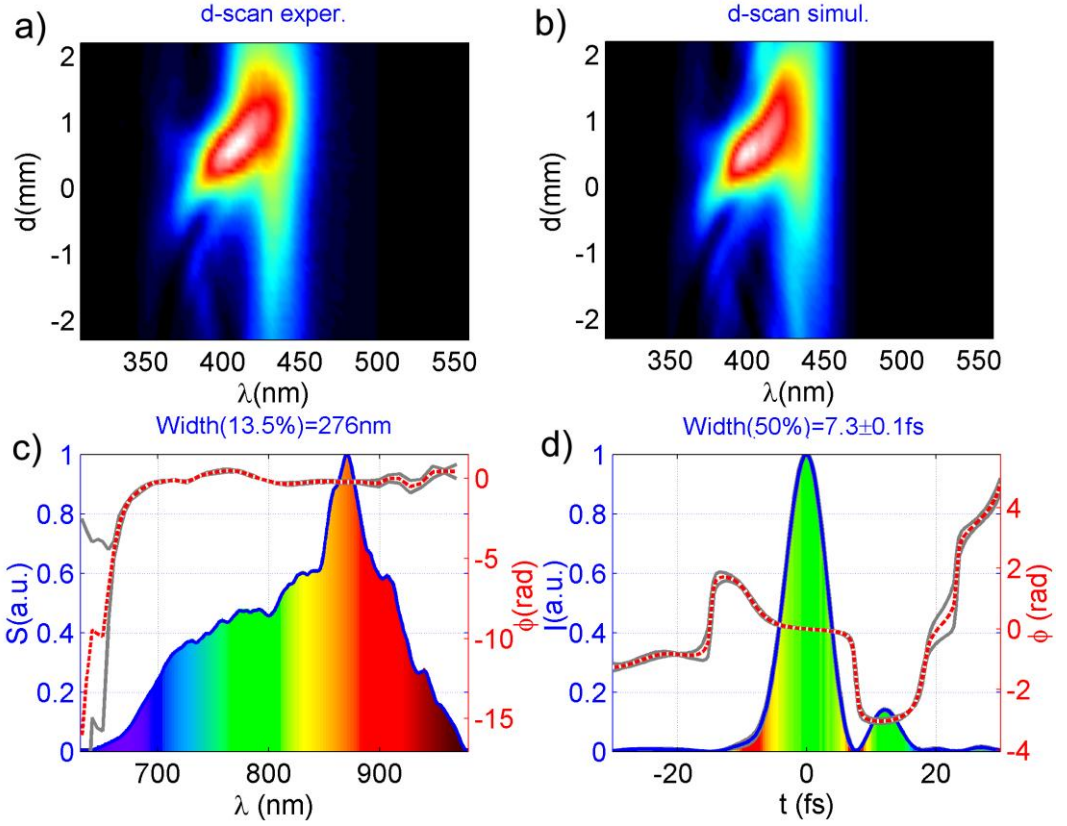


Fig. 9.2. (a) Experimental and (b) retrieved d-scan trace of the reference pulse. (c) Spectrum (blue) and phase (dashed red) of the retrieved pulse. (d) Intensity (blue) and phase (dashed red) of the reference pulse. The gray curves in (c) and (d) represent the standard deviation of the retrievals. (c) and (b) correspond to the optimum compression.

For the sake of clarity, in this section we will show the measurement of the reference pulse with the d-scan. In fact, this measurement was taken with the experimental setup depicted in Fig. 9.3, which also includes the spatiotemporal characterization. For the d-scan, BK7 wedges (Femtolasers GmbH) were used with antireflection-coating and an angle of 8º. Simultaneously to the d-scan, the pulse was focused in a nonlinear crystal

(BBO, type I, $20\mu m$ thick) by an off-axis parabolic (OAP) mirror with a focal length of 5 cm. The SHG signal produced in the BBO crystal was collimated by a lens and a blue filter was used to remove residual infrared radiation before the detection with a calibrated fiber-coupled spectrometer (HR4000, Ocean Optics Inc.).

The dispersion scan was done, as usual, by translating one wedge along the direction illustrated in Fig. 9.1 (Fig. 9.3). The total scan corresponded to 59 points with a step of $0.6mm$ in the direction of the scan. This is translated into a total glass insertion of $d = 4.84mm$ in the propagation direction of the pulse (thickness). We measured three independent d-scans of the pulse in order to perform several pulse retrievals. The program used for the d-scan retrievals was implemented and run by Miguel Miranda (Universidade do Porto, Portugal).

The experimental d-scan trace is shown in Fig. 9.2a. The corresponding retrieved trace is given in Fig. 9.2b and shows a good matching to the measurement. The spectrum and phase of the retrieved pulse for the best achieved compression are shown in Fig. 9.2c. The full width at $1/e^2$ of the characterized spectrum is $276nm$. The standard deviation of the phase (gray curve) for the different retrievals shows the small precision error present in the retrieval. In Fig. 9.2d the temporal intensity and phase of the pulse is depicted. The Fourier-limited duration of the measured spectrum is $6.7\,fs$ (FWHM) and the duration of the retrieved pulse is $7.3 \pm 0.1\,fs$ (FWHM). The gray curves are the standard deviation of the amplitude and phase calculated from the different traces, showing a small variation between them: $< 0.4\,rad$ for the spectral phase, $< 0.1rad$ for the temporal phase and $< 0.035$ for the normalized temporal intensity evolution. The carrier frequency subtracted in the temporal phase plot corresponds to the wavelength $800nm$.

## 9.3. Experimental setup

The experiments were performed with a Ti:sapphire ultrafast oscillator (Femtolasers Rainbow CEP) at a repetition rate of 80 MHz, with a central wavelength around 800 nm, a Fourier-transform limit of $\approx 7$ fs and an energy per pulse of 2.5 nJ. The experimental setup (Fig. 9.3) for the full characterization of these pulses is divided into two main parts, corresponding to the combination of the d-scan technique [22] (seen in the previous section) for measurement of the reference pulse, and the STARFISH technique [25] (presented in Chapter 4) for the spatiotemporal characterization of the test pulse.

Regarding the STARFISH setup, we replaced the usual beam splitter for ultrashort pulses (that we have used in previous experiments with pulses longer than 30 fs) by an ultra-broadband beam splitter (BS, Venteon GmbH). The BS produces a replica of the oscillator pulses, to be used as reference pulse in the SI. A flip mirror is used to obtain the measurement of the reference pulses using the d-scan. The test pulse is focused by a 5-cm focal length OAP after an iris that selects the most energetic part of the pulse's profile (diameter of 5 mm). The pulses focused by the OAP are spatiotemporally characterized by scanning their spatial profile along the x-axis with the test pulse fiber. This is performed for different propagation distances around the focus by scanning the

z-axis with the fiber. The resulting spectral interferences after the single-mode fiber coupler are detected in a spectrometer (HR4000, Ocean Optics Inc.).

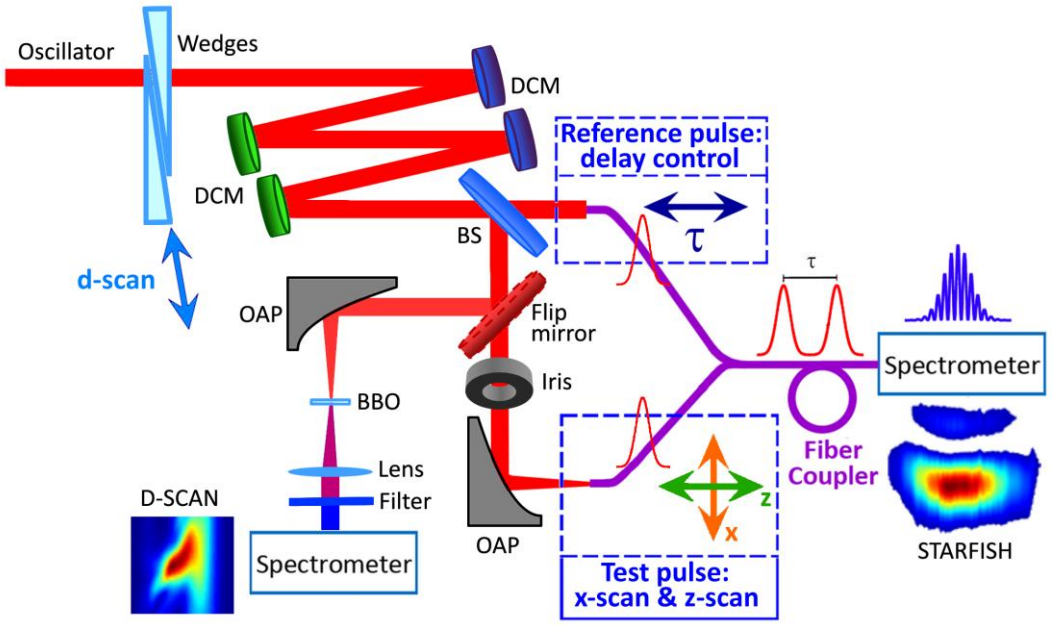


Fig. 9.3. Experimental setup for the spatiotemporal characterization of few-cycle pulses focused by an off-axis parabola (OAP) of 5-cm focal length. The pulses are simultaneously compressed and characterized using the dispersion scan (d-scan) technique, where a compressor based on a wedge pair and two pairs of double chirped mirrors (DCM) enables tracking the second-harmonic generation (SHG) signal in a nonlinear crystal (BBO) as a function of dispersion. The pulses are divided by a broadband beam splitter (BS) and coupled for the spectral interferometry of STARFISH. The test and reference pulses are combined in a fiber optic coupler and sent to the spectrometer. The position of the test fiber performs the scan (in the spatial, x, and the longitudinal, z, coordinates).

As said before, we measured the reference pulse with the d-scan, whose setup is based on a set of chirped mirrors and a glass wedge pair (BK7, angle 8º). The SHG of the pulse in a BBO ( $20\mu m$ ) was measured as a function of the glass insertion (d-scan trace). The chirped mirrors were two pairs of double-chirped mirrors (DCM, Venteon GmbH), with each pair composed of two types of mirrors, named 'blue' and 'green', designed to compensate for the oscillations in the group delay (we explain it below, see Fig. 9.4). The group delay dispersion (GDD) introduced by the DCMs is approximately $-120\,fs^2$ per two bounces at 800 nm.

A chirped mirror is a dielectric mirror especially designed for broadband operation [27]. A dielectric mirror is a set of different dielectric layers of a certain thickness, which reflect a particular wavelength. In a chirped mirror, multilayers are designed to reflect different wavelengths at different depths. In our particular case, bluer frequencies are reflected closer to the mirror surface than redder frequencies, since the aim is to introduce negative dispersion in the pulse (in order to compensate for materials dispersion). Of course, the dispersion introduced by the chirped mirror can be designed in a different way, if desired.

However, broadband chirped mirrors are afflicted by oscillations in the group delay, as shown in Fig. 9.4. These oscillations may strongly destroy the pulse structure,

producing smaller satellites and reducing the peak intensity of the main pulse. Several approaches have been implemented to suppress the oscillations, for example double-chirped mirrors (DCM) as those used in the present experiment. In the case of DCM, two mirrors are designed to introduce opposite oscillations, reducing considerably the residual ringing of the pair [28] (Fig. 9.4a). In next chapter, we will use ultra-broadband chirped mirrors (UltraFast Innovations GmbH) designed to operate under two different angles of incidence. The 'double-angle' chirped mirrors almost compensate the group delay dispersion oscillations from two bounces [29] (Fig. 9.4b). The reflectivity of the chirped-mirrors will also depend in the multilayers design and optimization (Fig. 9.4).

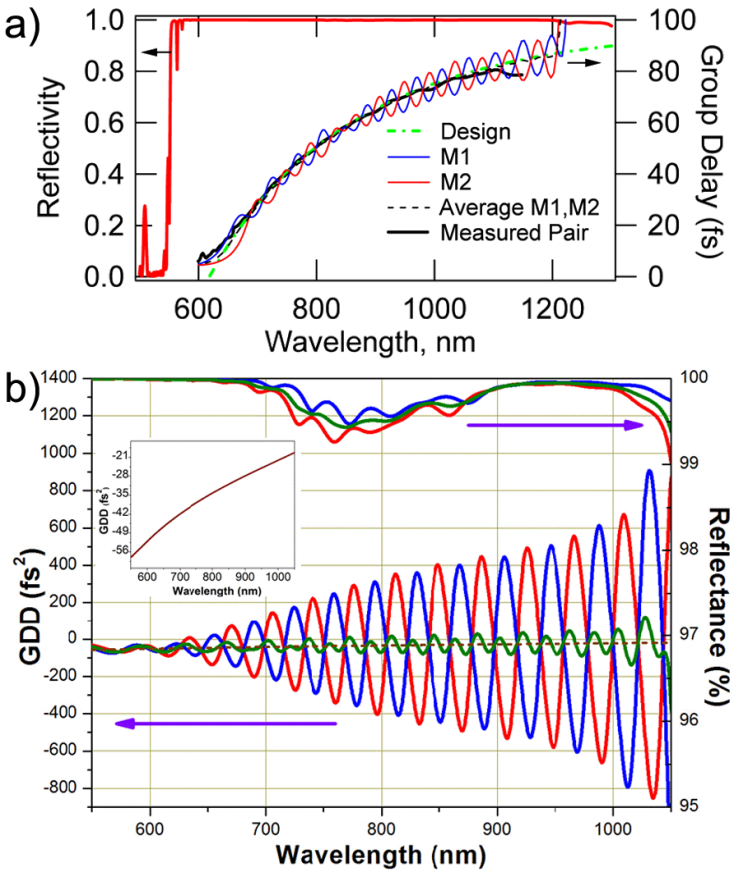


Fig. 9.4. Reflectivity curve and group delay oscillations for (a) double-chirped mirrors (DCM) and (b) double-angle chirped mirrors. In the first case, two different mirrors are designed with opposite group delay oscillations. In the second case, one mirror is designed to introduce opposite oscillations at two different angles of incidence. In both cases, the combination of the red and blue curves of the group delay provides the almost compensated green curve. Figures extracted from [28] and [29], respectively.

Concerning the application of STARFISH in the regime ultra-broadband pulses, the calibrations of the fiber coupler done in Section 4.2 confirmed that it can be applied to the measurement of few-cycle focused pulses. The broad operating bandwidth, extending from around 550 to 1000 nm comprises the pulse spectrum of the oscillator. For the numerical aperture $NA$, we measured a half-width of the collection angle of the input fiber of $\theta_{50\%} \simeq 5^{o}$, defined as the angle of incidence at which the coupling efficiency falls to 50%.

In this experiment, the oscillator pulses focused with a focal length $f = 50mm$ were measured, and an iris with a radius $r_M = 2.5mm$ was used before the OAP. The maximum angle of the wave vectors, $\theta_M \approx 2.86^{\circ}$, is estimated from $\tan\theta_M = r_M / f$ (see discussion in Section 4.2.5). From the calibration of the transmission of the fiber coupler (Fig. 4.8b), the transmission of the spectral power density will be $\geq 75\%$ (therefore $\geq 86\%$ in amplitude). Taking also into account that the outer part of the oscillator mode (before focusing) is less intense, this means that the effect of the *NA* in the measurements of the focused pulses can be neglected.

## 9.4. Characterization of few-cycle pulses delivered by an oscillator

### *9.4.1. Spatiospectral and spatiotemporal characterization: STARFISH*

We used STARFISH to characterize the focusing region of the oscillator after the OAP ($f = 50\,mm$). The measurements were taken for 7 consecutive propagation distances z around the focus, in order to track the evolution of the focused pulses: $z = f + \{-1.5\ -1.0\ -0.5\ 0\ 0.5\ 1.0\ 1.5\}\,mm$. The spatiospectral (and spatiotemporal) amplitude and phase were retrieved for each z-plane. The spatial features in the transverse plane were measured in one axis (x-axis), since the system was assumed to have cylindrical symmetry. Similar sets of measurements can be performed in the full x-y plane just by spatially scanning with two perpendicular linear actuators.

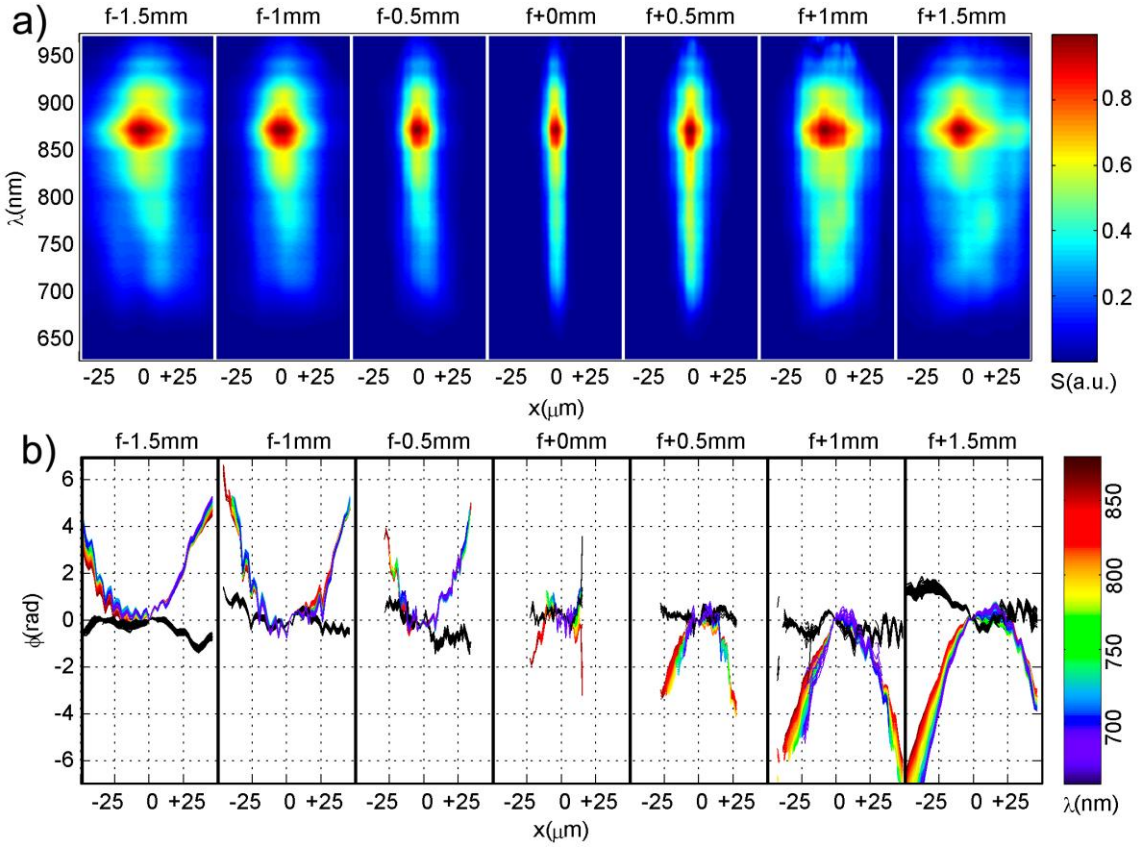


Fig. 9.5. (a) Normalized spatiospectral intensity and (b) frequency-resolved wavefront at different propagation distances z around the focus of the OAP, the latter represented in different colored curves for each wavelength (see the colorbar). The black curves are the error obtained in the wavefronts from two independent measurements.

The evolution of the spatially-resolved spectrum is shown in Fig. 9.5a as a function of the longitudinal position z. The x-axis extends from -25 to 25 $\mu m$ in all cases. The x-scan was done in steps of $1\mu m$. During propagation, it is mainly the spatial width (x-axis) that is changing, whereas the spectrum is almost undistorted. Owing to the broad bandwidth of the pulses, the effect of smaller focal spot size due to diffraction for the shorter wavelengths is visible in the spatially-resolved spectrum at the focus of the OAP in Fig. 9.5a. Apart from this effect, the main consequence is a change of the relative amplitude of the spectral components, in particular the fact that shorter wavelengths exhibit slightly larger amplitudes with respect to longer wavelengths. To show this effect more clearly, in Fig. 9.6 we plot the on-axis spectrum as a function of the propagation distance $S(\lambda, z; x = 0)$. Other small distortions can be attributed to a misalignment of the OAP or to a non-homogeneous spatial profile of the oscillator (before the OAP).

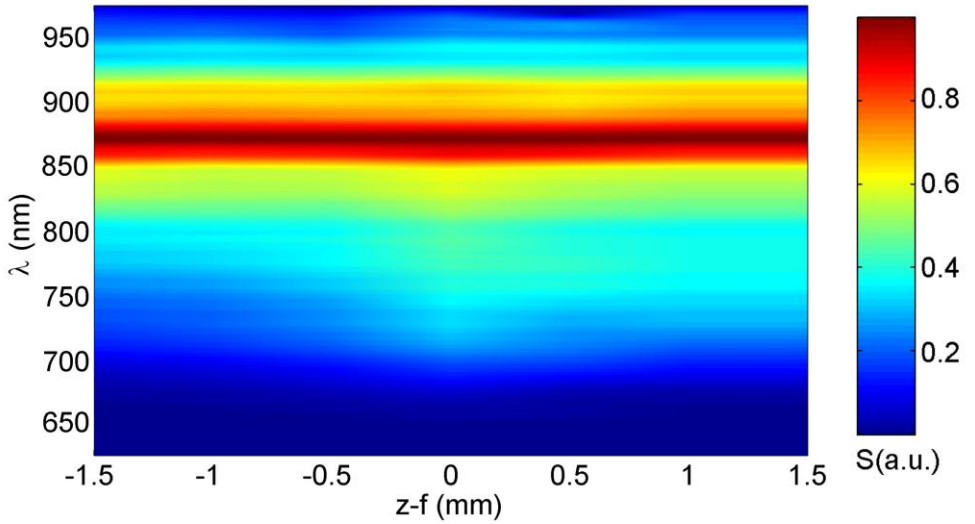


Fig. 9.6. Normalized on-axis spectrum (for x=0) at different propagation distances z around the focus of the OAP.

In Fig. 9.5b, the spatiospectral phase (or wavefront) is represented for the same set of axial distances. Since STARFISH retrieves the frequency-resolved wavefront [30] (with a small noise due to phase drifts), we represent the phase $\phi(x)$ for different wavelengths $\lambda_0$. For greater clarity, we represent these wavefronts, $\phi(x; \lambda = \lambda_0)$, using a different color for each wavelength and shifted to $\phi(x; \lambda = \lambda_0) = 0$ in $x = 0$, which is equivalent to removing the spectral phase on-axis. To corroborate the result, we took two independent measurements ($x$-scans) for each position $z$. As a result, we also represent the error (black curves) calculated from their difference. In spite of the presence of some noise, these measurements can be used to determine qualitatively and quantitatively the convergence and divergence of the pulse, thus helping to identify the propagation distance analyzed in each measurement. As observed in the measurements, for the pulses focused by the OAP the redder wavelengths have smaller curvature than the bluer ones, as given by the dependence of the wave number on wavelength, $k \propto \lambda^{-1}$.

In the spatiotemporal domain, the intensity of the pulses along the focusing region is given in Fig. 9.7a. Here, the temporal features are also roughly constant both in the x-

axis and along z, with the spatial width (x-axis) of the pulses exhibiting the largest variation as the pulse approaches and moves away from the focus. Figure 9.7b depicts slices of the on-axis (x=0) temporal intensity, with the instantaneous wavelength (calculated from the inverse of the derivative of the temporal phase) shown in different colors that give us information on the temporal chirp of the pulses. Owing to the overall positive chirp of the pulses, combined with the relative amplitude decrease of redder wavelengths with respect to the bluer part of the spectrum (as mentioned above), the temporal intensity presents a small decrease in the leading part of the pulse in the planes closer to the focus. The chirp is almost constant along the direction of propagation. These results are consistent with the expected almost constant temporal profile in the focusing region.

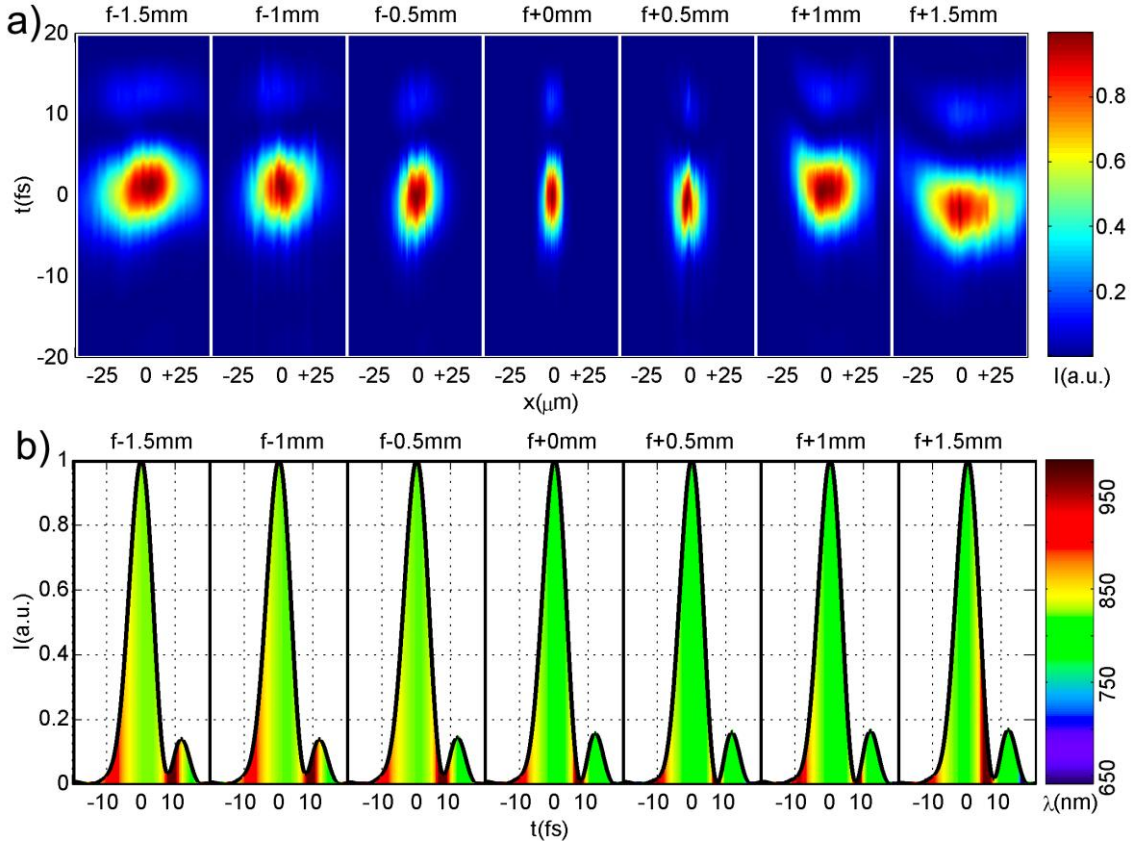


Fig. 9.7. (a) Normalized spatiotemporal intensity at different propagation distances z around the focus of the OAP. (b) Normalized on-axis intensity (x=0) colored by the instantaneous wavelength of the pulse for the same propagation distances.

### *9.4.2. Comparison of the on-axis results*

Here, we compare the spectral and temporal retrievals obtained on-axis (x=0) for the 7 propagation distances characterized. From each spatiospectral (and spatiotemporal) measurement, we have extracted the characterization on-axis and have calculated the statistics of the 7 retrievals. For the spectral domain, in Fig. 9.8a, the mean spectral power (blue curve) and the corresponding standard deviation (gray curves) are represented, together with the spectral phase (red curve) and its standard deviation (gray curves). From the results, it is clear that the spectral amplitude deviation is higher than

the phase deviation, indicating that the differences observed in the temporal profiles of Fig. 9.7b are mainly originated by the differences in the spectral amplitude. In Fig. 9.8b, the temporal duration (FWHM) of the on-axis pulses is plotted as a function of the propagation distance. The variation of these widths is compared with the FWHM of the Fourier-transform limit (FTL) of the corresponding spectra, exhibiting a correlation between the width of the FTL and the actual width of the pulses. This result again supports the idea that the differences mainly come from the amplitude and not from the phase. As can be seen from Fig. 9.6, the explanation of this result is that the spectral amplitude reshaping due to the focusing flattens the spectrum close to the focus (since the shape of the input spectrum on Fig. 9.2c has lower signal for shorter wavelengths) and this induces a small reduction in the FTL and the duration of the pulse, as seen in Fig. 9.8b. The correlation between Fig. 9.6 and Fig. 9.8b is clear.

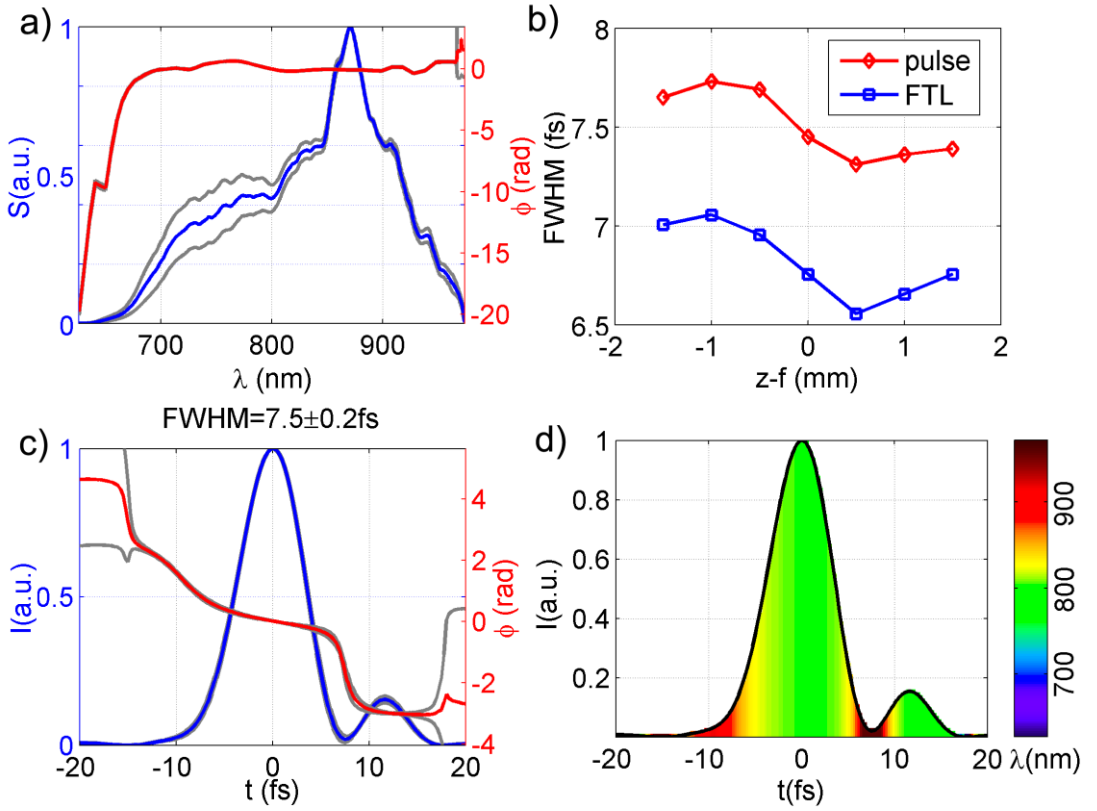


Fig. 9.8. (a) Mean of the spectral amplitudes (blue curve) and phases (red curve) retrieved on-axis for the five propagation distances, and corresponding standard deviation (gray curves). (b) Temporal width (FWHM) of the on-axis intensity reconstructions of the pulses for different propagation distances, and comparison with the FWHM of the Fourier-transform limit (FTL) of the corresponding spectra. (c) Mean of the temporal amplitudes (blue curve) and phases (red curve) retrieved on-axis for the five propagation distances, and standard deviation (gray curves). (d) Intensity colored by the instantaneous wavelength (see colorbar) of the mean of the on-axis measured pulses.

As mentioned above, the variations observed in the spectral domain are also present in the temporal domain. Fig. 9.8c shows the mean temporal intensity (blue) and its standard deviation (gray). The same applies for the temporal phase (red) and its deviation (gray). Here, it is also observed that the difference in the phase is smaller than the difference in the amplitude. The statistics of the pulse width retrieved on-axis gives

a FWHM of $7.5 \pm 0.2\,fs$, which is consistent with the retrieval of the d-scan. In Fig. 9.8d, the mean temporal profile colored and the mean instantaneous wavelength are also represented, showing the good match with the results of Fig. 9.7b.

These results can be interpreted as the validation of the current experimental implementation of the d-scan technique (and could also be extrapolated to other techniques, in which the pulses to be characterized are focused in the nonlinear crystal with an OAP), in the sense that it is assumed that the focus of the OAP does not distort the temporal (or equivalently spectral) amplitude and phase of the pulse. Here, we have found that small differences can occur, although they do not hinder proper pulse retrieval.

### *9.4.3. Measurement of the peak irradiance of ultrashort laser pulses*

As discussed in Chapter 1, here we are measuring the irradiance of the pulses, which is given in $W/cm^2$ units. However, in the literature of our field, this magnitude is usually referred to as the intensity of the pulse. Here, therefore, we will also follow this criterion. The measurement of the peak intensity of ultrashort laser pulses is often difficult to address, many times owing to the high intensities involved. We will show how the characterization of the spatiotemporal intensity of the pulses can be used to calculate an estimation of the peak intensity. In previous chapters, we have represented the intensity in arbitrary units (a.u.), in the cases where the spatiotemporal distribution is the important result and the absolute value is irrelevant (e.g. linear propagation after diffractive optical elements), and in the cases where the absolute value was unknown (e.g. in the filamentation).

The integral in the two spatial coordinates and the temporal dimension gives the energy of the pulse $E$, as given in Eq. (9.2), where $I_E(r,t)$ represents the experimental normalized spatiotemporal intensity distribution at a certain $z$, and $\kappa_{rt}$ represents the peak intensity of the pulse:

$$E = \kappa_{rt} \int_{-\infty}^{\infty} \left[ \int_{0}^{\infty} I_E(r,t)\, 2\pi r\, dr \right] dt\,. \tag{9.2}$$

Since we are assuming cylindrical symmetry, the characterization was done only in one spatial dimension (x-axis). The scan was performed in the full axis, i.e., over the two sides of the beam profile with respect to the center (x=0). Consequently, we have double information and we obtain two values of the peak intensity per measurement, corresponding to the integration in the polar radius $r_1 \equiv \{|x| : x \geq 0\}$ and $r_2 \equiv \{|x| : x \leq 0\}$, respectively.

Often, the full spatiotemporal information is not available and we have to make approximations to obtain the peak intensity. Here, we will do a first rough calculation just for comparison. To simplify, we can consider a focused pulse with a Gaussian profile both in the temporal and in the spatial coordinates, thus with separable dependence in time and space. In this case, the irradiance $I_G(r,t)$ is given by

$$I_G(r,t) = \kappa_G \exp\left\{-(4\ln 2)\, r^2 / FWHM_x^2\right\} \exp\left\{-(4\ln 2)\, t^2 / FWHM_t^2\right\}, \tag{9.3}$$

where $FWHM_t$ and $FWHM_x$ are, respectively, the pulse full widths in the temporal and the spatial coordinates. We take the $FWHM_t$ from the on-axis intensity widths, whose results are shown in Fig. 9.8b. To calculate the spatial width $FWHM_x$, we consider the full width in the x-axis after integration in wavelengths of the spatiospectral traces shown in Fig. 9.5a. The results for $FWHM_x$ are shown in Fig. 9.9a as a function of the propagation distance. After integrating the Gaussian irradiance $I_G(r,t)$, we obtain the following relation between the pulse energy, the x- and t-widths, and the peak intensity:

$$E = \int_{-\infty}^{\infty}\left[\int_{0}^{\infty} I_G(r,t)\,2\pi r\,dr\right]dt = 1.536\kappa_G\left(\pi\frac{FWHM_x^2}{4}\right)FWHM_t\,. \qquad (9.4)$$

From Eq. (9.4) we see that the Gaussian peak intensity $\kappa_G$ is proportional to the pulse energy and inversely proportional to the temporal width, $FWHM_t$, and the spatial section, $(\pi/4)FWHM_x^2$. The factor 1.536 depends on the spatial and the temporal profile of the pulse, in this case Gaussian functions.

The energy per pulse $E = P/f_{rep}$ is calculated from the measured average power $P$ and the pulse repetition rate $f_{rep} = 80MHz$. The power measured after the $5mm$ iris and the OAP was $P = 80\,mW$, so the energy per pulse was $E = 1nJ$. We consider that the fraction of this energy that is lost (spatially spread) in the focus is negligible, assuming a well focused pulse without diffraction losses. Other factors can also affect the result, for example part of the radiation being incoherent (e.g. amplified spontaneous emission) or small pre- or post-pulses that are not measured. Therefore, the peak intensity obtained by this procedure should be considered as an estimate of the actual value.

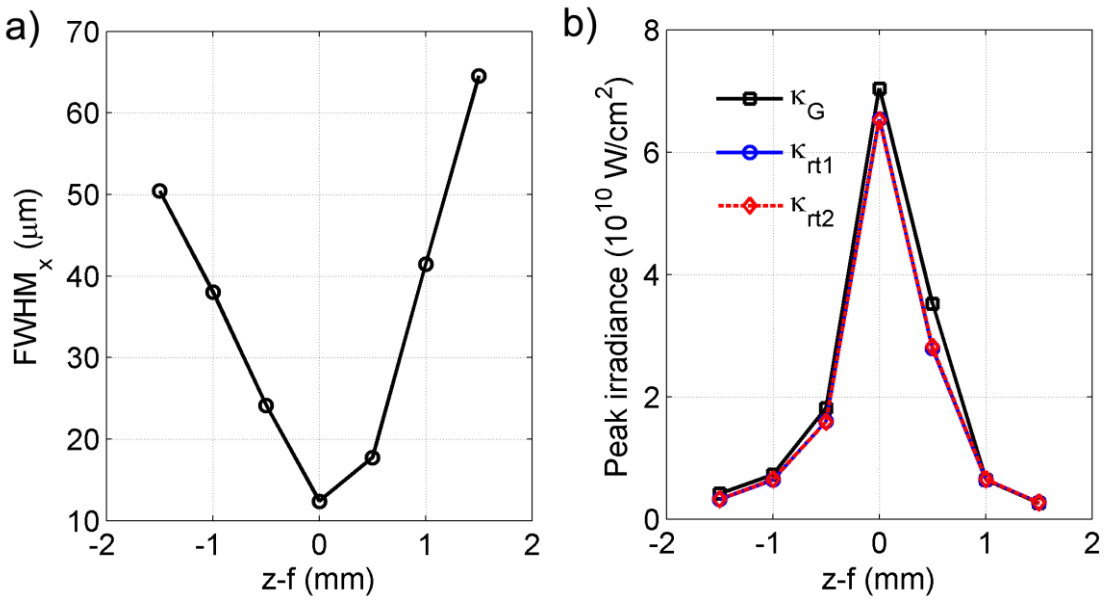


Fig. 9.9. (a) Experimental spatial width (FWHM) as a function of the propagation distance. (b) Peak intensity as a function of the propagation distance calculated from the assumption of spatial and temporal Gaussian shape (black curve-squares) and from the measured spatiotemporal intensity using the right-hand-side (blue curve-circles) and the left-hand-side (red dashed curve-diamonds) of the x-axis.

The comparison of the results for the peak intensity as a function of the propagation distance is shown in Fig. 9.9b. As expected, the peak intensity is higher closer to the focus, where the spatial width decreases. The values obtained at the focus ( $z = f$ ) are $\kappa_G = 6.92 \cdot 10^{10} W/cm^2$, $\kappa_{rt1} = 5.67 \cdot 10^{10} W/cm^2$ and $\kappa_{rt2} = 5.63 \cdot 10^{10} W/cm^2$ in the Gaussian irradiance approximation, for the measured spatiotemporal irradiance from the set $r_1 \equiv \{|x| : x \geq 0\}$ and from the set $r_2 \equiv \{|x| : x \leq 0\}$, respectively. The two values for the full spatiotemporal calculation overlap, whereas the Gaussian estimation gives higher values. This occurs because the irradiance is more spread in the temporal dimension than in a Gaussian function with the same $FWHM_t$ and, accordingly, the actual peak intensity is lower. In general, assuming a certain profiles and uncoupled space-time dependence is not enough to estimate the peak intensity.

## 9.5. Conclusions

Current techniques for the temporal characterization of laser pulses have already reached the few-cycle regime. In particular, the d-scan technique is very powerful due to its simple and low-demanding experimental implementation. The large operating spectral bandwidth of the fiber optic coupler based interferometer makes possible the application of the STARFISH technique for the spatiotemporal characterization of few-cycle pulses, provided that the d-scan is used to measure the reference pulse for the SI.

We have reconstructed spatiotemporally the pulses delivered by an ultrafast oscillator (6.7 fs FWHM Fourier-transform limit) focused by an OAP. The full retrieval of the amplitude-and-phase in the spatiotemporal and spatiospectral domains gives additional information that is lost with usual temporal characterization techniques. We have measured pulses with durations below 8 fs (FWHM) and have studied the evolution of the pulses along the focusing region. We found that temporal dependence of the pulses is practically preserved around the focus of the OAP, presenting small changes in the spectral and temporal amplitude (due to the dependence of the focal spot size for different wavelengths in ultra-broadband pulses), and almost invariant spectral and temporal phases. OAPs are important devices that find many uses in pulse focusing and characterization (especially of ultra-broadband pulses), precisely because of the absence of dispersion and chromatic aberrations, provided that they are properly aligned. STARFISH allows us to know whether the focusing is properly performed in both the xy-plane (in fact, we measured only the x-axis) and the z-axis.

We have calculated the peak intensity (or the peak irradiance) of the pulses from the spatiotemporal reconstruction of the pulse propagation in linear regime. In the case of pulses with spatiotemporal coupling (e.g. see the results for diffracted pulses in Chapters 5-7), it is not enough to consider separately the space and the time dependence. In general, is difficult to measure the absolute value, so this estimation can be helpful in many situations. In the case of nonlinear pulses with high intensities, the damage in the collecting fiber may prevent the access to this information. A sample of the pulse may be taken, in a similar way to how it is done for the filament in Chapter 8, to avoid damaging the fiber.

We expect the availability of spatiotemporal characterization techniques in the few-cycle regime to be extremely helpful to study processes involving ultrafast oscillators, as well as processes employing high-energy pulses such as pulse post-compression and high-order harmonic generation, among others. In the next chapter, we will show the application to the characterization of pulses post-compressed in an argon-filled hollow-core fiber.

## References


[1] A. Baltuška, Z. Wei, M. S. Pshenichnikov, D. A. Wiersma, and R. Szipöcs, "All-solid-state cavity-dumped sub-5-fs laser," Appl. Phys. B 65, 175–188 (1997).

[2] H. M. Crespo, J. R. Birge, E. L. Falcão-Filho, M. Y. Sander, A. Benedick, and F. X. Kärtner, "Nonintrusive phase stabilization of sub-two-cycle pulses from a prismless octave-spanning Ti:sapphire laser," Opt. Lett. 33, 833-835 (2008).

[3] T. Udem, R. Holzwarth, and T. W. Hänsch, "Optical frequency metrology," Nature 416, 233-237 (2002).

[4] A. A. Eilanlou, Y. Nabekawa, K. L. Ishikawa, H. Takahashi, and K. Midorikawa, "Direct amplification of terawatt sub-10-fs pulses in a CPA system of Ti:sapphire laser," Opt. Express 16, 13431-13438 (2008).

[5] M. Nisoli, S. De Silvestri, O. Svelto, R. Szipöcs, K. Ferencz, Ch. Spielmann, S. Sartania, and F. Krausz, "Compression of high-energy laser pulses below 5 fs," Opt. Lett. 22, 522-524 (1997).

[6] C. P. Hauri, W. Kornelis, F.W. Helbing, A. Heinrich, A. Mysyrowicz, J. Biegert, and U. Keller, "Generation of intense, carrier-envelope phase-locked few-cycle laser pulses through filamentation," Appl. Phys. B 79, 673-677 (2004).

[7] G. Stibenz, N. Zhavoronkov, and G. Steinmeyer, "Self-compression of millijoule pulses to 7.8 fs duration in a white-light filament," Opt. Lett. 31, 274–276 (2006).

[8] T. Brabec and F. Krausz, "Intense few-cycle laser fields: Frontiers of nonlinear optics," Rev. Mod. Phys. 72, 545-591 (2000).

[9] B. Alonso, I. J. Sola, J. San Román, O. Varela, and L. Roso, "Spatiotemporal evolution of light during propagation in filamentation regime," J. Opt. Soc. Am. B 28, 1807-1816 (2011).

[10] B. Alonso, M. Miranda, F. Silva, V. Pervak, J. Rauschenberger, J. San Román, I. J. Sola, and H. Crespo, "Generation and spatiotemporal characterization of 4.5-fs pulses from a hollow-core fiber compressor," submitted (2012).

[11] B. Alonso, M. Miranda, I. J. Sola, and H. Crespo, "Spatiotemporal characterization of few-cycle laser pulses," Opt. Express 20, 17880-17893 (2012).

[12] I. A. Walmsley and C. Dorrer, "Characterization of ultrashort electromagnetic pulses," Adv. Opt. Photon. 1, 308-437 (2009).

[13] R. Trebino and D. J. Kane, "Using phase retrieval to measure the intensity and phase of ultrashort pulses: frequency-resolved optical gating," J. Opt. Soc. Am. A 10, 1101–1111 (1993).

[14] C. Iaconis and I. A. Walmsley, "Spectral phase interferometry for direct electric-field reconstruction of ultrashort optical pulses," Opt. Lett. 23, 792–794 (1998).

[15] A. S. Wyatt, I. A. Walmsley, G. Stibenz, and G. Steinmeyer, "Sub-10 fs pulse characterization using spatially encoded arrangement for spectral phase interferometry for direct electric field reconstruction," Opt. Lett. 31, 1914–1916 (2006).

[16] J. R. Birge, H. M. Crespo, and F. X. Kärtner, "Theory and design of two-dimensional spectral shearing interferometry for few-cycle pulse measurement," J. Opt. Soc. Am. B 27, 1165–1173 (2010).

[17] A. Baltuška, M. S. Pshenichnikov, and D. A. Wiersma, "Amplitude and phase characterization of 4.5-fs pulses by frequency-resolved optical gating," Opt. Lett. 23, 1474–1476 (1998).

[18] A. Baltuška, M. S. Pshenichnikov, and D. A. Wiersma, "Second-harmonic generation frequency-resolved optical gating in the single-cycle regime," IEEE J. Quantum Electron. 35, 459–478 (1999).

[19] S. Akturk, C. D'Amico, and A. Mysyrowicz, "Measuring ultrashort pulses in the single-cycle regime using frequency-resolved optical gating," J. Opt. Soc. Am. B 25, A63-A69 (2008).

[20] G. Stibenz and G. Steinmeyer, "Interferometric frequency-resolved optical gating," Opt. Express 13, 2617-2626 (2005).

[21] G. Stibenz, C. Ropers, Ch. Lienau, Ch. Warmuth, A. S. Wyatt, I. A. Walmsley and G. Steinmeyer, "Advanced methods for the characterization of few-cycle light pulses: a comparison," Appl. Phys. B. 83, 511-519 (2006).

[22] M. Miranda, T. Fordell, C. Arnold, A. L'Huillier, and H. Crespo, "Simultaneous compression and characterization of ultrashort laser pulses using chirped mirrors and glass wedges," Opt. Express 20, 688-697 (2012).

[23] M. Miranda, T. Fordell, C. Arnold, F. Silva, B. Alonso, R. Weigand, A. L'Huillier, and H. Crespo, "Characterization of broadband few-cycle laser pulses with the d-scan technique," Opt. Express 20, 18732-18743 (2012).

[24] A. S. Wyatt, A. Grün, P. K. Bates, O. Chalus, J. Biegert, and I. A. Walmsley, "Accuracy measurements and improvement for complete characterization of optical pulses from nonlinear processes via multiple spectral-shearing interferometry," Opt. Express 19, 25355-25366 (2011).

[25] B. Alonso, I. J. Sola, O. Varela, J. Hernández-Toro, C. Méndez, J. San Román, A. Zaïr, and L. Roso, "Spatiotemporal amplitude-and-phase reconstruction by Fourier-transform of interference spectra of high-complex-beams," J. Opt. Soc. Am. B. 27, 933-940 (2010).

[26] J. A. Nelder and R. Mead, "A simplex method for function minimization," Comput. J. 7, 308–313 (1965).

[27] R. Szipöcs, K. Ferencz, C. Spielmann, and F. Krausz, "Chirped multilayer coatings for broadband dispersion control in femtosecond lasers," Opt. Lett. 19, 201-203 (1994).

[28] L. Matos, D. Kleppner, O. Kuzucu, T. R. Schibli, J. Kim, E. P. Ippen, and F. X. Kaertner, "Direct frequency comb generation from an octave-spanning, prismless Ti:sapphire laser," Opt. Lett. 29, 1683-1685 (2004).

[29] V. Pervak, I. Ahmad, M. K. Trubetskov, A. V. Tikhonravov, and F. Krausz, "Double-angle multilayer mirrors with smooth dispersion characteristics," Opt. Express 17, 7943-7951 (2009).

[30] B. Alonso, R. Borrego-Varillas, O. Mendoza-Yero, I. J. Sola, J. San Román, G. Mínguez-Vega, and L. Roso, "Frequency resolved wavefront retrieval and dynamics of diffractive focused ultrashort pulses," J. Opt. Soc. Am. B 29, 1993-2000 (2012).

# CHAPTER 10

# SUB-5-FS PULSES FROM HOLLOW-FIBER POST-COMPRESSION

**Contents**



*The results in this chapter have been submitted for publication: B. Alonso et al., "Generation and spatiotemporal characterization of 4.5-fs pulses from a hollow-core fiber compressor" (2012).*

## 10.1. Generation and applications of intense few-cycle pulses

The advent of sources capable of delivering ultrashort and ultra-intense light pulses has led to numerous applications in atomic, molecular and nuclear physics [1-3]. In particular, intense few-cycle pulses have opened the way for attosecond physics [4] and metrology [5] via the extreme ultraviolet (XUV) attosecond pulse trains that can be obtained by high-harmonic generation (HHG) [6]. Intense near-infrared pulses close to the single-cycle regime have made possible the generation of isolated attosecond pulses [5,7,8].

The technique of chirped pulse amplification (CPA) combined with Ti:sapphire laser technology has provided many laboratories with intense ultrashort pulses in the 20 to 100 fs range (the lower limit essentially imposed by gain narrowing effects). Although sub-10-fs pulses can be directly obtained from CPA [9] and optical parametric CPA systems [10], they have proved challenging and are still the subject of much research and development.

For this reason, two post-compression techniques are usually employed for the generation of intense few-cycle pulses, based on the spectral broadening of light either during propagation in a gas-filled hollow-core fiber (HCF) [11,12] or during the filamentation of light [13]. In Chapter 8, we explained the process of the filamentation, as well as the post-compression in an HCF that we used to create the reference pulse. One of the main differences between them is the nature of the guiding. In the case of the filamentation, we illustrated how the equilibrium between the self-focusing (of the Kerr-effect) and the defocusing (due to ionization) led to a self-guiding of the pulses along a filament light channel. In the case of the HCF, the guiding is created by the fiber, that is, by geometrical constraints. In both processes, the high intensities reached during the guiding trigger nonlinear processes, responsible for spectral broadening, originated mainly from self-phase modulation (SPM). As we discussed in Chapter 8, the commonly positive spectral phase of the output pulses is compensated by chirped mirrors (CMs), by a pair of diffraction gratings, or by prism compressors.

The nonlinear nature of the spectral broadening (from SPM) provides a broader spectrum in the center of the beam where the intensity of the pulse is higher. As a consequence, the post-compressed pulses are inhomogeneous and present spatial chirp. As we have already commented, the temporal profile of filament-compressed pulses has been shown to depend on the radial coordinate [14]. Since in filamentation there is no geometrical guiding, its propagation is in principle accessible, although the high intensities may damage the detection system (as we discussed in Chapter 8). Therefore, many efforts are being devoted to the characterization of the filament propagation in terms of temporal [15], spatiotemporal [16,17] and peak intensity dynamics [18]. The performance of filamentation and HCF post-compression has been compared experimentally [19]. In particular, the authors reported that the HCF presents more symmetrical spectral distribution (with respect to the axis) and smaller dependence of the spectral broadening and shift with respect to the radial coordinate (that is, presents less spatial chirp). Recently, a spatially resolved measurement of the spectral and

temporal profile of HCF-compressed pulses has been presented, in which small spatial chirp (as said above) is observed [20].

As explained in Section 9.1, some of the now "standard" techniques for the temporal measurement of ultrashort pulses [21] have been adapted for ultra-broadband few-cycle pulses [22-24]. In this chapter, we will use the d-scan technique [25] (Section 9.2) to characterize the few-cycle reference pulse, similarly to the previous chapter. The d-scan technique –initially demonstrated with a few-cycle oscillator– was also very recently used to temporally characterize pulses post-compressed in an HCF [26], which present additional difficulties due to the higher energy, larger spectral bandwidth, stronger phase modulations, and higher instability compared to pulses from an oscillator. In order to retrieve the full spatiotemporal amplitude and phase, we will use the STARFISH technique [27] (Chapter 4), which was already proved to measure few-cycle pulses [28] (Section 4.2.4 and Chapter 9).

In this work, we generated and characterized sub-two-cycle 4.5 fs pulses (4.1 fs Fourier-limited) from post-compression of 25 fs (Fourier-limit) amplified pulses in an argon-filled HCF [29]. The d-scan technique was used to measure the reference pulse required by STARFISH and applied the latter for the spatiotemporal characterization of the mode compressed at the output of the fiber, where the pulse structure and spatial chirp were studied. These pulses were also focused using an off-axis parabolic mirror and we measured their focus in the spatiotemporal domain.

The full spatiotemporal characterization of intense few-cycle lasers provides useful information for the study of the dynamics and characteristics of filamentation [17,30] and HCF post-compressed pulses. In future experiments, it may be used to tackle the comparison between both post-compression techniques, continuing the work of Gallmann and co-workers [19]. This information is relevant for the optimization of the process itself and for the applications (e.g., HHG) of the generated pulses.

## 10.2. Experimental setup for the post-compression and its spatiotemporal characterization

We post-compressed pulses delivered by a $1kHz$ Ti:sapphire CPA amplifier (Femtolasers FemtoPower Compact PRO CEP) in a gas-filled HCF and chirped mirror (CM) compressor. The complete experimental setup is depicted in Fig. 10.1. The amplified pulses, with a Fourier-transform limit (FTL) of 25 fs, were coupled in the hollow fiber with a 1.5-m focal length lens. The HCF had an inner diameter of $250\mu m$, a length of $1m$, and was filled with argon at a pressure of 960 mbar. The pulse energy before the HCF was $375\mu J$ and the output of the fiber was $150\mu J$ (transmission of 40 %). The amplifier's compressor adjusted the chirp of the input pulse on the HCF to optimize the spectral broadening (Fig. 10.3c) and the transverse mode profile (Fig. 10.2b) at the HCF output. Additionally, we also optimized the fiber output with an iris (7-mm diameter) placed just before the lens for the fine control of the input energy and the input mode being coupled into the HCF (Fig. 10.2a). Moreover, the post-compression was optimized for a very stable output mode, as required both for subsequent applications and for (multi-shot) pulse characterization. The quality of the

d-scan and STARFISH traces is an indication of this stability, since shot-to-shot variations would strongly affect them. In parallel, the raw d-scan traces already provided a fast diagnosis to ensure that the temporal profile corresponded to clean compressed pulses without satellites that could occur in the HCF, given that it only takes a few seconds to acquire them and the shape of the trace gives direct, interpretable information about the structure of the pulse [25]. Owing to the nonlinearity of the argon gas inside the HCF, the input spectrum was broadened to a 4.1-fs FTL spectrum extending from 540 to 990 nm (Fig. 10.3c). A spherical silver mirror at near-normal incidence ($ROC = -3000mm$) was placed after the HCF to collimate the spectrally broadened pulses.

To complete the post-compression of the pulses, a compressor made of a glass wedge pair and a set of ultra broadband CMs was used. The wedges (Femtolasers GmbH) were made of BK7 with an antireflection-coating and an angle of 8º. We used 'double angle' CMs (UltraFast Innovations GmbH), which are designed in such a way that when two bounces are combined, with incidence angles of 5º and 19º respectively, the residual group delay oscillations are minimized [31] (see Fig. 9.4b in Section 9.3). We used five pairs of mirrors for a total number of five bounces at each angle, as illustrated in Fig. 10.1 (we have identified the CMs with different colors, orange and purple, for 5º and 19º incidence, respectively). The nominal group delay dispersion (GDD) of the CMs was around $-50\,fs^2$ per bounce at 800 nm. The variable insertion of one of the wedges allowed us to fine tune the ultimate post-compressed duration of the pulses, and was also used as part of the d-scan technique (Section 9.2). Note that for the post-compression we have used a higher gas pressure than in the previous work [26], which provided a broader spectrum here. Also, the compression in [26] was performed using different CMs.

For the characterization of the post-compressed pulses, we used the STARFISH technique [27] (Chapter 4) assisted by the d-scan technique [25] (see details in Section 9.2) to measure the reference pulse, in a configuration similar to that of the previous chapter. A replica of the pulse to be characterized was created with a dispersion-balanced (same dispersion in the reflected and transmitted beams) broadband beam splitter (600-1500 nm), BS (Venteon GmbH). One pulse replica was measured with the d-scan (after the flip mirror) and it was subsequently used as the reference pulse in STARFISH. In the present setup, for the d-scan we focused the pulses with an off-axis parabolic (OAP) mirror (focal length of 5 cm) in a nonlinear crystal (BBO, $20\mu m$ thick, cut for type I SHG at 800 nm). The second-harmonic generation (SHG) signal was collimated with a lens and a blue filter was used to remove the remaining fundamental frequency signal before detection with the spectrometer (HR4000, Ocean Optics Inc.).

In STARFISH, a single-mode, $4\mu m$ core diameter, broadband fiber optic coupler [27,28] was used to combine the reference pulse (already characterized by the d-scan) and the (unknown) test pulse. The spectral interferogram (SI) of the $\tau$-delayed pulses was measured in a standard fiber-coupled spectrometer (S2000, Ocean Optics Inc.).

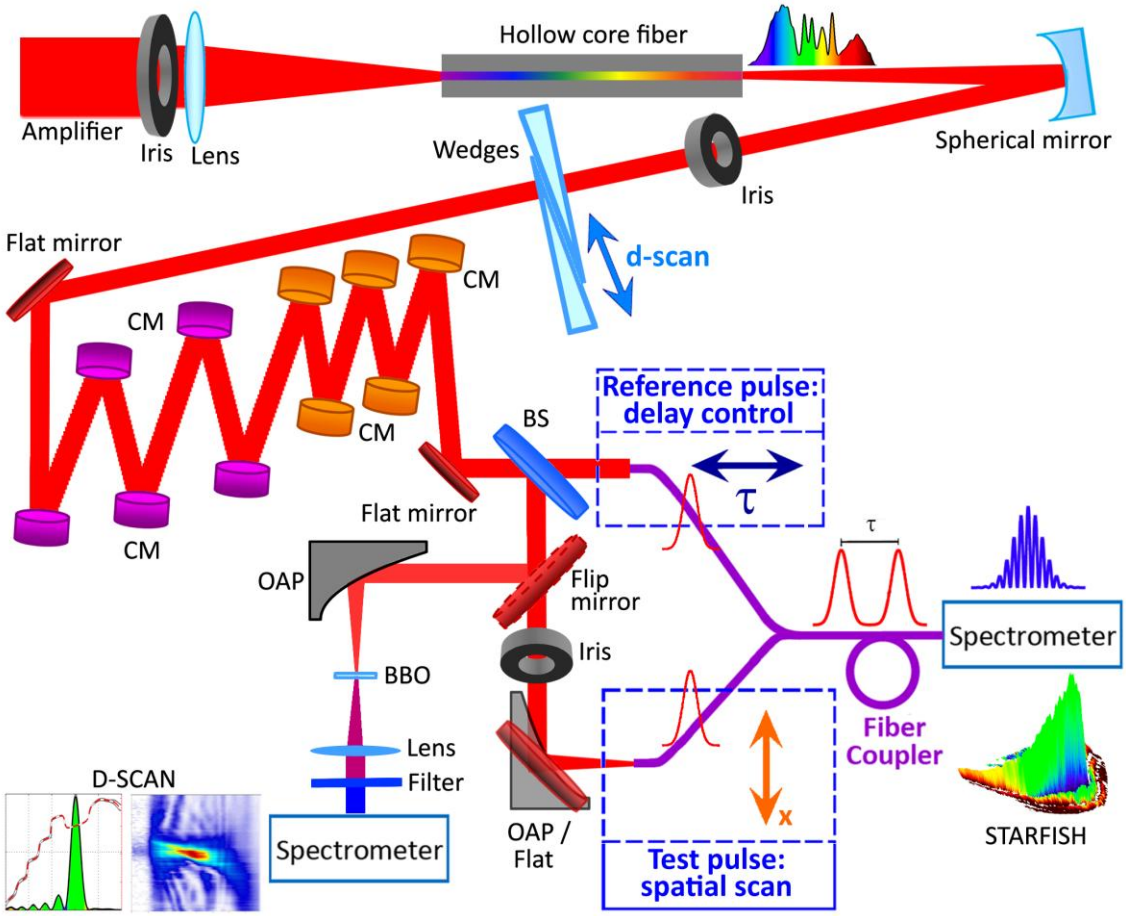


Fig. 10.1. Experimental setup for the generation and spatiotemporal characterization of post-compressed pulses. The amplified pulses are spectrally broadened in a hollow-fiber and the output mode is collimated with a spherical mirror. Then, the pulses are simultaneously compressed and characterized by a dispersion scan (d-scan) with a compressor made of a pair of wedges and 5 pairs of chirped mirrors (CM), while tracking the second-harmonic generation (SHG) in a nonlinear crystal (BBO). The pulses are divided by a beam splitter (BS) to perform the spectral interferometry of STARFISH. The test and reference pulses are combined in a fiber optic coupler and sent to the spectrometer. The position of the test fiber scans the spatial coordinate (x-axis). The output mode of the hollow-fiber (test pulse) is measured without focusing (flat mirror) and with focusing (off-axis parabola, OAP, 5-cm focal length).

The spatiotemporal STARFISH characterization of the few-cycle pulses was first performed directly after the CM setup, so a flat mirror was used to direct the pulses to the test fiber. This mirror was then replaced with a 5-cm focal length OAP to study the focusability of the pulses, and to characterize them around the focal region. The test pulse was spatially scanned over one axis (x-scan), assuming cylindrical symmetry.

Before the wedges and CM compressor, an iris of 10-mm diameter was used to select the spatial mode after collimation of the fiber output (see Fig. 10.2b). On account of the 10-mm iris before the wedges and the losses inside the compressor itself, the pulse energy decreased from $150\mu J$ to $90\mu J$ before the BS. The beam was not perfectly collimated after the spherical mirror, since it diverged more than would have been expected for a collimated beam with the same waist. In fact, the beam size of the pulses increased up to 13 mm just before the last mirror prior to the test fiber (the optical path in the CM setup was 169 cm). At this position, we selected the spatial mode with a

diaphragm to eliminate the residual (mostly conical) emission around the main portion of the beam.

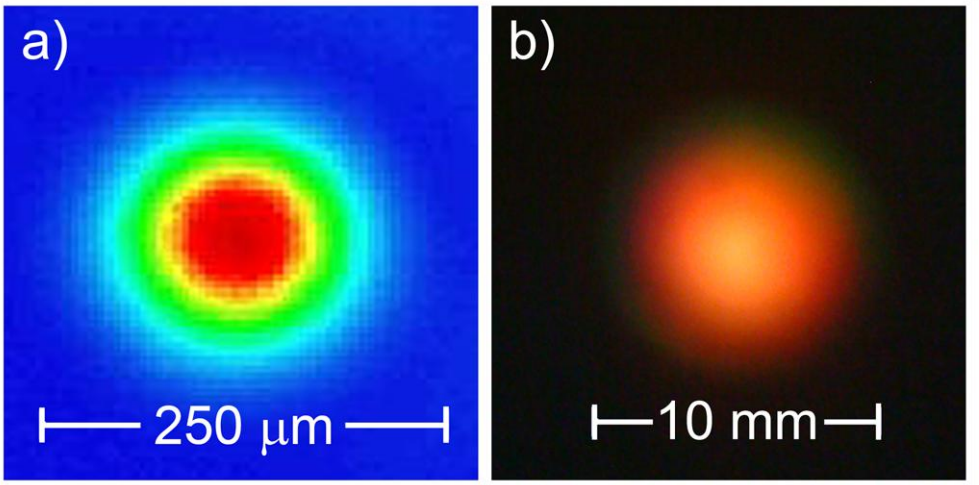


Fig. 10.2. (a) Input mode coupled at the entrance of the HCF with an inner diameter of $250\mu m$. (b) Spatial profile of the output mode of the HCF after collimation.

The spectral phase of the reference pulse was retrieved by the d-scan technique (Section 9.2) by optimizing the simulated SHG trace compared with the experimental trace using a numerical iterative algorithm [25]. The spatiotemporal amplitude and phase characterization was obtained by the STARFISH technique [27] (Chapter 4).

## 10.3. Spatiotemporal analysis of sub-5-fs pulses after hollow-fiber post-compression

### *10.3.1 Characterization of the reference pulse with the d-scan*

As said before, the spectrally broadened amplified pulses are compressed with five pairs of broadband chirped mirrors and a pair of BK7 glass wedges (angle 8º). This compressor is also a part of the d-scan technique setup for the characterization of the reference pulse, which is required for the SI. The d-scan trace was taken by measuring the SHG signal while varying the glass insertion. The total range of insertion (in the propagation direction) was $d = 4.34mm$ using a lateral insertion step of $0.215mm$, which corresponds to 146 sampling points. The resulting experimental d-scan trace is shown in Fig. 10.3a.

The d-scan algorithm was executed five times with different input conditions (five different starting guesses) in order to ensure the convergence of the retrieved phase. The retrieved trace is given in Fig. 10.3b, and is in very good agreement with the experimental trace. The experimental spectrum and the retrieved phase of the pulse for maximum compression are shown in Fig. 10.3c. The full width at $1/e^2$ of the maximum (in intensity) of the hollow-fiber spectrum is $402nm$. The standard deviation of the phase (gray curves) for the different runs of the algorithm provides the information of the precision error. The spectral phase retrieved is precise except for the shorter wavelengths owing to the experimental d-scan trace being cropped in the bluer part of the spectrum, as will be explained below. In Fig. 10.3d, the retrieved temporal intensity

and phase of the corresponding pulse are represented. The optimum spectral phase has a small contribution of negative third-order dispersion that produces the pre-pulses. The corresponding standard deviations (gray curves) are very small, which means that the spectral phase deviation for shorter wavelengths hardly affects the temporal retrieval. The duration of the pulse is $4.5 \pm 0.1 fs$ (intensity FWHM), close to its FTL of $4.1 fs$. The carrier wavelength calculated from the center of gravity of the spectral power density (in frequency) is $\lambda_g = 739nm$. The temporal intensity in Fig. 10.3d has been color-filled with the instantaneous wavelength of the pulse $\lambda_t$. From the tilt of the phase in the pre-pulses we see that they are slightly redder than the main pulse (centered at $\lambda_t = 739nm$), as illustrated by the color fill. The small deviation of the instantaneous wavelength from the carrier wavelength is an evidence of the good compression achieved. The main reason why the final pulse duration deviates from the FTL is the divergence in the spectral phase introduced by the broadband beamsplitter for wavelengths below 600 nm, since this element is designed to work above this wavelength.

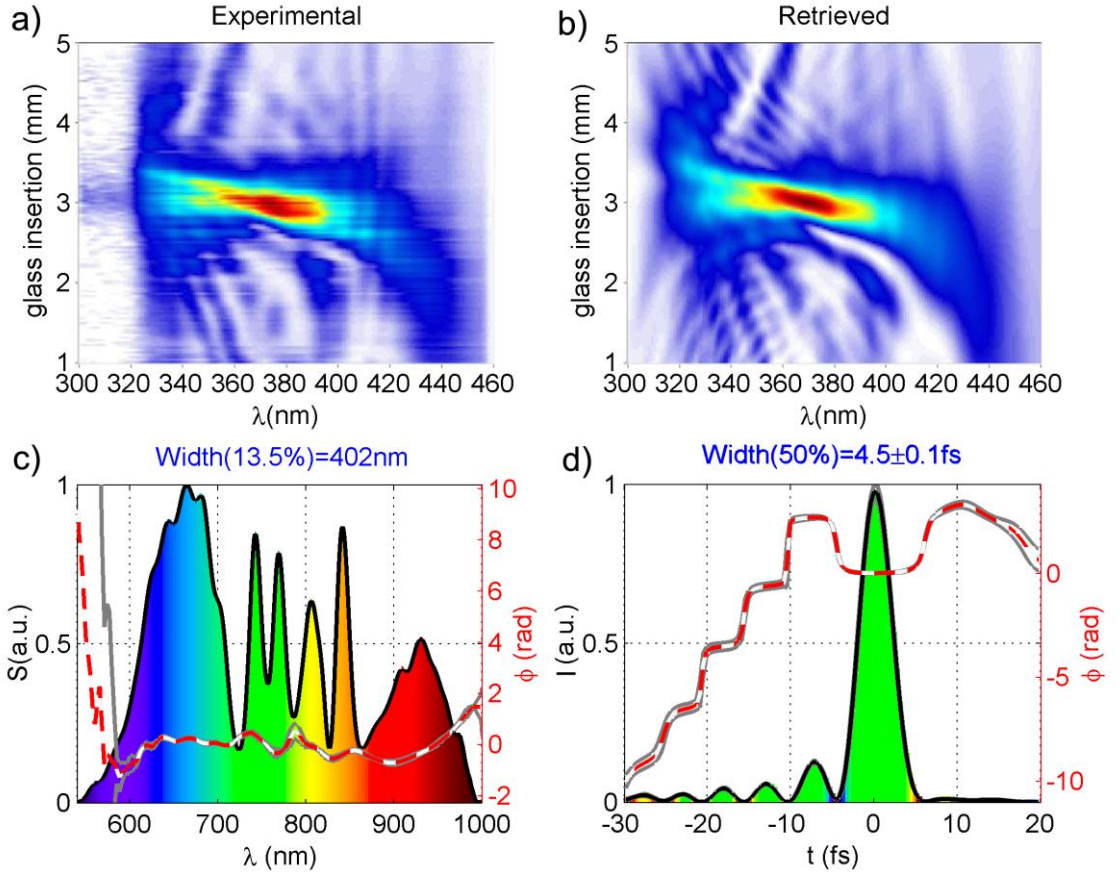


Fig. 10.3. (a) Experimental and (b) retrieved d-scan traces of the reference pulse. (c) Spectral intensity (black) and phase (dashed red) of the retrieved pulse. (d) Temporal intensity (black) and phase (dashed red) of the reference pulse. The gray curves in (c) and (d) represent the standard deviation of the spectral phase, and of the temporal intensity and phase, respectively. The intensity profile (d) is color-filled by the instantaneous wavelength following the same color scale than in (c).

The lack of signal below 320 nm in the experimental trace may be partly due to the cut-off of the blue filter and by UV absorption in the collimating lens. This justifies the

difference between measured and retrieved traces in that spectral region. To minimize this effect, a spatial mask can be used instead of the filter or lens, which spatially separates the fundamental and the SHG [26]. The phase distortion introduced by the beamsplitter for wavelengths below 600 nm may also contribute to the smaller SHG signal observed at shorter wavelengths. In spite of this, thanks to the trace redundancy in the d-scan technique (owing to the coupling between fundamental and up-converted wavelengths in the trace explained in Section 9.2), it is possible to recover phase information for regions where no SHG signal has been measured at all, as was shown in [25,26].

As mentioned above, the optimal pulse compression with this system is close to the FTL. To further analyze this compression, we calculated the chronocyclic or time-frequency Wigner distribution function [32,33] of the pulse and the FTL of the spectrum. In Section 4.2.5, we already used the spatial Wigner distribution function, Eq. (4.2), to gain further insight into the wave vector distribution within the spatial profile. Although in the chronocyclic Wigner distribution the time and frequency play a role in equal conditions, we will refer to it simply as the temporal Wigner distribution, in order to distinguish it from the spatial Wigner distribution [32]. Analogously, we will use here the equivalent for the temporal dependence. For a certain function defined in the time domain (in our case the electric field $E(t)$ of the pulses), the Wigner distribution can be interpreted as the probability (despite its taking positive and negative values) to find a certain wavelength (or frequency $\omega$) at a given time $t$, i.e., it gives us the spectral distribution within the pulse. The definition of the temporal Wigner distribution function $W_T$ is [32,33]

$$W_T(t,\omega) = \int_{-\infty}^{\infty} E(t+\frac{t'}{2})E^*(t-\frac{t'}{2})e^{-i\omega t'}dt'. \qquad (10.1)$$

The calculations for the pulse retrieved by the d-scan and for the FTL of the spectrum are shown in Fig. 10.4a and 10.4b, respectively. The information given by $W_T$ is related to the instantaneous frequency (see Fig. 10.3d), although $W_T$ provides the whole information of the temporal distribution of wavelengths, in contrast to the single value of the effective instantaneous wavelength. This gives further insight into the pulse structure and compression, and can give a visual and intuitive idea of how far we are from the FTL by comparing the Wigner distributions of the retrieved pulse and of its FTL (Figs. 10.4a and 10.4b). In our case, since most of the spectrum is contained in the main peak of the pulse (like in the FTL pulse, except for the tails of the spectrum), this means that almost the whole spectrum is well compressed (i.e., its spectral phase is well compensated for). Moreover, when comparing the scales of the plots, a small loss of signal occurs in the measured pulse with respect to its FTL. This is in agreement with the fact that the peak intensity of the pulse for the d-scan retrieval is 0.8 times the FTL peak intensity. The time and frequency marginals of $W_T$ are also given in the plots. The time and frequency marginals are the result of the integration of $W_T(t,\omega)$ over the frequency and time axes, respectively, which in this case provide the temporal intensity (left) and the power spectral density (bottom) of the pulse. As we said in Sections 1.3

and 9.2, the marginals of the 2D-traces are useful for cross-checking or calibrating the trace in the FROG and d-scan techniques, respectively.

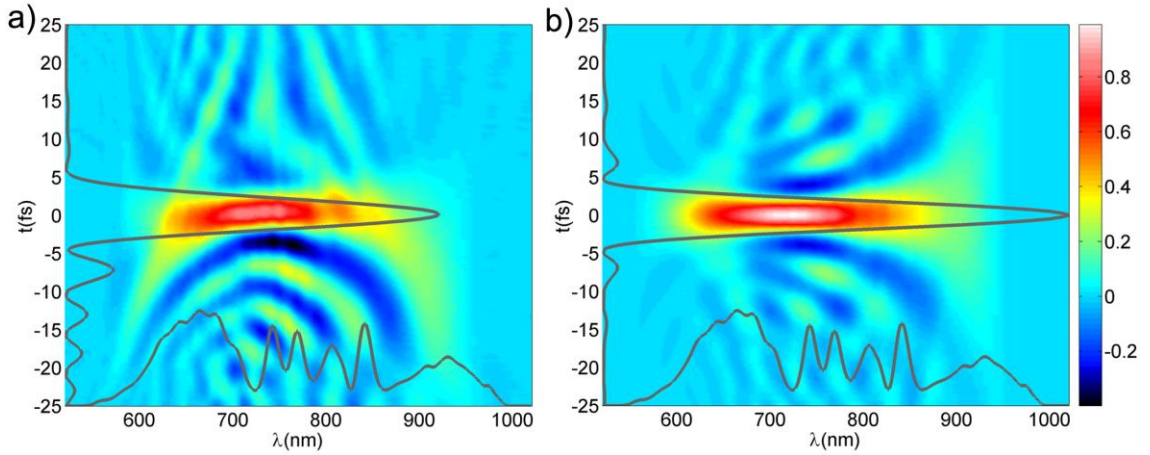


Fig. 10.4. Wigner distribution functions and corresponding marginals for the electric field of the (a) experimental pulse and (b) Fourier-transform limit of the spectrum. The two functions are represented in the same (arbitrary) units in order to compare the respective signal strength.

### *10.3.2 Spatiospectral and spatiotemporal characterization of the output mode*

The output mode of the post-compression of the intense pulses in the HCF was characterized in the spatiotemporal domain. The spatial profile was scanned with the fiber across the 13-mm diameter of the pulse with steps of $50\mu m$ (261 sampling points). The spatially-resolved spectrum (Fig. 10.5a) shows that the spectral distribution is fairly constant across the x-coordinate, only presenting less broadening in the bluer part of the spectrum for the outermost part of the spatial profile. The frequency-resolved wavefront (Fig. 10.5b) presents a curvature responsible for the beam divergence (already observed during beam propagation), which will be taken into account to simulate the focus of the pulse in Section 3.3.

The pulse-front curvature in the spatiotemporal intensity (Fig. 10.5d) corresponds to the expected curvature of a diverging beam. It exhibits a relatively small variation of $\approx 30\,fs$ from the center to the periphery of the beam ($\approx 13mm$ diameter), although it is large compared to the pulse duration. Nevertheless, we will see that the presence of wavefront and pulse-front curvature do not compromise the focusability of the beam and a tight focus is achieved. The spatiotemporal intensity is shown in Fig. 10.5e, color-filled with the instantaneous wavelength to better illustrate the spatial dependence of the temporal chirp. The main peak color shifts from bluer to redder values as we move away from the center of the pulse ($x = 0$), as expected from the spatially-resolved spectrum in Fig. 10.5a.

The pulse duration (intensity FWHM) as a function of $x$ is presented in Fig. 10.5c for the retrieved pulse and for the FTL of the spectrum. The pulse duration varies approximately from 4.5 fs on-axis to 5.0 fs in the wings, whereas the FTL varies from 4.0 fs to 4.5 fs.

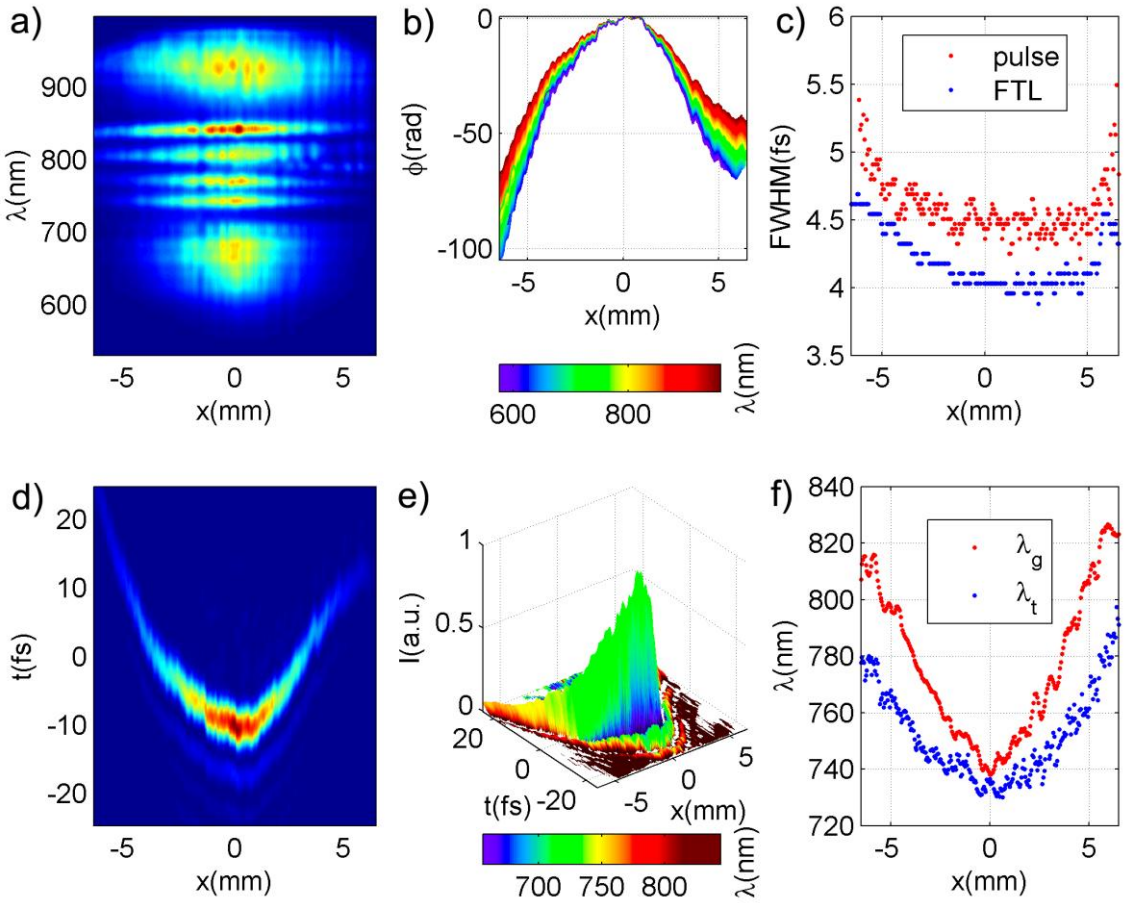


Fig. 10.5. Intense pulse post-compressed in an HCF; experiment: (a) Normalized spatiospectral intensity and (b) frequency-resolved wavefront, the latter represented in different colored lines for each wavelength (see the colorbar). (c) Fourier-limit (blue) and retrieved pulse duration (red). (d) Normalized spatiotemporal intensity and (e) same as (d), but color-filled with the instantaneous wavelength (see the colorbar). (f) Instantaneous wavelength at the pulse-front (blue) and center wavelength (red).

In Fig. 10.5f, we show the carrier wavelength dependence on $x$, both for the center of gravity of the spectrum ($\lambda_g$) and the instantaneous wavelength ($\lambda_t$) evaluated at the maximum of the pulse (i.e. at the pulse front). We see that $\lambda_g$ varies from 740 nm (on-axis) to 820 nm (wings), whereas $\lambda_t$ varies from 735 nm (on-axis) to 790 nm (wings). These results are in agreement with previous works where blue-shift and larger spectral broadening and pulse shortening were observed on-axis in comparison with the outer part of the spatial profile [19] (similar behavior was observed for the filamentation in Section 8.4). Redder pre-pulses with the same curvature than the main pulse (the pulse front) are observed, similarly to the reference pulse. There is almost no chromatic aberration in the wavefront (Fig. 10.5b) since all wavelengths have practically the same curvature, except for the intrinsic wave number dependence $\phi(x_0,\lambda) \propto k \propto \lambda^{-1}$ (similar to the results given for a focusing refractive lens in Section 4.4.2 [34]), as we will calculate in the next section.

### *10.3.3 Spatiospectral and spatiotemporal characterization of the focus*

The pulses were focused with an OAP (f = 5 cm). The focus was spatially resolved with the test fiber, which scanned the transverse profile across $30\mu m$ in steps of $1\mu m$

($x$-axis). Despite the $4\mu m$ fiber core diameter, we have demonstrated in Section 4.2.3 and in the measurements of Chapter 6 (focus of the kinoform diffractive lens) that using a smaller step allows us to recover the structure and size of focused pulses [34]. In this experiment, a neutral-density filter was placed before the BS (note that the dispersion before the interferometer is compensated in the SI) to avoid damage or nonlinear effects in the collecting fiber, so the linear focus was characterized. The spectrum as a function of the x-coordinate (Fig. 10.6a) presents a spatial chirp, with increasing red-shift for increasing values of $x$. The spatiotemporal distribution corresponds to a well-defined focus in space and time (Fig. 10.6d), with a spatial width of $10\mu m$ (FWHM) and a temporal duration on-axis of $4.5\ fs$ (FWHM). The instantaneous wavelength combined with the intensity (Fig. 10.6e) inherits the spatial chirp from the frequency domain (shown in Fig. 10.6a). Since the input pulse is symmetric in $x$ (Fig. 10.5), the spatial chirp may be originated by a slight misalignment in the OAP. The frequency-resolved wavefronts (Fig. 10.6b) show a slight divergence, meaning that the measurement was not taken exactly at the focus, but just before it. Also, the wavefronts for the different wavelengths have a gradual relative tilt, which is an evidence of the spatial chirp originated by the asymmetric focusing phase introduced by the misalignment.

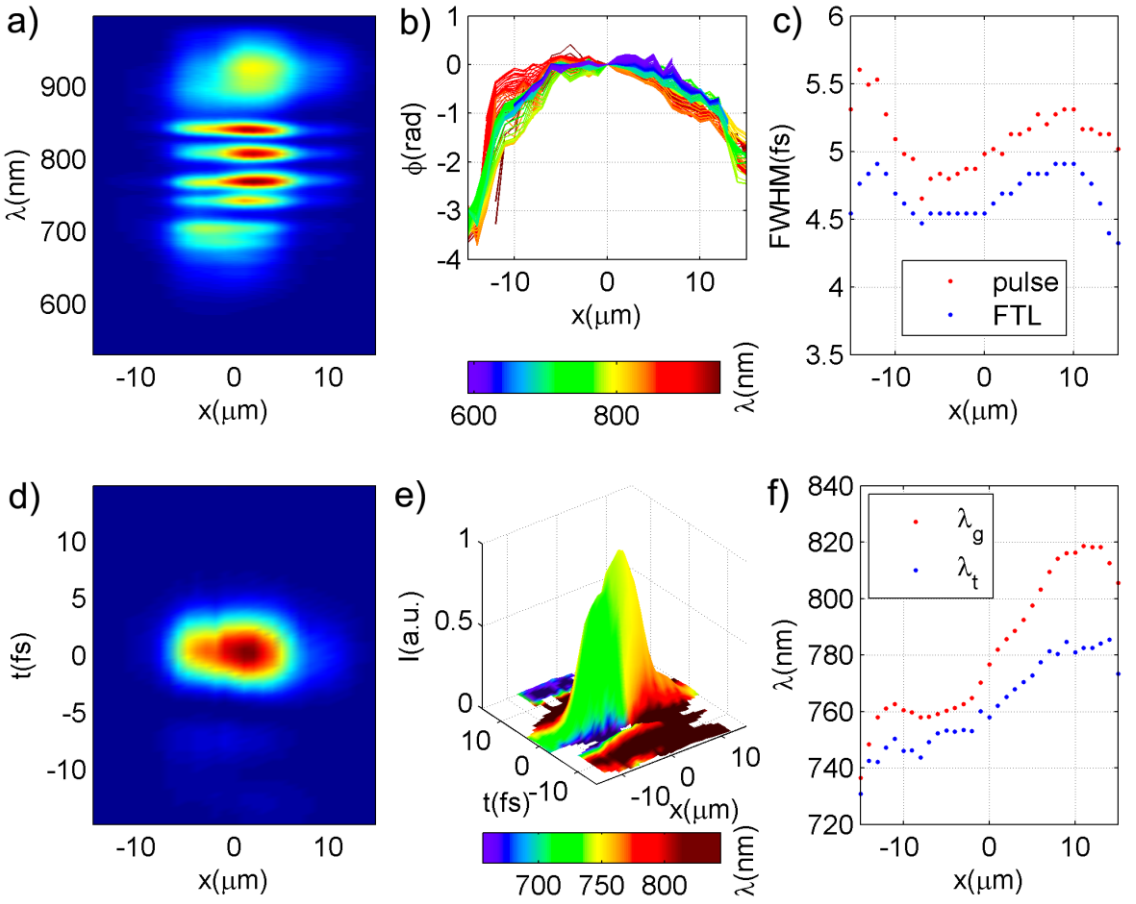


Fig. 10.6. Post-compressed pulses focused with an OAP; experiment: (a) Normalized spatiospectral intensity and (b) frequency-resolved wavefront, the latter represented in different colored lines for each wavelength (see the color-bar). (c) Fourier-limit (blue) and pulse duration (red). (d) Normalized spatiotemporal intensity and (e) same as (d), color-filled by the instantaneous wavelength (see the color-bar). (f) Instantaneous wavelength at the pulse-front (blue) and center wavelength (red).

An estimation of the peak irradiance of the pulses focused with the OAP can be obtained in terms of pulse duration and spot size, assuming Gaussian beams and pulse shapes with widths given by the experimental spatial and temporal FWHM, respectively. The expression for the peak irradiance is $I_{\max} = 0.651 \cdot E/(\Delta t \cdot S)$ [28] (see Section 9.4.3), where $E = 45\mu J$ is the pulse energy after the beam splitter, $\Delta t = 4.5\,fs$ is the temporal FWHM, $S = \pi(\Delta x/2)^2$ is the spot section (since $\Delta x = 10\mu m$ is the spatial FWHM) and 0.651 is the factor coming from the assumption of Gaussian shapes. In our case, we estimate a peak irradiance of $I_{\max} = 8.3\times10^{15}\,W/cm^2$.

The FWHM intensity of the Fourier-transform limited (FTL) pulse increases along the $x$-axis from 4.5 to 4.9 fs and the retrieved pulse duration from 4.8 to 5.3 fs (Fig. 10.6c). Similar behavior is observed for the carrier (central) wavelength $\lambda_g$ that varies from 760 nm to 810 nm (Fig. 10.6f). Again, the instantaneous wavelength at the pulse-front, $\lambda_t$, is blue-shifted with respect to $\lambda_g$.

We studied the effect of the spatiospectral phase (or wavefront) of the mode before focusing (Fig. 10.5b). This phase is mainly quadratic and can be written as $\phi(x;\lambda) = (\pi/\lambda)(x^2/f_{in})$, corresponding to a diverging beam with a focal length $f_{in}$. From the fit to the phase $\phi(x;\lambda)$ for each wavelength, we extracted the focal length $f_{in} = -4724 \pm 26mm$ (regression coefficient $R = 0.9989$). When combined with the focal length of the OAP, $f_{OAP} = 50mm$, we obtained the effective focal length $f_{eff} = 50.53\,mm$. Assuming that only this quadratic phase is present, this will simply cause a shift in the focal position along the propagation axis, but higher order curvature terms in the wavefront may distort the focal spot.

Finally, we analyzed the effect of the numerical aperture ($NA$) of the fiber coupler (the test pulse fiber arm). In Section 4.2.5, we measured a coupling efficiency of 50% at an angle of incidence of $\theta = 5^o$ [28]. Here, we used the experimental dependence of the coupling efficiency on the angle $\theta$, denoted by $T(\theta) \equiv \xi_m(\theta)$, to study its effect in the measurement of the focus of the OAP. In the ray-tracing approximation, the angle $\theta$ is translated to the input spatial plane as $\tan\theta \approx r/z$, where $z = f$ for observation at the focus (this gives the function $T(r)$ plotted in Fig. 10.7a). In the present case, the spatial intensity profile of the beam has a Gaussian-like shape, so the less efficiently coupled part of the profile, the periphery, is the part with the least contribution. Figure 10.7a shows the spatial intensity profile $I(r)$ for the almost collimated beam, the fiber transmission $T(r)$, and the modified spatial profile $I(r)\cdot T(r)$ considering ray tracing. The experimental spatially-resolved spectrum before the OAP (collimated beam) is shown in Fig. 10.7b (extracted from Fig. 10.5a), which can be compared with the same magnitude modified by $T(r)$ in Fig. 10.7c (this plot illustrates the spectrum of the focused pulse that would be collected due to the numerical aperture of the fiber). From Fig. 10.7, it can be seen that the most affected part is the periphery of the spatial profile.

The distribution of the orientation of the wave vectors inside a monochromatic Gaussian beam was discussed in depth in Section 4.2.5, using the spatial Wigner distribution function [32]. Far from the Rayleigh zone, it corresponds to a well defined angle (see Fig. 4.10), which can be simply calculated by ray tracing, as a function of the transverse spatial coordinate [35]. Since larger angles occur in the periphery of the

beam, outside the focal region, the angular filtering of the *NA* of the fiber results in a reduction of the spatial width, which can be estimated by the correction explained in the previous paragraph (see Fig. 10.7). Conversely, at the focus position all the wave vectors (from the ray tracing) overlap and the wave vector spreading is independent from the spatial coordinate (see Fig. 4.10), so the ray tracing approximation is obviously unacceptable there [35]. For this reason, in the focus (where we measured the pulse), the effect of the *NA* coupling will be ideally a reduction in the collected signal without spatial distortion, as discussed in Section 4.2.5. In our case, the *NA* of the pulse is slightly lower than the *NA* of the detection fiber (see the curves $I(r)$ and $T(r)$ in Fig. 10.7a, respectively), so the effect of the *NA* of the fiber on the spatiotemporal measurements will be small (Fig. 10.7). The modification (decrease in spatial width) in the spatiospectral domain is illustrated by comparing Fig. 10.7b (actual) and Fig. 10.7c (modified), which corresponds in the spatial domain (after wavelength integration) to the comparison between the curves $I(r)$ and $I(r)\cdot T(r)$, respectively. Note that this estimation of the profile modification corresponds to the worst case scenario, in which ray-tracing can be applied (out of the Rayleigh zone), so the experimental measurement of the focus (Fig. 10.6) is very close to reality.

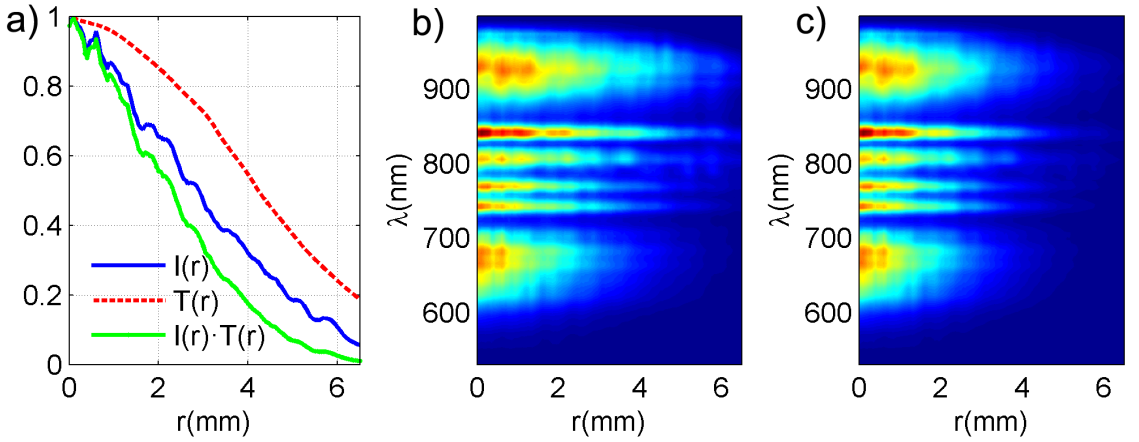


Fig. 10.7. (a) Spatial profile of the collimated pulse (blue), transmission of the fiber due to the numerical aperture (red) and corrected spatial distribution (green). (b) Actual experimental spatially-resolved spectrum of the collimated pulse. (c) Calculated spatially-resolved spectrum [(b) modified by T(r)], corresponding to the spectrum of the focused pulse that would collect the fiber owing to the numerical aperture.

## 10.4. Conclusions

We have generated sub-two-cycle pulses by post-compression in an argon-filled hollow-core-fiber of 25-fs (Fourier-transform limited) amplified pulses from a 1 kHz Ti:sapphire laser. The post-compression was optimized to have a broadband spectrum corresponding to few-cycle pulses (4.5 fs FWHM, 4.1 fs FTL) and a homogeneous (near-Gaussian) spatial profile with a significantly stable mode. Optimum compression was achieved by compensating the spectral phase with a pair of wedges and ultra-broadband chirped mirrors. The post-compressed pulses were characterized in the spatiotemporal domain using the STARFISH technique and the reference pulse was measured with the d-scan technique. We first studied the output mode of the hollow-

fiber and found that the spectral broadening and the blue-shift are significantly larger at the center (x=0) of the pulse than in the periphery. This resulted in an increase in pulse duration from 4.5 fs at the beam center up to 5 fs at the periphery. A symmetric spatial chirp (relative to x=0) was consequently observed in the spatiotemporal reconstruction. Also, the measured wavefront corroborated the divergence predicted from the observation of the spatial size growth during the propagation.

The pulse was also focused with an off-axis parabolic mirror (f = 5 cm) producing a measured focal spot size of $10\mu m$ (FWHM). In this case, an asymmetric spatial chirp was observed, which was attributed to a slight misalignment of the mirror. The experimental spectrum, wavefront, intensity and temporal chirp are consistent with this statement. The effect of the numerical aperture of the collection fiber on the focused pulse measurement was also studied. Although not negligible, it did not prevent us from obtaining detailed information on the structure of the focused pulse.

The broadband, intense 4.5 fs pulses (4.1 fs Fourier-limited) that were characterized in the spatiotemporal domain using STARFISH in conjunction with d-scan are in the range of the lower pulse duration measurable by state-of-the-art temporal characterization techniques in the near-infrared. The possibility of measuring high-energy, low repetition rate pulses in this range shows promise for future applications to the further study and optimization of filament and hollow-fiber compressed pulses. In the future, it would be worth carrying out further work towards the generation and characterization of even shorter pulses (near single-cycle).

## References


[1] A. Baltuška, Th. Udem, M. Uiberacker, M. Hentschel, E. Goulielmakis, Ch. Gohle, R. Holzwarth, V. S. Yakovlev, A. Scrinzi, T. W. Hänsch, F. Krausz, "Attosecond control of electronic processes by intense light fields," Nature 421, 611-615 (2003).

[2] S. Baker, J. S. Robinson, C. A. Haworth, H. Teng, R. A. Smith, C. C. Chirilã, M. Lein, J. W. Tisch, and J. P. Marangos, "Probing proton dynamics in molecules on an attosecond time scale," Science 312, 424-427 (2006).

[3] K.W.D. Ledingham, P. McKenna, R.P. Singhal, "Applications for nuclear phenomena generated by ultra-intense lasers," Science 300, 1107-1111 (2003).

[4] T. Brabec and F. Krausz, "Intense few-cycle laser fields: Frontiers of nonlinear optics," Rev. Mod. Phys. 72, 545-591 (2000).

[5] M. Hentschel, R. Kienberger, Ch. Spielmann, G.A. Reider, N. Milosevic, T. Brabec, P. Corkum, U. Heinzmann, M. Drescher, F. Krausz, "Attosecond metrology," Nature 414, 509-513 (2001).

[6] Y. Mairesse, A. de Bohan, L. J. Frasinski, H. Merdji, L. C. Dinu, P. Monchicourt, P. Breger, M. Kovačev, R. Taïeb, B. Carré, H. G. Muller,P. Agostini, and P. Salières, "Attosecond Synchronization of High-Harmonic Soft X-rays," Science 302, 1540-1543 (2003).

[7] G. Sansone, E. Benedetti, F. Calegari, C. Vozzi, L. Avaldi, R. Flammini, L. Poletto, P. Villoresi, C. Altucci, R. Velotta, S. Stagira, S. D. Silvestri, and M. Nisoli, "Isolated single-cycle attosecond pulses," Science 314, 443–446 (2006).

[8] I. J. Sola, E. Mevel, L. Elouga, E. Constant, V. Strelkov, L. Poletto, P. Villoresi, E. Benedetti, J. P. Caumes, S. Stagira, C. Vozzi, G. Sansone, and M. Nisoli, "Controlling attosecond electron dynamics by phase-stabilized polarization gating," Nature Phys. 2, 319–322 (2006).

[9] A. A. Eilanlou, Y. Nabekawa, K. L. Ishikawa, H. Takahashi, and K. Midorikawa, "Direct amplification of terawatt sub-10-fs pulses in a CPA system of Ti:sapphire laser," Opt. Express 16, 13431-13438 (2008).

[10] S. Witte, R. Zinkstok, W. Hogervorst, and K. Eikema, "Generation of few-cycle terawatt light pulses using optical parametric chirped pulse amplification," Opt. Express 13, 4903-4908 (2005).

[11] M. Nisoli, S. De Silvestri, O. Svelto, R. Szipöcs, K. Ferencz, Ch. Spielmann, S. Sartania, and F. Krausz, "Compression of high-energy laser pulses below 5 fs," Opt. Lett. 22, 522-524 (1997).

[12] B. Schenkel, J. Biegert, U. Keller, C. Vozzi, M. Nisoli, G. Sansone, S. Stagira, S. De Silvestri, and O. Svelto, "Generation of 3.8-fs pulses from adaptive compression of a cascaded hollow fiber supercontinuum," Opt. Lett. 28, 1987-1989 (2003).

[13] C. P. Hauri, W. Kornelis, F.W. Helbing, A. Heinrich, A. Mysyrowicz, J. Biegert, and U. Keller, "Generation of intense, carrier-envelope phase-locked few-cycle laser pulses through filamentation," Appl. Phys. B 79, 673-677 (2004).

[14] A. Zaïr, A. Guandalini, F. Schapper, M. Holler, J. Biegert, L. Gallmann, A. Couairon, M. Franco, A. Mysyrowicz, and U. Keller, "Spatio-temporal characterization of few-cycle pulses obtained by filamentation," Opt. Express 15, 5394-5404 (2007).

[15] D. Faccio, A. Lotti, A. Matijosius, F. Bragheri, V. Degiorgio, A. Couairon, and P. Di Trapani, "Experimental energy-density flux characterization of ultrashort laser pulse filaments," Opt. Express 17, 8193-8200 (2009).

[16] J. Odhner and R. J. Levis, "Direct phase and amplitude characterization of femtosecond laser pulses undergoing filamentation in air," Opt. Lett. 37, 1775-1777 (2012).

[17] B. Alonso, I. J. Sola, J. San Román, O. Varela, and L. Roso, "Spatiotemporal evolution of light during propagation in filamentation regime," J. Opt. Soc. Am. B 28, 1807-1816 (2011).

[18] X. Sun, S. Xu, J. Zhao, W. Liu, Y. Cheng, Z. Xu, S. L. Chin, and G. Mu, "Impressive laser intensity increase at the trailing stage of femtosecond laser filamentation in air," Opt. Express 20, 4790-4795 (2012).

[19] L. Gallmann, T. Pfeifer, P. M. Nagel, M. J. Abel, D. M. Neumark and S.R. Leone, "Comparison of the filamentation and the hollow-core fiber characteristics for pulse compression into the few-cycle regime," Appl. Phys. B. 86, 561-566 (2007).

[20] T. Witting, F. Frank, C. A. Arrell, W. A. Okell, J. P. Marangos, and J. W. G. Tisch, "Characterization of high-intensity sub-4-fs laser pulses using spatially encoded spectral shearing interferometry," Opt. Lett. 36, 1680-1682 (2011).

[21] I. A. Walmsley and C. Dorrer, "Characterization of ultrashort electromagnetic pulses," Adv. Opt. Photon. 1, 308-437 (2009).

[22] A. Baltuška, M. S. Pshenichnikov, and D. A. Wiersma, "Amplitude and phase characterization of 4.5-fs pulses by frequency-resolved optical gating," Opt. Lett. 23, 1474–1476 (1998).

[23] A. S. Wyatt, I. A. Walmsley, G. Stibenz, and G. Steinmeyer, "Sub-10 fs pulse characterization using spatially encoded arrangement for spectral phase interferometry for direct electric field reconstruction," Opt. Lett. 31, 1914–1916 (2006).

[24] J. R. Birge, H. M. Crespo, and F. X. Kärtner, "Theory and design of two-dimensional spectral shearing interferometry for few-cycle pulse measurement," J. Opt. Soc. Am. B 27, 1165–1173 (2010).

[25] M. Miranda, T. Fordell, C. Arnold, A. L'Huillier, and H. Crespo, "Simultaneous compression and characterization of ultrashort laser pulses using chirped mirrors and glass wedges," Opt. Express 20, 688-697 (2012).

[26] M. Miranda, T. Fordell, C. Arnold, F. Silva, B. Alonso, R. Weigand, A. L'Huillier, and H. Crespo, "Characterization of broadband few-cycle laser pulses with the d-scan technique," Opt. Express 20, 18732- 18743 (2012).

[27] B. Alonso, I. J. Sola, O. Varela, J. Hernández-Toro, C. Méndez, J. San Román, A. Zaïr, and L. Roso, "Spatiotemporal amplitude-and-phase reconstruction by Fourier-transform of interference spectra of high-complex-beams," J. Opt. Soc. Am. B. 27, 933-940 (2010).

[28] B. Alonso, M. Miranda, I. J. Sola, and H. Crespo, "Spatiotemporal characterization of few-cycle laser pulses," Opt. Express 20, 17880-17893 (2012).

[29] B. Alonso, M. Miranda, F. Silva, V. Pervak, J. Rauschenberger, J. San Román, I. J. Sola, and H. Crespo, "Generation and spatiotemporal characterization of 4.5-fs pulses from a hollow-core fiber compressor," submitted (2012).

[30] B. Alonso, R. Borrego-Varillas, I. J. Sola, O. Varela, A. Villamarín, M. V. Collados, J. San Román, J. M. Bueno, and L. Roso, "Enhancement of filamentation postcompression by astigmatic focusing," Opt. Lett. 36, 3867-3869 (2011)

[31] V. Pervak, I. Ahmad, M. K. Trubetskov, A. V. Tikhonravov, and F. Krausz, "Double-angle multilayer mirrors with smooth dispersion characteristics," Opt. Express 17, 7943-7951 (2009).

[32] J. Paye, "The chronocyclic representation of ultrashort light pulses," IEEE J. Quantum Electron. 28, 2262-2273 (1992).

[33] J. Paye and A. Migus, "Space-time Wigner functions and their application to the analysis of a pulse shaper," J. Opt. Soc. Am. B 12, 1480-1490 (1995).

[34] B. Alonso, R. Borrego-Varillas, O. Mendoza-Yero, I. J. Sola, J. San Román, G. Mínguez-Vega, and L. Roso, "Frequency resolved wavefront retrieval and dynamics of diffractive focused ultrashort pulses," J. Opt. Soc. Am. B 29, 1993-2000 (2012).

[35] E. Kim, H. Kim and J. Noh, "Measurement of the Spatial Wigner Distribution Function of Laser Light by Using a Sagnac Interferometer," J. Korean Phys. Soc. 46, 1342-1346 (2005).

# CONCLUSIONS

We have developed a technique for the spatiotemporal (and spatiospectral) measurement of the amplitude and phase of ultrashort laser pulses based on spatially-resolved spectral interferometry, which we refer to as STARFISH. The key point is the use of a single-mode fiber optic coupler and a commercial spectrometer for the implementation of the spectral interferometry, which are used in a plug-and-play basis. STARFISH is a referenced technique, in the sense that a reference (known) pulse is used to characterize a test (unknown) pulse. The spatial profile of the test pulse is scanned by the corresponding fiber input, in order to retrieve the spatiotemporal distribution of the pulse. The propagation of the pulse is studied by measuring the pulse at different propagation planes, which was simply done by translating the fiber input or by translating the "experiment" (e.g. focusing lens).

The technique is very simple, robust and versatile, as shown with the measurement of a wide variety of pulses with strong spatiotemporal coupling. The interferometer assisted by the fiber coupler is alignment friendly. Moreover, the fact that the reference pulse is not spatially scanned provides stability, noise reduction and eliminates the requirement of homogeneous reference pulse. Thanks to the linearity of the detection ─except for the characterization of the reference─, the technique is suitable both for low and high intensity pulses. In fact, most of the experiments have been conducted with intense amplified pulses. In addition, it can be applied both for collimated and focused pulses, thanks to the spatial resolution of the fiber core $\sim 4\,\mu m$. In this respect, the numerical aperture of the measurable pulses is limited by the collecting fiber, which has a full width cone aperture of ~10º for a 50% in transmission.

The full characterization of the phase in the spatiospectral domain provides the information of the frequency-resolved wavefront of the pulses even in the case of focused pulses. This wavefront sensing, in terms of frequency-resolution and spatial resolution, is difficult to achieve, or cannot be achieved, with conventional sensors. The drawback is the multi-shot nature of the technique that may introduce noise in the retrieval because of interferometric instabilities. We have worked on this and have found that highly reduced noise can be achieved by isolating the setup (covering from the air flows) and using appropriate acquisition times.

We have also applied the technique to the measurement of nonlinear processes in which the test pulse experiences spectral broadening and the intensities are very high.

For this purpose, we have implemented two different ways, regarding the requirement of a reference pulse with greater or equal spectral content than the test pulse. In a first experiment, we conducted nonlinear propagation in parallel to broaden the spectrum of the reference, whereas in a second experiment we sampled the spectrally broadened test pulse to take a reference.

Regarding the temporal and spectral ranges, the technique is also very versatile. The ranges are given by the fiber optic coupler response and the spectrometer resolution and free spectral range. Concerning the spectrometer, we have used three different commercial devices. The first of them, with 0.1 nm of resolution in the interval 700-900 nm, was compatible with the measurement of pulses with spectrum contained in that interval, and temporal durations from around 20 fs to few picoseconds. The other two spectrometers had a larger spectral range and lower resolution, so they were suitable for the measurement of spectra compatible with few-cycle pulses and durations of several hundreds of femtoseconds. The lower pulse duration in this case is limited by the fiber coupler, which operates from around 550 nm to 1000 nm, which means that pulses of ~4 fs can be measured.

STARFISH has succeeded in a wide range of experiments and applications. In the field of diffractive optics, it has played the roles to predict and corroborate the spatiotemporal dynamics of diffracted pulses. By means of comparison between the experimental results and the theoretical simulations, the good agreement found between them has served to validate both the theoretical models and the experimental measurements. Multiple applications have been carried out from the study of the general behavior of a focusing zone plate along different propagation regions, to the characterization of diffractive pulse shapers and a dispersion compensation module, going through the rich dynamics of a focusing kinoform diffractive lens.

Very enlightening results in the study of the nonlinear dynamics of light during propagation under filamentation regime have been obtained. The characterization of this process is still very difficult to address from the experimental point of view, and therefore the results obtained are very valuable in order to interpret the pulse-splitting, self-compression, energy-density flux and the rich dynamics present during this process. This information is very promising to help in the control and the optimization of the filamentation process and their applications, such as pulse post-compression and subsequent generation of high-order harmonics.

In the same way, its application to few-cycle pulses shows a high potential for further studies towards the generation of intense few- and single-cycle pulses. Firstly, the study of the focusing dynamics of low-intensity and ultra-broadband pulses of an oscillator confirmed its applicability for subsequent experiments. Secondly, intense sub-two-cycle pulses were generated in a hollow-core fiber. The characterization of their spatiospectral and spatiotemporal structure proved a broadening and compression that are dependent on the radial coordinate owing to the nonlinear nature of the process.

All together, make STARFISH a consolidated and very powerful diagnostic tool, which can be applied in very different scenarios in a versatile way. In the future, we expect that the capabilities of STARFISH will continue to grow and that other fields of application will be opened.

# APPENDIX A

## LASER SYSTEMS

In the experiments presented in this thesis, we have used different laser systems property of the Universidad de Salamanca (USAL), Universitat Jaume I (UJI) in Castellón and Universidade do Porto (UP) in Portugal.

The laboratory of ultrafast and ultra-intense lasers of the University of Salamanca was equipped in 2003 with a commercial chirped pulse amplification (CPA) Ti:sapphire laser system manufactured by Spectra Physics. We wish to recall at this point that in CPA the pulse is stretched in time, amplified and then compressed, in order to avoid intensity damage in the amplification.

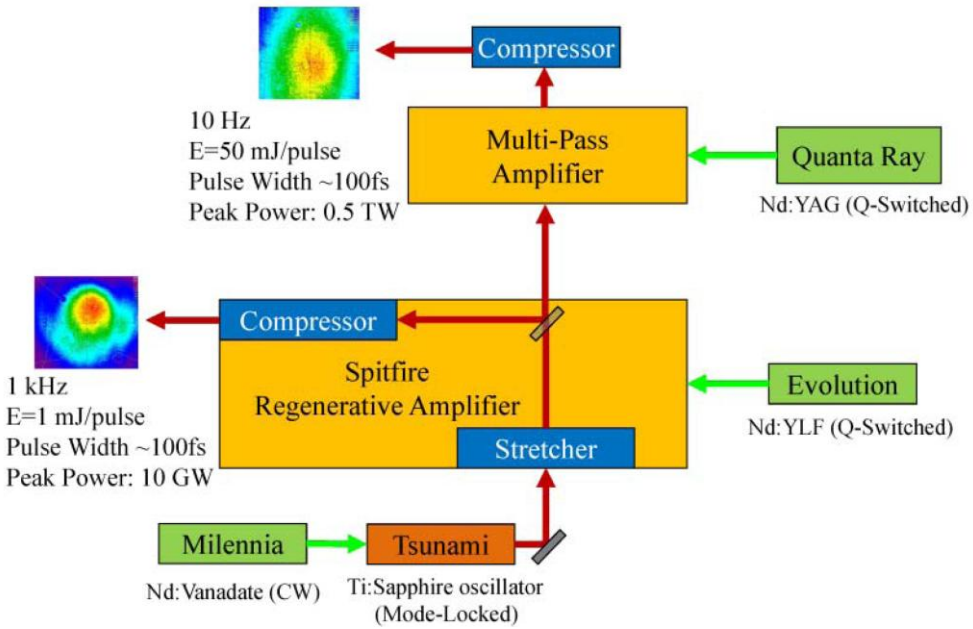


Fig. A.1. Layout of the laser system of Spectra Physics. The pulses delivered by a Ti:sapphire oscillator are amplified in a chirped pulse amplification (CPA) scheme. There are two amplified outputs, with single and double amplification stages, respectively.

The layout of the Spectra Physics laser system is depicted in Fig. A.1. The first amplification of the pulses delivered by an ultrafast mode-locking oscillator is done in a regenerative amplifier, which provides a relatively high-repetition rate (1 kHz) output of ~120-fs pulses with central wavelength of 795 nm, with moderate energy (~1 mJ) and peak power (<10 GW). Before compression, the pulses are sampled at a repetition rate of 10 Hz and directed to a second amplification stage (multi-pass) that also provides ~120-fs pulses with central wavelength 795 nm. The maximum energy per pulse is 50 mJ, which corresponds to almost 0.5 TW of peak power, although we have not used pulses with so high an energy. The 10 Hz output has been used in the measurements presented in Chapters 2, 3, 4 and 8, whereas the 1 kHz output was used in Chapter 6.

The USAL laboratory was equipped with a new laser system manufactured by Amplitude Technologies in 2007. This system was also based on CPA Ti:sapphire technology. In this case, the pulse duration was ~30 fs and the maximum energy per pulse 500 mJ, so it could reach a peak power of around 20 TW. This laser was used with low energy per pulse (in linear regime) in Chapters 4 and 5. Currently, this laser has been transferred to the Centro de Láseres Pulsados (CLPU), where it has been integrated in the chain of the future petawatt laser in Salamanca. In Fig. A.2 we show a picture of the laser systems room at the basement of the Physics building of the USAL.

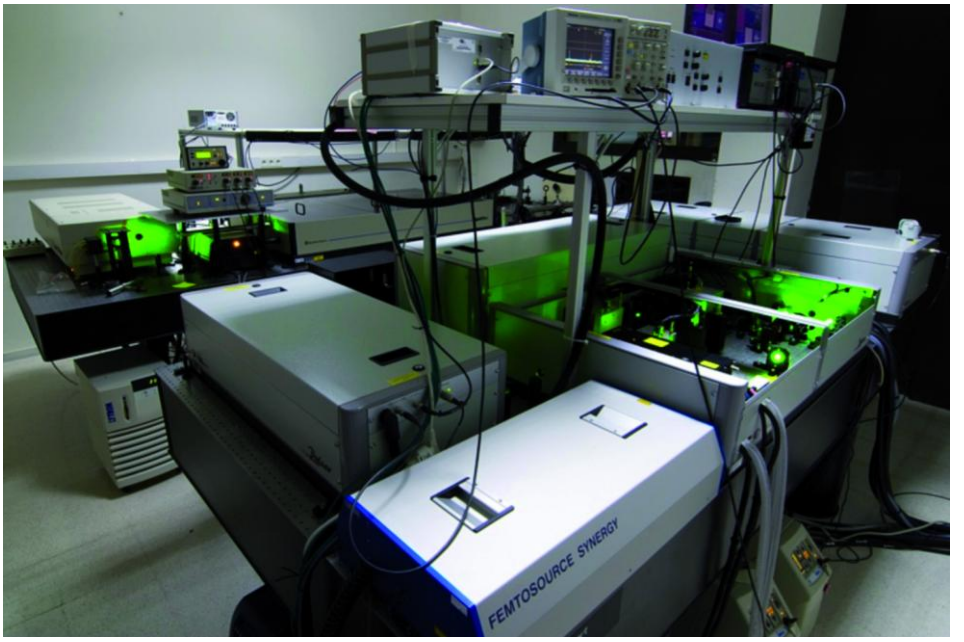


Fig. A.2. Picture of the two laser systems used in the laboratory of ultrafast and ultra-intense lasers of the Universidad de Salamanca. In the front of the photo is the system of Amplitude (~30 fs), whereas in the rear is the Spectra Physics system (~120 fs).

The laboratory of the group of diffractive optics of the Universitat Jaume I (Castellón) is equipped with a commercial laser system manufactured by Femtolasers. The Ti:sapphire oscillator (Femtosource) delivers 12-fs pulses (Fourier-limit) at a repetition rate of 75 MHz and with a maximum pulse energy of 4 nJ. The pulses are amplified in a CPA configuration (Femtopower Compact PRO), reaching a pulse energy of 0.8 mJ with a 30-fs pulse duration and a repetition rate of 1 kHz. In Fig. A.3, a picture of the amplifier is shown. We used the amplified pulses source in Chapter 7.

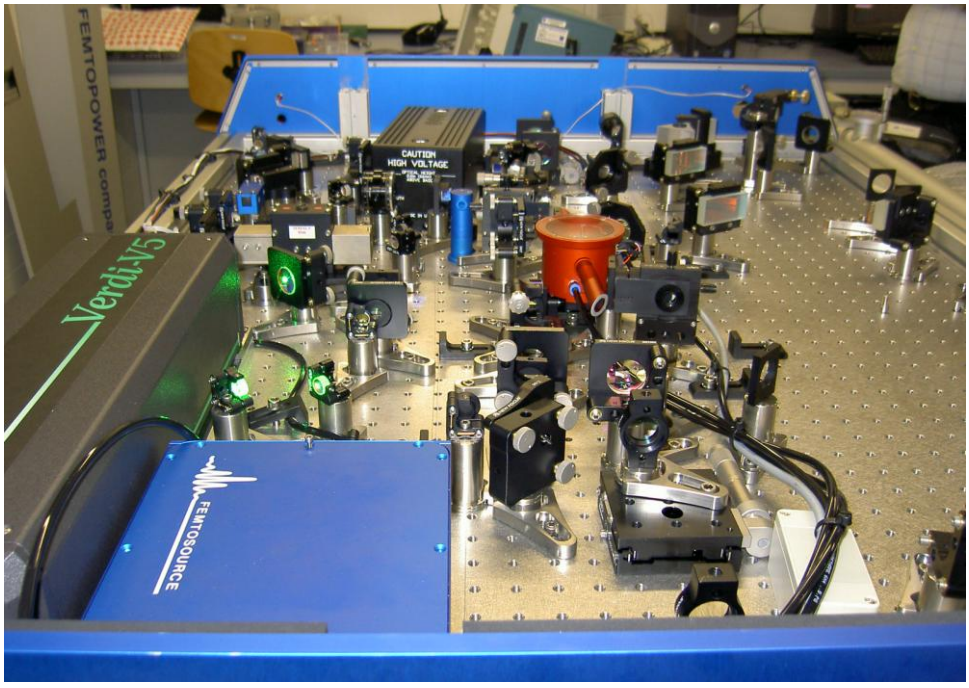


Fig. A.3. Inside view of the amplifier of the laser system (Femtolasers) of the Universitat Jaume I (Castellón).

In the femtosecond-laboratory of the Universidade do Porto, we used an ultrafast oscillator with carrier-envelope phase (CEP) stabilized (Femtosource Rainbow CEP) and an amplifier (FemtoPower Compact PRO CEP). Both of them are commercial equipment manufactured by Femtolasers. The oscillator (Fig. A.4a) delivers pulses with Fourier-transform limit below 7 fs at a repetition rate of 80 MHz, with a central wavelength around 800 nm and energy per pulse up to 5 nJ. This source was used in Chapter 9. The amplifier is similar to the system in the UJI, although it is CEP-stabilized and uses a prism compressor instead of a grating compressor. It provides 1 kHz, ~1 mJ, 25-fs pulses (Fourier limit) and was used in the hollow-core fiber (Fig. A.4b) post-compression experiment presented in Chapter 10.

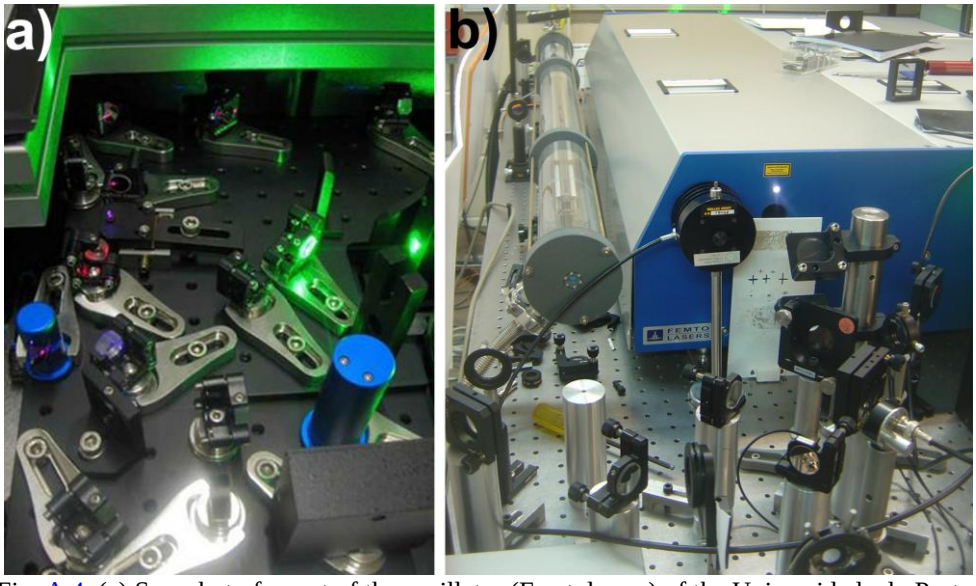


Fig. A.4. (a) Snapshot of a part of the oscillator (Femtolasers) of the Universidade do Porto. (b). Picture of the laser system (Femtolasers) and the hollow-core fiber used to post-compress the pulses in the Universidade do Porto.

# RESUMEN

**Contenido**

# BREVE RESUMEN

En este resumen se pretenden mostrar los estudios realizados en el marco de la presente tesis. Por motivos de espacio, no se incluyen todos los resultados obtenidos que han sido presentados en los capítulos anteriores.

El propósito de esta tesis es el desarrollo de una técnica para medir la amplitud y fase espaciotemporal de los pulsos láser ultracortos y sus aplicaciones. El núcleo de la tesis se divide en tres partes, que corresponden a la presentación de la técnica (R.2), las aplicaciones a óptica difractiva (R.3), a óptica no lineal y a pulsos de pocos ciclos ópticos (R.4). En la Sección R.1 de introducción se presentan el marco y la motivación de la tesis, los conceptos básicos sobre pulsos láser ultracortos, y el estado del arte de las técnicas ya existentes para la caracterización de los pulsos. La Sección R.2 comienza revisando la caracterización de pulsos por medio de interferometría espectral, para después presentar la técnica que hemos desarrollado para la caracterización espaciotemporal de los pulsos (STARFISH), la cual se basa en un acoplador de fibra óptica como parte del interferómetro. En la Sección R.3, presentamos las aplicaciones que involucran elementos ópticos difractivos en régimen de propagación lineal. Esta parte cubre los fundamentos del acoplamiento espaciotemporal durante la propagación de pulsos difractados por una placa zonal (Capítulo 5), la aplicación a una lente difractiva kinoforme incluyendo la medida del frente de ondas resuelto espectralmente. La aplicación a procesos no lineales y a pulsos de pocos ciclos se presenta en la Sección R.4, en la que estudiamos la dinámica de la propagación de pulsos intensos en el régimen de filamentación. Posteriormente, se presenta la aplicación de STARFISH a pulsos de pocos ciclos generados en un oscilador ultrarrápido, y a continuación, a la post-compresión de pulsos amplificados en una fibra hueca. Por último, se resaltan las principales conclusiones de la tesis.

# R1. INTRODUCCIÓN

## R1.1.Perspectiva general y motivación

Desde el descubrimiento del láser, esta fuente de luz con propiedades tan particulares ha estado evolucionando continuamente en paralelo a sus aplicaciones en muchos campos de la ciencia y la tecnología. La propiedad más significativa de la radiación láser es la coherencia. A pesar de que habitualmente se habla de lo láseres como fuentes monocromáticas, este no es el caso de los pulsos láser ultracortos sobre los que versa la presente tesis. La radiación monocromática está compuesta de una sola frecuencia (o longitud de onda, o color) y, en el dominio temporal, corresponde a una emisión continua e infinita. Este trabajo se ocupa de láseres pulsados, que son muy breves (y finitas) emisiones de radiación láser y distribuidas en el tiempo, en nuestro caso regularmente (la separación temporal entre pulsos viene dada por la inversa de la tasa de repetición del láser). Una forma de producir radiación pulsada consiste en introducir pérdidas temporales en una cavidad láser, un mecanismo conocido como *Q-switching* [1], con el que se alcanza el régimen de los nanosegundos. Sin embargo, el rando de pulsos láser ultracortos (en general, para nosotros significará por debajo de 100 fs) se logra por medio del *mode-locking*, el cual se basa en la emisión acoplada de múltiples modos longitudinales (con frecuencias diferentes) de la cavidad láser. In la radiación pulsada se producen breves emisiones de radiación dependientes del tiempo, conocidas como pulsos láser. En el dominio espectral (frecuencias), el pulso está definido por la amplitud de los modos y la relación entre las emisiones de los distintos modos, la cual se conoce como fase espectral. Análogamente, en el dominio temporal el pulso viene dado por una amplitud y fase temporales. La relación entre el pulso en el dominio espectral y temporal es la transformada de Fourier. Para obtener pulsos más cortos, es necesario tener anchos de banda espectrales de emisión más grandes. En nuestro caso, trabajaremos con láseres de titanio:zafiro, los cuales tienen una curva de ganancia ancha desde 660 nm a 1180 nm (en longitudes de onda) aproximadamente. La amplia banda espectral de emisión de estos láseres de estado sólido permite producir directamente pulsos por debajo de 10 fs.

En muchas aplicaciones, el conocimiento detallado del campo eléctrico de los pulsos es de gran interés, independientemente de si se trata del resultado o de la entrada del experimento. El objetivo de esta tesis es la medida de la amplitud y la fase de los pulsos. Como veremos con más detalle en la Sección 1.3, las duraciones de los pulsos son demasiado cortas para ser medidas directamente por medios electrónicos. Por esta razón, los pulsos se caracterizan utilizando métodos ópticos, en los que típicamente es el propio pulso corto el que actúa como la sonda [2,3]. El campo eléctrico es una magnitud

que depende del tiempo y las tres coordenadas espaciales, esto es, $E(x,y,z,t)$. El eje z se define como la dirección de propagación del pulso (a pesar de no ser siempre estrictamente cierto, la radiación láser se considera direccional). En una cierta distancia de propagación, es decir, el plano $z = z_0$, el campo eléctrico depende del tiempo y de las dos coordenadas espaciales transversales $x, y$. La dependencia espacial $(x, y)$ del pulso se puede caracterizar sin tener en cuenta la evolución temporal (por ejemplo, [4]), cuya dependencia se integra. Sin embargo, en muchos casos, el campo eléctrico no es una función separable en la forma $E(x,y,t) = E_{xy}(x,y)E_t(t)$, por lo que en estos casos una caracterización separada del perfil temporal y el perfil espacial no es una vía válida para conocer el campo del pulso eléctrico. Vamos a proponer una nueva técnica para caracterizar el acoplamiento espaciotemporal de los pulsos, la cual se llama STARFISH [5] (Sección R.2). Nuestro interés en la caracterización de pulsos ultracortos proviene de sus aplicaciones. Por un lado, se utilizan para examinar materiales con una excelente resolución temporal. Por otro lado, la concentración de la energía del pulso en dichos eventos cortos aumenta la intensidad pico de la luz hasta valores extremos, abriendo un nuevo régimen de interacción luz-materia [6]. En cualquiera de estas aplicaciones el conocimiento completo del campo eléctrico es esencial.

El acoplamiento espaciotemporal en pulsos láser ultracortos es muy diverso, siendo originado tanto en régimen lineal como no lineal de propagación de la luz. En [7], los autores revisan diferentes tipos de distorsiones espaciotemporales (por ejemplo, véase la Fig. R.1). En régimen lineal, por lo general las distorsiones se derivan de problemas geométricos a menudo causados por la propagación dependiente de la longitud de onda de la luz, combinada con un espectro ancho. Por ejemplo, un pulso de entrada homogéneo (sin distorsión) se *chirpea* espacialmente después de la refracción en una ventana plano-paralela inclinada (Fig. R.1a). Por *chirp* espacial (o dispersión espacial) nos referimos a una distribución espacialmente dependiente de la frecuencia del pulso.

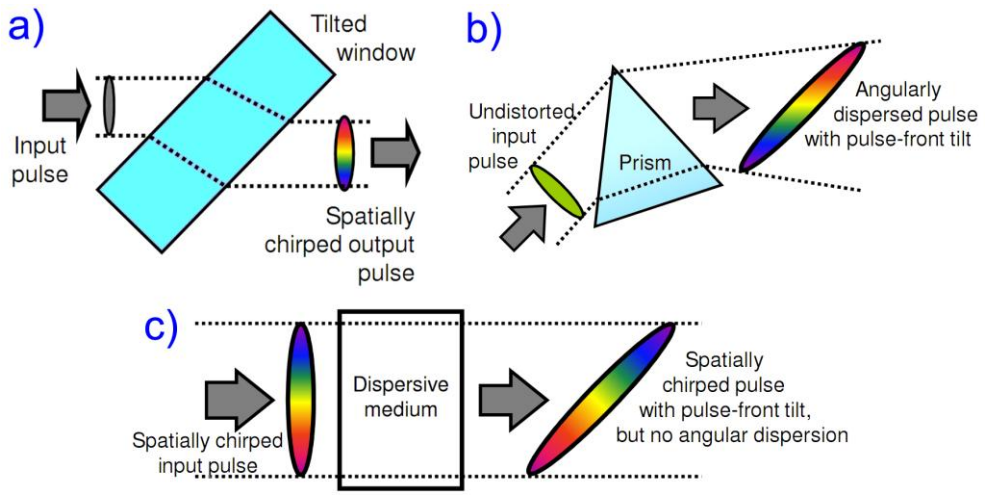


Fig. R.1. Ejemplos de distorsiones espaciotemporales. (a) *Chirp* espacial originado por una ventana inclinada. (b) Pulso angularmente dispersado con *chirp* espacial e inclinación del frente de pulsos después de un prisma (lo mismo se aplica para una red de difracción). (c) La combinación de *chirp* espacial de entrada con un medio dispersivo introduce inclinación en el frente de pulsos. Figura extraída de [3].

En el caso de un prisma o una red de difracción, el pulso presenta dispersión angular e inclinación del frente de pulsos (Fig. R.1b). Debido a la dispersión angular, las frecuencias de los pulsos se propagan en direcciones diferentes. El frente de pulsos se inclina cuando las frecuencias llegan en momentos diferentes en una cierta distancia de propagación o plano de observación.

Estas imágenes sencillas nos ayudan a entender que, a pesar de considerar sólo los casos más "sencillos" de distorsiones espaciotemporales, estos están estrechamente relacionados y a menudo son difíciles de discriminar. Por ejemplo, un pulso de entrada que sólo tenga *chirp* espacial, adquiere inclinación en su frente de pulsos después de atravesar un medio dispersivo (donde las frecuencias se propagan con velocidades diferentes), como se ilustra en la Fig. R.1c. Aparte de estos ejemplos, los elementos ópticos tales como lentes también introducen distorsiones espaciotemporales debido a aberraciones (cromática, esférica, astigmatismo…) [8,9]. En realidad, la focalización de pulsos ultracortos a menudo está asociada a aberraciones debidas al gran contenido espectral del pulso.

La propagación de la luz después de elementos ópticos difractivos (DOE) es un excelente ejemplo de acoplamiento espaciotemporal. La Sección R.3 de esta tesis se dedica a la caracterización y aplicaciones de la óptica difractiva en el campo de pulsos ultracortos. Debido a la intrínseca dependencia de la longitud de onda (o cromática) en la difracción y, teniendo en cuenta la amplia banda espectral de los pulsos, los DOE introducen un acoplamiento espaciotemporal de forma natural.

En el camino hacia pulsos ultra-intensos ha habido una tecnología clave, la amplificación de pulsos *chirpeados* (CPA) [12], que se basa en el estiramiento temporal del pulso antes de la amplificación, y después comprimirlo de nuevo. La compresión en los amplificadores se realiza a menudo con pares de redes de difracción o con pares de prismas en una configuración que introduce dispersión negativa. Como consecuencia de ello, el pulso a la salida de un amplificador puede presentar *chirp* espacial y/o inclinación del frente de pulsos si no están perfectamente compensados. Excepto en las medidas del oscilador ultrarrápido, utilizaremos sistemas láser CPA en los experimentos llevados a cabo a lo largo del presente trabajo.

En la Sección R.4, vamos a presentar los resultados relativos a los procesos no lineales y pulsos de pocos ciclos ópticos ($<10\,fs$). En los procesos no lineales como filamentación [11,13], hay un fuerte acoplamiento espaciotemporal (y espacioespectral) originado por la dependencia de la propagación no sólo en la fase, sino también en la intensidad. Durante la propagación del filamento, el espectro del pulso se modifica. Debido a la intensidad espacialmente dependiente del pulso, esta modificación depende de la coordenada espacial. Por ejemplo, en la evolución de la distribución espacioespectral del pulso, se puede observar diferentes estructuras durante la propagación. En este caso, el *chirp* espacial tiene una estructura más compleja que los casos presentados en la Fig. R.1. En el dominio espaciotemporal, también hay un fuerte acoplamiento asociado a una dinámica muy rica, incluyendo división del pulso (en el dominio temporal) o emisión cónica (radiación angular y espectralmente dependiente) [13].

En general, los acoplamientos espaciotemporales descritos anteriormente ya se han estudiado desde el punto de vista teórico. Por ejemplo, se ha desarrollado una teoría para describir las distorsiones espaciotemporales [14] y las aberraciones cromáticas de lentes también se han estudiado analítica [15] y numéricamente [16]. Los DOE también se han estudiado numéricamente incluyendo la dependencia espaciotemporal y espacioespectral [17], así como hay estudios teóricos de la dinámica de la filamentación [13,18].

Sin embargo, la dificultad para medir los acoplamientos espaciotemporales ha causado un conocimiento incompleto de los pulsos desde el punto de vista experimental, hasta que las primeras técnicas de caracterización espaciotemporal se introdujeron durante los últimos años [5,9,19-23]. La información experimental de la estructura espaciotemporal de los pulsos es muy enriquecedora con el fin de optimizar el diseño de los sistemas ópticos o la propagación de los pulsos, tanto en regímenes lineales como no lineales. En realidad, la caracterización espaciotemporal de pulsos láser ultracortos es un campo muy activo. Posteriormente, presentaremos las técnicas para su caracterización espacial, temporal y espaciotemporal. Hay una amplia gama de aplicaciones de la caracterización espacio-temporal, que se espera que crezca en el futuro.

## R1.2.Descripción y caracterización de los pulsos

En este resumen, no vamos a entrar en los fundamentos de la generación de radiación láser, tipos de láser o sus aplicaciones [24], sino que nos limitaremos a describir los pulsos. El campo eléctrico de un pulso es una magnitud con amplitud y fase dependientes de las tres coordenadas espaciales ( $x, y, z$ ) y del tiempo $t$ [25]. A pesar de ser una función real (ya que representa una magnitud física), se expresa normalmente como una función compleja $E = A\exp\{i\Omega\}$. La magnitud $A = |E|$ es la amplitud y la fase es $\Omega$, siendo ambas funciones de $x, y, z, t$ en el caso de pulsos láser ultracortos [26]. El campo eléctrico real es simplemente la parte real de la representación compleja, esto es, $E = |E|\cos(\Omega)$. La expresión completa para el campo eléctrico está dada por

$$E(x,y,z,t) = A(x,y,z,t)\times\exp\left\{i\left[\omega_0 t - \vec{k}\cdot\vec{r} + \varphi(x,y,z,t)\right]\right\}, \qquad \text{(R.1)}$$

donde $\omega_0$ es la frecuencia angular central y $\vec{k}$ es el vector de ondas, cuya orientación $\vec{k}/|\vec{k}|$ da la dirección de propagación del pulso. Por convenio, se elige el eje z como dirección de propagación del pulso, cuando $\vec{k}$ se puede considerar un escalar, entonces $\vec{k}\cdot\vec{r}$ es simplemente $kz$. El módulo $k$ se conoce como el número de ondas y es el equivalente espacial de la frecuencia angular $\omega_0$ en el tiempo. Por lo tanto, el campo eléctrico (la parte real) oscila en el tiempo $t$ y en el espacio $z$ (la dirección de propagación). En la Ec. (R.1), la cantidad $\varphi$ es la fase espaciotemporal después de la sustracción de los términos oscilatorios $\omega_0 t$ y $-kz$.

La frecuencia angular está relacionado con la frecuencia lineal $\nu$ por $\omega_0 = 2\pi\nu$. La frecuencia $\nu = 1/T$ es el número de oscilaciones por segundo (medido en $Hz$), donde $T$ es el período de las oscilaciones. El periodo espacial se conoce como la longitud de

onda $\lambda_0$ de la luz en el vacío y se relaciona con el número de onda por $k = 2\pi / \lambda_0$. Las magnitudes de espacio y tiempo de la onda electromagnética están conectadas por la velocidad de la luz en el vacío $c$ a través de las relaciones $\lambda_0 = cT$ y $\omega_0 = ck$.

Si el pulso se propaga dentro de un medio, la velocidad de propagación está dada por $v = c / n(\omega)$, donde $n(\omega)$ es el índice de refracción del medio. Puesto que $n(\omega) \geq 1$, la velocidad es siempre $v \leq c$. Además, la longitud de onda en el medio es $\lambda_n = \lambda_0 / n(\omega_0)$ y el número de ondas se modifica en consecuencia, $k = 2\pi n(\omega_0) / \lambda_0 = \omega_0 n(\omega_0) / c$.

Dado que el pulso se propaga en el eje z, en general se observará el campo eléctrico en un cierto plano que corresponde a la distancia de propagación $z = z_0$. Así, se descartará la dependencia en z, expresando el campo eléctrico como

$$E(x,y,t) \equiv E(x,y,z,t)|_{z=z_0} = A(x,y,t) \times \exp\left\{i\left[\omega_0 t + \varphi(x,y,t)\right]\right\}. \qquad \text{(R.2)}$$

Nótese que el término $-kz_0$ es una simple constante que puede ser incluida en la definición de $\varphi$. En los casos que incluyen la propagación de los pulsos en su estudio, vamos a considerar el campo eléctrico espaciotemporal, $E(x,y,t)$, para diferentes distancias de propagación. El objetivo de la caracterización espaciotemporal es la medida de la amplitud y la fase de los pulsos dada por Ec. (R.2).

Para la descripción temporal de los pulsos ultracortos, dejaremos momentáneamente a un lado la dependencia espacial $(x, y)$. Bajo esta consideración, la dependencia temporal del campo eléctrico $E(t)$ de un pulso se expresa

$$E(t) = A(t) \exp\left\{i\left[\omega_0 t + \varphi(t)\right]\right\}, \qquad \text{(R.3)}$$

donde $\omega_0$ es la frecuencia portadora (o frecuencia central), y $\varphi(t)$ es la fase temporal. La función $A(t)$ se conoce como envolvente del pulso, ya que las oscilaciones del campo eléctrico están contenidas entre las curvas $+A(t)$ y $-A(t)$. En el caso de un pulso gaussiano, su envolvente viene dada por $A(t) = A_0 \exp\{-2\ln 2\left(t / \Delta t\right)^2\}$. El campo eléctrico es el producto de la envolvente y las oscilaciones de la portadora (con un periodo $T$). La intensidad temporal del pulso es $I(t) = |E(t)|^2 = [A(t)]^2$, y con la presente definición de la envolvente, la duración del pulso se calcula como la anchura a media altura de la intensidad (FWHM), en este caso $\Delta t$.

Como se ha dicho anteriormente, los pulsos láser ultracortos no son monocromáticos. De hecho, el pulso está compuesto por múltiples ondas con diferentes frecuencias, amplitudes y fases. El espectro del láser representa su contenido de frecuencias. En realidad, el campo eléctrico puede ser expresado, de forma equivalente, en los dominios temporal y espectral. En el dominio espectral, la representación compleja del campo $E_f(\omega) = A_f(\omega)\exp\{i\phi(\omega)\}$ está determinada por la amplitud espectral $A_f(\omega)$ y la fase espectral $\phi(\omega)$. La densidad espectral de potencia se define $S(\omega) = |E_f(\omega)|^2 = [A_f(\omega)]^2$. Nos referiremos a ella simplemente como el espectro, lo que da la información de la amplitud espectral del pulso. El campo en frecuencias se puede expresar como

$$E_f(\omega) = \left|E_f(\omega)\right| \exp\left\{i\phi(\omega)\right\} = \sqrt{S(\omega)} \exp\left\{i\phi(\omega)\right\}. \qquad \text{(R.4)}$$

Las representaciones del campo eléctrico en el tiempo y en frecuencias están conectadas por la transformada de Fourier (FT), que denotaremos $\mathcal{F}$. Las relaciones

son $\mathcal{F}\{E(t)\}=E_f(\omega)$ y $\mathcal{F}^{-1}\{E_f(\omega)\}=E(t)$. En el caso particular de láser de pulsos ultracortos, su espectro es una distribución amplia de frecuencias, por lo que se dice que tienen un espectro de banda ancha o un ancho de banda espectral grande. Como se dijo anteriormente, la duración temporal y de ancho de banda espectral de los pulsos se da típicamente como la FWHM de la intensidad y el espectro, respectivamente. En el caso de pulsos gaussianos, el espectro está dada por

$$S(\omega)=A_{f,0}^2\exp\left\{-4\ln 2\left[(\omega-\omega_0)/\Delta\omega\right]^2\right\}, \qquad \text{(R.5)}$$

donde las FWHM están relacionadas por $\Delta t\,\Delta\omega=4\ln(2)$. Esto explica que con el fin de reducir la duración del pulso, es necesario aumentar el ancho de banda espectral.

En este punto, es importante comentar la influencia de la fase. El pulso en el dominio temporal será diferente dependiendo de la fase espectral $\phi(\omega)$. Si la fase espectral $\phi(\omega)=cte$, se dice que el pulso está limitado por transformada de Fourier (FTL) y por lo tanto tiene la duración temporal ($\Delta t$) más corta compatible con el espectro $S(\omega)$. Consideremos un espectro gaussiano centrado en la frecuencia $\omega=\omega_0$, dado por la Ec. (R.5). Si este espectro es FTL, entonces el campo eléctrico oscilará a la frecuencia portadora. De la propiedad de traslación de la FT, una fase espectral lineal $\omega t_0$ sólo introduce un desplazamiento del pulso en el dominio temporal, que puede ser entendido como un cambio en el origen del eje del tiempo. Por el contrario, si el pulso tiene una fase arbitraria espectral, la amplitud y la fase del pulso en el tiempo serán modificadas. En cuanto a la fase temporal $\Omega(t)=\omega_0 t+\varphi(t)$, queremos remarcar que $\varphi(t)$ depende del tiempo. La consecuencia es que la frecuencia de la oscilación temporal varía dentro del pulso, la cual puede ser calculada como

$$\omega(t)=\omega_0+d_t\varphi(t)=d_t\Omega(t), \qquad \text{(R.6)}$$

donde $d_t$ denote la derivada respect al tiempo. La función $\omega(t)$ se llama frecuencia instantánea del pulso. Siempre que $\omega(t)$ no sea una constante, se dice que el pulso tiene *chirp* temporal o que está *chirpeado* temporalmente.

Recuperando la dependencia espacial junto a la dependencia temporal, el campo eléctrico en un plano de observación determinado, definido por $z=z_0$, se puede expresar en el dominio espaciotemporal, dado por la Ec. (R.2). Hemos visto que la dimensión temporal es análoga a la dimensión de frecuencia, y que están conectadas por la FT. Entonces, el campo puede ser expresado de forma equivalente en el dominio espacioespectral a través de

$$E_f(x,y,\omega)=\mathcal{F}\left\{E(x,y,t)\right\}. \qquad \text{(R.7)}$$

Hay algunas definiciones importantes con respecto a la amplitud y la fase de los pulsos en los dominios espaciotemporal y espacioespectral, respectivamente. El frente de pulsos es la superficie definida por la ubicación temporal de los máximos de intensidad a lo largo de su perfil espacial $(x,y)$. Por ejemplo, la curvatura del frente de pulsos de un haz convergente es cuadrática, mientras que un haz colimado tiene un frente de pulsos plano. En la Fig. R.1c, se representa un ejemplo de frente de pulsos

inclinado. En el caso de distribuciones espaciotemporales más complejas, puede ser difícil definir el frente de pulsos.

En cuanto a la fase, en el dominio espacioespectral, el frente de ondas de un pulso se define (para cada frecuencia $\omega = \omega_j$) como una superficie de fase constante. Siguiendo el último ejemplo, de nuevo un haz convergente tiene un frente de ondas esférico y un haz colimado tiene un frente de ondas plano. El frente de ondas del pulso puede ser dependiente de la frecuencia, por ejemplo cuando diferentes frecuencias del pulso son divergentes o convergentes, como en la aplicación de la lente difractiva kinoforme.

En términos radiométricos, la irradiancia del pulso viene dada por $I(x,y,t) = |E(x,y,t)|^2$, y corresponde a la potencia de la radiación electromagnética por unidad de superficie. En nuestro campo, habitualmente se habla de intensidad en lugar de irradiancia, de forma que nosotros utilizaremos el término intensidad a partir de ahora. En el dominio espacial, se puede definir la intensidad espacial (nótese que en realidad es la fluencia y se mide en $J/cm^2$), y que está dada por

$$I(x,y) = \int_{-\infty}^{\infty} |E(x,y,t)|^2 \, dt \, . \qquad \text{(R.8)}$$

Análogamente, la intensidad temporal, $I(t)$, que hemos definido anteriormente es el flujo o potencia radiante (se mide en unidades de potencia), aunque nosotros nos referiremos a ella como intensidad.

Durante su propagación, los pulsos experimentan difracción, dispersión, efectos no lineales, etc. La combinación de estos procesos puede conducir a acoplamientos espaciotemporales, puesto que el pulso evoluciona con un acoplamiento entre las cuatro coordenadas: tres coordenadas espaciales y el tiempo/frecuencia. En esos casos, una caracterización completa del campo eléctrico $E(x,y,t)$, para una determinada $z = z_0$, es obligatorio. Sin embargo, esta medida es difícil de lograr. Muchas veces, se realiza una caracterización independiente del perfil temporal y espacial de los pulsos, con la consiguiente pérdida de información.

La longitud de onda central de los láseres pulsados de titanio:zafiro está entorno a $\lambda_0 = 800\,nm$, lo que significa que los pulsos oscilan con una frecuencia óptica $\nu_0 = 0.375 \cdot 10^{15}\,rad/s$, siendo $T = 2.67 \cdot 10^{-15}\,s$ el periodo del ciclo óptico. Esta rápida variación es imposible de ser detectada por la respuesta de los dispositivos electrónicos. Como se mencionó anteriormente, esta limitación se supera utilizando métodos ópticos. En realidad, un proceso lineal sólo proporciona el espectro, o la fase relativa con respecto a un pulso de referencia (por medio de interferometría espectral). Por lo tanto, los auto-referenciados métodos, que miden la amplitud y la fase del pulso, se basan normalmente en procesos no lineales como generación de segundo armónico (SHG) u otros.

Los avances en la tecnología láser son muy rápidos y, en consecuencia, las técnicas para caracterizarlos tienen que ser adaptadas o inventadas para los nuevos desafíos. El campo de los láseres ultracortos no es una excepción. Durante las últimas décadas, muchas técnicas se han desarrollado para medir el perfil temporal de los pulsos (sin tener en cuenta la dependencia espacial), las cuales se revisan en [2].

Una de las técnicas más consolidadas para la medida de pulsos ultracortos se conoce como FROG (*Frequency-Resolved Optical Gating*) [27]. Un esquema común de FROG usa la autocorrelación de segundo orden a partir del SHG del pulso en un cristal no lineal, pero también se utilizan muchos otros sistemas. Por ejemplo, otros tipos generalizados de FROG se basan en la auto-difracción [28], o la generación de tercer armónico (THG) [29]. En general, se obtiene una traza 2D experimental, que directamente relacionada con el campo eléctrico del pulso a medir. Experimentalmente, una línea de retardo escanea el tiempo relativo entre dos réplicas del pulso que se someten a un proceso determinado (por ejemplo, SHG). La señal resultante es resuelta espectralmente con un espectrómetro. La traza experimental, conocida como el espectrograma, codifica la información completa del pulso. Esta técnica requiere un algoritmo numérico para recuperar el pulso. El algoritmo optimiza el pulso recuperado mediante la comparación de una traza simulada con la traza experimental, de manera iterativa. Este es un método auto-referenciado que recupera tanto la intensidad temporal como la fase del pulso. La redundancia de datos de la traza (una función 2D se utiliza para obtener el campo 1D) da robustez al resultado de la medida.

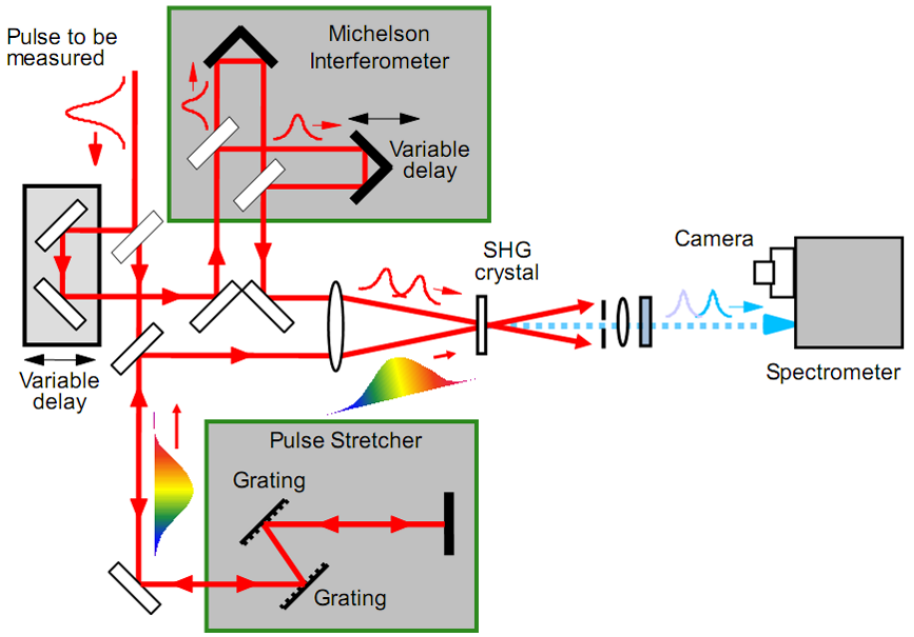


Fig. R.2. Montaje experimental para la técnica SPIDER. El pulso de entrada (desconocido) se divide en dos réplicas en un divisor de haz. Entonces, una réplica se *chirpea* (por ejemplo, en un estirador de redes de difracción) y la otra réplica se divide en dos réplicas con un retardo temporal controlado. Las dos réplicas retardadas sufren un proceso de suma de frecuencias en un cristal no lineal, y la interferencia espectral de los dos pulsos se registra en un espectrómetro. Figura extraída de [3].

Otro método consolidado que también mide la amplitud y fase temporales de los pulsos es el SPIDER (*Spectral Phase Interferometry for Direct Electric-field Reconstruction*). Es una técnica directa y auto-referenciada para medir pulsos ultracortos [30]. Dos réplicas del pulso desconocido hacen generación de suma de frecuencias (análogo a SHG) con un pulso que se ha estirado en el tiempo, y que posee un *chirp* a fin de tener una longitud de onda instantánea diferente a lo largo del perfil temporal (véase Fig. R.2). Por esta razón y por el retardo $\tau$ entre las réplicas, cada una

de ellas se suma con dos ondas cuasi-monocromáticas, cuyas frecuencias están separadas una pequeña cantidad $\Omega$ (el *shear* espectral). Entonces, los dos pulsos generados con un retardo $\tau$ van a interferir en el dominio espectral proporcionando la señal de SPIDER

$$S_{SPIDER}(\omega) = S(\omega) + S(\omega+\Omega) + 2\sqrt{S(\omega)S(\omega+\Omega)}\cos\left[\phi(\omega+\Omega) - \phi(\omega) + \omega\tau\right]. \quad \text{(R.9)}$$

Usando análisis de FT de las franjas de interferencia [31], se puede calcular la diferencia de fase espectral del pulso evaluado en frecuencias separadas por el *shear* $\Omega$, esto es, $\phi(\omega-\Omega)-\phi(\omega)$. Esta cantidad está relacionada con la derivada de la fase espectral. Por lo tanto, la fase del pulso desconocido se calcula a partir de dicha cantidad a través de la concatenación de la fase para frecuencias consecutivas, es decir, mediante la integración de la diferencia de fase. Esto requiere una calibración muy precisa del *shear*.

Descartamos ahora la dependencia temporal de los pulsos, a fin de describir la caracterización de su perfil espacial. Esta caracterización implica el conocimiento de la amplitud y la fase del campo eléctrico como una función de las coordenadas espaciales transversales $(x, y)$. Con el fin de medir la amplitud, se puede utilizar una CCD para registrar la intensidad espacial.

En cuanto a la medida de la fase espacial del pulso (es decir, el frente de ondas), la técnica más extendida es el Hartmann-Shack [4]. El sensor consta de una matriz de microlentes que focalizan pequeñas selecciones espaciales del pulso, y que son detectados en una CCD. La posición de cada foco no se desvía con respecto al eje óptico para frentes de ondas planos. La desviación de la matriz de puntos focales respecto a los ejes ópticos de cada microlente da la magnitud de la inclinación local del frente de ondas. La combinación de esta información sobre el perfil espacial proporciona toda la información del frente de ondas. Además, a partir de la intensidad de la matriz de los focos, se puede conseguir la intensidad espacial.

La mayoría de las técnicas para la caracterización espaciotemporal de pulsos ultracortos se han introducido en la última década. Los esquemas iniciales para este propósito pretendían medir diferencias de fase introducidas por elementos ópticos [8] y, más recientemente, por la propagación no lineal [32]. Estos sistemas se basaban en interferometría espectral resuelta espacialmente y no caracterizaban el haz de referencia, lo que es esencial para realizar reconstrucciones completas espaciotemporales.

En los últimos años se han introducido diversas técnicas que sí miden la amplitud y fase espaciotemporal, como por ejemplo STRIPED FISH [22], SEA TADPOLE [9] o Shackled-FROG [23].

En esta tesis, se presenta un esquema novedoso para realizar interferometría espectral resuelta espacialmente, basado en un acoplador de fibra óptica. Nos referimos a ella como STARFISH (*SpatioTemporal Amplitude-and-phase Reconstruction by Fourier-transform of Interference Spectra of Highly-complex-beams*) [5]. En esta técnica, el acoplador de fibra es la parte clave y hace que el sistema sea sencillo, robusto y versátil. La técnica será presentada en detalle en la próxima sección.

# R2. LA TÉCNICA: STARFISH

## R2.1.Interferometría espectral

En la interferometría espectral (SI), dos pulsos colineales, el test y la referencia, están retrasadas en el tiempo una cantidad $\tau$. La referencia es el pulso conocido, cuya espectral fase debe ser previamente caracterizada. El test es el pulso desconocido que queremos caracterizar. El campo eléctrico de cada pulso en el dominio espectral se expresa como $E_f(\omega) = |E_f(\omega)| \exp\{i\phi(\omega)\}$. Usando la definición de la transformada de Fourier y sus propiedades, se puede calcular el espectro de interferencia, es decir, el espectro de la suma de los pulsos test y referencia. El espectro total se expresa como

$$S(\omega) = S_{test}(\omega) + S_{ref}(\omega) + 2\sqrt{S_{test}(\omega) S_{ref}(\omega)} \cos[\phi_{test}(\omega) - \phi_{ref}(\omega) - \omega\tau], \quad \text{(R.10)}$$

que es la suma de los espectros test y referencia —las contribuciones que no interfieren— y el término cruzado interferencial: un ejemplo se representa en la Fig. R.3. El término de interferencia es una contribución oscilante, cuya amplitud es proporcional al producto cruzado de los espectros del test y de la referencia, mientras que las periódicas franjas vienen del coseno y tienen un período $1/\tau$ proporcional a la inversa del retardo. En nuestro caso, el signo del retardo en la Ec. (R.10) es positivo, porque se elige el criterio del pulso de referencia viajando por delante del pulso. Cuando no se dice lo contrario, significa que mantenemos este criterio.

La fase relativa entre los pulsos test y referencia está codificada en la SI dada por la Ec. (R.10). En particular, se codifica en el término coseno, por lo que es necesario realizar un tratamiento de datos para obtenerla. Existen distintas implementaciones para extraer esta información. Nosotros utilizaremos el algoritmo de interferometría espectral por transformada de Fourier (FTSI) [31], que es el más extendido debido a que la fase se recupera precisa y unívocamente con un análisis de FT. Además, el uso de algoritmos rápidos para el cálculo numérico de la FT permite una rápida recuperación de la fase. El esquema de la Fig. R.3 representa todos los pasos llevados a cabo en el algoritmo. En primer lugar, una IFT se aplica al espectro interferencial, visto en la Ec. (R.10), produciendo de este modo en el dominio del tiempo los tres picos representados en la figura. Un pico está centrado en $t = 0$ y corresponde a la contribución no interferencial de los espectros individuales de los pulsos. Los otros dos picos, procedentes del término interferencial, están centrados en $t = \pm\tau$. Si se desea, los espectros test y referencia se pueden restar antes de este paso para eliminar el pico central. Con el criterio que hemos elegido para el signo del retado (pulso de referencia antes del pulso test), se puede expresar el coseno de las interferencias como la suma de dos funciones exponenciales imaginarias, $\exp\{i(+\phi_{test}(\omega) - \phi_{ref}(\omega) - \omega\tau)\}$ y $\exp\{i(-\phi_{test}(\omega) + \phi_{ref}(\omega) + \omega\tau)\}$, que

corresponden respectivamente a las señales centradas en $t=+\tau$ y $t=-\tau$. A continuación, se selecciona el pico de la derecha ($t=+\tau$) multiplicando la IFT por una puerta numérica. Nosotros usamos una función supergaussiana como puerta para evitar la introducción de saltos bruscos en el cálculo numérico (línea verde en la figura). La señal filtrada en el dominio del tiempo se representa en rojo (el pico lateral centrado en $t=+\tau$). Puesto que los datos experimentales se adquieren en longitudes de onda, ha de hacerse la conversión a frecuencias antes de aplicar el IFT.

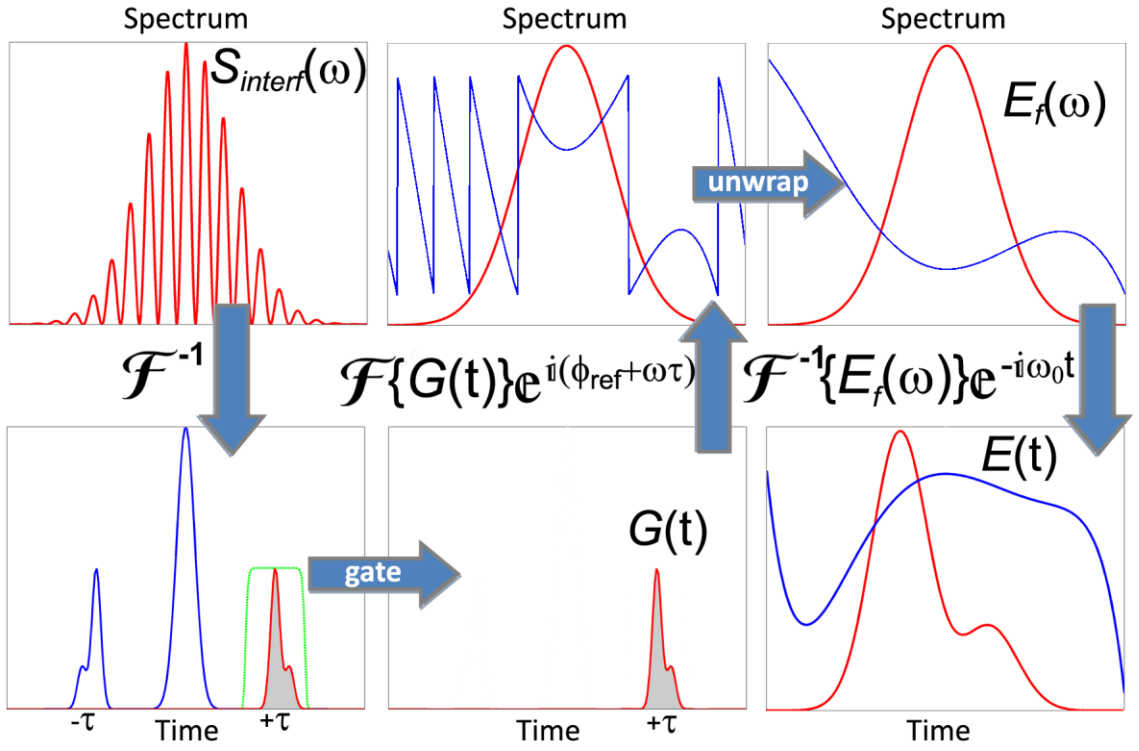


Fig. R.3. Esquema del algoritmo implementado para la interferometría espectral por transformada de Fourier (FTSI). En primer lugar, se aplica a las interferencias espectrales una transformada de Fourier inversa. En el dominio del tiempo, se selecciona el pico lateral y se aplica de nuevo una transformada de Fourier directa. En el dominio de las frecuencias, se corrigen el término $\omega\tau$ y la fase de referencia. Esto da la amplitud y fase espectral del pulso test, que puede ser traducida al dominio temporal aplicando de nuevo una transformada de Fourier inversa. En nuestro caso, se mide la amplitud espectral del pulso directamente con el espectrómetro.

## R2.2.Caracterización espaciotemporal: STARFISH

La SI descrita anteriormente permite caracterizar temporalmente un pulso test a partir de un pulso de referencia conocido. De cara a la caracterización espaciotemporal, se medirá la SI en función de las coordenadas espaciales transversales, es decir, la SI resuelta espacialmente. El montaje experimental más extendido para la SI resuelta espacialmente utiliza un interferómetro de Mach-Zehnder. Aquí, se propone una ventajosa implementación experimental de SI resuelta espacialmente, en la que se utiliza un acoplador de fibra óptica monomodo (con brazos de longitud casi igual) para recombinar los dos pulsos con el fin de realizar la SI. Esta propuesta es la técnica de caracterización STARFISH. Su desarrollo y las aplicaciones constituyen el núcleo principal de esta tesis.

El esquema de la configuración experimental de STARFISH se muestra en la Fig. R.4. En primer lugar, el haz láser de entrada es dividido en dos réplicas por un divisor de haz. Una réplica se utiliza como el pulso de referencia, por lo que tiene que ser calibrado por una medida temporal estándar, típicamente SPIDER o FROG. La otra réplica es el pulso test que se quiere caracterizar. El interferómetro se completa con un acoplador de fibra óptica que recombina los pulsos y los envía juntos a un espectrómetro comercial conectorizado por una fibra óptica. El montaje está diseñado a fin de que el camino óptico del brazo test y el brazo de referencia se compensen (sean casi iguales), y el retardo $\tau$ necesario para la SI se ajusta en fino por medio de la posición longitudinal del brazo de fibra que recoge el pulso de referencia. Durante una medida, la fibra de referencia recoge un punto espacial fijado en donde se realizó la calibración temporal (se puede utilizar un iris para asegurarlo experimentalmente). El brazo de fibra que recoge el pulso test es el que realiza el barrido espacial de dicho pulso: la entrada de la fibra se desplaza transversalmente a la dirección de propagación del pulso, es decir, a través de un plano z, donde z denota una cierta propagación distancia. Dado que los pulsos referencia y test están temporalmente retrasados, se pueden medir sus interferencias espectrales en el espectrómetro. El barrido espacial de la fibra del test permite realizar la SI resuelta espacialmente, a partir de la cual se caracterizará el pulso test.

La SI se realiza en diferentes posiciones del perfil espacial (véase la Fig. R.4) del pulso test (en un plano transversal), lo cual extiende la recuperación de la diferencia de fase a la dimensión espacial. Esta información se obtiene aplicando el algoritmo FTSI descrito anteriormente. Por este procedimiento, STARFISH proporciona directamente la fase espacioespectral (es decir, el frente de ondas) de los pulsos $\phi(x,\lambda)$. Debido al cálculo numérico, esta fase se obtiene expresada en el intervalo $(-\pi,\pi)$. Para obtener el frente de ondas como una función continua de la longitud de onda $\lambda$, basta simplemente con "desplegar" esta fase. Finalmente, la amplitud y la fase en el dominio espaciotemporal se obtienen por transformada de Fourier inversa (de frecuencia a tiempo).

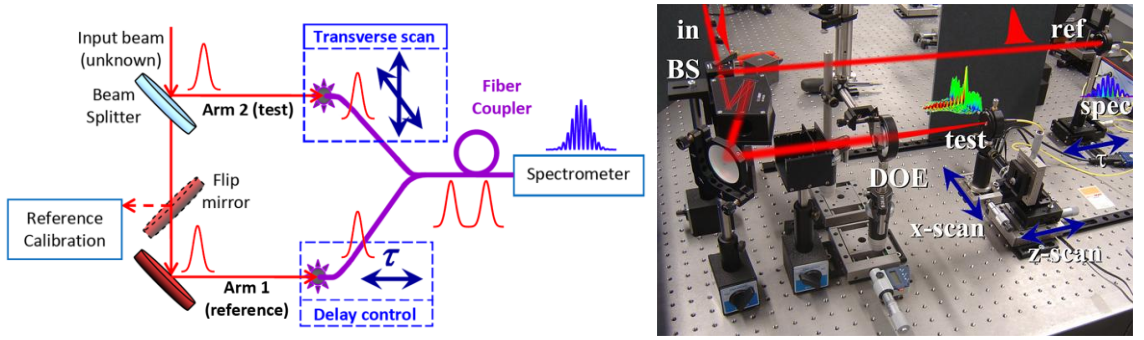


Fig. R.4. Esquema del montaje experimental de STARFISH, basado en el acoplador de fibra para realizar la interferometría espectral (izquierda). Fotografía de un experimento de óptica difractiva con STARFISH, en el cual se mide la propagación de los pulsos en el dominio espaciotemporal (derecha).

El montaje experimental de STARFISH es muy simple, puesto que sólo necesita un acoplador de fibra óptica y un espectrómetro estándar para la detección. También es

muy versátil, en el caso de requerir un rango espectral o resolución diferentes, basta con cambiar el espectrómetro en una configuración *plug-and-play*, sin ninguna variación del montaje (si la banda de operación de los otros elementos es la adecuada, esto es, del divisor de haz y los espejos). El uso de fibras para recoger los pulsos nos permite deshacernos del alineamiento de los haces en la parte de recombinación del interferómetro. Dado que los dos pulsos tienen que ser colineales para llevar a cabo la SI, en un interferómetro estándar (por ejemplo, Mach-Zehnder) esto es muy exigente, ya que cada vez que se cambia un parámetro, la alineación tiene que ser rehecha. En el caso del acoplador de fibra, es suficiente con recoger los dos pulsos en su respectivo brazo de fibra, y siempre serán colineales una vez recombinados en la parte de fibra común. La ventaja en el alineamiento permitirá llevar a cabo estudios sistemáticos más fácilmente que con un interferómetro convencional.

Es muy importante darse cuenta de que la fibra de referencia está fijada durante una medida. Mientras que la fibra test escanea espacialmente el pulso, la fibra de referencia está fijada recogiendo el mismo punto espacial del pulso de referencia. Este punto corresponde a la posición en la que ha sido caracterizado el pulso de referencia, típicamente sobre el eje, aunque esto no es obligatorio. Este hecho significa que la referencia no tiene que ser espacialmente homogéneo, en contraste con el sistema basado en el Mach-Zehnder [33]. Esta ventaja también implica que no se necesita un filtro espacial para crear un pulso de referencia homogénea. En realidad, el efecto de la fibra de referencia puede ser interpretado como un filtro espacial ya que su pequeño núcleo recoge una sección de $4\mu m$ de diámetro del pulso de referencia, que puede considerarse como localmente homogéneo. Durante el barrido espacial del pulso test, todas las SI adquiridas son relativos a la referencia fija, lo que permite la reconstrucción espaciotemporal del pulso test, incluso en el caso de un pulso de referencia inhomogéneo. El uso de un acoplador de fibra también proporciona más estabilidad al sistema, debido a la reducción de la propagación en el espacio libre y de componentes ópticos, lo que es una ventaja ya que estamos haciendo experimentos de interferometría. Este punto será crucial para la medida directa y precisa del frente de ondas y de pulsos.

A continuación, vamos a mostrar un ejemplo de aplicación de STARFISH a la medida del frente de pulsos y del frente de ondas de una onda convergente, creada enfocando el haz con un lente de distancia focal 50 cm (Fig. R.5) [3,34]. El haz test fue escaneado transversalmente a una distancia de propagación de 31 cm después de la lente, es decir, antes del foco. Los pulsos láser de entrada tenían una duración de 35 fs y el pulso de referencia se calibró con el diagnóstico SPIDER. Se examinaron 4 mm del perfil del haz en pasos de $20\mu m$ (201 puntos). El retardo entre la referencia y el test fue de 550 fs. En la Fig. R.5a se muestra la traza de la interferencia espectral de referencia y test en función de la longitud de onda y la posición transversal. La evolución de las franjas con la posición es cuadrática, de acuerdo con la curvatura del frente de ondas y el frente de pulsos del haz test. La reconstrucción de la intensidad espaciotemporal se muestra en la Fig. R.5b, en la que se observa la convergencia del haz: la región periférica del haz llega antes de que la región central, a una cierta distancia de propagación. Se ajustó la curvatura recuperada del frente de pulsos (véase el ajuste en

línea discontinua azul) y se obtuvo un valor de 18.6 cm para el radio de curvatura, de acuerdo con el valor esperado de 19 cm, si se asume propagación gaussiana del haz. Se comprobó que las modulaciones espaciales presentes en la reconstrucción no son un artificio de la reconstrucción, sino que están presentes en su propio perfil espacial. Esto se debe a la utilización de pulsos láser amplificados.

Entonces, se calculó el frente de ondas del haz convergente. Se recuperó el frente de onda en un eje $\phi(x;\lambda=\lambda_j)$ para diferentes longitudes de onda del espectro del pulso (Fig. R.5c). Para representar cada longitud de onda se ha utilizado un color diferente. La fase esperada es cuadrática, dada por la expresión $\phi(x;\lambda=\lambda_j)=-(\pi/\lambda_j R)x^2$. Las longitudes de onda más cortas corresponden a las curvaturas mayores, en acuerdo con el experimento. A continuación, se calculó el coeficiente del término cuadrático de la fase para cada longitud de onda que se define como $\kappa(\lambda_j)=-\pi/\lambda_j R$ (véase la línea continua azul). De la regresión lineal de los datos se obtuvo un valor de $R=-189.8\pm1.7\,mm$, también en buen acuerdo con el valor esperado ($R=-190\,mm$). El ajuste se representa como una línea roja discontinua, donde el área sombreada en gris representa la incertidumbre obtenida directamente a partir del ajuste.

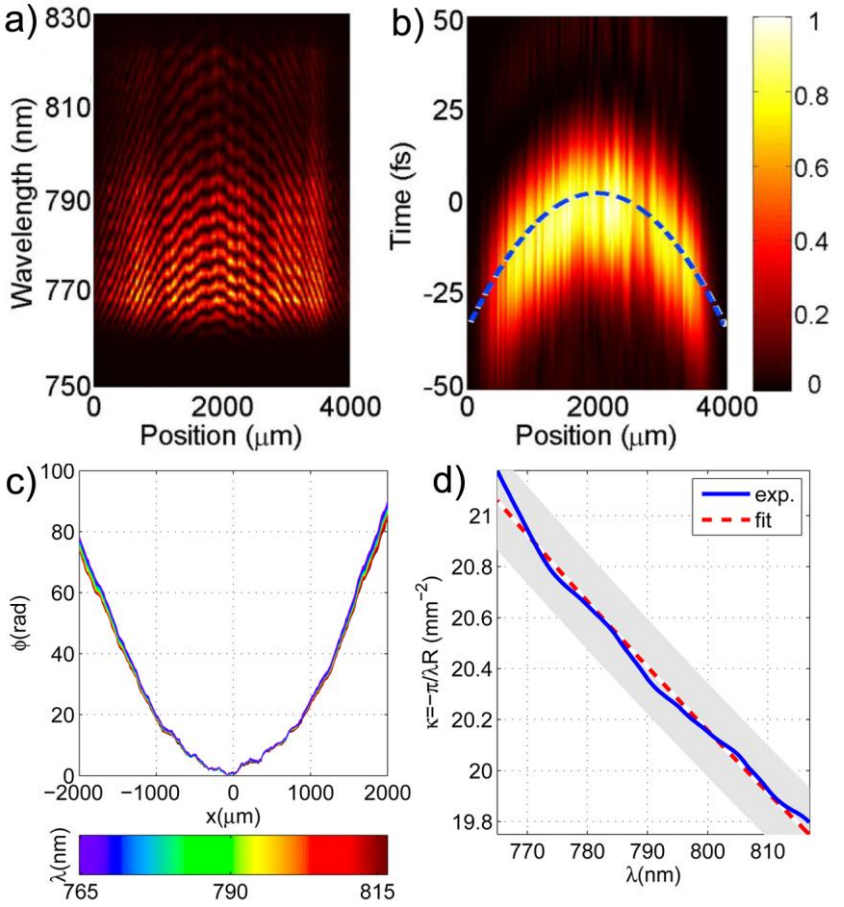


Fig. R.5. Haz convergente, pulsos de 35fs. (a) Traza de interferometría espectral resuelta espacialmente. (b) Reconstrucción del perfil de intensidad espaciotemporal. (c) Frente de ondas en función de la longitud de onda. El frente de ondas para cada longitud de onda se representa en el color dado por la barra de colores. (d) Curvatura de los frentes de onda (línea azul) y valor teórico (línea discontinua roja).

# R3. APLICACIONES EN ÓPTICA DIFRACTIVA

## R3.1.Focalización con una placa zonal

Esta sección está dedicada a la presentación de algunos de los principales resultados de STARFISH aplicado al campo de la óptica difractiva, que se han llevado a cabo gracias a una intensa colaboración con el Grup de Recerca d'Òptica de Castelló (GROC) de la Universitat Jaume I (UJI) de Castellón, España. Las simulaciones numéricas de la placa zonal fueron realizadas por investigadores del GROC-UJI.

Los elementos ópticos difractivos (DOE) consisten esencialmente en máscaras de amplitud o fase que se han diseñado para difractar los pulsos de la manera deseada dependiendo de la aplicación. Por ejemplo, las placas zonales de Fresnel (anillos concéntricos binarios de amplitud) se pueden utilizar para enfocar un haz utilizando la difracción [35], como una alternativa a las lentes convencionales o espejos curvados basados en refracción y reflexión, respectivamente. De la misma manera, las lentes de fase conocidas como lentes difractivas kinoformes también se pueden utilizar para enfocar el pulso con mayor eficiencia que las placas zonales de amplitud [36].

El uso de los DOE está muy extendido para aplicaciones tanto en régimen lineal y no lineal. Estos elementos pueden ser diseñados para manipular el campo eléctrico de pulsos láser ultracortos y lograr las formas de pulso deseadas en el experimento [37]. Por ejemplo, se han utilizado para adaptar procesos como generación de segundo armónico [38], generación de supercontinuo [39], filamentación [40], generación de armónicos de orden elevado [41] y muchos otros. Recientemente, se ha aplicado experimentalmente un módulo compensador de dispersión basado en difracción para evitar la distorsión espaciotemporal de los múltiples focos generados por una red de difracción [42].

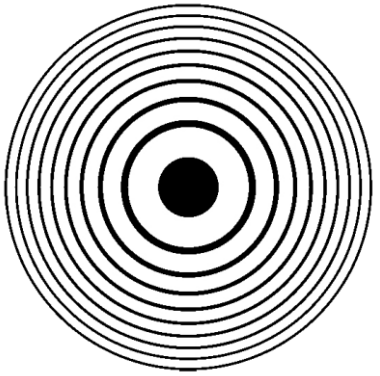

Fig. R.6. Elemento óptico difractivo utilizado en el presente trabajo. Esta placa zonal consta de varios anillos de amplitud concéntricos. La luz después de la placa se difracta de acuerdo a la distribución de dichos anillos.

En el caso de una placa zonal, como la que se muestra en la Fig. R.6, la distribución de los anillos va a determinar la focalización de los pulsos. Este DOE va a producir múltiples focos a lo largo del eje óptico, cuya estructura espaciotemporal y espacioespectral va a evolucionar a medida que varía la distancia de propagación de los pulsos [35]. La estructura del DOE define la diferencia de tiempo de llegada de las ondas de contorno ─procedentes de los bordes de los anillos─ en una cierta distancia de propagación z. Hay dos diferencias de tiempo correspondientes, respectivamente, a la diferencia entre los bordes de un anillo $\Delta t_1$ y que entre dos anillos vecinos $\Delta t_2$. A medida que aumenta la distancia de propagación a distancia, las diferencias de tiempo se reducen, lo que define tres regiones con diferentes comportamientos: de campo cercano, de Fresnel y de campo lejano. En el campo cercano, los tiempos $\Delta t_1$ y $\Delta t_2$ son más grandes que la duración del pulso, por lo que se observa un tren de pulsos con subestructura (pulsos dobles debido a los dos bordes del anillo). En la región de Fresnel, la subestructura se pierde, mientras que el tren de pulsos (que proviene de los anillos) aún está presente, ya que $\Delta t_2$ es mayor que la duración del pulso. Finalmente, en la región de campo lejano todas las ondas de contorno se funden en un pulso más largo, en el que la subestructura no puede ser distinguida debido al solapamiento de las distintas contribuciones de contorno. Este cambio de comportamiento entre las fronteras de las regiones será gradual.

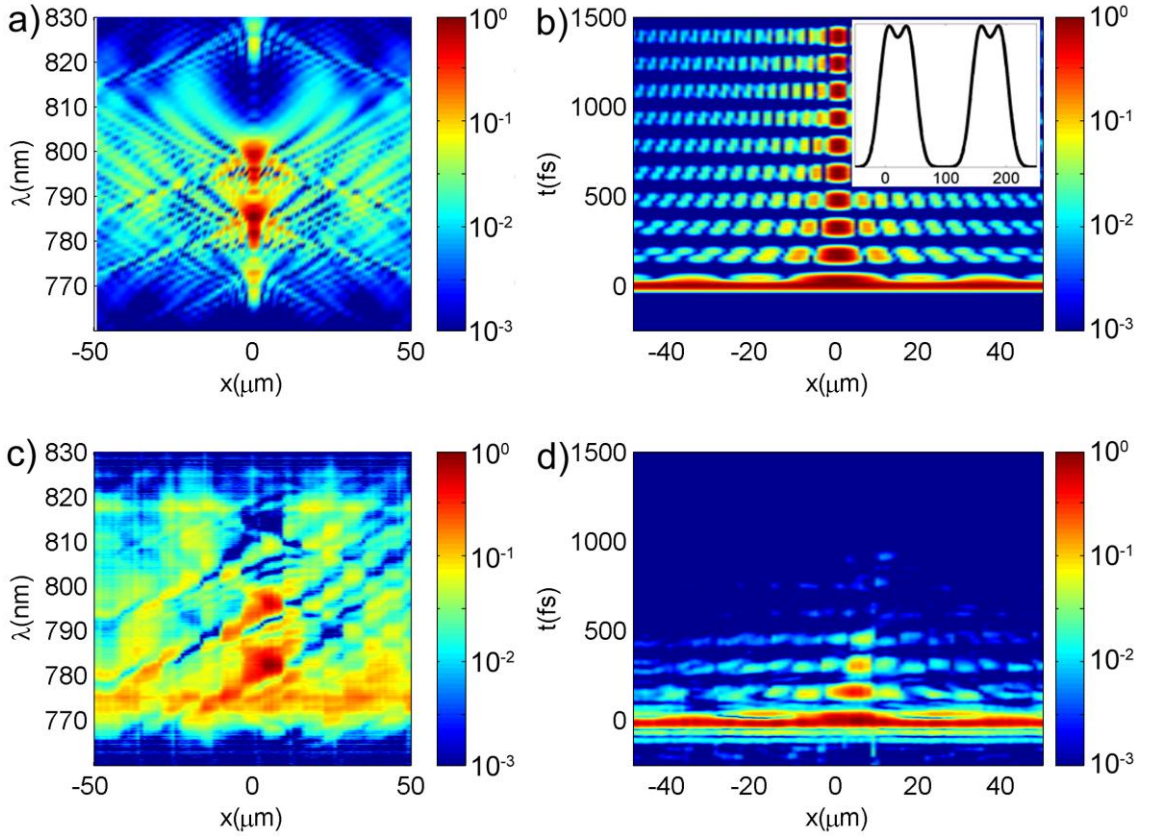


Fig. R.7. Espectro normalizado resuelto espacialmente (a) simulado y (c) experimental, y la intensidad espaciotemporal correspondiente para el (b) simulado y (d) experimental, en la distancia de propagación z = 35 mm. (b) Recuadro: Zoom de la intensidad en el eje temporal que muestra los dos primeros pulsos dobles del tren.

En particular, mostramos en la Fig. R.7 la distribución para la posición axial z = 35 mm (región de campo cercano) después del DOE. Hay un espectro muy estructurado, presentando algunos picos agudos (Fig. R.7a). Su dependencia con la coordenada transversal corresponde a una compleja distribución espaciotemporal del haz. En el dominio espaciotemporal (Fig. R.7b), hay un tren de pulsos dobles. Los picos de doble pulso están ligeramente separados (27 fs) y se distinguen en la simulación teórica (véase el zoom temporal de la intensidad en eje, $x = 0$, en el recuadro de la Fig. R.7b), y tienen una FHWM en intensidad de aproximadamente 65 fs. Fuera del eje ($x \neq 0$), las estructuras de doble pulso están separadas espacialmente y se pueden distinguir mejor. Los 10 pulsos dobles del tren están separados por 150 fs aproximadamente. En este experimento, ciertos pares de dos pulsos son poco visibles. La caída de los últimos pulsos del tren se debe principalmente a que provienen de los anillos exteriores del DOE y tienen una apertura numérica mayor de la detectable con la fibra, para esa distancia de propagación (campo cercano). También se analizaron las regiones de Fresnel y de campo lejano, comprobando teórica y experimentalmente la dinámica prevista.

## R3.2.Focalización con una lente difractiva kinoforme

Las aplicaciones de las lentes difractivas kinoformes (KDL) mencionadas anteriormente se basan en la dependencia cromática del foco, cuya distancia focal está dado por la expresión $f(\lambda) = f_c \lambda_c / \lambda$, donde $\lambda$ denota cualquier longitud de onda del pulso, $\lambda_c$ es la longitud de onda central del pulso, y $f_c$ es la focal longitud para $\lambda_c$. Las KDL son placas zonales de Fresnel especialmente diseñadas y modificadas, en las cuales los anillos opacos y transparentes son sustituidos con un perfil parabólico y transparente [36]. Para mejorar la eficiencia de la KDL, el perfil parabólico se trunca cada vez que hay un cambio de fase de $2\pi$ debido al espesor del material, como se ilustra en la Fig. R.8, lo que resulta en anillos con una amplitud máxima de fase $2\pi$. Los anillos están más cerca fuera de eje debido a la dependencia parabólica.

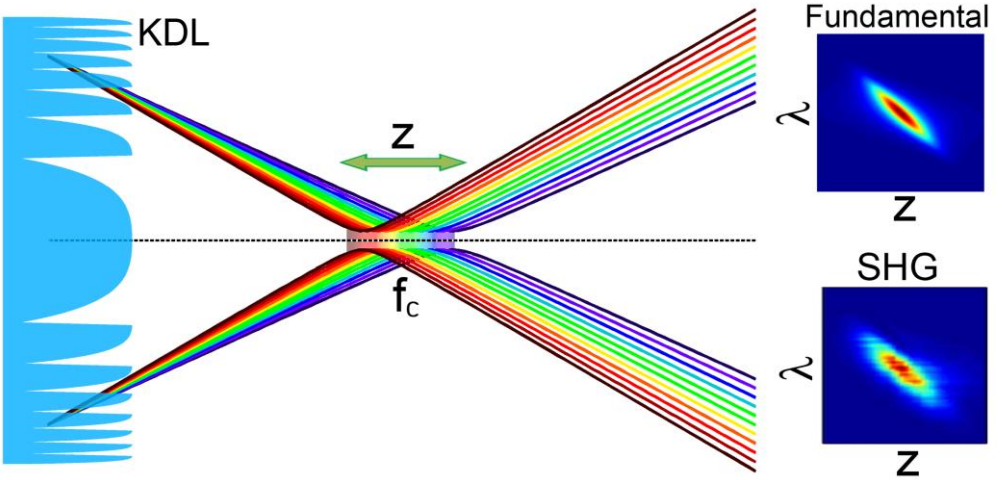


Fig. R.8. Esquema de una lente difractiva kinoforme (KDL) que focaliza un pulso láser ultracorto. Las longitudes de onda más cortas (rojas) focalizan antes que las más largas (azules). El espectro fundamental en el foco a lo largo del eje óptico se desplaza desde los rojos hasta los azules, de la misma forma que la generación de segundo armónico (SHG) en un cristal no lineal que se desplace a lo largo del foco (traza SHG extraída de [38]).

La dependencia focal en la longitud de onda, $f(\lambda) \propto \lambda^{-1}$, es responsable de una focalización cromática. Dado un haz de entrada colimado focalizado por una KDL, las longitudes de onda más largas (rojas) focalizarán antes que las longitudes de onda más cortas (azules). En nuestro caso, los pulsos láser ultracortos tienen un ancho de banda espectral considerable que hará que este efecto sea muy notable. Se ilustra este hecho en la Fig. R.8, donde se representa con diferentes colores (para distinguir las longitudes de onda, de roja a azul), el tamaño transversal del haz como una función de la distancia de propagación. Como consecuencia de ello, el espectro del pulso a lo largo del eje óptico se desplazará de longitudes de onda más rojas a más azules en la región de focalización (denotada por la flecha). La evolución simulada del espectro se representa en la traza marcada como "fundamental". Este hecho se ha aplicado, entre otros, para sintonizar la longitud de onda central de la SHG en un cristal no lineal desplazando el cristal a lo largo de la región de focalización (véase la traza de SHG experimental extraída de [38]). La relación entre la dependencia de la propagación lineal (en la traza fundamental) y la traza SHG es directa, y todo el espectro del pulso puede ser cubierto con sólo colocar el cristal en la posición correcta.

Los pulsos laser a la entrada tenían una duración 100 fs y longitud de onda central 795 nm. La distancia focal para $\lambda_c$ es $f_c = 106.6mm$ [34]. Las medidas experimentales de la región focal explorada (indicada por "z" en la Fig. R.8) se presentan en Fig. R.9 y R.10, en función de la distancia de propagación. Se muestra el resultado antes, en y después del foco para la longitud de onda. El espectro resuelto espectralmente (Fig. R.9a) muestra claramente que las longitudes de onda más rojas focalizan primero (su anchura espacial es más pequeña), en $z = f_c$ lo hace la longitud de onda central y, finalmente, está enfocada la longitud de onda más azul. El frente de ondas resuelto en frecuencias (Fig. R.9b) muestra que primero todas las longitudes de onda están convergiendo hacia el foco, entonces las longitudes de onda más rojas empiezan a divergir, mientras que las longitudes de onda más azules aún convergen y, después de foco, todas las longitudes de onda divergen.

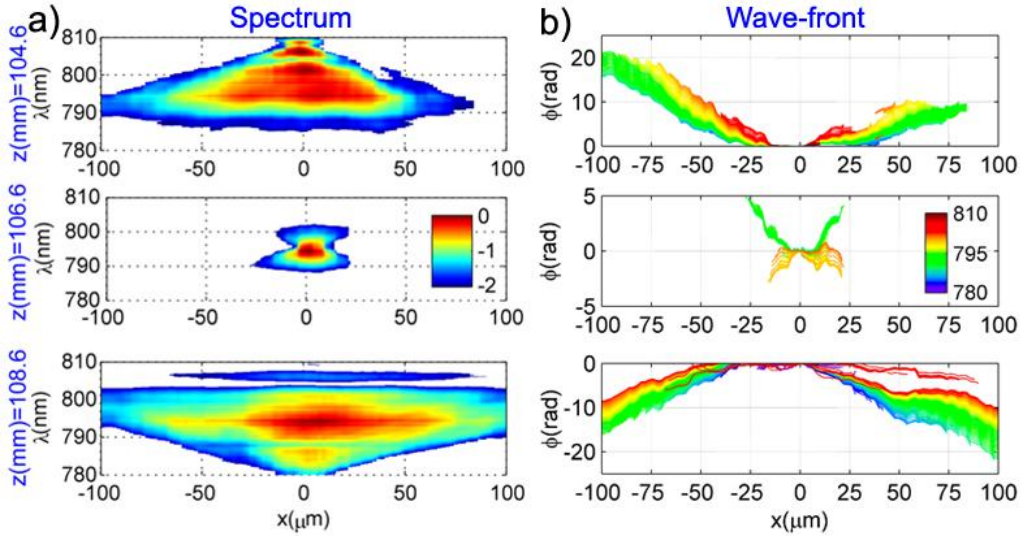


Fig. R.9. (a) Espectro resuelto espacialmente y (b) frente de ondas resuelto espectralmente, antes, en y después del foco (de arriba a abajo) de una lente difractiva kinoforme. Los diferentes colores representan cada longitud de onda en (b).

De las medidas resueltas espacialmente tomamos distintos cortes del espectro en el eje (Fig. R.10a-c), la intensidad en el eje (Fig. R.10d-f), y representamos la superficie de iso-intensidad correspondiente a $I(x,y,t)=\alpha \cdot I_{max}$ para $\alpha=0.1$ (Fig. R.10g-i). Hay desplazamiento al rojo antes de foco y al azul después de foco, debido a la focal cromática. En el foco, esto lleva a un estrechamiento espectral, que es el responsable de un pulso más largo en eje con respecto al pulso de entrada. Fuera de foco, la duración del pulso se reduce y hay *chirp* negativo y positivo, antes y después de foco, respectivamente. La superficie de iso-intensidad representa la evolución de la estructura del pulso combinada con la información del *chirp*. Hay una inversión del papel desempeñado por las longitudes de onda más rojas y más azules con respecto al foco. En $z = f_c$, la distribución se rige por las propiedades de los focos de los DOE [35].

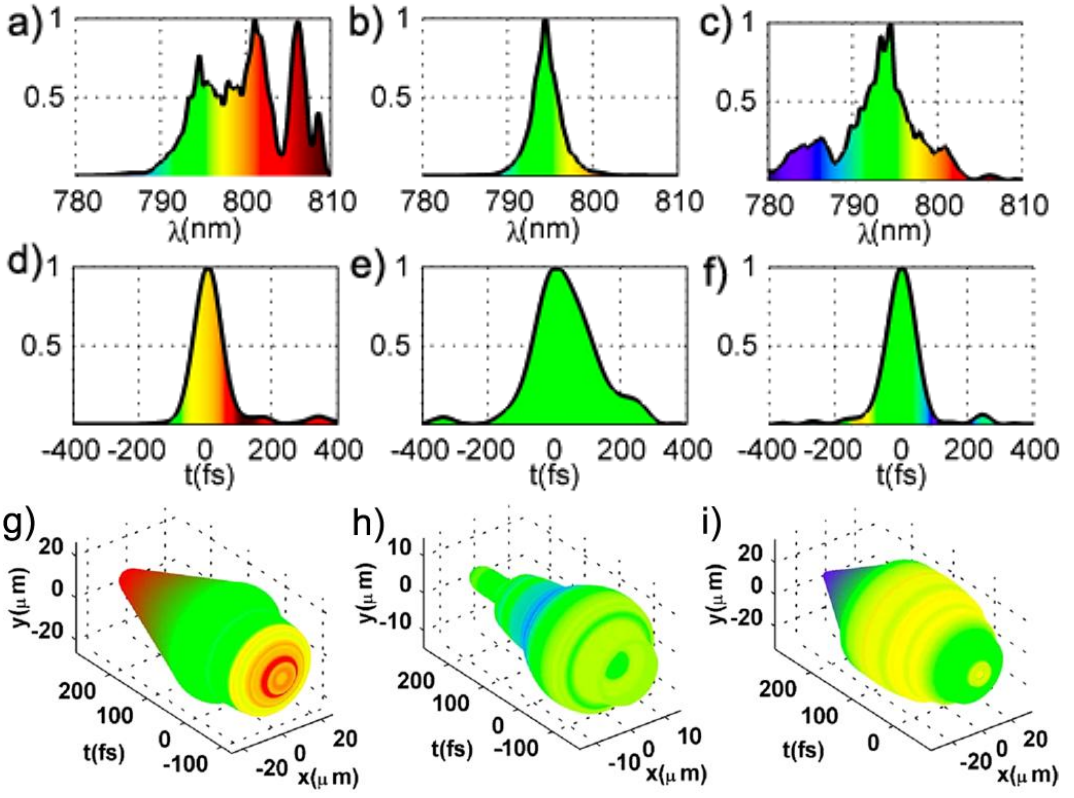


Fig. R.10. (a, b, c) Espectro en el eje, (d, e, f) intensidad en el eje, y (g, h, i) superficie de iso-intensidad coloreada por la longitud de onda instantánea, correspondientes a antes, en y después de foco (de izquierda a derecha).

La KDL presenta una dinámica muy rica que es muy útil para aplicaciones lineales y no lineales, por ejemplo, SHG, generación de supercontinuo, filamentación… Que sepamos, es la primera vez que es posible medir el frente de ondas de pulsos focalizados resuelto espectralmente.

# R4. ÓPTICA NO LINEAL Y PULSOS DE POCOS CICLOS

## R4.1.Dinámica de la filamentación

La propagación de la luz en régimen de filamentación consiste en el auto-guiado de la luz debido a un equilibrio entre la auto-focalización causada por el efecto Kerr y la defocalización originada por el plasma creado por ionización [43], lo cual se ilustra en la Fig. R.11. La auto-focalización se produce cuando el haz excede la potencia crítica para superar la difracción. El proceso ha atraído un gran interés durante los últimos años gracias a sus aplicaciones, por ejemplo para post-compresión, detección remota por LIBS, o la generación de radiación de terahercios [43]. Desde el punto de vista experimental, el proceso es muy difícil de caracterizar. Una de las razones es la alta intensidad existente en la región filamentación, de modo que por lo general, se mide el perfil temporal del pulso en el eje después de la etapa de filamentación. Además, hay un fuerte acoplamiento espaciotemporal de la luz durante el proceso, siendo la responsable de la dinámica como la división del pulso o ciclos de enfoque-reenfoque.

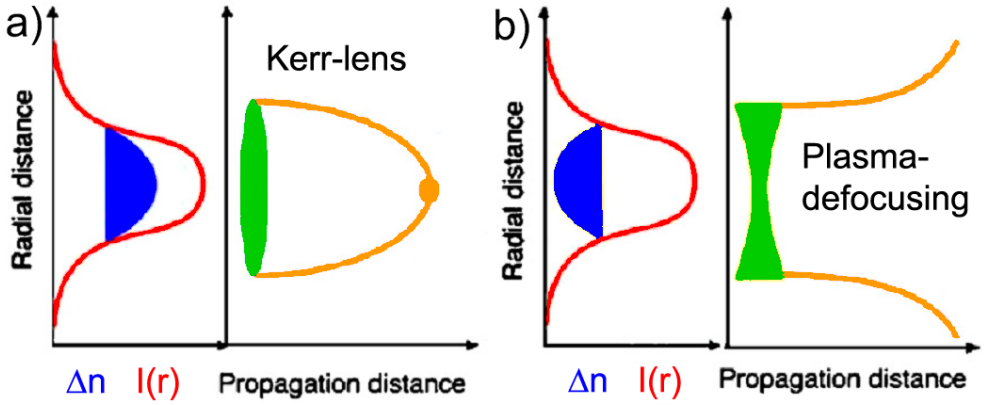


Fig. R.11. (a) Representación del efecto Kerr debido a la no linealidad del medio, que produce el autoenfoque del haz. (b) El plasma producido por la ionización tiene el efecto de desenfoque de una lente divergente. Figura extraída de [43].

Por esta razón, adaptamos STARFISH para la caracterización de la propagación no lineal de la luz [4]. En el caso de la filamentación, el espectro se ensancha debido a la auto-modulación de fase (SPM), el *self-steepening* y la ionización [43,44]. Por lo tanto, para el pulso de referencia es necesario utilizar una fibra hueca (con aire a presión atmosférica) seguida de un compresor de redes de difracción con el fin de obtener un espectro ensanchado por SPM. Sin embargo, la alta intensidad del filamento podría dañar la fibra, por lo que se utilizó una placa de vidrio para tomar una muestra del filamento, en combinación con un sistema de imagen 4f de la placa a la entrada de la

fibra. Esto también asegura propagación lineal dentro del sistema de imagen 4f. La distancia de propagación observada se varía cambiando la posición del iris de entrada y la lente de focalización (f=1.5 m). Se utilizaron pulsos de entrada de 100 fs a una longitud de onda central de 795 nm. La energía de la entrada era de 0.7 mJ y el diámetro del haz de entrada era de 4 mm.

En la Fig. R.12 se muestran los resultados de una selección de distancias de propagación (antes, durante y después del filamento). El espectro resuelto espacialmente (Fig. R.12a) y la intensidad espaciotemporal (Fig. R.12b) están representados en escala logarítmica. El foco no lineal ocurre antes que el lineal (150 cm) debido a la auto-focalización no lineal. En el dominio espacioespectral, puede seguirse el guiado del filamento, incluyendo los anillos espaciales (debidos a la emisión cónica) y el ensanchamiento espectral, más grande y más desplazado hacia los en el eje, comparado con la periferia. En la Fig. R.12b, se observa el acoplamiento espaciotemporal, así como división del pulso, competición de pulsos y auto-compresión en el eje de tiempo. Se incluye la sección de la intensidad en el eje (Fig. R.12c) para ilustrar esta dinámica. La comparación con las simulaciones teóricas apoya nuestras conclusiones [44].

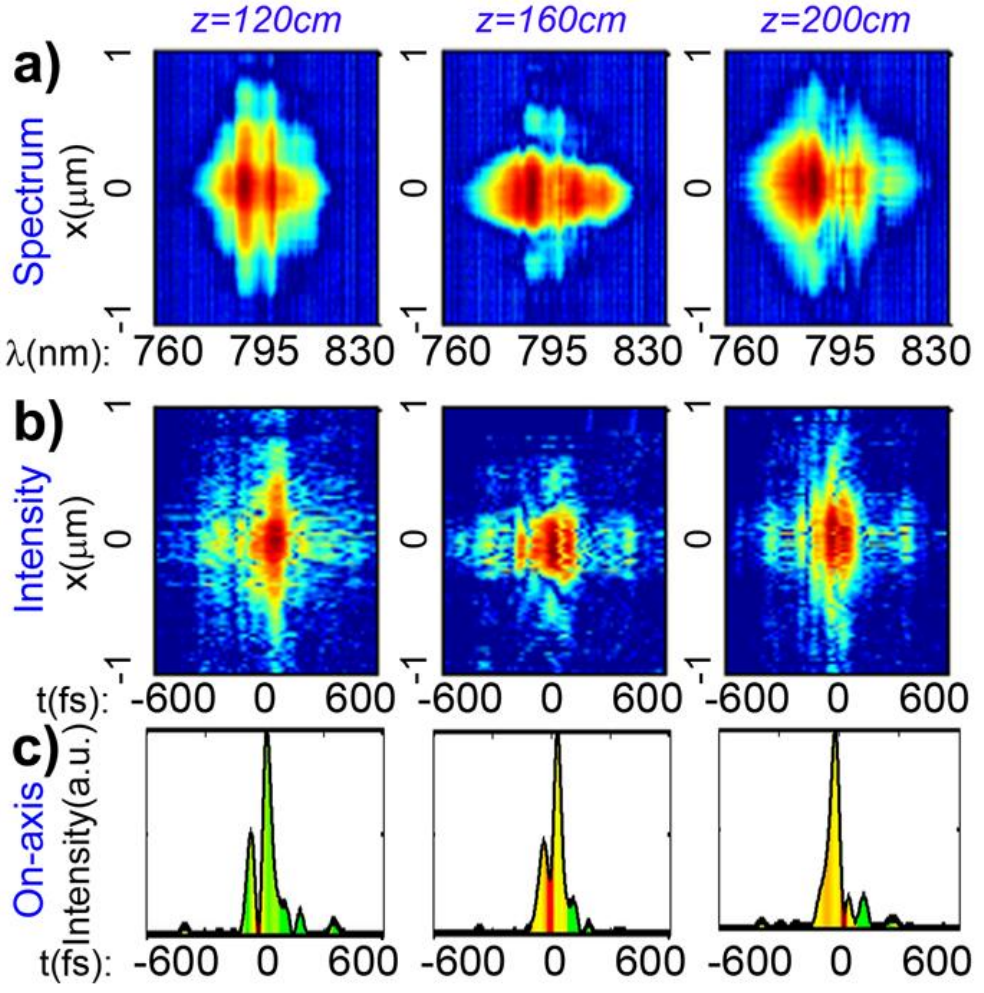


Fig. R.12. (a) Espectro resuelto espacialmente, (b) intensidad espaciotemporal, y (c) intensidad en eje, para diferentes distancias de propagación antes, durante y después del filamento.

## R4.2.Pulsos de pocos ciclos ópticos

El potencial para alcanzar pulsos de pocos ciclos (por debajo de 10 fs) mediante técnicas de post-compresión [45] nos llevó a la necesidad de adaptar STARFISH a este régimen. Por esta razón, hicimos nuevos experimentos en el laboratorio de femtosegundos del IFIMUP de la Universidade do Porto (UP), donde se desarrolló la técnica d-scan para la compresión y medida temporal de pulsos de pocos ciclos [46,47]. Usamos esta técnica para la medida del pulso referencia, que se utilizó para la posterior caracterización espaciotemporal con STARFISH. Se calibró la transmisión del acoplador de fibra óptica y se caracterizó la apertura numérica de la fibra en función de la longitud de onda. De esta manera, se encontró que se puede aplicar la técnica a pulsos con gran ancho de banda, con espectros en el rango de 550-1000 nm [48]. A continuación, se aplicó para estudiar el acoplamiento espaciotemporal de pulsos de pocos ciclos.

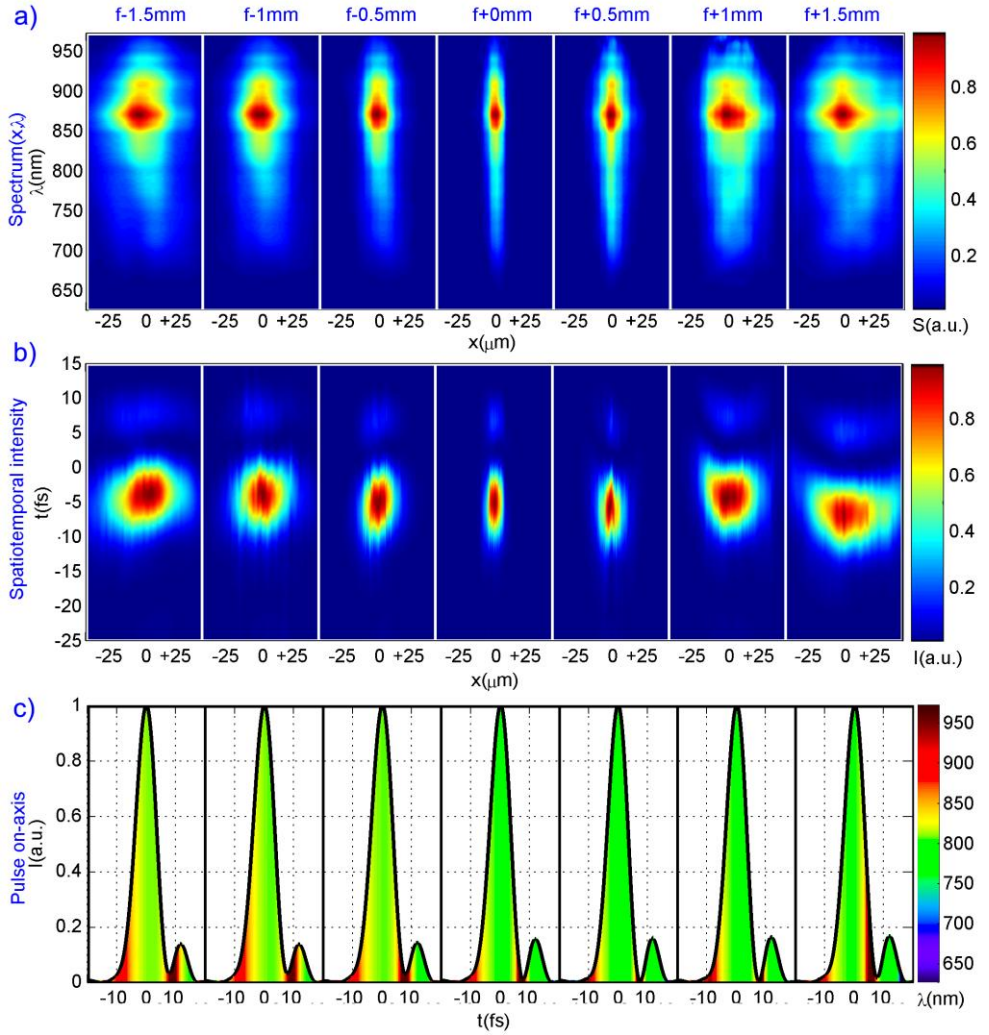


Fig. R.13. Evolución experimental del (a) espectro resuelto espacialmente, (b) la intensidad espaciotemporal, y (c) la intensidad en eje, a lo largo de la región de focalización (ver etiquetas en la parte superior de la figura).

En un primer experimento, se midieron pulsos de pocos ciclos focalizados por un espejo de parábola fuera de eje (espejo OAP) con distancia focal $f = 50mm$. La dinámica de focalización de pulsos de banda ultra ancha usando espejos OAP es de gran

importancia ya que se utilizan a menudo en experimentos de *high-field* o de elevada intensidad, como por ejemplo la generación de armónicos de orden elevado (HHG), y los espejos OAP son muy sensibles al alineamiento. En la Fig. R.13 se representan las medidas experimentales. En el espectro resuelto espacialmente y la intensidad espaciotemporal (Fig. R.13a y R.13b), se puede observar que los perfiles espectrales y temporales se conservan a lo largo de la región de, mientras que la anchura espacial es principalmente el único parámetro que cambia debido a la focalización [48]. La intensidad en el eje (Fig. R.13c) se representa para demostrar esta conclusión, dado que el perfil temporal permanece apenas sin cambios para las siete distancias de propagación exploradas. La duración promedio del pulso en el eje es $7.5 \pm 0.2\, fs$ (FWHM). También se da una estimación de la irradiancia pico a partir de la caracterización espaciotemporal de los pulsos [48].

En un reciente experimento, realizado también en la UP, hemos aplicado la post-compresión de pulsos intensos en una fibra hueca (HCF) [49]. A partir de pulsos amplificados de 25 fs, hemos llegado a pulsos de 4.5 fs (Fig. R.14b) con un espectro (Fig. R.14a) de 402 nm (anchura total a $1/e^2$) compatible con pocos pulsos de 4.1 fs. Estos son los pulsos más cortos medidos con la técnica STARFISH. La caracterización espacioespectral (Fig. R.14c) y espaciotemporal (Fig. R.14d) de la post-compresión en HCF nos permitió estudiar el *chirp* espacial de los pulsos con detalle. Hemos medido desplazamiento hacia los azules y pulsos más cortos sobre el eje con respecto a la periferia del perfil espacial, lo que está causado por la no linealidad que es más alta en el centro (donde el haz es más intenso). También hemos medido y simulado el foco de este pulso con un espejo OAP con el fin de verificar su idoneidad para experimentos posteriores, por ejemplo, de HHG.

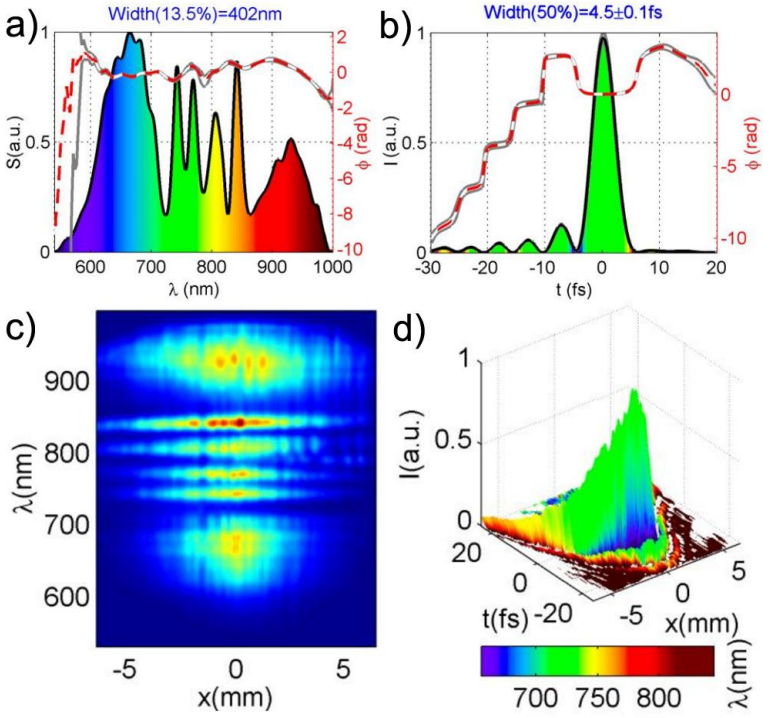


Fig. R.14. Amplitud y fase (a) espectral y (b) temporal de la medida del pulso en eje. (c) Espectro resuelto espacialmente y (d) intensidad espaciotemporal coloreada con la longitud de onda instantánea.

# R5. CONCLUSIONES

Se ha desarrollado una técnica para la medida espaciotemporal (y espacioespectral) de la amplitud y fase de pulses láser ultracortos basada en interferometría espectral resuelta espacialmente, la cual se conoce como STARFISH. El punto clave es el uso de un acoplador de fibra óptica monomodo y un espectrómetro comercial para la implementación de la interferometría espectral, los cuales se usan en una configuración *plug-and-play*. STARFISH es una técnica referenciada, en el sentido de que un pulso de referencia (conocido) se usa para caracterizar un pulso desconocido (test). El perfil espacial del pulso test se escanea con la correspondiente entrada de la fibra, para recuperar la distribución espaciotemporal del pulso. La propagación del pulso se estudia midiéndolo en distintos planos de propagación, lo cual se hace simplemente trasladando la entrada de la fibra o trasladando el "experimento" (p.ej., la lente focalizadora).

La técnica es muy simple, robusta y versátil, como se ha demostrado con la medida de una gran variedad de pulsos con fuerte acoplamiento espaciotemporal. El interferómetro asistido por acoplador de fibra reduce las exigencias del alineamiento. Además, el hecho de que el pulso de referencia no se escanee espacialmente proporciona estabilidad, reducción del ruido y elimina el requerimiento de que el haz de referencia sea espacialmente homogéneo. Gracias a la linealidad de la detección ─excepto en la caracterización de la referencia─, la técnica es apropiada para pulsos tanto con baja como con alta intensidad. En realidad, la mayoría de los experimentos se han hecho con pulsos intensos amplificados. Igualmente, se puede aplicar tanto para pulsos colimados como focalizados, gracias a la resolución espacial del núcleo de la fibra de $\sim 4\,\mu m$. En este aspecto, la apertura numérica de los pulsos medidos está limitada por la fibra colectora, cuya anchura total del cono de apertura es de ~10º para una transmisión del 50%.

La caracterización completa de la fase en el dominio espacioespectral proporciona información del frente de ondas de los pulsos resuelto espectralmente, incluso en el caso de pulsos focalizados. Esta detección del frente de ondas, en términos de resolución espacial y en frecuencias, es difícil o imposible de ser alcanzada con sensores convencionales. El inconveniente es la naturaleza multi-tiro de la técnica que puede introducir ruido en la reconstrucción debido a inestabilidades interferométricas. Se ha trabajado en este punto y se ha encontrado que se puede reducir considerablemente el ruido aislando el montaje (cubriendo para evitar corrientes de aire) y usando tiempos de adquisición adecuados.

Hemos aplicado la técnica a la medida de procesos no lineales en los cuales el pulso test experimenta ensanchamiento espectral y las intensidades son muy elevadas Se ha hecho de dos formas diferentes, en lo que se refiere al requerimiento de que el pulso de referencia tengo un contenido espectral igual o mayor que el del pulso test. En un

primer experimento, hicimos propagación no lineal en paralelo para ensanchar el espectro de la referencia, mientras que en un segundo experimento tomamos una parte del pulso test ensanchado espectralmente para tener un pulso de referencia.

Respecto a los rangos temporal y espectral, la técnica también es muy versátil. Vienen dados por la respuesta del acoplador de fibra óptica y la resolución y rango espectral libre del espectrómetro. En lo que concierne al espectrómetro, hemos utilizado tres aparatos comerciales diferentes. El primero de ellos, con una resolución de 0.1 nm en el intervalo 700-900 nm, es compatible con la medida de pulsos con espectro contenido en dicho intervalo, y duraciones temporales desde unos 20 fs hasta pocos picosegundos. Los otros dos espectrómetros tienen un rango espectral mayor y menor resolución, así que son apropiados para la medida de espectros compatibles con pulsos de pocos ciclos y duraciones de varias centenas de femtosegundos. En este caso, la menor duración posible está limitada por el acoplador de fibra, que opera desde 550 nm hasta 1000 nm aproximadamente, lo cual significa que se pueden medir pulsos de ~4 fs.

STARFISH ha sido aplicado en un amplio rango de experimentos y aplicaciones. En el campo de óptica difractiva, ha jugado los roles de predecir y corroborar la dinámica espaciotemporal de los pulsos difractados. A través de la comparación entre los resultados experimentales y las simulaciones teóricas, el buen acuerdo encontrado entre ellos ha servido para validar tanto los modelos teóricos como las medidas experimentales. Se han hecho múltiples aplicaciones, desde el estudio del comportamiento general de una placa zonal focalizadora a lo largo de distintas regiones de propagación, hasta la caracterización de *shapers* difractivos y módulos compensadores de dispersión, pasando por la rica dinámica de la focalización con una lente difractiva kinoforme.

Se han obtenido resultados muy ilustrativos en el estudio de la dinámica no lineal de la luz propagándose en régimen de filamentación. La caracterización de este proceso es muy difícil de llevar a cabo desde el punto de vista experimental, de modo que los resultados obtenidos son muy valiosos de cara a interpretar la división del pulso, la auto-compresión, flujos de energía-densidad y la rica dinámica presente durante este proceso. Esta información es muy prometedora para ayudar en el control y la optimización del proceso de filamentación y en sus aplicaciones, tales como post-compresión de pulsos y la posterior generación de armónicos de orden elevado.

Del mismo modo, la aplicación de pulsos de pocos ciclos ópticos muestra un gran potencial para experimentos adicionales hacia la generación de pulsos intensos de pocos ciclos o de un único ciclo. En primer lugar, el estudio de la dinámica de focalización de pulsos de baja intensidad y gran ancho de banda de un oscilador ha confirmado su pertinencia para posteriores experimentos. En segundo lugar, se generaron pulsos intensos de menos de dos ciclos en una fibra hueca. La caracterización de su estructura espacioespectral y espaciotemporal demostró que el ensanchamiento espectral y la compresión dependen de la coordenada radial debido a la naturaleza no lineal del proceso.

Todo ello, hace que STARFISH sea una herramienta de diagnóstico consolidada y muy potente, que se puede aplicar en escenarios muy diversos de forma versátil. En el futuro, esperamos que las capacidades de STARFISH continúen creciendo y que se abran otros campos de aplicación.

# REFERENCIAS


[1] Anthony E. Siegman, Chapter 17: "Physical properties of Gaussian beams" in *Lasers*, University Science Books (1986).

[2] I. A. Walmsley and C. Dorrer, "Characterization of ultrashort electromagnetic pulses," Adv. Opt. Photon. 1, 308-437 (2009).

[3] En la página web del grupo del Prof. Trebino, http://frog.gatech.edu/, se pueden encontrar totoriales y referencias sobre pulsos laser ultracortos y su caracterización.

[4] R. V. Shack and B. C. Platt, "Production and use of a lenticular Hartmann screen," J. Opt. Soc. Am. 61, 656-660 (1971).

[5] B. Alonso, I. J. Sola, O. Varela, J. Hernández-Toro, C. Méndez,, J. San Román, A. Zaïr, and L. Roso "Spatiotemporal amplitude-and-phase reconstruction by Fourier-transform of interference spectra of high-complex-beams," J. Opt. Soc. Am. B. 27, 933-940 (2010).

[6] Robert W. Boyd, *Nonlinear Optics*, 2nd Ed., Academic Press (2003).

[7] S. Akturk, X. Gu, P. Bowlan, and R. Trebino, "Spatio-temporal couplings in ultrashort laser pulses," J. Opt. 12, 093001 (2010).

[8] J. Jasapara and W. Rudolph, "Characterization of sub-10-fs pulse focusing with high-numerical-aperture microscope objectives," Opt. Lett. 24, 777-779 (1999).

[9] P. Bowlan, P. Gabolde, and R. Trebino, "Directly measuring the spatio-temporal electric field of focusing ultrashort pulses," Opt. Express 15, 10219-10230 (2007).

[10] O. Mendoza-Yero, B. Alonso, O. Varela, G. Mínguez-Vega, I. J. Sola, J. Lancis, V. Climent, and L. Roso, "Spatio-temporal characterization of ultrashort pulses diffracted by circularly symmetric hard-edge apertures: theory and experiment", Opt. Express 18, 20900-20911 (2010).

[11] B. Alonso, I. J. Sola, J. San Román, O. Varela, and L. Roso, "Spatiotemporal evolution of light during propagation in filamentation regime", J. Opt. Soc. Am. B 28, 1807-1816 (2011).

[12] D. Strickland, and G. Mourou, "Compression of amplified chirped optical pulses," Opt. Commun. 56, 219-221 (1985).

[13] A. Couairon and A. Mysyrowicz, "Femtosecond filamentation in transparent media," Phys. Rep. 441, 47-189 (2007).

[14] S. Akturk, X. Gu, P. Gabolde, and R. Trebino, "The general theory of first-order spatio-temporal distortions of Gaussian pulses and beams," Opt. Express 13, 8642-8661 (2005).

[15] Z. Bor, "Distortion of femtosecond laser pulses in lenses," Opt. Lett. 14, 119-121 (1989).

[16] U. Fuchs, U. D. Zeitner, and A. Tünnermann, "Ultra-short pulse propagation in complex optical systems," Opt. Express 13, 9903–9908 (2005).

[17] S. P. Veetil, C. Vijayan, D. K. Sharma, H. Schimmel, and F. Wyrowski, "Diffraction induced space-time splitting effects in ultra-short pulse propagation," J. Mod. Opt. 53, 1819–1828 (2006).

[18] A. Couairon, M. Franco, G. Méchain, T. Olivier, B. Prade, and A. Mysyrowicz, "Femtosecond filamentation in air at low pressures: Part I: theory and numerical simulations," Opt. Commun. 259, 265-273 (2006).

[19] S. Rivet, "Caractérisation complète d'un faisceau laser impulsionnel femtoseconde: mise en évidence et analyse du couplage spatio-temporel dans la propagation linéaire et non-linéaire," Ph.D. Thesis, Université de Bordeaux I (2001).

[20] C. Dorrer, E. M. Kosik, and I. A. Walmsley, "Direct space-time characterization of the electric fields of ultrashort optical pulses," Opt. Lett. 27, 548-50 (2002).

[21] J. Trull, O. Jedrkiewicz, P. Di Trapani, A. Matijosius, A. Varanavicius, G. Valiulis, R. Danielius, E. Kucinskas, A. Piskarskas, and S. Trillo, "Spatiotemporal three-dimensional mapping of nonlinear X waves," Phys. Rev. E 69, 026607 (2004).

[22] P. Gabolde and R. Trebino, "Single-shot measurement of the full spatio-temporal field of ultrashort pulses with multi-spectral digital holography," Opt. Express 14, 11460-7 (2006).

[23] E. Rubino, D. Faccio, L. Tartara, P. K. Bates, O. Chalus, M. Clerici, F. Bonaretti, J. Biegert, and P. Di Trapani, "Spatiotemporal amplitude and phase retrieval of space-time coupled ultrashort pulses using the Shackled-FROG technique," Opt. Lett. 34, 3854-3856 (2009).

[24] B. Alonso, R. Borrego-Varillas, C. Hernández-García, J. A. Pérez-Hernández, and C. Romero (editors), *El láser, la luz de nuestro tiempo*, Globalia Ediciones Anthema (2010).

[25] Eugene Hecht, *Optics*, 4th Ed., Addison Wesley (2002).

[26] Claude Rullière (editor), *Femtosecond Laser Pulses: Principles and Experiments*, 2nd ed., Springer (2004).

[27] Rick Trebino (editor), *Frequency-Resolved Optical Gating: The Measurement of Ultrashort Laser Pulses*, Kluwer Academic, (2002).

[28] D. J. Kane and R. Trebino, "Characterization of arbitrary femtosecond pulses using frequency-resolved optical gating," IEEE J. Quantum Electron. 29, 571–579 (1993).

[29] T. Tsang, M. A. Krumbügel, K. W. Delong, D. N. Fittinghoff, and R. Trebino, "Frequency-resolved optical-gating measurements of ultrashort pulses using surface third-harmonic generation," Opt. Lett. 21, 1381–1383 (1996).

[30] C. Iaconis and I. A. Walmsley, "Spectral phase interferometry for direct electric-field reconstruction of ultrashort optical pulses," Opt. Lett. 23, 792–794 (1998).

[31] L. Lepetit, G. Cheriaux, and M. Joffre, "Linear techniques of phase measurement by femtosecond spectral interferometry for applications in spectroscopy," J. Opt. Soc. Am. B 12, 2467-74 (1995).

[32] D. E. Adams, T. A. Planchon, A. Hrin, J. A. Squier, and C. G. Durfee, "Characterization of coupled nonlinear spatiospectral phase following an ultrafast self-focusing interaction," Opt. Lett. 34, 1294-6 (2009).

[33] B. Alonso, I. J. Sola, O. Varela, C. Mendez, I. Arias, J. San Román, A. Zaïr, and L. Roso, "Spatio-temporal characterization of laser pulses by spatially resolved spectral interferometry," Opt. Pura Apl. 43, 1-7 (2010).

[34] B. Alonso, R. Borrego-Varillas, O. Mendoza-Yero, I. J. Sola, J. San Román, G. Mínguez-Vega, and L. Roso, "Frequency resolved wavefront retrieval and dynamics of diffractive focused ultrashort pulses," J. Opt. Soc. Am. B 29, 1993-2000 (2012).

[35] O. Mendoza-Yero, B. Alonso, O. Varela, G. Mínguez-Vega, I. J. Sola, J. Lancis, V. Climent, and L. Roso, "Spatiotemporal characterization of ultrashort pulses diffracted by circularly symmetric hard-edge apertures: theory and experiment," Opt. Express 18, 20900–20911 (2010).

[36] V. Moreno, J. F. Román, and J. R. Salgueiro, "High efficiency diffractive lenses: Deduction of kinoform profile", Am. J. Phys. 65, 556-562 (1997).

[37] O. Mendoza-Yero, B. Alonso, G. Mínguez-Vega, I. J. Sola, J. Lancis, and J. A. Monsoriu, "Synthesis of fractal light pulses by quasi-direct space-to-time pulse shaping," Opt. Lett. 37, 1145-1147 (2012).

[38] G. Mínguez-Vega, C. Romero, O. Mendoza-Yero, J. R. Vázquez de Aldana, R. Borrego-Varillas, C. Méndez, P. Andrés, J. Lancis, V. Climent, and L. Roso, "Wavelength tuning of femtosecond pulses generated in nonlinear crystals by using diffractive lenses," Opt. Lett. 35, 3694-3696 (2010).

[39] C. Romero, R. Borrego-Varillas, A. Camino, G. Mínguez-Vega, O. Mendoza-Yero, J. Hernández-Toro, and J. R. Vázquez de Aldana, "Diffractive optics for spectral control of the supercontinuum generated in sapphire with femtosecond pulses," Opt. Express 19, 4977-4984 (2011).

[40] Y. Fu, H. Xiong, H. Xu, J. Yao, B. Zeng, W. Chu, Y. Cheng, Z. Xu, W. Liu, and S. L. Chin, "Generation of extended filaments of femtosecond pulses in air by use of a single-step phase plate", Opt. Lett. 34, 3752-3754 (2009).

[41] R. Bartels, S. Backus, E. Zeek, L. Misoguti, G. Vdovin, I. P. Christov, M. M. Murnane, and H. C. Kapteyn, "Shaped-pulse optimization of coherent emission of high-harmonic soft X-rays," Nature 406, 164-166 (2000).

[42] R. Martínez-Cuenca, O. Mendoza-Yero, B. Alonso, I. J. Sola, G. Mínguez-Vega, and J. Lancis, "Multibeam second-harmonic generation by spatiotemporal shaping of femtosecond pulses," Opt. Lett. 37, 957-959 (2012).

[43] A. Couairon and A. Mysyrowicz, "Femtosecond filamentation in transparent media," Phys. Rep. 441, 47-189 (2007).

[44] B. Alonso, I. J. Sola, J. San Román, O. Varela, and L. Roso, "Spatiotemporal evolution of light during propagation in filamentation regime", J. Opt. Soc. Am. B 28, 1807-1816 (2011).

[45] B. Alonso, R. Borrego-Varillas, Í. J. Sola, Ó. Varela, A. Villamarín, M. V. Collados, J. San Román, J. M. Bueno, and L. Roso, "Enhancement of filamentation postcompression by astigmatic focusing," Opt. Lett. 36, 3867-3869 (2011).

[46] M. Miranda, T. Fordell, C. Arnold, A. L'Huillier, and H. Crespo, "Simultaneous compression and characterization of ultrashort laser pulses using chirped mirrors and glass wedges," Opt. Express 20, 688-697 (2012).

[47] M. Miranda, T. Fordell, C. Arnold, F. Silva, B. Alonso, R. Weigand, A. L'Huillier, and H. Crespo, "Characterization of broadband few-cycle laser pulses with the d-scan technique," Opt. Express 20, 18732-18743 (2012).

[48] B. Alonso, I. J. Sola, J. San Román, O. Varela, and L. Roso, "Spatiotemporal evolution of light during propagation in filamentation regime," J. Opt. Soc. Am. B 28, 1807-1816 (2011).

[49] B. Alonso, M. Miranda, F. Silva, V. Pervak, J. Rauschenberger, J. San Román, I. J. Sola, and H. Crespo, "Generation and spatiotemporal characterization of 4.5-fs pulses from a hollow-core fiber compressor," submitted (2012).